The Use of PET/CT for the Tracking of Positron Labelled Cell Therapies to Investigate Cell Distribution and Therapeutic Efficacy in the Diseased Lung

Christina Katsiva

A dissertation submitted in partial fulfillment

of the requirements for the degree of

Doctor of Philosophy

Faculty of Engineering

Department of Medical Physics and Biomedical Engineering

University College London

July 2025

I, Christina Katsiva confirm that the work presented in this thesis is my own. Where information has been derived from other sources, I confirm that this has been indicated in the thesis.

Abstract

Lung cancer is the leading cause of cancer death worldwide with new treatment options urgently needed. Cell therapies can potentially answer this unmet clinical need and improve the life expectancy of lung cancer patients. However, the clinical translation of cell treatments is hindered by the limited knowledge of *in vivo* distribution of the therapeutic cells in patients. In this work, a clinically translatable direct radiolabelling method of [^{89}Zr]Zr-oxine was developed for a GMP grade mesenchymal stem cell therapy for the treatment of lung cancer.

In vitro studies were conducted to assess cell viability and toxicity due to the radiolabelling process. Results showed time and amount of radioactivity dependent sensitivity to [^{89}Zr]Zr-oxine labelling, as well as that the GMP kit formulation used for radiolabelling was non-toxic to the cells. For the application of the radiolabelling method *in vivo*, an orthotopic mouse model of lung cancer was developed, that represented clear areas of tumour tissue and lung parenchyma, allowing for the clear segmentation of those areas using imaging, for the understanding of the *in vivo* distribution of the therapeutic cells in the diseased lung. Furthermore, preclinical phantom studies were conducted to assess a preclinical PET/CT system ahead of the *in vivo* imaging study, identifying the significantly higher noise present in ^{89}Zr imaging studies.

The radiolabelling method developed was applied to the orthotopic mouse model of lung cancer, for the longitudinal *in vivo* tracking of the GMP mesenchymal stem cell therapy using PET/CT imaging. Naïve and tumour bearing mice were utilised and the cells were successfully tracked *in vivo* up to 7 days post-injection. Quantitative measurements were acquired for different organs with the majority of radioactivity accumulating in the lungs. No differences were identified between tumour bearing and control mice. After the application of corrections a statistically significant difference was identified between lung and tumour, in agreement with the *ex vivo* measurements conducted, highlighting the importance of applying corrections for the interpretation of

imaging findings. Finally, clinical phantoms were acquired to assess the image quality and quantitative accuracy of clinical PET/CT systems for the identification of the optimal imaging protocol that could be applied in clinical cell tracking studies of ^{89}Zr using PET/CT imaging.

This thesis, presents a clinically translatable direct radiolabelling method of [^{89}Zr]Zr-oxine for mesenchymal stem cells that can be applied as part of clinical trials, to understand the *in vivo* distribution of the therapeutic cells using PET/CT imaging, and assess the therapeutic efficacy and possible adverse effects of a stem cell therapy.

Impact Statement

Cell therapies are developed for a vast range of pathologies and clinical trials are conducted to assess the safety and therapeutic efficacy of prospective cell treatments. Despite the need to understand the *in vivo* distribution of a cell treatment, *in vivo* cell tracking by imaging is rarely utilised during clinical trials to understand the biodistribution of cells in patients, due to the lack of safe and easily clinically applicable methods of cell tracking.

In vivo cell tracking by PET/CT imaging using ^{89}Zr is a promising method that could be applied in patients, to understand the *in vivo* distribution of a cell treatment. In this thesis, a clinically translatable direct radiolabelling method using [^{89}Zr]Zr-oxine was developed for a clinical GMP mesenchymal stem cell therapy for lung cancer. The radiolabelling method was first assessed *in vitro* to validate that the method was non-toxic to the cells. Then the radiolabelled cells were successfully tracked *in vivo* in naïve and tumour bearing mice using PET/CT imaging. Finally, the preclinical imaging findings were applied to clinical phantoms, to understand the challenges of imaging with ^{89}Zr, and to identify the optimal imaging protocol for *in vivo* cell tracking studies using ^{89}Zr in patients.

To summarise, the work of this thesis provides a clinically translatable radiolabelling method that can be applied as part of a clinical trial to offer information on therapeutic cell distribution, therapeutic cell homing to tumours, and therapeutic efficacy of a stem cell treatment, and has identified optimal imaging protocol parameters that can be used in patient studies.

Summary of Contributions

Poster presentations

The following conference contributions have been presented from the work of this thesis:

- C. Katsiva, B. F. Holman, M. M. Murillo, P. S. Patrick, and T. L. Kalber. *Assessment of a lung cancer mouse model using microCT and PET/CT imaging*, Preclinical Nuclear Imaging Symposium (PNI) 2023, Hull - United Kingdom.
- C. Katsiva, P. S. Patrick, M. M. Murillo, B. F. Holman, and T. L. Kalber. *Development of minimally invasive orthotopic lung cancer mouse models for translational research using preclinical imaging*, European Molecular Imaging Meeting (EMIM) 2024, Porto - Portugal.
- C. Katsiva, P. S. Patrick, M. M. Murillo, B. F. Holman, D. J. Stuckey, M. F. Lythgoe and T. L. Kalber. *Assessment of a one-step GMP grade kit for ^{89}Zr-oxine direct labelling of stem cells and PET in vivo tracking of a clinical stem cell product in a mouse model of lung cancer*, European Molecular Imaging Meeting (EMIM) 2025, Bilbao - Spain.

Award

Cohen Award - post graduate research excellence award (2000 £), 2024, The Worshipful Company of Scientific Instrument Makers.

Acknowledgements

Completing this PhD has been one of the most challenging and rewarding experiences of my life. It was a turbulent journey and I am deeply grateful to everyone who supported me along the way.

First and foremost, I would like to express my deepest gratitude to my primary supervisor, Prof Tammy Kalber, for her unwavering guidance, insightful feedback, and continuous support throughout the course of my research. I am also deeply grateful to Dr Stephen Patrick, Prof Mark Lythgoe, Prof Daniel Stuckey, Prof Jack Wells and Dr Ian Harrison for supporting me and always being happy to offer guidance and answer my questions at every stage of my research. My gratitude also goes to Dr Amaia Carrascal-Miniño, Dr Vincent Muczynski and Prof Sam Janes for their invaluable support at critical stages of my project.

I have been fortunate to be part of the amazing Centre for Advanced Biomedical Imaging (CABI) that holds a very special place in my heart. My PhD experience would not have been the same anywhere else. I got the chance to work with an incredible group of colleagues and make lifelong friends, whose support, helpful discussions, and shared coffee and lunch breaks made the tough days easier. I would like to especially thank Dr Shereen Nizari who supported me in more ways than I can count, your kindness and encouragement meant everything.

I am truly thankful to Dr Beverley Holman and everyone at the Department of Nuclear Medicine at Royal Free Hospital for providing guidance and supporting my research. Furthermore, I would like to thank my industrial GSK supervisors Mr Fred Wilson and Dr Miguel Murillo for offering valuable advice during my PhD. My gratitude also goes to the EPSRC Centre for Doctoral Training i4health and the UCL Department of Medical Physics and Biomedical Engineering for providing technical resources and pastoral support that have enabled this research.

To my close friends, Eleni Theodoridou, Eleni Papaioannou, Zoi Papari and Federica

Ninno, thank you for reminding me there is a world beyond the PhD and for being my escape when I needed it most.

Finally, I owe my deepest thanks to my family. Your love, patience, and belief in me have been my foundation. To my parents and my brothers your support means more than I can express.

I acknowledge that this work is co-funded by the EPSRC Centre for Doctoral Training in Intelligent, Integrated Imaging In Healthcare (i4health) (EP/S021930/1) and GlaxoSmithKline Research & Development Ltd (BIDS3000035237). The work is also supported by the Department of Nuclear Medicine at Royal Free Hospital, London - United Kingdom.

Table of Contents

List of Figures

List of Tables

List of Abbreviations

2D: two-dimensional

3D: three-dimensional

ADSCs: Adipocyte-Derived Stem Cells

AFC: Air Fraction Correction

AFOV: Axial Field of View

ALK: Anaplastic Lymphoma Kinase

ATP: Adenosine Triphosphate

BFC: Blood Fraction Correction

BLI: Bioluminescent Imaging

BRAF: V-Raf murine sarcoma viral oncogene homolog B1

BSA: Bovine Serum Albumin

Bq: Becquerel

CAR: Chimeric Antigen Receptor

CBM: Continuous Bed Motion

CEA: Carcinoembryonic Antigen

CRS: Cytokine Release Syndrome

CT: Computed Tomography

DDG: Data Driven Gating

DFO: Desferrioxamine

DMSO: Dimethyl Sulfoxide

DR4 and DR5: Death Receptor 4/5

DTPA: Diethylenetriamine pentaacetate

EGFR: Epidermal Growth Factor Receptor

EtOAc: Ethyl Acetate

FBP: Filtered Backprojection

FBS: Foetal Bovine Serum

FDG: 2-deoxy-2-fluoro-D-glucose or Fluorodeoxyglucose

FOV: Field of View

FWHM: Full Width at Half Maximum

GEMMs: Genetically Engineered Mouse Models

GMP: Good Manufacturing Practices

HEPES: 4-(2-hydroxyethyl)-1-piperazineethanesulfonic acid

HS: High Sensitivity

HSV1-tk: Herpes Simplex Virus type 1 thymidine kinase

HU: Hounsfield Units

IF: Immunofluorescence

IMS: Industrial Methylated Spirits

LAFOV: Long Axial Field of View

LOR: Line of Response

LSO: Lutetium Oxyorthosilicate

MET: Mesenchymal-Epithelial Transition

MGV: Mean Grey Values

MPM: Malignant Pleural Mesothelioma

MRD: Maximum Ring Difference

MRI: Magnetic Resonance Imaging

MSCTRAIL: Mesenchymal Stem Cells engineered to express TRAIL

MSCs: Mesenchymal Stem Cells

NECR: Noise Equivalent Count Rate

NEMA: National Electrical Manufacturers Association

NIS: Sodium Iodide Symporter

NK: Natural Killer

NNK: 4-(methylnitrosamino)-1(3-pyridyl)-1-butanone

NSCLC: Non-Small Cell Lung Cancer

NSG: NOD Scid Gamma

NTRK: Neurotrophic Tropomyosin Receptor Kinase

OSEM: Ordered Subset Expectation Maximization

PD-1: Programmed Death 1

PD-L1 and PD-L2: Programmed Death-Ligand 1/2

PDXs: Patient-Derived Xenografts

PET: Positron Emission Tomography

PHA: Pulse Height Analyser

PMT: Photomultiplier tube

PS: phosphatidylserine

PSF: Point Spread Function

PVE: Partial Volume Effect

QC: Quality Control

RC: Recovery Coefficient

RET: Rearranged during Transfection

RLU: Relative Light Units

ROS-1: ROS proto oncogene 1

SAFOV: Short Axial Field of View

SCLC: Small Cell Lung Cancer

SD: Standard Deviation

SF: Scatter Fraction

SI: International System of Units

SNR: Signal to Noise Ratio

SOC: Spill Over Correction

SOR: Spill-Over Ratio

SPECT: Single-Photon Emission Computed Tomography

SPIONs: Superparamagnetic Iron Oxide Nanoparticles

SS: Step-and-Shoot

SUV: Standardized Uptake Value

SiPM: Silicon Photomultiplier

TACTICAL: Targeted Stem Cells Expressing TRAIL as a Therapy for Lung Cancer

TFE: Tissue Fraction Effect

TLC: Thin Layer Chromatography

TOF: Time-of-Flight

TRAIL: Tumour necrosis factor (TNF)-related apoptosis-inducing ligand

UHS: Ultra-High Sensitivity

UK: United Kingdom

USA: United States of America

VATS: Video-assisted thoracoscopic surgery

WBC: White Blood Cells

WHO: World Health Organisation

bpm: breaths per minute

cps: counts per second

hESCs: human Embryonic Stem Cells

hPSCs: human Pluripotent Stem cells

hiPSCs: human induced Pluripotent Stem Cells

mAbs: monoclonal Antibodies

rhTRAIL: recombinant human TRAIL

CHAPTER 1

Introduction

According to the Global Cancer Observatory of the International Agency for Research on Cancer - World Health Organisation (WHO), lung cancer is currently the third most common cancer type in the world, after breast and prostate cancers, however it has the highest mortality rate. Compared with breast cancer, which is the most common type of cancer, lung cancer has a 28% higher mortality rate [1]. For England, according to Cancer Research UK, lung cancer has an approximate 20% 5 year survival rate, for all stages and types [2]. Furthermore, it is estimated by the WHO that by 2050 there is going to be an 86% increase in new cases and an 95% increase in new deaths, due to lung cancer, worldwide [1].

Smoking tobacco is the leading cause of lung cancer [3, 4]. Despite changes in the smoking habits of the general population, new lung cancer cases are expected to increase, which can be attributed to a few different factors. The ageing population affects the increase in cases, as lung cancer risk increases with age and the latency period for lung cancer development can be decades, depending on the type of lung cancer [5]. Today detection and diagnosis has improved thanks to Computed Tomography (CT), that can identify lung cancer tumours which may have gone undiagnosed in the past. Lung cancer screening programmes are being established for the early diagnosis of lung cancer, as early diagnosis improves survival. These programmes offer CT scans to at risk individuals with higher probability of developing lung cancer and contribute to the increase in new cases. Such programmes have been established in the United States of America (USA), Japan, South Korea, Croatia and in parts of Canada and of the United Kingdom (UK). Pilot projects are also underway in Australia and Germany [6]. Finally, non-smoking related lung cancer cases contribute to the increase of incidences as well, and the causes can

include air pollution, radon gas, occupational exposures like asbestos, coal fumes and silica, genetic mutations like epidermal growth factor receptor (EGFR) and anaplastic lymphoma kinase (ALK) and second hand smoke [3, 4].

1.1 Types of lung cancer

Lung cancer is a broad term and there are two main types that it can be divided into: Small Cell Lung Cancer (SCLC) and Non-Small Cell Lung Cancer (NSCLC) [7]. SCLC arises from the airway submucusa as a primary tumour mass. Histology shows that this lung cancer type originates from neuroendocrine cells of the basal bronchial epithelium. It makes up approximately 15% of all lung cancer cases and it is characterised by contralateral lung, lymph node, bone, brain, liver and adrenal gland metastases [7, 8]. NSCLC accounts for approximately 85% of all lung cancer cases and it can be further divided into three types: squamous-cell carcinoma, adenocarcinoma, and large-cell carcinoma. Squamous-cell carcinoma comprises almost 30% of all cases and it arises in the bronchial tubes in the centre of the lungs from early versions of squamous cells in the airway epithelial cells. Adenocarcinoma is the most common type as it accounts for about 40% of all cases. It usually occurs in the periphery of the lung and it arises from small airway epithelial type II alveolar cells. Finally, large-cell carcinoma often starts in the centre of the lungs, but sometimes into the nearby lymph nodes and into the chest wall as well as distant organs. This type of cancer shows no evidence of squamous or glandular maturation, so it is often diagnosed through exclusion of other possibilities [9].

1.2 Treatment options for lung cancer - Current standard of care

The current standard of care for lung cancer can be generally divided into the following categories that are briefly discussed.

Thoracic surgery can be the standard of care for people that have early-stage, resectable lung cancer and are deemed fit enough to undergo surgery. Despite the fact that surgical techniques have been improved, including less invasive video-assisted thoracoscopic surgery (VATS) for lung resections, only about 17% of patients qualify for surgery [10].

Radiation therapy is the external irradiation of the lung tumours, delivering large radiation doses to the tumour while limiting exposure of normal tissues. Radiation therapy can be applied by either using x-rays or proton beams, with proton beam therapy improving the radiation exposure of normal tissues and thus the side-effects due to radiation damage. Despite improvements in the different delivery techniques of the radiation doses and the introduction of proton beam therapy, radiation therapy is primarily reserved for people with early stage disease that are unable to undergo surgery [11].

In the case of NSCLC, in contrast to SCLC, chemotherapy has improved over recent years and it is becoming more targeted and individually tailored to each patient. This is based on the identification of driver genetic mutations: EGFR, ALK and ROS proto oncogene 1 (ROS-1) [10]. Targeted therapies rely on the identification of specific tumour mutations and targetable mutations that have approved therapies can be seen at the following table 1.1 [12].

Mutation/Fusion	Targeted drugs
EGFR exon 19 deletion and the exon 21 L858R	Osimertinib, Erlotinib, Gefitinib, Afatinib, Dacomitinib
ALK fusions	Alectinib, Crizotinib, Ceritinib, Brigatinib, Lorlatinib
ROS-1	Crizotinib, Entrectinib, Lorlatinib
RET	Selpercatinib, Pralsetinib
NTRK fusions	Larotrectinib, Entrectinib
MET exon 14 splice (skipping)	Capmatinib, Tepotinib, Crizotinib
BRAF V600E	Dabrafenib + Trametinib

Table 1.1: Target gene mutations and fusions alongside the targeted drugs for the treatment of NSCLC. The abbreviations stand for: epidermal growth factor receptor (EGFR), anaplastic lymphoma kinase (ALK), ROS proto oncogene 1 (ROS-1), Rearranged during transfection (RET), Neurotrophic tropomyosin receptor kinase (NTRK), Mesenchymal-epithelial transition (MET) and V-Raf murine sarcoma viral oncogene homolog B1 (BRAF) [12].

For NSCLC, targeted treatment has been established as the optimal first line treatment only for stage IV untreated patients that have the EGFR exon 19 deletion and L858R exon 21 mutations, as well as those with ALK fusions. For other mutations the optimal sequencing of drugs has not been determined yet [13]. Chemotherapy, such as Cisplatin, Carboplatin, and Pemetrexed, can have serious side effects and result in widespread toxicity, as they treat the whole body. The newer targeted treatments have high specificity and are better tolerated by patients than standard chemotherapy, as they cause less widespread toxicity. However, targeted treatments can only be administered to patients whose tumours have these specific mutations and a histological diagnosis needs to be obtained in those physically fit enough to have this treatment. There is also the possibility of drug resistance to the administered target drug to occur. After the initial suppression by a targeted drug, some cancer cells can acquire new mutations that can prevent the drug from binding effectively any longer [10, 14].

The newest treatment option for lung cancer are immune checkpoint inhibitors (pembrolizumab, nivolumab and atezolizumab). They act through the programmed

death-ligand 1/2 (PD-L1 and PD-L2) and programmed death 1 (PD-1) receptor pathway. PD-L1 and PD-L2 are proteins that suppress the immune system by binding with the PD-1 receptor on activated T cells. Cytotoxic T cells (characterised by CD8+) cause cytotoxic death of cancer cells when activated by tumour antigens. Some cancer cells have been found to express PD-L1 and PD-L2 on their cell membrane, which protects them from the immune system. These immunotherapies block the PD-L1/2 and PD-1 receptor pathway and in this way they allow the immune system to identify the cancer cells, so that they can undergo cytotoxic T cell mediated death [10]. Immunotherapy is usually combined with chemotherapy to maximise the therapeutic effect, however, the combination increases the overall burden of side effects [15].

1.3 Cell therapies and clinical trials

Despite improvements in conventional treatment options, lung cancer is still the leading cause of cancer death worldwide, which means that there is the need for the development, validation and rapid translation of new lung cancer treatments [16]. New cell-based therapies could potentially answer the currently unmet clinical needs and improve the life expectancy of lung cancer patients.

A cell therapy can be defined as the transfer of allogeneic or autologous cellular material into a person for medical reasons. It can be a stem cell and non-stem cell based, unicellular or multicellular therapy and it can either employ patient or donor cells, that might have undergone manipulations in formulation or genetic engineering. The method of cell administration varies and it can be topical, injection, infusion or bioscaffold surgical implantation. Cell therapies are applied in multiple therapeutic areas, such as immunotherapy, regenerative medicine, and cancer therapy. The beginning of cell therapy administration can be dated back to the end of the 19^{th} century and since then it is a continuously evolving therapeutic practice [17]. According to data on the ClinicalTrials.gov database on April 2025 there were approximately 7,000 active

(recruiting and not recruiting) and more than 8,500 completed clinical trials, in the world, utilising a cell therapy product [18]. The two main cell types utilised as cell treatments, in cancer therapy, are Chimeric antigen receptor (CAR)-T cells and Stem Cells.

1.3.1 CAR-T cell therapy

CAR-T cells have engineered synthetic receptors that function to redirect T cells, to recognise and eliminate cells that express a specific target antigen. CAR-T cell therapy has revolutionised treatment responses on certain subsets of B cell leukaemia or lymphoma, however there are many challenges that limit its therapeutic efficacy in solid tumours, like lung cancer tumours [19, 20].

Clinically approved CAR-T cell therapy is an autologous type of therapy, meaning that blood has to be removed from the patient to acquire the T cells. Allogeneic CAR-T cell therapies are in development to circumvent the limitations of the time-consuming and highly personalised manufacturing of autologous CAR-T cells, however, currently none have been clinically approved [21].

For patients to qualify for CAR-T cell treatment an invasive biopsy is needed to test whether a specific target antigen is present. Furthermore, there is the probability of developing Cytokine Release Syndrome (CRS) which is the most common and potentially serious side effect of CAR-T cell therapy. CRS is a systemic inflammatory response that occurs when CAR-T cells become activated in the body and release large amounts of cytokines, which are small proteins that help cells communicate in immune responses. These cytokines signal a rapid and robust immune activation that can affect multiple organs. Therefore, patients are monitored closely and the severity of CRS is categorised in order to manage and treat it, by providing supportive care, such as fluids, oxygen and medications to manage fever and inflammation. In more severe cases corticosteroids for immunosuppression can be administered or Tocilizumab which is a monoclonal antibody that blocks the IL-6 receptor, a key cytokine involved in CRS. Finally, the host and

tumour micro-environment interactions with CAR-T cells can critically alter the CAR-T cell function and the responses between patients are highly variable [19].

For NSCLC, CAR-T cell therapy has had limited success thus far due to neurological and on-target/off-tumour toxicity, cytokine release syndrome, the lack of tumour-specific antigens, an immunosuppressive tumour micro-environment, low levels of infiltration into the tumour, and tumour antigen escape [20].

1.3.2 Stem cell therapy

Stem cells exist in embryonic tissues as well as fetal and adult tissues and they are undifferentiated cells with high potential for self-renewal, proliferation, and mono or multidirectional differentiation. There are different types of stem cells. Human pluripotent stem cells (hPSCs) mainly include embryonic stem cells (hESCs) and induced pluripotent stem cells (hiPSCs). Pluripotent stem cells have the ability to differentiate into cells of all three germ layers (endoderm, mesoderm, and ectoderm). Embryonic stem cells are derived from the inner cell mass of the embryo, while induced pluripotent stem cells are adult cells reprogrammed to become pluripotent. Adult stem cells are multipotent, which means that they can become several specific types of cells, or unipotent which means that they can produce tissue-specific terminally differentiated cells [22].

Mesenchymal Stem Cells (MSCs) are a specific type of adult stem cell, usually collected and isolated from bone marrow, umbilical cord and adipose tissue. MSCs are multipotent and they can differentiate into osteoblasts, chondrocytes and adipocytes in normal differentiation medium *in vitro* [22]. MSCs can be donated, easily extracted and expanded *in vitro* and once they have been isolated they have a number of characteristics that make them appealing vectors for delivery of therapeutic agents. One of their key properties is their tumour tropism, that is, their propensity to migrate toward sites of tumour. Another characteristic is their low immunogenic state in that they elicit a weak

allogeneic immune response when they are delivered to a non-identical, non-matched recipient [23].

A major challenge of cancer treatment is the targeted delivery of the treatment to the cancer site. MSCs can act like Trojan horses to deliver an anti-cancer molecule [24]. Tumour necrosis factor (TNF)-related apoptosis-inducing ligand (TRAIL) is a well-studied and characterised pro-apoptotic agent that is also known as APO2 ligand. It is a type II transmembrane protein with 281 amino acids and a member of the TNF death ligand superfamily. TRAIL triggers the extrinsic apoptotic pathway as it binds to the cognate death receptor 4 (DR4) or DR5 on target cells, resulting in apoptosis induction in transformed or cancerous cells, but not in normal cells. Conventional chemotherapy and external irradiation trigger the intrinsic apoptotic pathway, while TRAIL's trigger of the extrinsic apoptotic pathway is a unique therapeutic approach with very few off-target adverse effects that characterise chemotherapeutic agents and radiation [25, 26]. The selective tumour-specific cytotoxicity of TRAIL has made it an ideal candidate for cancer treatment, however, its limited bioavailability and poor pharmacokinetic profile have made its use challenging. The half-life of recombinant human TRAIL (rhTRAIL), that is a soluble, lab-produced, recombinant version of the human TRAIL protein, is very short at around 30 min [25, 27]. In order to circumvent this problem, MSCs have been engineered to constitutively express TRAIL, by a membrane bound form of TRAIL, expressed on the surface of the MSCs [25]. The application of MSCTRAIL has demonstrated reduced tumour load after treatment in preclinical cancer models of pancreatic cancer [28], glioma [29], lung cancer metastasis [30] and malignant pleural mesothelioma [31].

As MSCTRAIL triggers the extrinsic apoptosis pathway it can be administered in conjunction with chemotherapy to potentially maximise the therapeutic effect, as the simultaneous activation of both pathways could be triggered to harness synergistic effects. There is known synergy between traditional chemotherapy agents and TRAIL, which

results in increased apoptosis by amplification of apoptotic signals through crosstalk between the two apoptotic pathways [25]. In the case of lung cancer, intravenously delivered MSCs have been shown to preferentially move towards lung cancer tissue. The success of MSCTRAIL in preclinical models led to a clinical trial utilising these cells for metastatic lung cancer [24].

1.3.3 TACTICAL clinical trial

Targeted Stem Cells Expressing TRAIL as a Therapy for Lung Cancer (TACTICAL) is a clinical trial that aimed to evaluate the safety and anti-tumour activity of MSCTRAIL in combination with standard of care therapy in metastatic NSCLC (ClinicalTrials.gov - Identifier: NCT03298763). The patients taking part in the trial had locally advanced stage III or metastatic stage IV, advanced - unresectable NSCLC. They were scheduled to receive 3 cycles of MSCTRAIL in combination with standard of care therapy, followed by a further cycle of standard of care therapy. Finally, each patient's further treatment was at the discretion of their clinician. The MSCs were umbilical cord tissue-derived [32].

The trial was split into two phases. Phase I was a single site dose de-escalation designed trial with a modified Bayesian continual reassessment model to estimate the recommended Phase II dose. Phase II was a multicentre, randomised, non-blinded trial comparing MSCTRAIL and first line standard of care therapy versus first line standard of care therapy alone. The current standard of care therapy accepted for this trial were Cisplatin (or Carboplatin), Pemetrexed and Pembrolizumab [32]. As part of Phase II of the TACTICAL clinical trial, an additional sub-study was approved to implement *in vivo* cell tracking of the stem cell therapy to 3 patients, using cell radiolabelling with Zirconium-89 (^{89}Zr) and imaging with Positron Emission Tomography (PET).

1.4 *In vivo* cell tracking

In vivo cell tracking by imaging relies on the difference in contrast between the cells of interest and the rest of the cells in the body. There are cases that intrinsic features of the cells of interest can be exploited for imaging. For example, tracking of thyroid cancer metastases can be done using the sodium iodide symporter (NIS), the carcinoembryonic antigen (CEA) can be used for colorectal cancer imaging, and melanin can be used for visualising melanomas. However, for *in vivo* cell tracking applications of transplanted therapeutic cells, it is necessary to introduce contrast agents or contrast-generating features into the cells for imaging. Labelling of the therapeutic cells can be performed by two main approaches: indirect or direct [33].

Indirect cell labelling is when genetic engineering of the cells is conducted, so that they ectopically express a reporter, that can be an imaging target. The imaging target renders the transplanted cells different from the surrounding cells in the body and they can be imaged after the administration of a suitable contrast agent. The genetic engineering of the cells can be conducted by viral transduction or by gene editing approaches [33].

Direct cell labelling is when the labelling process is performed *in vitro*, by incubation of the cells with the labelling agent. Then the labelled cells can be administered to an animal or patient for imaging. The cell uptake of the labelling agent can either be achieved by normal cellular processes, through phagocytosis or via internalizing receptors, or by assisted uptake of the labelling agent, using cell permeant contrast agents [33].

For indirect cell labelling methods, the genetic manipulation of cells by stable transfection of a reporter gene means that the presence of the reporter gene protein is throughout the lifespan of the cell and is passed on during cell division, something that allows *in vivo* imaging over time, potentially over the lifetime of the patient or animal. Depending on the reporter genes used, cell viability and proliferation information may also be acquired, as there are proteins that do not function in a dead cell, like

NIS. Nonetheless, for long-term imaging, repeated administrations of tracer are required. Furthermore, the need for genetic manipulation of the cells to allow imaging contrast is often a barrier to clinical translation due to regulatory restrictions [34].

On the other hand, direct cell labelling is in principle a simpler cell tracking method, as any chemical agent capable of either entering (by phagocytosis) or binding to the cell membrane can potentially be used for cell labelling. An important advantage of direct cell labelling is that since the cells do not need to be genetically modified, the method presents a lower regulatory barrier for clinical application compared to indirect methodologies. Furthermore, direct cell labelling provides good signal to noise ratio, as the imaging probe is retained within the cells being tracked, compared to the indirect method which tends to have high background tracer uptakes. Nevertheless, direct labelling methods do not allow imaging of cell proliferation, and can be restricted by the efflux of the labelling agent from cells over time [34].

There are different imaging modalities that can be utilised for *in vivo* cell tracking, as it will be explained in the following sections 1.4.1 to 1.4.3.

1.4.1 Bioluminescent Imaging

Bioluminescent imaging (BLI) relies on the detection of light emitted from cells or tissues. Bioluminescence is the enzymatic generation of visible light by enzymes called luciferases, which catalyse the oxidation of a substrate to release photons of light. Bioluminescence from the North American firefly (Photinus pyralis) is the most commonly used and the firefly luciferase gene expression produces the enzyme luciferase, which converts the substrate D-luciferin to non-reactive oxyluciferin. The reaction can be seen in the following equation 1.1 [35].

$$Luciferin\,substrate + Oxygen \quad \xrightarrow{Luciferase} \quad Oxyluciferin + Light \tag{1.1}$$

Mammals do not naturally emit bioluminescence, so BLI is widely applied in preclinical research, to visualise molecular and cellular processes, in various animal models. BLI requires genetic engineering of the cells to express luciferase and the substrate luciferin needs to be provided in order to induce light production, usually by intraperitoneal (i.p.) injection. These engineered cells can be tracked *in vivo* by detecting the location and intensity of the light signal. The light emitted is able to penetrate tissue depths of several mm to cm, however, the photon intensity decreases with increasing tissue depth, with the decrease being wavelength dependent [35]. The animals are imaged using sensitive charge-coupled device (CCD) cameras for light detection, after luciferin has been administered [36].

1.4.2 MRI

Magnetic Resonance Imaging (MRI) can be used for *in vivo* cell tracking, by either direct labelling, or by indirect labelling using reporter genes. Superparamagnetic iron oxide nanoparticles (SPIONs) have been utilised for the direct labelling of cells for the last 3 decades. However, the quantification of the cells can be challenging due to the dephasing effect SPIONs have on the surrounding magnetic spins, leading to a "blooming artifact" and an overestimation of the cell number. Reporter genes provide an indirect method for labelling and tracking cells *in vivo* using MRI. The cells are genetically modified through the insertion of a reporter gene that encodes proteins, able to generate contrast on MRI. The most published MRI reporter gene is ferritin for T2/T2* contrast. Ferritin is a universal iron-storage protein found in all mammalian cells, helping to regulate iron release in a controlled manner. Studies have shown that ferritin overexpression is safe and non-cytotoxic and can be used for *in vivo* cell tracking [37].

MRI can provide excellent spatial resolution of cell localisation in specific organs, however, pulmonary MRI has historically been challenging and has had limited clinical impact, due to the poor signal to noise ratio and short T2*, caused by magnetic

susceptibility differences between air and lung parenchyma. Hyperpolarised gases, like Helium-3 (^{3}He) and Xenon-129 (^{129}Xe), as inhaled MRI contrast agents can be used to acquire information on the function and microstructure of the lung, offering valuable information for the understanding of lung diseases. However, *in vivo* tracking of therapeutic cells in the lungs, using hyperpolarised gases is limited by the short half-life of the hyperpolarised agents and the rapid signal decay, which hinders the long-term tracking of cells needed [38].

1.4.3 Nuclear Imaging

Direct cell radiolabelling with the γ emitting isotope Indium-111 (^{111}In), has been routinely used since the 1970's, to track autologous leukocytes, for the detection of infection and/or inflammation sites, initially by γ scintigraphy and today by single-photon emission computed tomography (SPECT). This conventional radiolabelling method has been applied to cell based therapies, however, for the understanding of their biodistribution in the body, the detection of small lesions and small numbers of cells is required, which is beyond the sensitivity of SPECT imaging with ^{111}In. Therefore, the need for positron-emitting radiolabelling of the treatments was created, in order to exploit the better resolution, sensitivity and quantification of PET imaging [39].

Indirect cell radiolabelling methods using reporter genes for *in vivo* cell tracking have been developed. The herpes simplex virus type 1 thymidine kinase (HSV1-tk), is a foreign reporter, that is not naturally expressed in mammals and it can be used for PET imaging using for example 9-[4-^{18}F-fluoro-3-(hydroxymethyl)butyl]guanine (^{18}F-FHBG). Another reporter that has been developed for imaging is the human sodium iodide symporter (hNIS), which is a human host-compatible reporter that facilitates both PET and SPECT imaging using radiotracers like ^{18}F-tetrafluoroborate (^{18}F-BF_4^-) or ^{99m}Tc-pertechnetate ($^{99m}TcO_4^-$). The use of foreign proteins for imaging can elicit an immune response in non-immunocompromised animals or patients causing the destruction of

the administered therapeutic cells by the immune system. Therefore, the reporter choice becomes imperative for the experimental design. Host-compatible reporters are preferential, nonetheless, they should not be expressed in organs of interest for the intended cell tracking study, as this would affect the detectability of traceable cells and the interpretation of the imaging findings [40].

^{89}Zr is a positron emitting isotope with increasing interest for clinical use in recent years [41]. It is a transition metal in Group IVB of the periodic table and it decays by positron emission and electron capture to the metastable Yttrium-99m (^{99m}Y), which then decays through γ-rays emission to the stable isotope Yttrium-89 (^{89}Y). ^{89}Zr has a physical half-life of 78.41 hours (h), which means that multiple image acquisitions can be acquired over multiple days and prospective treatments can be visualised and assessed over a several day period [42].

^{89}Zr is a favourable choice in immuno-PET applications, which are emerging applications, that use radiolabelled monoclonal antibodies (mAbs), to acquire imaging data [41, 42]. MAbs are also known as immunoglobulins and they are designed to target a specific epitope on an antigen [43]. The physical half-life of ^{89}Zr can be utilised to acquire multiple imaging acquisitions for *in vivo* tracking of the mAbs [44]. The most widely used chelator in ^{89}Zr-immuno-PET applications is Desferrioxamine (DFO). A variety of different bioconjugation strategies have been employed to attach DFO to antibodies, with the most common strategy being isothiocyanate-bearing derivative of DFO, DFO-NCS, which is a commercially available bifunctional chelator that forms stable, covalent thiourea linkages with the lysines of the antibody. Then the DFO-mAbs can be radiolabelled with ^{89}Zr allowing for the longitudinal imaging of the antibodies *in vivo* using PET/CT imaging [45].

Apart from mAbs, ^{89}Zr could be used to assess the spatial and temporal distribution of cell therapies, which are currently rarely studied due to the challenges of clinical imaging techniques for cell tracking. Cells can be radiolabelled using [^{89}Zr]Zr-oxine,

where oxine (8-hydroxyquinoline) is a lipophilic molecule, that can pass through the cell membrane, which is composed of lipids, and thus carry the radioactivity inside the cell. Once the radioactivity is inside the cell, [^{89}Zr]Zr-oxine can be stably retained within the cell allowing for long-term tracking of the radiolabelled cells *in vivo* using PET/CT imaging, providing information on cell trafficking and distribution [39].

Cell therapies could provide potential treatment options to a number of disease areas, including oncology, and answer currently unmet clinical needs. An area with limited treatment options and poor survival rates, where cell therapies could provide potential treatments, is lung cancer and chronic respiratory diseases. However, the distribution of cell therapies in the lung of patients is currently unknown [46] and lung imaging can be challenging due to respiratory motion and the partial volume effect (PVE) [47]. The focus of this thesis is *in vivo* cell tracking by ^{89}Zr PET/CT imaging, therefore a detailed introduction of PET/CT imaging follows in this chapter.

1.5 Basic principles of Nuclear Imaging

1.5.1 Radioactive Decay

Unstable radionuclides, like ^{89}Zr undergo radioactive decay. This is a spontaneous process that is mathematically described in terms of probabilities and average decay rates. The average decay rate $\Delta N/\Delta t$ for N radioactive atoms of a radionuclide is given by:

$$\Delta N/\Delta t = -\lambda N \tag{1.2}$$

where λ is the decay constant of the radionuclide. It is characteristic of the radionuclide and it is the probability that any individual atom will undergo radioactive decay during a period of time. The units of λ are $(time)^{-1}$ [48].

The average decay rate $\Delta N/\Delta t$ is the activity of the sample. The International

System of Units (SI) for activity is the Becquerel (Bq), which is one disintegration per second. The symbol for activity is usually A and is given by the following equation:

$$A(Bq) =\mid \Delta N/\Delta t \mid= \lambda N \tag{1.3}$$

where λ is in units of $(sec)^{-1}$ [48].

As time goes by the number, N, of radioactive atoms decreases, so the activity, A, of the sample decreases. The number of atoms remaining after a period of time t, N(t), is given by the following equation:

$$N(t) = N(0)e^{-\lambda t} \tag{1.4}$$

where N(0) is the number of atoms at time point $t = 0$. The factor $e^{-\lambda t}$ is called the decay factor. Since activity is proportional to the number of atoms, the decay factor also applies to activity versus time, as can be seen in the following equation [48]:

$$A(t) = A(0)e^{-\lambda t} \tag{1.5}$$

The half-life ($T_{1/2}$) of a radionuclide is the time required for it to decay to 50% of its initial activity level. The half-life and the decay constant are related according to the following equations [48]:

$$T_{1/2} = \ln 2/\lambda \tag{1.6}$$

$$\lambda = \ln 2/T_{1/2} \tag{1.7}$$

1.5.2 Positron decay

Positron emission is a radioactive decay where a proton (p^+) in the nucleus is transformed into a neutron (n) and a positively charged electron. The positively charged electron, or positron (β^+) and a neutrino (v) are ejected from the nucleus. Schematically, the process

is the following:

$$p^+ = n + \beta^+ + v + energy \tag{1.8}$$

After the positron has been ejected from the nucleus, its kinetic energy is lost in collisions with the atoms of the matter. Depending on the positron's energy and the type of matter the positron can travel different distances, which is called positron range. Then the positron combines with an electron in an annihilation reaction, in which their masses are converted into energy. This energy appears in the form of two 511 keV annihilation photons [48]. A schematic representation of the annihilation reaction can be visualised in the following figure 1.1.

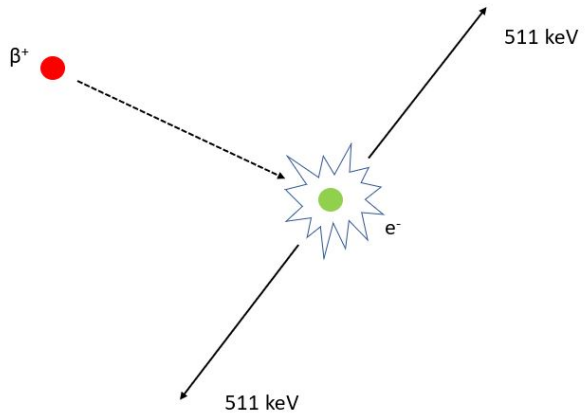

Figure 1.1: Schematic representation of the annihilation of a positron (β^+) and an electron (e^-). A pair of 511 keV annihilation photons are emitted.

PET imaging is based on the detection, in coincidence, of the two annihilation 511 keV photons that are produced, due to the annihilation of a positron and an electron. The annihilation photons are emitted simultaneously at approximately 180° opposing directions. The reason that they are not emitted at exactly 180° is due to residual momentum of the positron at the end of its range [48].

1.6 PET systems

PET imaging was first conceived in the late 1950's and since then it has become a critical imaging modality of clinical practice. Today it is commercially available combined with a CT scanner as a hybrid system known as PET/CT [49]. PET is a diagnostic imaging system that is based on the use of positron emitting isotopes. It provides functional information for both physiological and pathological processes, by imaging the differences in uptake of the radioactive tracer in different tissues [50].

Preclinical PET/CT systems started being developed in the 1990's when the first dedicated systems were manufactured, following the same design principles of clinical PET/CT systems. Due to the anatomical and physiological similarities between humans and animals, the use of animal models has revolutionised many fields of modern research such as basic biology, translational medicine and new pharmaceutical development. PET imaging has had a profound effect on drug development and biomedical research and it has become an indispensable tool, due to the quantitative information that it provides about biological processes at the molecular and cellular levels. Thanks to the importance of preclinical PET systems a number of commercial scanners are available with different configurations, architectural designs and diversified types of software [51].

The CT component of a PET/CT system, in both clinical and preclinical systems, is used for the anatomical localisation of the functional PET information, by co-registering the PET and CT images, as the resolution of PET images is lower than that of the CT images. Furthermore, PET images are affected by the attenuation of photons in the tissues and CT images are used to generate attenuation maps in order to correct the PET data, thus improving quantitative accuracy and image quality.

A general introduction of the principles of both clinical and preclinical PET/CT systems is discussed in this chapter. Where there are differences between them this will be clearly stated and explained.

1.7 CT and micro-CT systems

A CT system consists of an x-ray tube, a step-up high-voltage power supply and a detector array, which are mounted on a rotating gantry. The projection data are usually collected as the scanner performs a helical trajectory, where the system bed moves through the scanner while the x-ray tube and the detector array rotate around the subject [48]. Preclinical Mediso CT systems, that were used in this thesis, have the options of semicircular and zigzag trajectories for the projection data acquisition. In the semicircular scan method, the gantry conducts semicircular movements around the object and only one FOV can be acquired. In the zigzag scan method, the bed has an alternating inward and outward translate motion while the gantry is rotating around the object.

The projection data of CT systems are sorted into stacks of sinograms with each sinogram containing the data for a single transverse section through the subject. The images can be reconstructed using either analytical or iterative methods [48].

A CT scan provides an image of the linear attenuation coefficients, μ, inside the body. The linear attenuation coefficient represents the probability that a photon will be attenuated by unit length of tissue. The majority of x-ray interactions inside the body are by Compton scatter, due to the energies of the x-rays used (30-150 keV) and the relatively low effective atomic number of most body tissues (from approximately 6 for fat to approximately 14 for bone). Compton scatter depends primarily on the tissue density, so the pixel value in CT images is roughly proportional to the tissue density. This means that materials such as bone that have higher density show up with high pixel values, whereas lung tissue that has lower-density shows up with low pixel values [48].

The reconstructed pixel values of CT images represent an average μ across the range of energies present in the x-ray beam and this is depended on the x-ray tube voltage and the filter of the x-ray tube. For this reason, pixel values in CT images usually are

expressed on a normalised scale, with respect to the values for water, called Hounsfield units (HU), as can be seen in the following equation:

$$HU = 1000 \times \frac{\mu - \mu_{water}}{\mu_{water}} \tag{1.9}$$

By definition, water has a value of 0 HU and air of -1000 HU. Bone can have values as high as 3000 HU and soft tissues are similar to water in density and attenuation coefficient [48]. Lungs have a range of different densities, which means that the linear attenuation coefficient can vary. Lung is an organ of lung parenchyma (tissue) with air-filled structures and blood. In the case of lung cancer, tumour masses are present that have densities similar to soft tissue. Moreover, generally for cases of diseased lung, including cancer, oedema, pulmonary embolisms and pleural invasion can be present. All these different types have different HU values which is the reason why CT lung imaging is usually assessed at a level of -600 HU with a width of 1500 HU [52].

Micro-CT systems are preclinical CT systems that are based on the same physical principles as clinical CT scanners, but are designed for higher resolution *ex vivo* imaging of samples and *in vivo* imaging of small animals. There are a few key differences between micro-CT and clinical CT scanners that allow for higher resolution images. Micro-CT systems typically acquire the projection data in axial mode, where the bed is stationary while the x-ray tube and the detector array rotate around the object. They also use micro-focus x-ray sources that commonly utilise a fixed tungsten anode and operate at lower voltages (20-100 kVp) and much lower anode currents (50-1000 µA) than clinical scanners. Furthermore, micro-CT systems employ flat-panel detectors with small pixel sizes ($\leq$ 150 µm^2), in contrast to clinical CT systems that use curved detector arrays with larger pixel sizes. Finally, micro-CT systems can operate with higher radiation doses and longer scan times, compared to clinical CT systems, depending on the application. Micro-CT imaging can provide high resolution images of up to 5 µm for *ex vivo* samples, providing non-invasive information as well as high throughput [53].

1.8 Basic principles of PET systems

PET systems utilise detectors and appropriate energy and time windows for the detection of annihilation photon pairs that are referred to as coincidence events. The detectors consist of solid scintillation crystals, which have the property of emitting scintillations or flashes of light after the absorption of the annihilation photons, photodetectors that convert the light of the crystals to electrical signal and electronics that process and record the signal. The energy window defines the range of photon energies (measured in keV) that the PET system accepts as valid. The time window is defined as the time interval (in nanoseconds) during which two detected photons are considered a valid coincidence event. The energy and time windows are set in order to detect the photon pairs that originated from the same annihilation event and discard the rest [54].

When two annihilation photons are detected in coincidence, the system assumes that the annihilation event occurred somewhere along the line that connects the two detectors, and this line is called Line of Response (LOR). The time after a detection event during which the system is unable to record any additional events is called dead time and it is defined by the scintillation decay time and the electronics of the system, meaning that it varies between PET systems of different makes and models. During dead time the detection system is unable to process another event, which means that the photon will be lost, making dead-time loss a problem at high count rates [54].

The events detected by a PET system can be divided into three categories: true, random and scatter events. True events are defined as those that the two photons originated from the same annihilation event and are detected within the set energy and time window, without having been attenuated or deflected from their point of origin. Random events are defined as those that the two photons originated from two unrelated annihilation events, but are detected by a detector pair within the set energy and time window, thus creating a false LOR. Scatter events occur due to Compton scattering of the

photons in the body. One scattered photon and one annihilation photon or two scattered photons, that belong to the same annihilation event may fall within the set energy and time window, and create a false LOR. In figure 1.2 a graphic representation of the different events can be seen. Finally, a single event, as shown in figure 1.2, is a detected photon that came from an annihilation event where the other photon was not detected. These events can be discarded by the system, however, they are important because they increase the dead time of the system and they can result in losses of true events and in an increase of random events. The exclusion of random and scatter coincidences is highly important, because these events raise the background noise of the image and degrade image contrast [54].

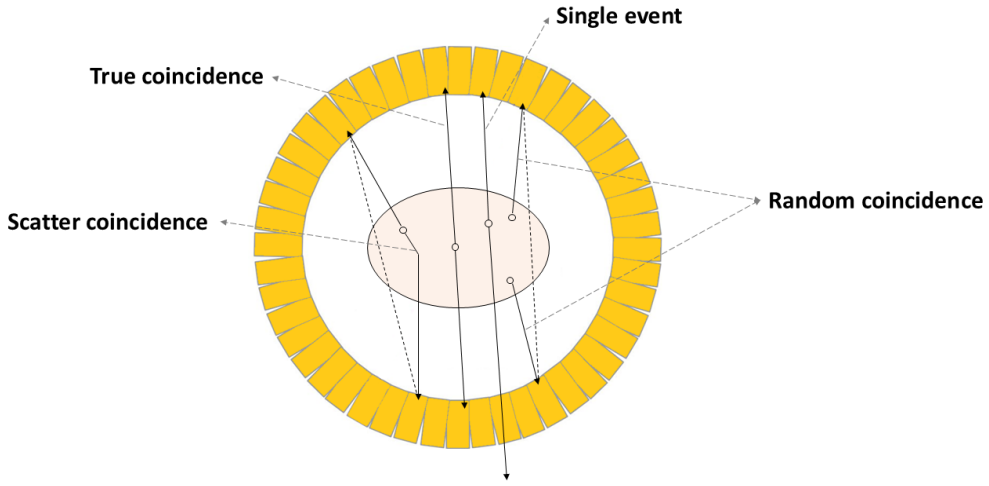

Figure 1.2: A graphic representation of the different events that can be detected by a PET system.

1.9 Performance characteristics of PET systems

1.9.1 Spatial Resolution

Spatial resolution characterises the ability of a PET system to accurately reproduce the variations of distribution of radioactivity in the subject and it can be empirically

defined as the minimum distance between two points, that can be identified as separate in an image. Spatial resolution is limited by a few factors. The intrinsic resolution of the scintillation crystals is one of them and spatial resolution is best at the centre of the field of view (FOV), while it deteriorates at its edges. Another factor is positron range, as positron range increases with the positron's initial energy and it decreases with the density of the medium. Noncolinearity is another factor and it is the small deviation of the two annihilation photons from the 180° angle of emission. This factor affects spatial resolution, because the LOR that is created between the two detectors, is somewhat displaced from the true LOR that intersects the point of annihilation. Finally, the reconstruction method and the filter of use can affect spatial resolution, especially when filtering is used to reduce the effects of noise in the image [54].

1.9.2 Sensitivity

The sensitivity of PET is defined as the number of detected counts per unit time per unit of activity. It is usually expressed in counts per second (cps) per kilobecquerel (kBq). It is affected by dead time, the pulse height analyser (PHA) window and the detection and geometric efficiencies. A large dead time means that there will be fewer registered events, so the sensitivity will be negatively affected. The PHA window is the energy discrimination window of the detected photons. The narrower that the window is, the more accurate the energy discrimination of the photons becomes, which improves spatial resolution, but it reduces sensitivity, making the PHA window range a trade off between the two. The detection efficiency depends on the density, thickness, atomic number and scintillation decay time of the crystal, all of which affect sensitivity. Finally, geometric efficiency is defined as the solid angle projected by the source at the detector. The increase of the distance between the source and the detector negatively affects geometric efficiency, and thus sensitivity [54].

1.9.3 Noise Equivalent Count Rate and Scatter Fraction

In PET, the noise in an image is defined as the random variation in pixel counts across it. It is given as a percentage by $(1/\sqrt{N}) \times 100$, where N stands for the counts in the pixel. Noise can be reduced by increasing the total counts in the image, which can be achieved either by increasing the scanning time, or by increasing the injected activity, or by improving the detection efficiency of the scanner. However, since all of these methods have their limitations there is always going to be noise present in the acquired images. PET image noise is characterised by the noise equivalent count rate (NECR), that is given by the following equation:

$$NECR = \frac{T^2}{T + S + R} \tag{1.10}$$

where T, R, and S are the true, random, and scatter coincidence count rates, respectively. Image noise can be minimised by maximising the NECR. Moreover, the NECR is proportional to the signal to noise ratio (SNR) ratio in the final reconstructed images, so it can be used to compare the performances of different PET systems [54].

The scatter fraction (SF) of a PET system is given by the following equation:

$$SF = \frac{C_s}{C_t} \tag{1.11}$$

where C_s and C_t are the scattered and total count rates detected, respectively. The lower that the SF value is, the better the performance of the scanner and the quality of the images are [54].

1.9.4 Contrast

Contrast in PET imaging is characterised by the relative variations in count densities between neighbouring areas in the image and it is affected by the following factors:

- Count density: A minimum number of counts is required in order to acquire an image with reasonable contrast, as low number of counts could lead to increased noise and poor contrast in the image. The count density is affected by the administered activity, the duration of the acquisition, the uptake by the tissue and the detection efficiency of the system [54].
- Scattered events: Scattered events affect image contrast as they increase the background noise in the image. The number of scattered events can be decreased by applying a narrow PHA window, but at the same time the total number of counts included in the image would be reduced [54].
- Motion: Movement during scanning can reduce image contrast and cause blurring [54]. There are two types of movement, patient and internal. Patient movement can be tackled by the comfortable positioning of the person on the system and by reducing the acquisition time. Internal movement is the physiological movement of organs, like respiratory motion due to breathing and cardiac motion due to cardiac beating [55].

1.9.5 Partial Volume Effect

The Partial Volume Effect (PVE) is the spill over of counts between different areas in an image. It is caused by the limited spatial resolution of the system and it can contribute to errors in quantitative measurements of activity concentrations of different areas of interest. The PVE can impact imaging studies if the effect changes between subjects or over time, so it is important to correct for it. A method of measuring the effect and the result of the PVE correction is the Recovery Coefficient (RC). In clinical PET imaging RC is the ratio of the reconstructed count density to the true count density and it can be determined by measuring the count density of different size objects, containing the same activity, both larger and smaller than the spatial resolution of the system [54].

In preclinical PET imaging the RC values are measured using a phantom containing

rods of different diameters. The RC is calculated as the ratio of the measurements for the different size rods to the measurement in a uniform area of the phantom [56].

1.9.6 Tissue Fraction Effect

The Tissue Fraction Effect (TFE) is part of the PVE and it is an important issue in lung imaging. The size of an image voxel is finite, which means that it may contain multiple different tissue components. In the case of lung, it may contain air, blood, parenchyma and if there is presence of disease, oedema, or tumour tissue. This means that the resulting voxel value will be the average signal from all the components of the voxel, and this is known as the TFE [47].

1.9.7 Point Spread Function

The point spread function (PSF) of a PET system describes how a point source of radioactivity appears in the reconstructed PET image and it can reflect the PVE. PSF is often modelled as a Gaussian function and the amount of blurring is calculated by the full width at half maximum (FWHM) of this function. PSF varies over the FOV, due to the geometry of the detector system. The scintillation crystals usually have a small cross section in order to provide high resolution and are quite long in the radial direction in order to provide high sensitivity. This means that by moving away from the centre of the scanner, the photons can hit the crystals at oblique angles, thus leading to degradation of the spatial resolution. PSF can be experimentally acquired in the whole FOV by scanning a rod at specified positions and then applying this information to the acquired data to correct for the degradation of spatial resolution [57].

1.10 PET data acquisition, image reconstruction and image processing

1.10.1 Data acquisition

The data in PET systems are acquired into a sinogram in a matrix of selectable size. This sinogram is a two-dimensional (2D) sum of the counts of the LORs in the distance and angle coordinates in a given plane. This means that each LOR, and hence each detector pair, corresponds to a particular element in the sinogram. For every coincidence event that a LOR is created, the corresponding pixel is located in the sinogram and a count is added to the pixel. In the final sinogram, the total counts in each pixel represent the number of coincidence events detected during scanning by the two detectors along a LOR. The sinograms are a 2D representation of the three-dimensional (3D) image [54].

The modes of data acquisition in PET systems can be either frame or list. In frame mode, the data is acquired directly into the sinogram. In list-mode, the digitised signals are encoded with a time stamp as they are received in sequence and stored as individual events. List-mode acquisition is more computationally expensive, but with modern PET systems and computers it can be used, as it offers flexibility in the manipulation of the data, because the data can be reconstructed for different acquisition times, smaller or equal to the actual acquisition time of the scan [54].

In PET systems data can be acquired in either Step-and-Shoot (SS) mode or continuous bed motion (CBM) mode. In SS mode, the table moves between consecutive acquisitions of adjacent bed positions. For this acquisition protocol, the scanning of the patient or animal is restricted by the fixed axial field of view (AFOV) size of the detector array, called a bed position. If only one bed position is needed to cover the area of interest for imaging, as is usually the case for mouse studies on preclinical PET systems, then the acquisition mode is called static. In CBM acquisition mode, the patient table moves

through the gantry while PET emission data is continuously acquired. The advantage of CBM mode is the increase of uniformity in the sensitivity profile across the AFOV, due to the fact that the density of LORs does not depend on their axial position, as it does in static mode [58].

Finally, PET imaging can be performed using dynamic acquisition in either frame or list-mode. In dynamic acquisition, imaging begins immediately after tracer injection, and data are collected over a series of time frames. In frame mode, the data are stored as sinograms for each predefined time interval. In list-mode, event data are recorded continuously with time stamps, allowing for retrospective framing and reconstruction [54].

1.10.2 Time-of-Flight

Clinical PET systems use the Time-of-Flight (TOF) technique, which is dependent on the timing resolution of the detectors. TOF technology utilises the difference in time in the arrival of two annihilation photons, related to the difference in distances travelled by them on the LOR, with respect to the midpoint between the detectors. Thus, it localises the point of annihilation within a smaller range of the LOR, by reducing the probability distribution along the LOR to the location of the annihilation event. TOF image reconstruction improves localisation and can provide high resolution images, but it requires sufficient detector efficiency and timing resolution. The enhanced resolution can improve the detection and quantification of areas of interest and the acquisition time or the injected activity can be reduced [57].

Conventional PET system's detectors are equipped with a photodetector called photomultiplier tube (PMT). PMTs convert the light photons produced in the crystal to an electrical pulse. They are vacuum glass tubes containing a photocathode at one end, several dynodes in the middle, and an anode at the other end. The PMTs are fixed onto the crystal by optical grease or optical light pipes. When light photons from the

crystal strike the photocathode of the PMT, electrons are emitted, which are accelerated toward the next closest dynode by the voltage difference between the dynodes. Each of these electrons is again accelerated toward the next dynode and then more electrons are emitted. The process of multiplication continues until the last dynode is reached and a pulse of electrons is produced, which is attracted toward the anode. The pulse is then amplified by an amplifier to a detectable pulse, that is then analysed by the PHA, and finally recorded [54]. Conventional PMT-based PET scanners can achieve a timing resolution from about 600 to 375 ps and this corresponds to the localisation of the annihilation event from 9.0 to 5.6 cm of the LOR, respectively [57].

On the other hand, state of the art PET systems that are equipped with silicon photomultiplier (SiPM) photodetectors offer better TOF timing resolution, and thus improved spatial resolution [59]. SiPM photodetectors use single-photon avalanche diodes operating in Geiger mode to detect the scintillation photons generated in the scintillation crystal. SiPMs are smaller than PMTs and they provide a 1,000 times larger gain and increased energy resolution [60]. Due to the high amplification, fast signal, and high light collection, SiPM-based PET systems can achieve a timing resolution as low as 214 ps, which is a localisation of the event as low as 3.2 cm of the LOR. The improvement in TOF timing resolution with SiPMs increases PET sensitivity, reduces noise and in conjunction with small-size crystals, provides improved image resolution. The sensitivity gain can be used to reduce the administered radioactivity to the patient or to shorten the acquisition time [61].

1.10.3 Coincidence mode

Commercial preclinical PET systems do not utilise the TOF technique. As mentioned in section 1.10.2, the TOF technique can localise an annihilation event as low as 3.2 cm of the LOR, something that can offer little value to a small animal study. Mediso preclinical PET/CT systems, that were used for the work of this thesis, utilise a method called

coincidence mode. The coincidence mode defines the possible LORs during acquisition, that the annihilation photons will be registered. One or more neighbours each side of the detector opposite may detect counts too, and the number of possible detectors can be chosen for the acquisition. Due to geometrical reasons, the coincidence mode defines the AFOV, which means that larger animals and phantoms may require higher coincidence mode. Furthermore, the coincidence mode affects the number of detected events and thus the sensitivity [62].

There are three coincidence modes available and a graphic representation of them can be seen in the following figure 1.3:

- 1 - 1 coincidence: Each detector module is in coincidence only with the directly opposite one. 1 - 1 mode has limited FOV, making it appropriate for point source measurements.
- 1 - 3 coincidence: Each detector module is in coincidence with an opposite one and its two neighbours, so altogether three modules. For small animals such as mice this is the recommended setting as it offers a good balance of spatial resolution and sensitivity.
- 1 - 5 coincidence: Each detector module is in coincidence with 5 opposing ones. This coincidence mode is appropriate for large animals such as rats and rabbits. It is the most sensitive mode as it collects the largest number of events [62].

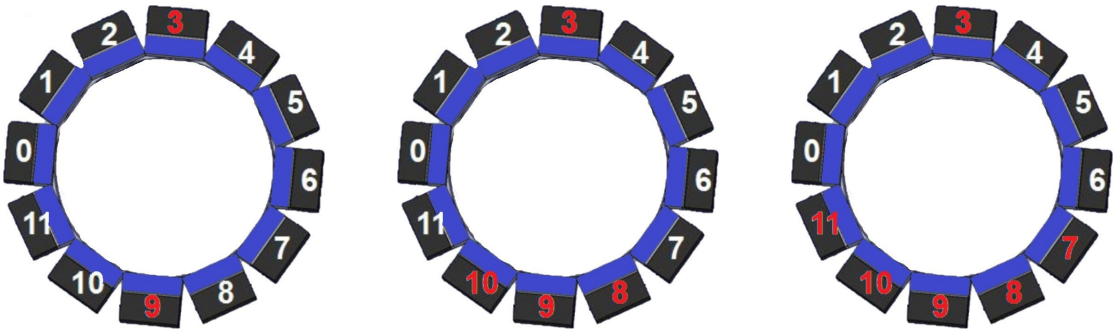

Figure 1.3: Graphical representation of a Mediso PET ring of 12 detectors showing the different coincidence modes: (a) 1 - 1 coincidence, (b) 1 - 3 coincidence, (c) 1 - 5 coincidence.

1.10.4 Image reconstruction algorithms and filters

The acquired raw PET data need to be reconstructed in order to form the images and the sinograms are used for their reconstruction. The images can be reconstructed to transverse (or transaxial or axial), coronal and sagittal planes [54]. The reconstruction methods that can be utilised can be divided into two categories, analytic and iterative. For analytic reconstruction, the most widely used algorithm is the filtered backprojection (FBP). FBP applies a ramp filter to the projection data and then back-projects them in order to form the image. The ramp filter enhances high frequency information, so the produced images are noisy. It is an algorithm that provides results fast and it had been extensively used in the past, however nowadays it has been predominantly replaced by iterative methods [54, 55].

In iterative reconstruction methods an initial estimate of the image activity is stored in a matrix size identical to the acquisition matrix. An initial constant value is usually assigned to all pixels in the estimate matrix. A set of simulated projections are unfolded from this estimate in order to be compared with the acquired projection. After the unfolding of all projections, each estimated one is compared with the analogous measured one. In the case of a difference between them, a weighted correction is applied to all

pixels in each estimated projection. An updated image is obtained by backprojecting all the corrected projections and it is entered into the algorithm as the estimated image for the next iteration. Multiple iterations are applied and their number is chosen by the user. Several algorithms have been developed for iterative methods [54]. The most commonly used iterative reconstruction method is the ordered subset expectation maximization (OSEM). This algorithm groups the projections into subsets, and an iteration is performed on each subset rather than each projection. It also uses a non-negativity constraint, which means that no voxel can contain a value less than zero [54, 55].

Smoothing filters can be applied to the images in order to reduce noise. Each filter has each own definition and characteristics. An example is the Gaussian filter that is a "low-pass" filter, which means that it preserves low-frequency structures while it eliminates high-frequency noise [54]. An all-pass filter can also be chosen during reconstruction, which means that no smoothing filter is applied and all frequencies are allowed, thus preserving spatial detail but noise is not reduced [63].

1.10.5 Data corrections

During the acquisition process the raw PET data is noisy and affected by PVE, attenuated and scattered events. This means that several corrections need to be applied to the images before quantitative measurements are conducted [57]. The corrections that are usually applied for both clinical and preclinical PET/CT studies are the following:

- Normalization: Normalization compensates for the variations of the response of the detectors due to their intrinsic properties, geometry and changing count rate. It is essential for the reduction of artifacts and modern systems usually use component-based approaches, which means that they use different factors for detector efficiency, geometry and dead time [57].
- Attenuation correction: In PET/CT systems the CT scan can be used for the

attenuation correction of the PET scan. This is highly important, because the annihilation photons may attenuate before their detection, due to penetration and scattering in the body. The probability of attenuation depends on the density of the tissues and the distance that they have to travel through that density of materials. In order to use the CT scan to correct for photon attenuation in PET, the pixel intensity in the CT image, which is expressed in HU, is converted into the mass attenuation coefficients of the 511 keV photons. By this process an attenuation map is created that is used for the photon attenuation correction of the PET emission scan [54].

- Scatter and random events correction: The distribution of scattered events depends on the detector geometry, the scattering medium and the distribution of the emission source. For the estimation of the scatter distribution, deterministic algorithms or Monte Carlo simulations can be used. Deterministic methods are the most studied as well as practical algorithms and they are widely used in commercially available systems, since they provide reasonable results. In the case of random events, their fraction is proportional to the amount of activity in the sample. The method that is usually used to estimate their amount is the "delayed window" technique. This technique utilises two windows. The standard coincidence window that registers the coincidence events, and a window that is significantly delayed with respect to the standard window, that again registers coincidences. Since random coincidences are formed due to random temporal correlation, there should be no true coincidences in the delayed coincidence window and this can be used to correct for the random coincidences in the standard window. The "delayed window" method is accurate and simpler for real-time implementation on a system, however the relatively fewer counts could introduce statistical noise in the emission image. The random coincidences are usually stored separately in order to be used during the reconstruction process [57].

1.10.6 PET radionuclides

Fluorine-18 (^{18}F) is the most widely used radionuclide in PET imaging and it can be produced in a cyclotron, primarily by proton irradiation of Oxygen-18 (^{18}O), which is a stable naturally occurring isotope of oxygen [64]. The decay properties of ^{18}F can be seen in table 1.2. The 2-deoxy-2-fluoro-D-glucose or Fluorodeoxyglucose (FDG) is a pharmaceutical that is radiolabelled with ^{18}F thus making the ^{18}F-FDG radiopharmaceutical. This radiopharmaceutical is vastly used in clinical practice for studying energy metabolism, which means that sites of metastasis in cancer patients can be identified and the patients can be staged [57]. PET/CT imaging offers functional information as it provides the detection of the spatial distribution of the ^{18}F-FDG radiopharmaceutical. Regions with high ^{18}F-FDG uptake may indicate metabolically active tumour areas, however ^{18}F-FDG uptake can be heterogeneous within a tumour. Tumour areas with high cell density, that are highly metabolically active will have high ^{18}F-FDG uptake, but regions of hypoxia will have little to no uptake. This makes ^{18}F-FDG PET imaging an appropriate choice for identifying hypoxic areas within tumours in both patient and animal studies of disease [65].

^{89}Zr is a radionuclide that can be produced by proton irradiation of ^{89}Y targets [66] and there is increasing interest for its application in clinical practice, due to its properties that can be seen in table 1.2, alongside ^{18}F. ^{89}Zr has a relatively long physical half-life and a low branching ratio, with respect to other PET radioactive isotopes [42, 67]. The relatively long physical half-life allows for longitudinal imaging over multiple days and the relatively low mean energy of the emitted positrons (396 keV) means that the mean positron range will be small (1.3 mm in water), resulting in high spatial resolution images. Moreover, ^{89}Zr emits high energy γ rays (909.9 keV, 99% abundance) that are important in both imaging and dosimetry considerations of patients and staff. The energy of the unattenuated γ rays (909.9 keV) allows them to be gated off, by setting an appropriate energy window, thus preventing their interference with the detection of

coincident photons (511 keV). However, attenuated 909.9 keV photons might be detected, if their energy is within the set energy window for the coincidence events. These photons will increase the random coincidences or appear as single events, thus affecting dead time, all of which mean that image quality will be negatively affected and there will be an increase in noise [42].

Property	**^{18}F**	**^{89}Zr**
Half-life	110.0 min	78.41 h
Branching β^+ (%)	96.9	22.3
E_{max} (keV)	634	902
E_{mean} (keV)	250	396
R_{max} (mm)	2.4	3.8
R_{mean} (mm)	0.6	1.3

Table 1.2: Properties of the PET radionuclides. E_{max} and E_{mean} are the maximum and mean positron energies, respectively. R_{max} and R_{mean} are the maximum and mean positron ranges in water, respectively [67].

The spectra of ^{18}F and ^{89}Zr can be visualised in the following figure 1.4. They were acquired using an ORTEC Spectroscopy Amplifier (Model 451) at the Nuclear Medicine Department of Royal-Free Hospital, London. The 511 keV peaks can be seen in red colour and they have been labelled alongside the 909.9 keV peak of ^{89}Zr.

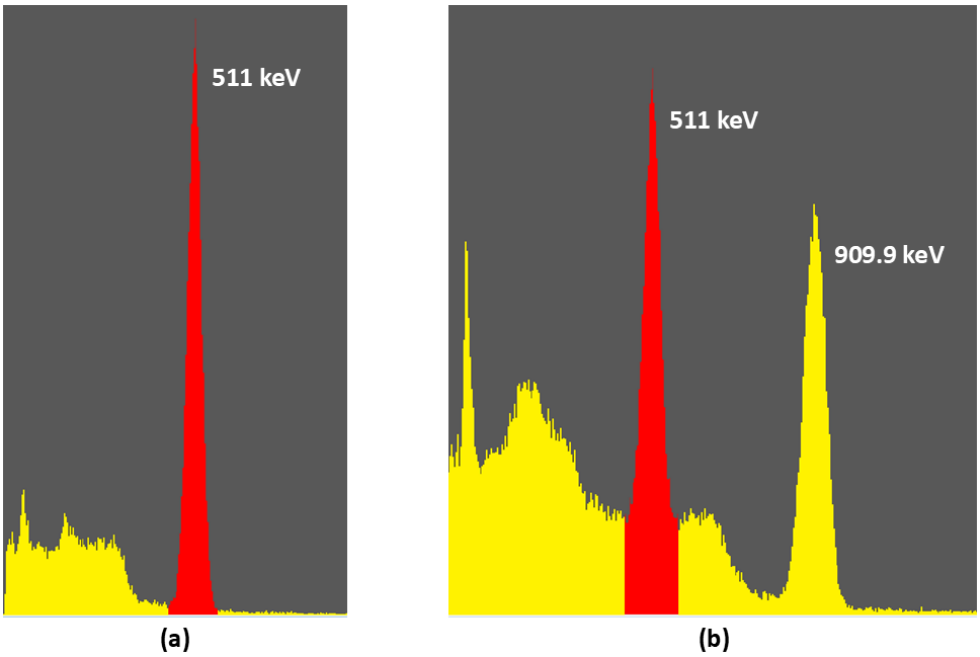

Figure 1.4: Spectra of radionuclides acquired on an ORTEC Spectroscopy Amplifier system: (a) Spectrum of ^{18}F, (b) Spectrum of ^{89}Zr.

1.11 Breathing motion correction

Breathing motion is an important challenge of PET imaging. During acquisition of a clinical PET/CT scan the patient is awake and breaths normally, while for a preclinical PET/CT scan the animal is under anaesthesia. The concentration of activity in the voxel, when detected using a PET system, is the average of the concentrations of the tissues moving through that voxel during the respiratory cycle, while the CT image acquired is typically a snapshot of a respiration phase.

Breathing motion corrections can be applied to the PET and CT data in both clinical and preclinical studies and there are different methods proposed in the literature to acquire the respiratory motion information. One method is respiratory motion tracking systems, which are external devices that estimate respiratory motion, by monitoring either a physiological characteristic or a physical parameter. The respiratory signal that

is provided from these systems is synchronised with the data in order to account for respiratory motion [68]. In the clinical setting these systems are rarely used, because they require training of the staff, time to set up, they might not be tolerated by the patients and the gating waveforms that they provide might not be useful [69]. In the preclinical setting, respiratory tracking systems are regularly used. Pneumatic air chamber sensors, or as they are commonly referred to "breathing pads", are centred on the diaphragm of anaesthetised animals, while the animal is in either supine or prone position. The sensor detects respiratory motion by measuring pressure changes caused by the animal's breathing. To ensure a strong signal output, a small amount of additional pressure is typically applied around the abdomen, by using adhesive medical tape. This setup allows for the detection of respiratory cycles and enables the synchronisation of image acquisition with specific phases of the breathing cycle [70].

Data Driven Gating (DDG) approaches are an alternative to the conventional hardware-based gating methods. In DDG the measured PET raw data is analysed in order to extract the respiratory motion information, meaning that this software-based method requires no additional setup time, in contrast to hardware-based methods. In DDG motion information is collected mainly from PET-active structures within the body instead of relying on external surface motion effects, which means that the success of gating is highly dependent on the statistical quality of the PET data [71]. For CT acquisitions, 4D imaging and gating have been developed in both human and preclinical settings, to study lung motion as well as eliminate motion artifacts. For both cases, a respiratory signal that can be correlated to time during image acquisition is required. In 4D imaging, the respiratory signal is used to sort projections into bins based on their respiration phase or amplitude and in gating it is used to either trigger acquisition during certain respiratory phases or retrospectively select a subset of the projections corresponding to certain respiratory phases for reconstruction [72].

1.12 Radiation dose

The absorption of energy from ionising radiation is important in diagnostic imaging as it can pose a potential hazard for the patient or animal. Therefore, it is necessary to analyse the energy distribution in body tissues quantitatively to assess any potential risks [48].

Absorbed dose, D, refers to the amount of energy deposited by ionising radiation per gram of absorber material. This quantity applies to any kind of absorber material, including body tissues. The unit of absorbed dose is the gray (Gy), which is 1 joule of energy deposited per kilogram (kg) of absorber [48].

The equivalent dose, H_T, takes into account the relative biologic damage caused by radiation interacting to a particular tissue or organ. Tissue damage per gray of absorbed dose depends on the type and energy of radiation, and how exactly the radiation deposits its energy in the tissue. For example, an α particle has a short range in tissue and deposits all of its energy in a very localised region, while γ rays and electrons deposit their energy over a wider area. The equivalent dose is calculated according to the following equation:

$$H_T = D_T \times w_R \tag{1.12}$$

where D_T is the absorbed dose in tissue T and w_R is the radiation weighting factor, that depends on the type of radiation. The SI unit of equivalent dose is the sievert (Sv) [48].

The effective dose represents the overall risk to the whole body from a non-uniform absorbed dose of radiation. It is calculated by assigning different weighting factors, w_T, to the equivalent doses delivered to individual organs. The effective dose, which has units of sieverts, is calculated according to the following equation:

$$E = \sum_T w_T \times H_T \tag{1.13}$$

where w_T is the tissue weighting factor for organ T, H_T is the equivalent dose and the summation is over all the organs [48].

PET radionuclides that have short half-lives and high branching ratios for positron decay are generally preferred for use in clinical practice for imaging. This is because by using a radionuclide with a short half-life, the dose to the patient can be reduced and by using a radionuclide with a high branching ratio, the image quality can be improved [42, 57]. The effective dose needs to be kept as low as reasonably possible, as imaging is conducted for diagnostic purposes. By keeping the effective doses to the patients as low as reasonably possible, the effective doses to the staff can be mitigated as well. In the case of ^{89}Zr the long half-life (78.41 h) and the high energy photons (909.9 keV) hinder the amount of activity that can be administered to the patient. For an administered activity of 37 to 74 MBq, the effective doses range from 20 to 40 mSv, which is about 2 to 4 times higher than the effective dose of an ^{18}F-FDG PET scan [73]. Therefore, extra care needs to be taken in ^{89}Zr imaging studies for the radiation protection of the patients as well as the staff.

1.13 Clinical Long Axial Field of View PET/CT systems

The idea of total-body PET was first conceived in the early 1990's, with the drive behind developing these systems being that the gain in signal collection efficiency, alongside the high spatial resolution, would offer higher sensitivity and improved detection of lesions. Current standard clinical PET/CT systems typically cover an AFOV of about 15 - 26 cm and they will be referred to as short axial field of view (SAFOV) systems. Increasing the FOV by axially spacing out the detector rings, increases the coverage of the patient's body but not the overall sensitivity. The viable solution of increasing the number of detector rings has, however, the accompanying down side of increased cost.

The Explorer consortium and United Imaging Healthcare Shanghai, in collaboration with the University of California Davis team, the University of Pennsylvania, and Siemens Healthineers, have all developed systems with long axial field of view (LAFOV), covering an axial length spanning from 64 to 194 cm. The Biograph Vision Quadra from Siemens Healthineers is a commercially available PET/CT system that combines SiPM detector technology with a body coverage of 106 cm. The Biograph Vision Quadra system essentially comprises the equivalent of 4 axially concatenated PET subsystems of the Biograph Vision 600 system [61]. A graphical representation of both SAFOV and LAFOV systems axial FOV body coverage can be seen at the following figure 1.5.

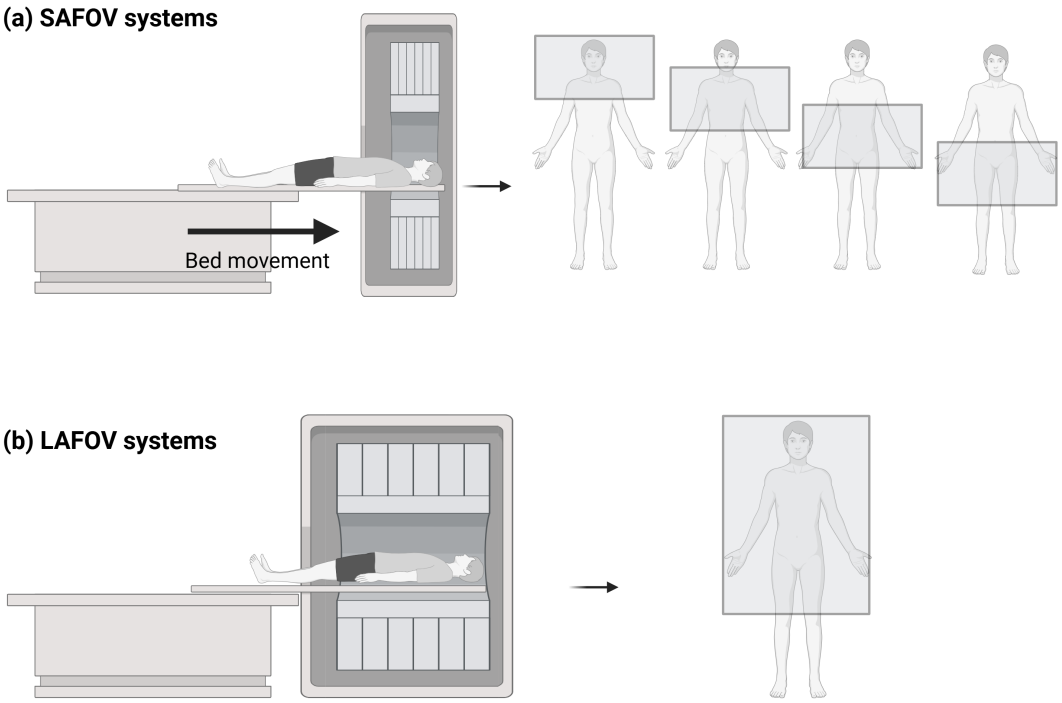

Figure 1.5: Graphical representation of the axial FOV body coverage of (a) SAFOV and (b) LAFOV systems [74].

LAFOV systems have important advantages compared to SAFOV systems. Thanks to the extended AFOV, LAFOV systems have improved sensitivity and reduced noise. The Biograph Vision Quadra system has an NECR 5 to 10 times higher and an axial peak

sensitivity up to 2.75 times higher than the Biograph Vision 600 system. Furthermore, in many clinical scenarios, time-consuming multiple bed positions must be imaged to cover the relevant portion of the patient using SAFOV systems, while this is circumvented with the extended AFOV of a LAFOV system which covers all major organs [61].

The increased sensitivity of LAFOV systems can be utilised to either reduce the administered activity, or reduce the scan acquisition time, or a combination of both. The reduction in administered activity is particularly desirable for situations where the radiation dose might pose a hazard to long-term health, such as for pregnant patients, young children and studies of normal volunteers. The reduction in administered activity can also be utilised in studies using radionuclides like ^{89}Zr, that the administered activity is limited due to radiation dose constraints. The increased sensitivity of LAFOV systems means that after administering low ^{89}Zr activities, longitudinal imaging can be conducted with reasonable acquisition times, allowing for the assessment of patients over time and for *in vivo* cell tracking studies it would provide information of the cell biodistribution over time. The increased sensitivity can also be used to reduce the scan acquisition time, thus improving patient comfort and minimising the probability of patient movement during scanning. From an operational perspective, the lower administered activity to patients will also reduce the radiation dose to staff members and the lower acquisition times will increase the department's throughput. Furthermore, the high sensitivity of these systems can extend the period of imaging that is feasible for relatively short-lived radionuclides, including ^{18}F, something that could improve the clearance in regions of significant background activity and increase the detection of small malignant lesions [75].

The LAFOV system that was utilised in this thesis was the Biograph Vision Quadra, as discussed in Chapter 6. The Biograph Vision Quadra system records all possible LORs using its maximum ring difference (MRD) of 322 detector rings (MRD 322), corresponding to an acceptance angle of 52°, which is called ultra-high sensitivity (UHS) mode. The MRD metric defines the maximum allowed axial ring separation between two

detectors and it determines the axial extent of LORs used in the reconstruction process. The system also offers the high sensitivity (HS) mode, that utilises LORs spanning an MRD of 85 detector rings (MRD 85), with an acceptance angle of 18°. MRD 85 is comparable to the SAFOV Biograph Vision 600 system's MRD of 80 crystal rings [61].

1.14 Hypothesis

Stem cell therapies are being developed for different pathologies, yet the distribution of the therapeutic cells in patients is usually unknown. *In vivo* cell tracking by imaging is a non-invasive method that can offer information on the distribution of a cell therapy in the body, providing quantitative measurements for the understanding of treatment response and possible off-target or adverse effects. ^{89}Zr is a positron emitting isotope that has a physical half-life which allows for the longitudinal imaging of a patient over multiple days. [^{89}Zr]Zr-oxine could be used for the *in vitro* direct radiolabelling of cells according to good manufacturing practices (GMP), for patient administration, in order to track the therapeutic cells *in vivo* by PET/CT imaging and acquire information on the therapeutic cell biodistribution.

1.14.1 Aims and Objectives

This project set out to develop a clinically translatable direct radiolabelling method for a MSC therapy and develop an imaging pipeline for the tracking of the cell therapy in patients by PET/CT imaging. Therefore, the aims of this thesis were to:

1. Develop a GMP clinically translatable direct radiolabelling method for MSCs using [^{89}Zr]Zr-oxine.
2. Optimise a minimally invasive orthotopic lung cancer mouse model, with distinct areas of tumour tissue and lung parenchyma, that would allow for the assessment of the therapeutic cell distribution in diseased and normal lung parenchyma.

3. Assess the *in vivo* ^{89}Zr preclinical imaging protocol, using a preclinical phantom on a preclinical PET/CT system.
4. Track the radiolabelled MSCs *in vivo* in naïve and tumour bearing mice to acquire longitudinal quantitative measurements in different organs.
5. Apply the preclinical imaging findings in the clinical setting, by utilising phantoms, and conduct phantom studies to identify challenges of clinical imaging with ^{89}Zr and the best imaging parameters for patient studies.

1.15 Thesis outline

In figure 1.6 a schematic overview of the structure of this thesis is presented. Following this introductory chapter, each chapter introduces the relevant literature, provides a detailed overview of the methodology applied, with a presentation and discussion of the results. Chapter 2 focuses on the direct radiolabelling method developed for MSCs using [^{89}Zr]Zr-oxine, and the *in vitro* assays used to assess cell viability and toxicity. Chapter 3 presents the minimally invasive orthotopic lung cancer mouse model developed to represent clear areas of lung tumour and healthy lung parenchyma. Chapter 4 is about the assessment of image quality and quantitative accuracy of a preclinical PET/CT system, for the prospective *in vivo* cell tracking of ^{89}Zr radiolabelled cells, by conducting preclinical phantom studies. Chapter 5 presents the *in vivo* mesenchymal stem cell tracking work, by imaging naïve and lung tumour bearing mice. Chapter 6 focuses on clinical PET/CT imaging using ^{89}Zr, by utilising clinical phantoms and applying the preclinical *in vivo* imaging findings to a clinical phantom. Chapter 7 provides an overall discussion of the thesis and summarises the main findings and limitations of this work, outlining the contributions to the body of literature and proposing avenues for future work.

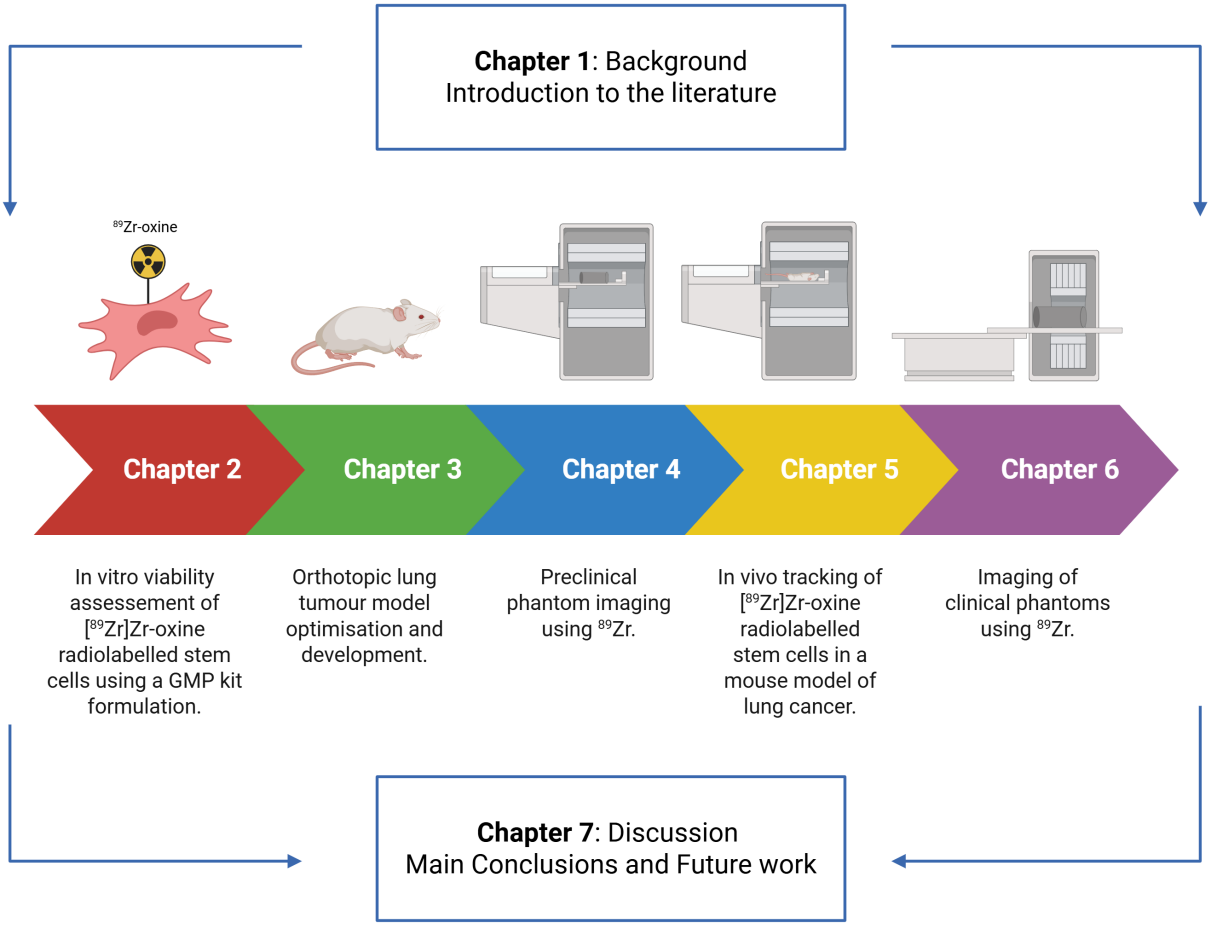

Figure 1.6: A schematic overview of the structure of this thesis [74].

CHAPTER 2

In vitro Viability Assessment of [^{89}Zr]Zr-oxine Radiolabelled Stem Cells using a GMP Kit Formulation

2.1 Introduction

A crucial part of the development of a cell-based therapy is understanding the *in vivo* cell biodistribution, survival and proliferation characteristics, first in naïve and animal models of disease and later in patients, as part of clinical trials. Therefore, there is a need for the development of *in vivo* cell tracking imaging methodologies for characterising cell therapies. The cell labelling methodology should be suitable for the cell type being monitored, clinically applicable, and provide non-invasive imaging of the cell therapy over an appropriate time frame of evaluation. As cell therapies are a living drug and radiolabelling methods could affect cell viability or therapeutic efficacy, each radiolabelling method should be assessed in each specific cell type, first *in vitro* for the validation of the radiolabelling method, and then in preclinical *in vivo* studies, for the accurate assessment of cell distribution by longitudinal non-invasive imaging [76].

There are two cell radiolabelling methods, known as indirect and direct. As was discussed in section 1.4, the indirect method requires genetic engineering of cells, to express a non-native enzyme, receptor or transporter, which acts as an imaging reporter gene. The reporter is usually permanently integrated into the cell's DNA by viral transduction, and it allows them to be targeted by subsequent injection of the reporter specific tracer used in molecular imaging. Whereas, direct radiolabelling methods involve the incorporation of the radiolabel into cells, *in vitro*, under sterile conditions prior to

administration and does not require genetic engineering of the cells. This allows for control of the amount of radioactivity added to the cell and provides good signal to noise ratio, as initially the administered radiation is completely contained within the cells being tracked, in contrast to the indirect method which tends to have high background tracer uptakes. The radiolabelling method chosen should always be assessed for toxicity and cell viability of the specific cell type, at clinically relevant activities needed for imaging the patient cell dose, before it can be clinically translated [40].

So far, the most important obstacle to overcome for the clinical implementation of [^{89}Zr]Zr-oxine radiolabelled cells has been the absence of a fast and easily clinically applicable method of cell radiolabelling that can be used under good manufacturing practices (GMP). The [^{89}Zr]Zr-oxine radiolabelling method developed by Ferris et al. [77] has been extensively used in the literature to radiolabel and track different cell types, *in vivo*, in mouse models, including T cells [78, 79], bone marrow cells [80, 81], dendritic cells, natural killer (NK) cells [82] and stem cells [46]. However, the method developed by Ferris et al. utilises chloroform as a solvent with subsequent evaporation and redissolution in a small amount of dimethyl sulfoxide (DMSO) [77]. The method is relatively simple for utilisation in research animals, however, for the GMP production of radiolabelled cell therapies, solvents and reagents that are clinically approved and biocompatible need to be used, while chloroform is not GMP-compliant for such applications. Furthermore, the method involves several steps, requires meticulous precision during the neutralisation step and uses organic solvents that require quality control tests and solvent evaporation, making it challenging to be applied in the clinic, as it needs extensive handling during the preparation process, increases the chance of user error, and the radiation dose to the radio-pharmacist conducting the process.

For clinical translation, a simple one-step method is required, such as the "kit" utilised for other clinical radiopharmaceuticals, for example [^{99m}Tc]Tc-D,Lhexamethylene-propyleneamine oxime ([^{99m}Tc]Tc-HMPAO, [^{99m}Tc]Tcexametazime).

A kit formulation that can be used under GMP, sterile conditions, would fast track the clinical translation and implementation of *in vivo* cell tracking as part of clinical trials. An oxine kit formulation developed and published by Man et al. is a GMP compliant, clinically translatable protocol that can be used for rapid, one-step preparation of [^{89}Zr]Zr-oxine, [^{64}Cu]Cu-oxine and [^{68}Ga]Ga-oxine for radiopharmaceutical applications. In Man et al. they assessed the kit formulation in radiolabelling human white blood cells (WBC) with [^{89}Zr]Zr-oxine, by applying a clinical protocol [76]. However, no clinical protocol for the GMP grade radiolabelling of stem cells, using a kit formulation, has been developed.

In this chapter, a clinically translatable radiolabelling method for MSCs, using [^{89}Zr]Zr-oxine, was developed by utilising the kit formulation of Man et al. and labelling a clinical MSC therapy GMP product. The therapeutic cells were the MSC cells engineered to express the TRAIL protein (MSCTRAIL) made via GMP production methods for administration to lung cancer patients, as part of the TACTICAL clinical trial. *In vitro* assays were applied for the assessment of cell viability due to potential toxicity from the kit formulation alone and due to radioactivity, for a range of clinically relevant amounts of radioactivity per million cells. Furthermore, measurements of activity retention were conducted. All *in vitro* measurements were conducted for up to 9 days after radiolabelling.

2.2 Materials and Methods

2.2.1 Optimisation of the procedure required for using the kit formulation for the production of [^{89}Zr]Zr-oxine for MSC cell radiolabelling

The kit formulation used in all radiolabelling studies was kindly provided by the team that developed and published it, in King's College London, London, United Kingdom [76]. The [^{89}Zr]Zr-oxalate was purchased from Revvity Health Sciences, Inc. (previously PerkinElmer Health Sciences, Inc.) and it was provided at 1.0-1.5 MBq/µL, on reference day, in 1 M oxalic acid.

The kit formulation developed and published by Man et al. consists of 8-hydroxyquinoline (oxine) with a final concentration of 0.5 mg/mL, 4-(2-hydroxyethyl)-1-piperazineethanesulfonic acid (HEPES) with a final concentration of 1 M and polysorbate 80 with a final concentration of 1 mg/mL, in ultrapure H_2O, adjusted to pH 7.9-8.0 with aqueous NaOH. HEPES is a buffer used to maintain the solution at pH 7-8, polysorbate 80, also known as Tween 80, is a surfactant used as an emulsifier, solubiliser, and stabiliser to dissolve the lipophilic [^{89}Zr]Zr-oxine in the aqueous solution and prevent its aggregation or precipitation. NaOH is a base to neutralise the acidic solution of the commercial [^{89}Zr]Zr-oxalate product. The kit formulation is filtered through a 0.2 µm membrane (Millipore), it is dispensed into sterile glass vials and stored at room temperature in the dark up to 1 year [76].

For the production of [^{89}Zr]Zr-oxine, different concentrations of kit formulation and [^{89}Zr]Zr-oxalate (in 1 M oxalic acid) were assessed as can be seen in the following table 2.1. The values are ordered in increasing volume of activity used.

Activity (MBq)	Volume of activity (µL)	Volume of kit (µL)	Activity volume to kit volume (%)
0.86	1	10	10.0
0.96	1	10	10.0
1.95	2	100	2.0
1.91	2	100	2.0
8.84	10	100	10.0
10.90	10	100	10.0
11.85	10	100	10.0
13.06	14	100	14.0
28.12	28	250	11.2
34.70	24	240	10.0
18.70	25	240	10.4

Table 2.1: The different volume combinations of activity ([^{89}Zr]Zr-oxalate in 1 M oxalic acid) and kit formulation used, for the production of [^{89}Zr]Zr-oxine, alongside the percentage of activity volume compared to the kit volume used.

The [^{89}Zr]Zr-oxalate was added to the kit formulation, in a glass vial (Certified CD™ Vial (Center Draining) Kit - SUPELCO®), behind lead shielding using a pipette. The glass vial was left at room temperature behind the lead shielding for 10 min. The product formation was confirmed by Thin Layer Chromatography (TLC) using Whatman No.1 paper (GE Healthcare) cut in 6 cm strips and 100% ethyl acetate (EtOAc) as the mobile phase [76]. One µL of the product formulation was put on one end of a 6 cm paper strip, with the position marked using pencil. The strip was then put in a 15 mL falcon tube containing 1 mL of EtOAc, so that the formulation was at the bottom above the level of the EtOAc with the lower edge of the Whatman No.1 paper strip submerged in the EtOAc. Once the EtOAc had absorbed and reached the top of the paper strip, the strip was cut in two parts; the lower part, where the formulation was positioned (2 cm), was the one associated with the unchelated ^{89}Zr and the upper part (4 cm) was associated with [^{89}Zr]Zr-oxine. Whatman No. 1 paper is a highly hydrophilic cellulose-based medium that retains polar impurities, such as the unchelated ^{89}Zr, at the point

of origin. Whereas, the lipophilic [^{89}Zr]Zr-oxine complex readily dissolves in EtOAc, a moderately polar organic solvent, and it migrates with the solvent to the top of the strip. This clear separation allows for the measurement of radiochemical yield. The paper strips were measured in a Wizard 2480 automated gamma counter (PerkinElmer). The radiochemical yield of the final product was calculated as the counts associated with the [^{89}Zr]Zr-oxine as a percentage of the total counts. A schematic representation of the preparation of [^{89}Zr]Zr-oxine can be seen in figure 2.1 (a).

2.2.2 Cell preparation

Two patient infusion bags of 200 x 10^6 MSCTRAIL cells in 30 mL each, were defrosted in a water bath at 37 °C. In a Class II Microbiological Safety Cabinet using aseptic technique, the cells were removed from the infusion bags using a spike adapter (OriGen Biomedical, Inc) and a 50 mL syringe for each one. Then the cells were mixed with MEM a, GlutaMAX™ Supplement, no nucleosides (Gibco™, Thermo Fisher Scientific Inc.) with 10% foetal bovine serum (FBS; Gibco™), in 1:1 ratio, in sterile 50 mL falcon tubes. The cells were then centrifuged at 300 g for 5 min and the media was removed by vacuum suction. Media was again added to the cells, 25 mL in each 50 mL falcon tube and the cells were mixed and counted, by mixing a 10 µL aliquot of cell suspension with 10 µL of Trypan Blue, which was then pipetted onto a haemocytometer and viewed on an inverted microscope. Then the cells were split in T175 flasks (Thermo Fisher Scientific) in MEM a, GlutaMAX™ Supplement, no nucleosides with 10% FBS, approximately 7 million cells per flask, and put in an incubator (GS Biotech) at 37 °C with 5% CO_2. The media in the flasks was changed the next day and the flasks were left in the incubator for a few days until they were confluent. Once the flasks were confluent the cells were detached by Trypsin-EDTA (0.05%) phenol red (Gibco™), and counted again by Trypan Blue. Finally, the MSCTRAIL cells were frozen in FBS with 10% DMSO, approximately 7 million cells in 1 mL, in cryovials (Fisherbrand™), for use in all future experiments.

2.2.3 Cell radiolabelling

For the *in vitro* cell viability assessment of [^{89}Zr]Zr-oxine radiolabelled MSCTRAIL cells, using the kit formulation, two *in vitro* studies were conducted. For the production of [^{89}Zr]Zr-oxine, as was explained in section 2.2.1, 10 µL of [^{89}Zr]Zr-oxalate (in 1 M oxalic acid) was added in 100 µL of kit formulation (total final volume 110 µL), in a glass vial, and left at room temperature behind lead shielding for 10 min, for both studies. The radiochemical yield of the final product was calculated as was explained before in 2.2.1.

For *in vitro* study 1, the MSCTRAIL cells were radiolabelled with 2 activity levels, by incubating the cells with different volumes of the [^{89}Zr]Zr-oxine/kit formulation. For *in vitro* study 2, the MSCTRAIL cells were radiolabelled with 4 activity levels, again by incubating the cells with different volumes of the [^{89}Zr]Zr-oxine/kit formulation.

All tissue culture and cell radiolabelling was conducted in a Class II Microbiological Safety Cabinet using aseptic technique. When samples needed to be centrifuged or measured in the dose calibrator (CRC-55tR), this was done using sterile closed falcon tubes.

The cryovials containing MSCTRAIL cells were defrosted in a water bath at 37 °C, mixed with MEM a, GlutaMAX™ Supplement, no nucleosides with 10% FBS, in 1:1 ratio and then washed twice with DPBS (Gibco™) (10 mL). For all the washes a centrifuge at 300 g for 5 min was used. The cells were counted by mixing a 10 µL aliquot of cell suspension with 10 µL of Trypan Blue, which was then pipetted onto a haemocytometer and viewed on an inverted microscope, as before. MSCTRAIL cells were then re-suspended in DPBS for radiolabelling. The [^{89}Zr]Zr-oxine that was prepared was added to the cells. A schematic representation of the cell radiolabelling process can be seen in figure 2.1 (b). The different initial activities added to the cells, the volumes used, and the number of cells, for both *in vitro* studies, can be seen in table 2.2.

The cells were left for 20 min behind lead shielding, at room temperature, with gentle swirling every 5 min. Then the cells were washed first with MEM a, GlutaMAX™

Supplement, no nucleosides with 10% FBS and then twice with DPBS (10 mL). During the washing process, the activities of the supernatants and the cell pellets were measured using a CRC-55tR calibrator to calculate the labelling efficiency as per the following equation:

$$LE(\%) = \frac{activity\ of\ cell\ fraction}{activity\ of\ cell\ fraction + activity\ of\ supernatant} \tag{2.1}$$

Two types of control cells, without radioactivity, were prepared under the same conditions as the radiolabelled cells, in both *in vitro* studies. Control cells that received 10 µL of kit formulation, adjusted for pH with 1 M HCL, for final pH of 7.5-8.0, to keep the pH conditions the same and control cells where no kit formulation was added. The two types of control cells will be mentioned as control cells with kit and control cells respectively. The control cells with kit were used to assess any possible toxicity to the cells due to the kit formulation and the cells that no kit formulation and no radioactivity was added were the controls of the experimental process. The different volumes used, and the number of control cells, for both *in vitro* studies, can be seen in the following table 2.2.

***In vitro* study**	**Initial Activity (kBq)**	**Volume of [^{89}Zr]Zr-oxine/kit formulation (µL)**	**Volume of cell suspension (µL)**	**Number of cells (million)**
1	345	3	300	2
	805	7	300	2
	control with kit	10	300	1
	control	N/A	300	1
2	5400	50	1500	7
	4320	40	1200	7
	1296	12	400	5
	648	6	200	5
	control with kit	10	300	3
	control	N/A	300	3

Table 2.2: The different activities, volumes, and number of cells utilised for the radiolabelling of MSCTRAIL cells in the two *in vitro* experiments.

Once the final washing process was completed all cells were counted by mixing with Trypan Blue, as before, and then they were re-suspended in MEM a, GlutaMAX™ Supplement, no nucleosides with 10% FBS, supplemented with 50 U/mL penicillin and 50 mg/mL streptomycin (Invitrogen) in 10,000 cells per 100 µL. The complete radiolabelling process, from the point of preparing the kit formulation, was approximately 2 h, because different radioactivity levels and control cells were prepared. The final activities and numbers of cells can be seen in the following table 2.3 for both experiments.

***In vitro* study**	**Final Activity (kBq)**	**Number of cells (million)**	**Activity (kBq/million cells)**
1	121	1.29	94
	140	1.54	91
2	1480	5.15	287
	1290	5.90	219
	320	4.05	79
	280	3.70	76

Table 2.3: The different final activities and numbers of MSCTRAIL cells for the two *in vitro* experiments.

2.2.4 *In vitro* cell viability assays

The MSCTRAIL cells were seeded at 10,000 cells in 100 µL into flat bottom 96-well culture plates (Costar®) straight after radiolabelling, n = 3 per condition and the well plates were kept in an incubator (GS Biotech) at 37 °C with 5% CO_2. The time points of measurements were 24 h (Day 1), 48 h (Day 2), 3 days (Day 3), 4 days (Day 4), 7 days (Day 7) and 9 days (Day 9). A separate well plate was seeded for each time point. The seeding density used aimed for approximately 65% confluent wells at seeding, based on published literature [46]. For *in vitro* study 1 the seeding density and resulting confluency was as intended. However, for *in vitro* study 2 the confluency was higher, and the wells were approximately 90% confluent. This resulted from a discrepancy in the seeding density which may have resulted from working with a larger number of cells and volumes than in study 1, leading to cells that were not as uniformly mixed, or limitations in the accuracy of the manual counting by Trypan Blue using a haemocytomer.

Adenosine triphosphate (ATP) is the energy source of all living cells. Upon cell death, the synthesis of ATP stops and the existing ATP pool degrades quickly, making ATP a widely accepted marker of cell viability. For ATP measurements, the CellTiter - Glo® Cell Viability kit (Promega), which provides a luminescence readout, was prepared according to the manufacturer's instructions [83]. In brief, the CellTiter-Glo Substrate vial was mixed with the CellTiter-Glo Buffer vial, and added at 1:1 ratio to the test wells and control wells containing only media. The luminescence light output was measured 10 min after reagent addition, using a plate reader (VarioSkan Lux, Thermofisher Scientific), as Relative Light Units (RLU). The wavelength range used for the measurements was 360-670 nm. Each measurement of wells containing cells was corrected for the control wells containing only media to calculate the relative ATP level of each well.

The XTT reagent (Roche) was used to measure the metabolic activity of the cells. Living cells with active metabolism reduce the yellow-coloured XTT tetrazolium salt to an orange formazan dye. This reduction process occurs via mitochondrial dehydrogenase

enzymes present in the metabolically active cells. The amount of orange formazan dye produced is directly proportional to the metabolic activity of the cells and the colour change can be quantified by measuring the absorbance using a plate reader. The reagent was prepared according to the manufacturer's instructions [84]. In brief, the XTT labelling agent vial was mixed with the electron coupling reagent vial, for the measurement of the reducing power of cells (NADH levels). To each well, 50 µL of reagent was added, including test wells and control wells containing only media, followed by a 4 h incubation at standard culture conditions (37 °C with 5% CO_2). The absorbance at 490 nm and 630 nm was recorded, then the absorbance of each well was corrected for background metabolism in control wells containing only media and the corrected absorbance at 630 nm was subtracted from the corrected absorbance at 490 nm.

For apoptosis and necrosis measurements the RealTime-Glo™ Annexin V Apoptosis and Necrosis Assay (Promega), a live-cell, real-time (kinetic) assay, was utilised. In the RealTime-Glo™ assay, annexin V binding measures the exposure of phosphatidylserine (PS) on the outer leaflet of the cell membrane during the apoptotic process by luminescence output. The detection reagent used in the apoptosis assay contains near-equimolar ratios of two annexin V fusion proteins (Annexin V-LgBiT and Annexin V-SmBiT) containing complementary subunits of NanoBiT® luciferase. The reagent also contains a time-released luciferase substrate that provides a constant source of substrate over experimental exposure periods. Because the Annexin V-LgBiT and Annexin V-SmBiT luciferase subunits have only modest affinity for each other, luminescence remains low until PS exposure brings the subunits into complementing proximity. The assay also includes a cell-impermeant, profluorescent DNA dye, which detects necrosis by fluorescence signal. The assay was freshly prepared according to the manufacturer's instructions [85], by combining all reagents in media and added in 1:1 ratio to the culture medium of test wells and control wells containing only media, 4 h before acquiring the first measurement. Measurements were acquired using the same well plate for up to 72

h, therefore for this assay 3 separate well plates were needed for measurements over the 9 day time course. The plates will be mentioned as plate 1 (days 1-3), 2 (days 4-6), and 3 (days 7-9). The luminescence light output and the fluorescence at excitation of 485 nm and emission of 520 nm were measured using a plate reader. All measurements of wells containing cells were corrected for the control wells containing only media.

As all well plates were seeded straight after radiolabelling, at time point 0, and were kept in the incubator for up to 9 days, the evaporation of media in the wells needed to be taken into consideration. Therefore, 50 µL of MEM a, GlutaMAX™ Supplement, no nucleosides with 10% FBS was added to all wells at 5 days post-seeding, to ensure that the volume within wells would be kept the same. The ATP and XTT assays were utilised for both *in vitro* studies, while the apoptosis and necrosis assay only for *in vitro* study 2.

2.2.5 Activity retention

For the activity retention measurements, at each time point, the growth media was removed and the well was washed with 100 µL DPBS (+ 1 mM EDTA) to remove any potential leaked radioactivity from the cells. This solution was the media fraction. The cells were then detached by adding 100 µL of Trypsin-EDTA (0.05%) phenol red and the plates were left in an incubator for 10 min under standard culture conditions (37 °C with 5% CO_2). Then the Trypsin-EDTA was removed and the wells were pooled with a further wash of 100 µL DPBS (+ 1 mM EDTA) to remove any radioactivity that could be left in the well. This solution was the cell fraction. The activity in media and cell fractions was measured using a Wizard 2480 automated gamma counter (PerkinElmer) and the percentage of activity retained was calculated as:

$$AR(\%) = \frac{counts\ of\ cell\ fraction}{counts\ of\ cell\ fraction + counts\ of\ media\ fraction} \tag{2.2}$$

Three individually seeded replicates were taken per time point for both *in vitro*

studies. A schematic representation can be seen in the following figure 2.1 (c).

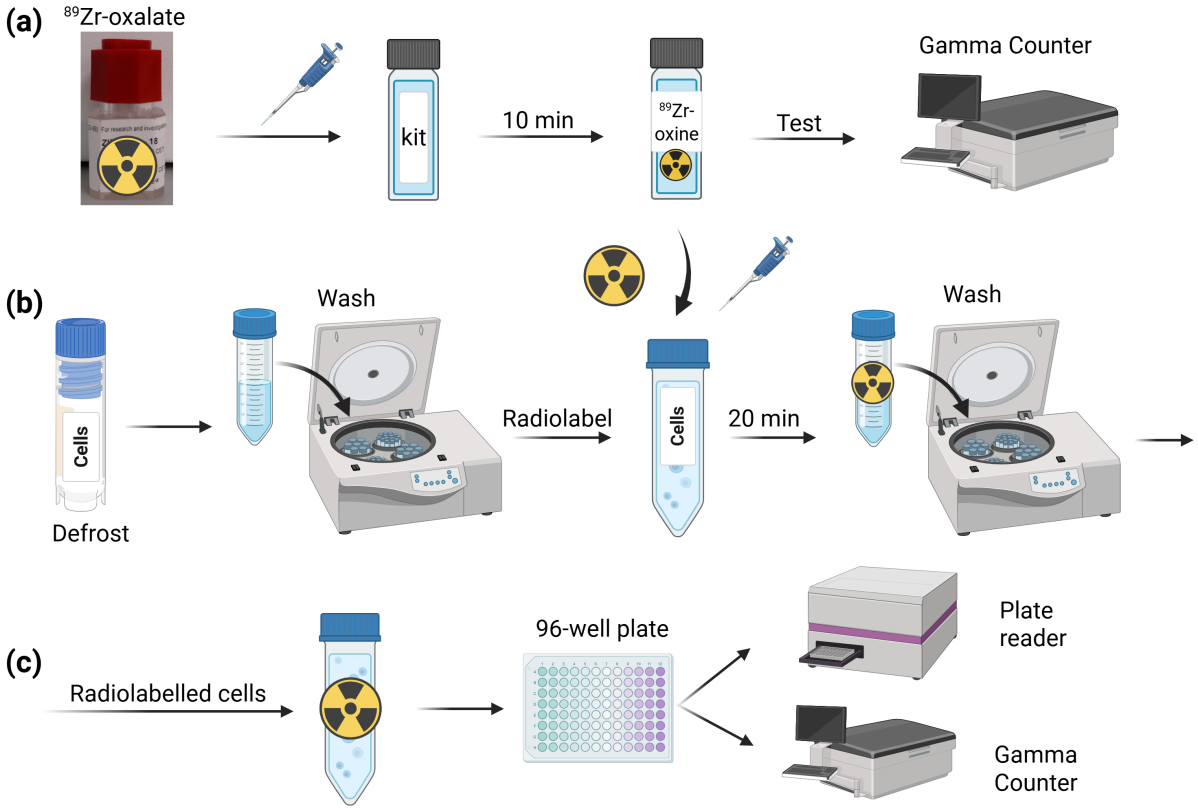

Figure 2.1: Schematic representation of the complete [^{89}Zr]Zr-oxine cell radiolabelling process, using the kit formulation, and the measurements conducted [74].

2.2.6 Statistical analysis

Statistical analysis was performed with GraphPad Prism version 8.0. Data are presented as mean ± standard deviation (SD). Two-way ANOVA was used for all of the experiments. Tukey's multiple comparisons test was used for the longitudinal *in vitro* activity retention. Dunnett's multiple comparisons test versus the control was conducted for the rest of the experiments. Statistical significance was identified for *p $\leq$ 0.05, **p $\leq$ 0.01, ***p $\leq$ 0.001.

2.3 Results

2.3.1 Production of [^{89}Zr]Zr-oxine using the kit

The radiochemical yield of [^{89}Zr]Zr-oxine was assessed for different volume combinations of [^{89}Zr]Zr-oxalate (in 1 M oxalic acid) and kit formulation. The different volume combinations used can be seen in the following table 2.4. The order of values is in decreasing radiochemical yield (%).

Activity (MBq)	**Volume of activity (µL)**	**Volume of kit (µL)**	**Activity volume to kit volume (%)**	**Radiochemical yield (%)**
1.95	2	100	2.0	86.82
1.91	2	100	2.0	83.66
0.86	1	10	10.0	82.70
0.96	1	10	10.0	79.25
8.84	10	100	10.0	73.72
10.90	10	100	10.0	71.85
28.12	28	250	11.2	70.72
34.70	24	240	10.0	69.72
11.85	10	100	10.0	65.59
18.70	25	240	10.4	64.91
13.06	14	100	14	61.77

Table 2.4: The [^{89}Zr]Zr-oxine radiochemical yield for different volume combinations of activity ([^{89}Zr]Zr-oxalate in 1 M oxalic acid) and kit formulation used, alongside the percentage of activity volume compared to the kit volume used.

A negative correlation was found between the volume of activity used compared to the kit volume and the radiochemical yield ($R^2 = 0.6068$).

2.3.2 Labelling efficiency

For *in vitro* study 1 the radiochemical yield was 61.77% and for *in vitro* study 2 it was 65.59%. The washing process, after the addition of radioactivity, results in the discarding of the unincorporated [^{89}Zr]Zr-oxine, that has not crossed the cell membrane, as well as in a loss of cells, that are discarded with the wash solutions. The reduction in the number of cells, after 3 washes, was 26.21 ± 8.43% on average, for both radiolabelled and control cells and for both *in vitro* studies. The labelling efficiency of the cells, as a percentage of each wash total (cells and supernatant), was 48.37 ± 1.88% on average for the first wash, while for the second and third washes was 86.12 ± 4.18% and 87.37 ± 6.17% on average, respectively. The labelling efficiency retained after the 3 washes, compared to the initial activity added, was 35.95 ± 1.97%, on average, for all activity levels tested.

2.3.3 Cell viability assays

The RLU measurements, corrected for background, of the ATP assay (relative ATP level) and the relative NADH level measurements of the XTT assay can be seen in figure 2.2 for *in vitro* study 1 and in figure 2.3 for *in vitro* study 2.

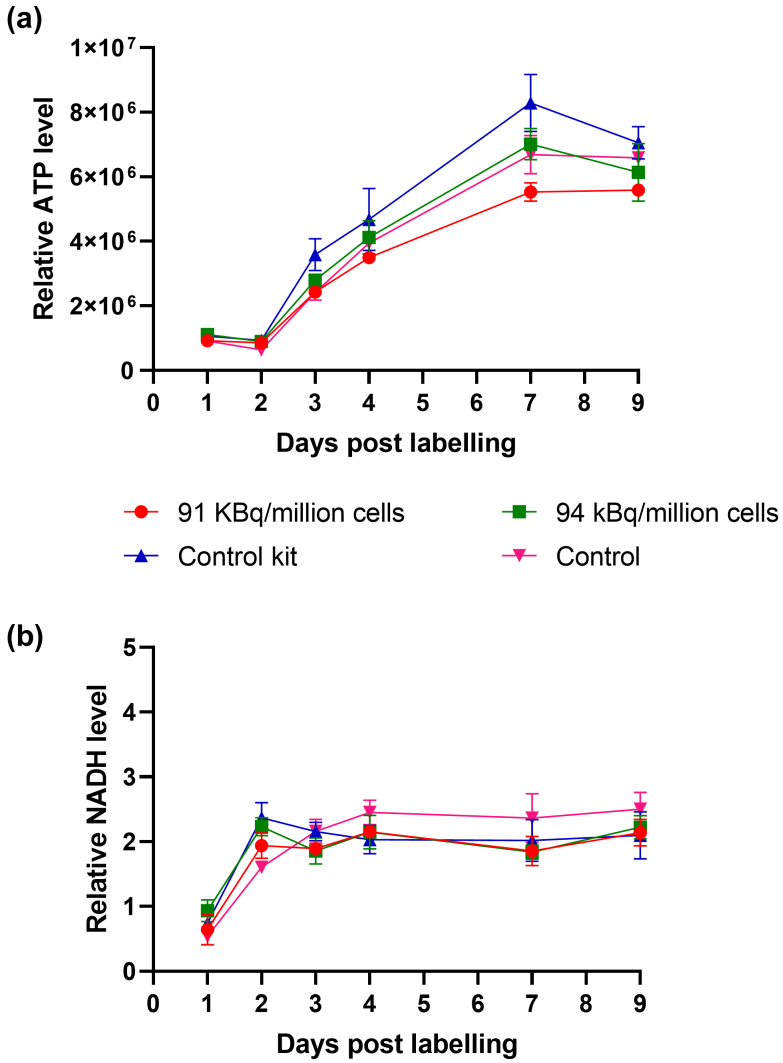

Figure 2.2: Measurements of *in vitro* study 1, for the 2 activity levels and the 2 controls: (a) Relative ATP level, (b) Relative NADH level. Data presented as mean ± SD.

For *in vitro* study 1, two-way ANOVA showed time dependent sensitivity for both ATP and NADH metabolism. The majority of variation was due to time, 93% for ATP and 81% for NADH ($p < 0.0001$) with a small effect from the radioactivity amount, 3% for ATP and 1% for NADH ($p = 0.0108$ for ATP and $p = 0.5532$ for NADH). Multiple comparisons showed no differences between the radioactivity levels and the control as well as the control with kit and the control.

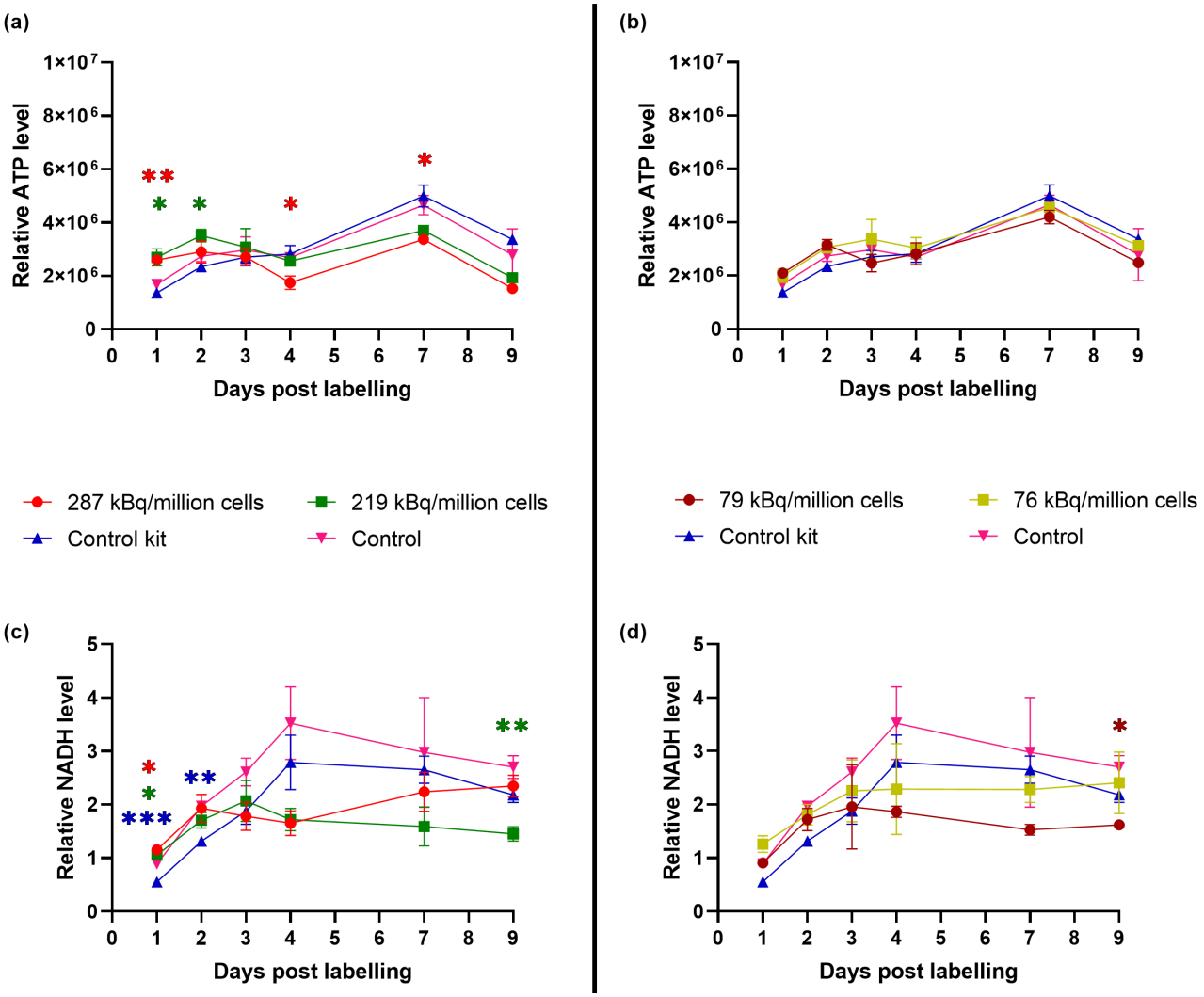

Figure 2.3: Measurements of *in vitro* study 2: (a) Relative ATP level for the 2 highest activity levels and the 2 controls, (b) Relative ATP level for the 2 lowest activity levels and the 2 controls, (c) Relative NADH level for the 2 highest activity levels and the 2 controls and (d) Relative NADH level for the 2 lowest activity levels and the 2 controls. Data presented as mean ± SD.

For *in vitro* study 2, two-way ANOVA showed time and amount of radioactivity dependent sensitivity for both ATP and NADH metabolism. The variation due to time was 60% for ATP and 43% for NADH ($p < 0.0001$) with a smaller but significant effect from the radioactivity amount, 6% for ATP and 17% for NADH ($p = 0.0170$ for ATP

and p = 0.0010 for NADH).

Multiple comparisons for the ATP assay showed an initial difference between the highest activity levels and the control (Day 1: p = 0.0061 for 287 kBq/million cells and p = 0.0438 for 219 kBq/million cells, Day 2: p = 0.0391 for 219 kBq/million cells). For the XTT assay an initial difference between the highest activity levels as well as the control with kit were found with the control (Day 1: p = 0.0292 for 287 kBq/million cells, p = 0.0211 for 219 kBq/million cells and p = 0.0006 for control with kit, Day 2: p = 0.0070 for control with kit). For days 4 and 7 ATP showed a significant difference with the control only for 287 kBq/million cells (p = 0.0402 and p = 0.0343 respectively). For the final time point of day 9, ATP assay showed no differences between the activity levels and the control, but the XTT assay showed a significant difference for the 219 kBq/million cells (p = 0.0062) and 79 kBq/million cells (p = 0.0180). Multiple comparisons of the ATP assay showed no difference between the control cells with kit and the control, while the XTT assay showed an initial difference between them. The initial differences between the activity levels and the controls (at days 1 and 2) could be attributed to seeding density differences between the wells. For the later time points the differences found could be attributed to radiation damage to the cells and the longitudinal nature of the experiment.

2.3.4 Apoptosis and necrosis assay

The apoptosis and necrosis assay measurements conducted in *in vitro* study 2 can be seen in figure 2.4. Annexin V binding is expressed by the luminescence signal, and secondary necrosis is expressed by the fluorescence signal. When luminescence and fluorescence signals emerge concurrently, it suggests a non-apoptotic phenotype. An increase in luminescence is indicative of early apoptosis and an increase in fluorescence with a concurrent decrease in luminescence suggests loss of membrane integrity and secondary necrosis of the cells.

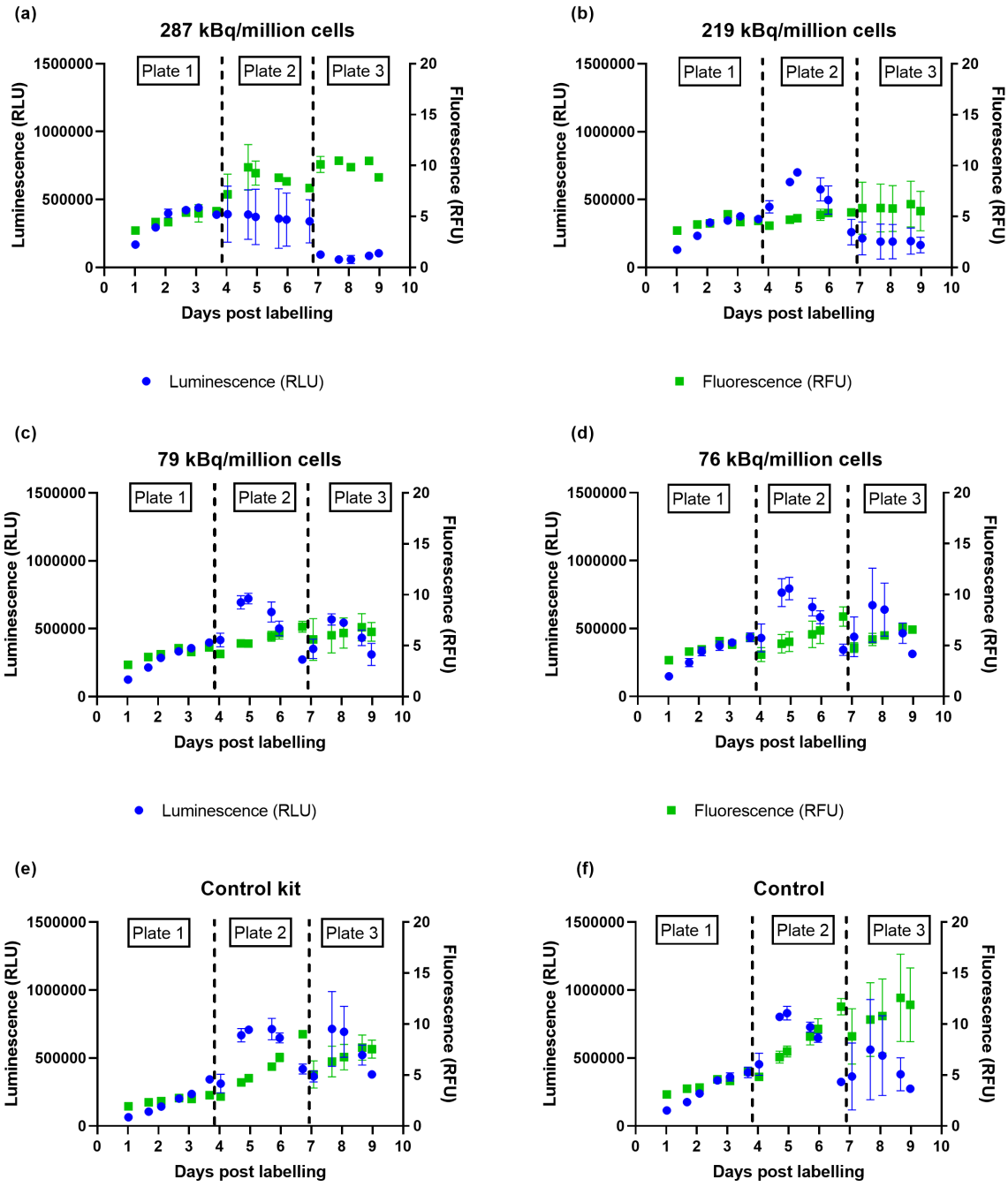

Figure 2.4: *In vitro* study 2: Annexin V Apoptosis and Necrosis assay over time for (a) 287 kBq/million cells, (b) 219 kBq/million cells, (c) 79 kBq/million cells, (d) 76 kBq/million cells, (e) control cells with kit, (f) control cells. Data presented as mean ± SD.

In figure 2.4 the luminescence and fluorescence signals emerge concurrently for the initial time points of plate 1 (0-3 days) for all activity levels and controls suggesting a non-apoptotic phenotype. For plate 2 (4-6 days) the emergence of luminescence signal suggests an early apoptotic phenotype for all activities and controls, except the highest activity tested (287 kBq/million cells). For the highest activity there is an increase in fluorescence signal from day 4 onwards suggesting loss of membrane integrity and secondary necrosis earlier than all the other activities and controls. Plate 3 (7-9 days) shows that for the second highest activity tested (219 kBq/million cells) there is an increase in fluorescence suggesting secondary necrosis from day 7 onwards. Finally, for the rest of the activities and controls for day 7 onwards the results suggest early apoptosis. The error bars for plate 3 are larger compared to the previous plates. Due to the longitudinal nature of the experiment and despite adding 50 µL of growth media in all wells at day 5 post-seeding, the variation between wells of plate 3 was greater than plates 1 and 2, thus affecting the interpretation of the results.

Two-way ANOVA for the apoptosis and necrosis assay, showed time and amount of radioactivity dependent sensitivity for both luminescence and fluorescence signals. The variation due to time was 51% for luminescence and 44% for fluorescence ($p < 0.0001$) with a smaller but significant effect from the radioactivity amount, 10% for luminescence and 23% for fluorescence ($p = 0.0004$ for luminescence and $p = 0.0005$ for fluorescence).

2.3.5 Longitudinal *in vitro* activity retention

The activity retention measurements over the 9 day period can be seen in figure 2.5, for all activity levels tested.

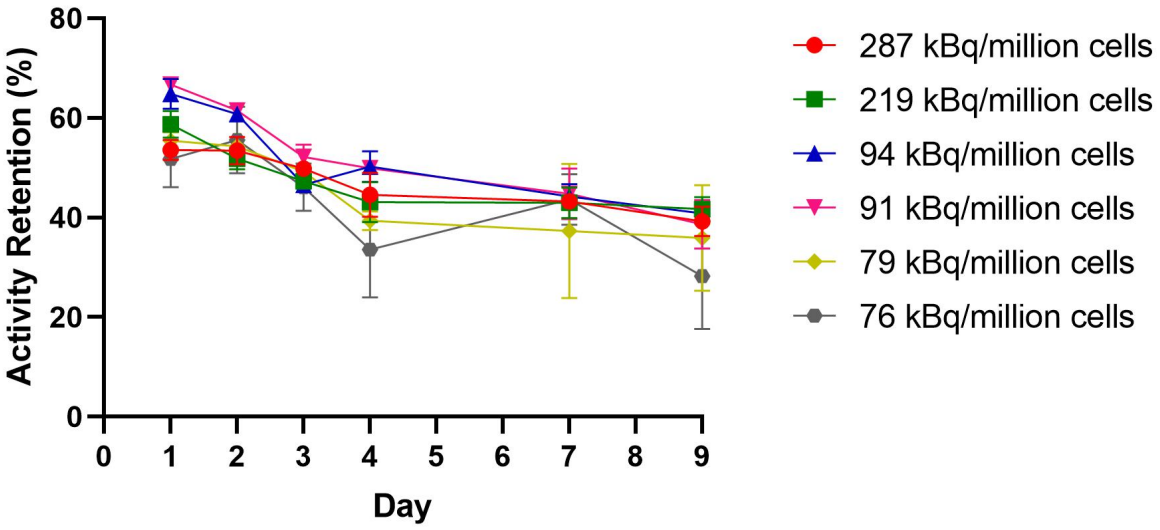

Figure 2.5: Activity retention of the radiolabelled MSCTRAIL cells, for the different activity levels of both *in vitro* studies, over time. Data presented as mean ± SD.

Two-way ANOVA showed that the majority of variation in activity retention (63%) was due to time ($p < 0.0001$), with a smaller but significant effect from labelling amount (11%, $p = 0.0075$). Most of the label loss occurred during the first 24 h after which label loss was slower, with a further 21% being lost between days 1 and 9, on average, for all activities tested. Multiple comparisons between the different activities for each time point showed no differences between them.

2.3.6 Brightfield images

Brightfield images of the wells were acquired using an EVOS FL Cell Imaging System (Thermo Fisher Scientific). In the following figures 2.6 to 2.9 a representative image of a

well for Day 1 and Day 7, for the highest and lowest activity levels tested, alongside the control with kit and control cells can be seen. The images show the well confluence for the different activity levels and controls.

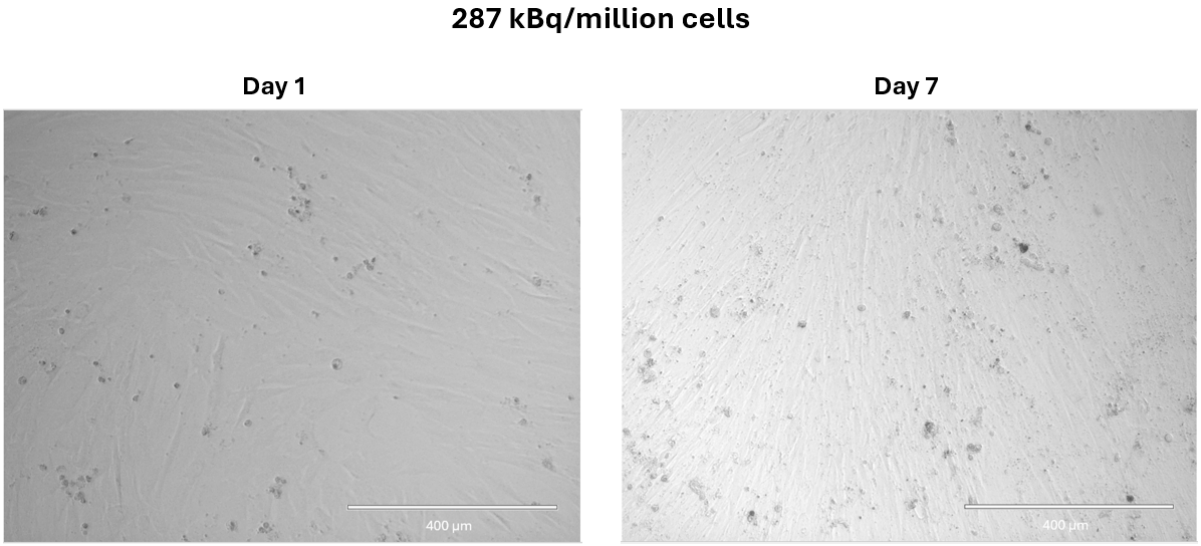

Figure 2.6: Well images of Day 1 and Day 7 for the 287 kBq/million cells activity level.

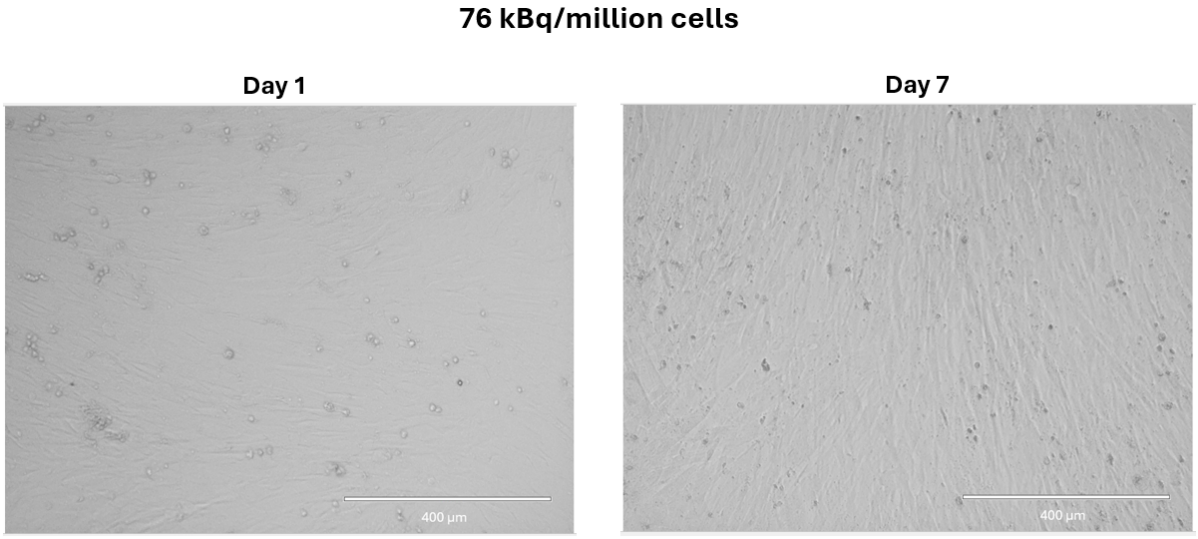

Figure 2.7: Well images of Day 1 and Day 7 for the 76 kBq/million cells activity level.

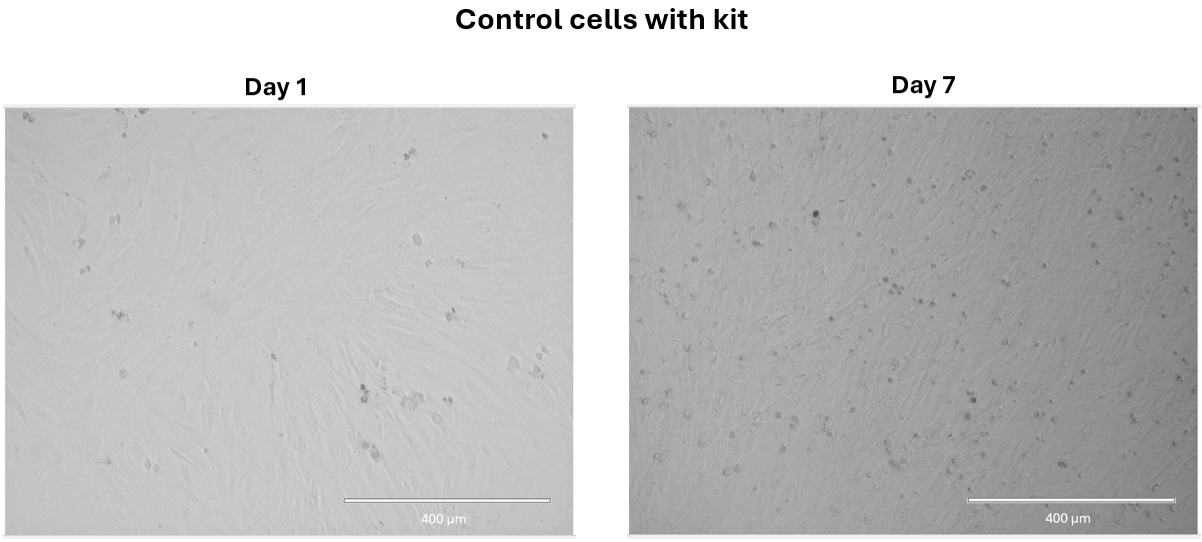

Figure 2.8: Well images of Day 1 and Day 7 for the control cells with kit.

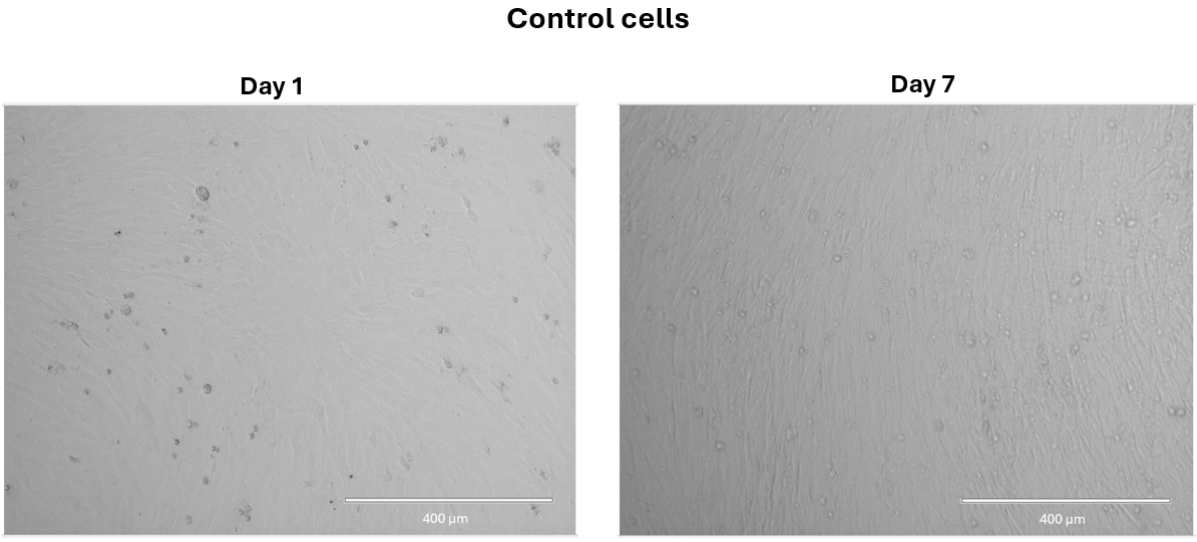

Figure 2.9: Well images of Day 1 and Day 7 for the control cells.

2.4 Discussion

Part of the development of novel cell therapies is the understanding of the cell biodistribution, viability and proliferation, *in vivo*. For the successful implementation of a cell therapy in clinical practice, clinical trials are conducted to assess the safety and efficacy of the therapy in patients. Imaging is a safe, clinical method that could be used to assess the *in vivo* biodistribution of stem cell treatments in patients. Nonetheless, imaging cell distribution in patients is not routinely conducted in novel cell therapies, as there is a lack of clinically applicable radiolabelling methods that are GMP standard and can be applied to stem cells in a radiopharmaceutical environment.

In this chapter, a clinically translatable method for the direct [^{89}Zr]Zr-oxine radiolabelling of MSCs was developed using a GMP grade kit formulation, that provides the preparation of [^{89}Zr]Zr-oxine in a single step, without the need of further processing of the commercially GMP available [^{89}Zr]Zr-oxalate. In Man et al. they assessed the radiochemical yield of [^{89}Zr]Zr-oxine with [^{89}Zr]Zr-oxalate (in 1 M oxalic acid), as the starting material, and they found that it was typically formed in 85-92% radiochemical yield (95% confidence interval, n = 15) [76]. Whereas, in this work the range of values was 61.77-86.82% with a mean value of 72.74 ± 8.25% (n = 11). The results of this work are lower than Man et al., and a negative correlation was identified between the volume of activity and the volume of kit formulation used. The oxalic acid of the ^{89}Zr commercial product is rapidly neutralised by the NaOH of the kit, therefore care must be taken in both the volume of oxalic acid and amount of radioactivity, in comparison to the volume of kit used, as higher amounts of oxalic acid could fail to be buffered properly by the NaOH in the kit, which will reduce the radiochemical yield of the final product and thus affect the cell radiolabelling efficiency. In Man et al. they found that 100 µL of HEPES-buffered formulation, containing 50 µg oxine and 52.5 µmol NaOH, was capable of buffering a maximum of 18 µL of [^{89}Zr]Zr-oxalate solution [76].

The washing process, after radiolabelling, was conducted to discard the unincorporated [^{89}Zr]Zr-oxine activity. According to Patrick et al., three washes were found to be sufficient to discard the unbound activity from the cells [46], therefore three washes were also used in this work. In Man et al. the labelling efficiency of WBC with [^{89}Zr]Zr-oxine, using the same kit formulation, was 48.7 ± 6.3% for the one wash that they conducted [76]. In this work, the labelling efficiency for the first wash was 48.37 ± 1.88%, which is in agreement. In Patrick et al. the highest labelling efficiency, retained after 3 washes, for the same stem cell product, using the radiolabelling method of Ferris et al., was between 29 and 33% [46], which is in agreement with the 35.95 ± 1.97% of this study.

In Man et al. the activity retention of WBC for ^{89}Zr was 86.6 ± 2.9% after 24 h [76], while in this work it was between 66.69 and 51.76%, on Day 1, for all activity levels tested. The values in this work are lower, however activity retention is cell type specific. In Patrick et al., the activity retention for the same stem cell product, longitudinally after radiolabelling, was approximately 58% on Day 1, decreasing to approximately 45% on Day 9 [46], which is in agreement with this work.

In Patrick et al. the ATP and XTT assays were also utilised, to assess the stem cell viability after [^{89}Zr]Zr-oxine radiolabelling, using the Ferris et al. method. In their work, they identified time and amount of radioactivity sensitivity of the cells, as was found in this chapter. They assessed a range of activities between 79 to 332 kBq/million cells and they found a significant difference between the radiolabelled cells and the control (stem cells in DPBS) only for days 7 and 9 [46]. In this work, the ATP assay showed a significant difference with the control for the highest activity level for days 4 and 7 and the XTT assay showed a significant difference for two activity levels for Day 9. Nonetheless, no consistent significant difference was shown for the final time points, between the radiolabelled cells and the control, for the different assays used. The differences that were found can be justified by the fact that as time goes by cell death can occur due to

radiation damage to the cells, an over-confluent well and due to the well media drying out due to evaporation in the incubator. The initial differences found between the activity levels and the controls (figure 2.3) could be attributed to seeding density differences between the wells.

Flow cytometry was conducted in Patrick et al. to confirm that [^{89}Zr]Zr-oxine radiolabelled MSCTRAIL cells maintained their apoptosis-inducing ability against cancer cell lines [46]. However, no flow cytometry could be conducted in this work to assess the viability of different activity levels of radiolabelled cells, as a flow cytometer for radioactive cells was not available. Therefore, in this chapter, the Annexin V Apoptosis and Necrosis assay was utilised for the different activity levels tested. The assay showed that by increasing the activity used per million cells, the cells went into secondary necrosis faster, which is in agreement with previous work [46], thus making the decision on the amount of radioactivity used highly important for longitudinal imaging.

A limitation of the *in vitro* studies was that evaporation occurred in the wells at the edges of the well plate due to the longitudinal nature of the experiment. Despite adding 50 µL of growth media in all wells at day 5 post-seeding, the evaporation effect at the edges of the well plate was not elevated, which explains that the variation between wells for the Annexin V Apoptosis and Necrosis assay of plate 3 was greater than plates 1 and 2. Thus, affecting the interpretation of the results, as was seen in figure 2.4. In future studies the addition of DPBS in all wells surrounding the edges could remedy the evaporation effect. Another limitation of the *in vitro* studies was that the seeding density was not consistent in the two studies, due to the limitations of the manual counting with hemocytometers. For *in vitro* study 1 the wells were approximately 65% confluent providing adequate space for cell proliferation, while for *in vitro* study 2 the wells were approximately 90% confluent thus limiting cell proliferation. In future studies an automated cell counter could be used to have standardised measurements of cell numbers.

In literature, different studies have been conducted to assess the viability of different

immune cell types after ^{89}Zr radiolabelling. In the work of Pham et al, they conducted [^{89}Zr]Zr-oxine radiolabelling using the Ferris et al. method and they assessed the viability of human NK cells by different assays. They found that for the activity level tested (16.7 $\pm$ 4.7 kBq/10^6 cells) there were no significant functional differences between the radiolabelled and unlabelled NK cell characteristics [86]. In the work of Sta Maria et al., they utilised [^{89}Zr]Zr-oxine radiolabelling by adapting the method of Weist et al. [78] and they assessed the viability of CAR T-cells by different assays. They found that the percentage viability and cell function between labelled (37 - 74 kBq per million cells) and unlabelled CAR-T cells was not significantly different [87].

The work of this chapter showed time and radioactivity sensitivity, as was expected and that the control cells with kit did not exhibit differences with the control cells, indicating no significant toxicity due to the kit formulation in MSCs. The kit formulation contains polysorbate 80 that can be toxic for cells with its effects on cell viability being concentration-dependent and varying across different cell types [88]. In this work, extra care was taken to avoid toxicity due to polysorbate 80, as this would hinder the kit's clinical translation. It was chosen to dilute the cells in a concentration of at least 1:30 [^{89}Zr]Zr-oxine/kit formulation to cell suspension. However, to achieve good radiolabelling efficiency it was chosen to have at least 5 million cells per mL in all experiments with radioactivity. Therefore, there was a trade off between the amount of kit formulation and thus the amount of radioactivity used, in a given volume, as well as the number of cells needed to achieve each radioactivity level. The lack of toxicity due to the kit indicates that the kit is suitable for the radiolabelling of MSCs in the clinical setting. The toxicity of the kit formulation only, was not reported in Man et al. for WBC [76] and more work is needed on different cell types to assess any possible kit toxicity before its application in clinical trials of different cell products.

The complete radiolabelling process conducted in this chapter took approximately 2 h, because different activity levels and control cells were prepared for the same

experiment. Whereas, when only one activity level was needed to be prepared, as was done for the *in vivo* experiments of Chapter 5, the process took approximately 50 min after defrosting the cells. The time needed for the complete radiolabelling process is critical in the clinical setting, as the viability of the cells is of the outmost importance. Viability decreases the longer the cells are handled after defrosting and dedicated studies need to be conducted for the viability of each individual cell product. For human bone marrow-derived MSCTRAIL cells the viability after defrosting was assessed by Yuan et al. and it was found that there is a 90 min window post-defrosting during which the MSCTRAIL cells typically maintain maximum viability when left in the cryopreservant (5% DMSO with 95% ZENALB4.5) [89]. For the work of this thesis, the washing process of the cells started immediately after defrosting, therefore the cells were only left in the cryopreservant (FBS with 10% DMSO) for approximately 5 min and the complete process was less than 1 h.

The washing process discards the unbound radioactivity, but results in the loss of cells as well. The work conducted in this chapter showed that the number of cells was reduced by 26.21 ± 8.43 % on average. The reduction of cells due to washing is something that needs to be taken into consideration for clinical applications, as the number of cells administered to the patient needs to be known. Furthermore, the methodology used for washing is important as will be discussed in section 7.2.

For imaging purposes, the amount of radioactivity needed per million cells, depends not only on the cell viability but also on the total number of cells that need to be administered, either to a patient during a clinical trial or to an animal for preclinical studies, as this will affect the total injected activity and thus the effective dose and the PET imaging quality. For the prospective preclinical longitudinal *in vivo* imaging studies utilising mice, the radiolabelled MSCTRAIL cells injected will be 1 million, meaning that the radioactivity per million cells needs to be increased to achieve longitudinal imaging. Therefore, the maximum radioactivity assessed in this work will be used for the *in vivo*

cell tracking work in Chapter 5.

2.5 Conclusion

In this chapter, a clinically translatable GMP grade direct radiolabelling method was developed for MSCs using [^{89}Zr]Zr-oxine. Different activities, as well as controls with and without the addition of the kit formulation, were assessed by applying different *in vitro* assays. The majority of variation was due to time with a smaller but generally significant effect from radioactivity. Multiple comparisons between groups, for each time point, did not generally show a difference between radiolabelled and control cells and no difference was shown between the control cells with and without kit at later time points. The effect of radioactivity on cell viability has been established, however the absence of toxicity due to the kit formulation identified in this work makes the GMP kit suitable for translation into the clinic for the radiolabelling of stem cells.

CHAPTER 3

Orthotopic Lung Tumour Model Optimisation and Development

3.1 Introduction

The use of animal models is crucial in the development, assessment and validation of new lung cancer treatments. A large number of mouse models have been developed and utilised in the literature, to study all types of lung cancer, yet each model has its own strengths and weaknesses that need to be carefully evaluated before the start of a study. For translational imaging studies the clinical representation of the model, as well as the imaging question aimed to be answered need to be taken into consideration before choosing the animal model. There are four major preclinical types of models. Models developed by utilising tumour cell lines, patient-derived xenografts (PDXs), genetically engineered mouse models (GEMMs) and chemogenic models [90].

Tumour cell lines can be used to develop xenograft (heterogeneous) models or syngeneic (homogeneous) models. The xenograft models are typically induced by administering human cancer cells into immunodeficient mice, while the syngeneic models are created by administering murine cancer cell lines into wild type or genetically engineered mouse strains. The method of administration of the cancer cells affects the model created. Orthotopic models are created by administering cancer cells into their anatomically correct location within the animal. Whereas ectopic models are created by administering the cells into a non-native site, such as under the skin, by subcutaneous injection, or in a different organ [91].

Patient-derived xenograft models are created by transferring human tumour fragments or cells, isolated from patient tumours, to immunodeficient animals. These

models can maintain the heterogeneity of the original human tumour, making them suitable for developing personalised treatment strategies. However, not all patient tumours will successfully engraft in mice. The success of engraftment can depend on the type of cancer, the stage of disease, and the specific characteristics of the tumour. Furthermore, the transplantation is commonly subcutaneous, thus creating ectopic models, that do not recapitulate the normal tumour micro-environment of a host tissue and are not representative of the human counterpart presentation [90].

Genetically engineered mouse models are mice that have had their genome deliberately altered. GEMMs can be created by different methods, depending on the type of genetic modification used. Transgenic mice have foreign DNA introduced into their genome (transgene) and a research area that transgenic mice are used is for Alzheimer's disease [92]. Knockout mice have a specific gene completely "knocked out" (deleted or inactivated). Conditional knockout mice have a gene deleted only in specific tissues or at specific stages of development. Knockout p53 mouse models have been used in cancer research for the understanding of the p53 pathway [93]. Knock-in mice have a specific genetic mutation or human gene inserted into the genome at a precise location. An example of a knock in mouse model was developed for the study of Huntington's disease [94]. CRISPR/Cas9-Edited mice are created by utilising the CRISPR/Cas9 gene-editing technology that allows for precise modifications in the genome (insertions, deletions, or specific point mutations) [90]. GEMMs are valuable in studying the role of individual genes and gene interactions as well as oncogene addiction. In GEMMs, the tumours develop after multistage pathogenesis and the imaging representation can be variable as multiple tumours can grow, and metastasis can occur. Finally, it can be time consuming to bring together all the desired mutations into a single genome and the breeding of the mice to generate the complex genome can be costly [90, 95].

Chemogenic models are created by administering a chemical compound to an animal via ingestion, inhalation, injection or dermal absorption, to induce a specific

disease or pathological state to the animal [96]. Models of lung cancer have been created by intraperitoneal (i.p.) injection or intra-gastric gavage administration of 4-(methylnitrosamino)-1(3-pyridyl)-1-butanone (NNK), which is a carcinogen found in tobacco and has been demonstrated to have a significant association with lung cancer [97]. Another chemogenic model of lung cancer has been established by repeated i.p. injections of urethane, which is a known carcinogen chemical compound [98]. Chemogenic models can mimic the clinical cancer progression of patients and they can be used to study the biological factors for cancer development and the therapeutic effects of drugs in development. Nevertheless, their development can be time-consuming as approximately 6 months up to 1 year is needed for tumour development depending on the model. Furthermore, the tumours occur unpredictably in the animals in terms of timing, location, number and size of lesions, making their use challenging for *in vivo* cell tracking, especially in the lung [96].

For imaging studies that aim to track cell therapies *in vivo*, in the diseased lung, clear tumour and healthy lung parenchyma areas are needed, to allow for their clear delineation, thus offering quantitative measurements of cell distribution in diseased and healthy tissue. Furthermore, for tracking human cell therapies in mice, severely immunocompromised mice are needed as models, to prevent immune rejection of the human cells. Therefore, the orthotopic cancer cell implantation in severely immunocompromised mice is the most appropriate choice to create the representation needed. The aim of this chapter was to develop and validate a minimally invasive orthotopic mouse model of lung cancer, that represented distinct tumour formation with clear areas of healthy lung parenchyma. The mouse model will be utilised for the *in vivo* cell tracking of radiolabelled MSCTRAIL cells, to acquire quantitative measurements, for the understanding of cell distribution in diseased and healthy lung tissue.

In this chapter, four orthotopic tumour models utilising two different human cancer cell lines were conducted, and tumour growth was monitored by preclinical

imaging and validated by histological analysis. Immunocompromised NOD Scid Gamma (NSG) mice were chosen, as human cell lines were administered, and the imaging methods applied were Bioluminescent Imaging (BLI), micro-CT and ^{18}F-FDG PET/CT imaging. BLI provided proliferation monitoring of the cancer cells during the first weeks after implantation. Whereas micro-CT imaging offered anatomical information, and tumour sizing and ^{18}F-FDG PET/CT provided functional metabolic information regarding tumour pathology. The A549 human lung adenocarcinoma and MSTO-211H (CRL-2081™) human malignant pleural mesothelioma cell lines, previously used for therapeutic characterisation of MSCTRAIL [99, 25], were utilised. The two cell lines were administered by four different, minimally invasive, methods in order to improve the chance of gaining the desirable representation. In Study - 1 the A549 cell line was administered by intravenous (i.v.) injection. In Study - 2 the MSTO-211H cell line was injected by intrapleural (i.pl.) injection in the right intrapleural space. In Study - 3 the A549 cell line was injected by intralobular (i.l.) injection into the left lung parenchyma and finally in Study - 4 the MSTO-211H cell line was injected by i.l. injection into the right lung parenchyma.

3.2 Materials and Methods

3.2.1 Cell Culture

All cancer cells were cultured at 37 °C with 5% CO_2. The A549 lung adenocarcinoma cells were cultured in DMEM (Gibco™, Thermo Fisher Scientific Inc.) supplemented with 10% FBS (Gibco™). The MSTO-211H human malignant pleural mesothelioma cells were cultured in RPMI (Gibco™) with 10% FBS. Both the A549 and MSTO-211H cell lines were transduced to express firefly luciferase [31] and they were a kind donation from Prof Sam Janes's laboratory at the Department of Respiratory Medicine - UCL.

3.2.2 Cell implantation in mice

Twenty female mice, 5 for each study, with severe combined immunodeficiency (NOD-SCID Gamma, strain NOD.CB17-Prkdc^{scid}/NCrCrl; Charles River, UK) were acquired at 6-8 weeks old. After a week of acclimatisation, the cell implantation took place and at that time they weighed 20-24 g. The weight of the animals was monitored twice per week for the whole duration of the studies. All procedures were carried out under the authority of project and personal licences issued by the Home Office - UK and were approved by the local Animal Welfare and Ethical Review Bodies at University College London - UK.

All procedures were performed under isoflurane anaesthesia (2% - 2.5% isoflurane in oxygen 1 L/min) and the four different modes of cancer cell administration can be visualised in figures 3.1, 3.2 and 3.3. For Study - 2 and 4 a small patch of fur was shaved over the right-hand side of the rib cage, and for Study - 3 over the left-hand side of the rib cage. The fur was removed so that the rib cage could be clearly visualised. The point of injection for the intrapleural and intralobular administrations was between the third and fourth rib up from the bottom of the rib cage. Both lungs were chosen to be assessed for i.l. injection, as no incision was done. The right lung is larger in size than the left,

however the left lung is a single lobe. During injection the mice breathed normally under anaesthesia. The number of cells, the volumes of injection and the injection depths are shown in table 3.1.

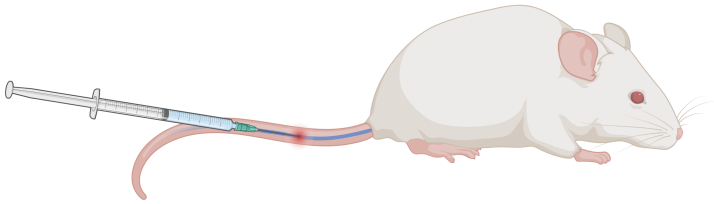

Figure 3.1: Study - 1: Intravenous injection in a mouse performed via the lateral tail vein [74].

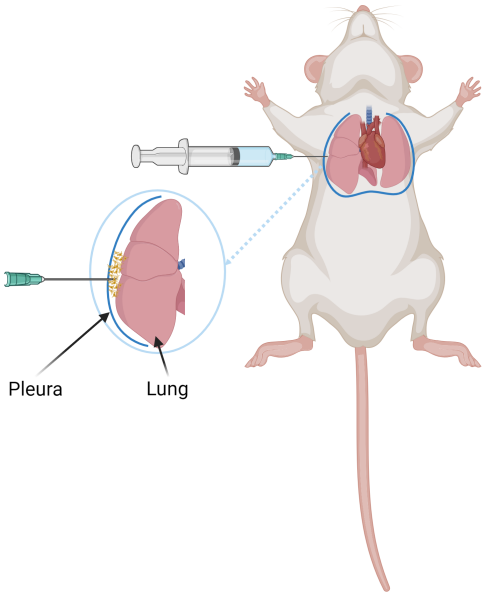

Figure 3.2: Study - 2: Intrapleural injection in a mouse performed via the right rib cage. The cell suspension was injected in the intrapleural space, and the cells are presented in yellow [74].

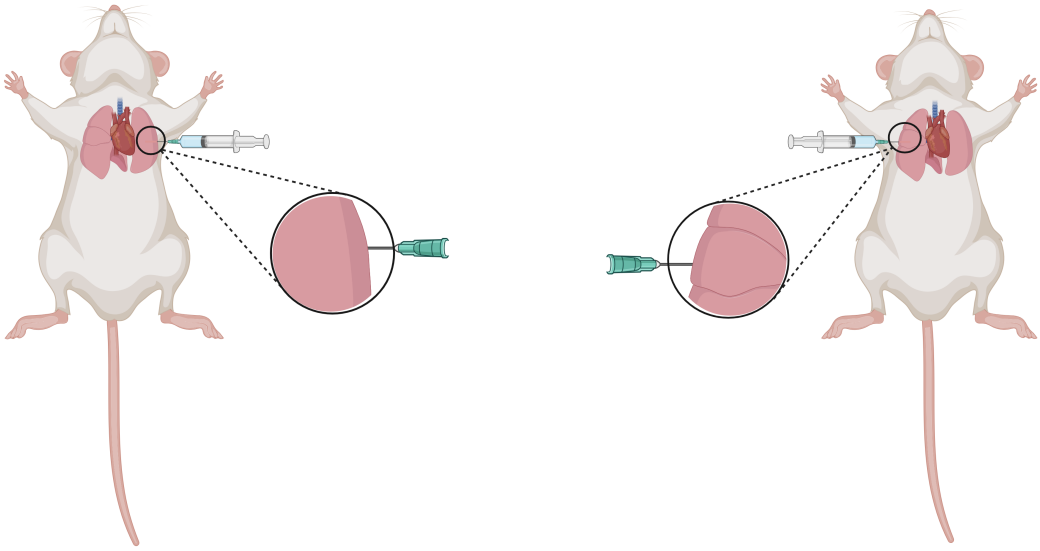

(a) (b)

Figure 3.3: (a) Study - 3: Intralobular injection in a mouse via the left rib cage. The cell suspension was injected into the left lung parenchyma. (b) Study - 4: Intralobular injection in a mouse via the right rib cage. The cell suspension was injected into the right lung parenchyma [74].

Study	Cell line	Number of cells	Injection method	Injection volume (µL)	Injection depth (mm)
1	A549	$1x10^5$	i.v.	200	N/A
2	MSTO-211H	$1x10^5$	i.pl.	100	1-3
3	A549	$1x10^5$	i.l.	20	6-8
4	MSTO-211H	$1x10^5$	i.l.	20	6-8

Table 3.1: Cancer cell implantation details for the four studies.

3.2.3 Imaging

All imaging studies were conducted under isoflurane anaesthesia with recovery (1.5% - 2.5% isoflurane in oxygen 1 L/min). At the start of the studies a 4 min breathing gated baseline micro-CT scan was acquired for each mouse, before any procedures took place. After the baseline micro-CT scan, the cancer cells were injected. BLI was conducted 1

to 2 times per week, up to 40 days after cancer cell implantation, in order to monitor the *in vivo* cancer cell proliferation. At 40 days post cancer cell implantation, weekly micro-CT scans were conducted until the end of the studies. In the case of Studies - 3 and 4 an ^{18}F-FDG PET/CT scan was conducted prior to sacrifice.

NSG mice are sensitive to anaesthesia therefore extra care was taken to use low doses of isoflurane anaesthesia and to keep the duration that the mice were under anaesthesia as short as possible. Furthermore, careful monitoring of the mice was conducted and their body temperature was kept at 37 °C by either positioning the mice on a heated pad or on a heated bed for imaging. The only imaging modality that the mice were not on a heated bed during scanning was the micro-CT, however the short 4 min acquisition did not cause any effects.

3.2.3.1 Bioluminescent Imaging

For BLI the mice were kept at 37 °C during anaesthesia. They were injected intraperitoneally (i.p.) with 150 mg/kg of D-Luciferin solution and imaged at 10 min post-injection for cancer cell proliferation monitoring, using an IVIS Spectrum In Vivo Imaging System (PerkinElmer). The automatic acquisition setting was chosen to ensure exposure times were optimised and sufficient signal was obtained without saturation. The acquisition times were between 1 to 2 min. The light output was quantified using ROI analysis and measured as Total Flux in photons/second (p/s).

The positioning of the mice was supine in all four studies. In figure 3.4 the final acquisition of Study - 3 can be visualised. The size of the ROIs was the same in all studies and the positioning of the ROI was adjusted on each mouse, to ensure that the whole chest area was within the ROI. Finally, a background ROI was utilised in every acquisition in order to correct the measurements for the background signal.

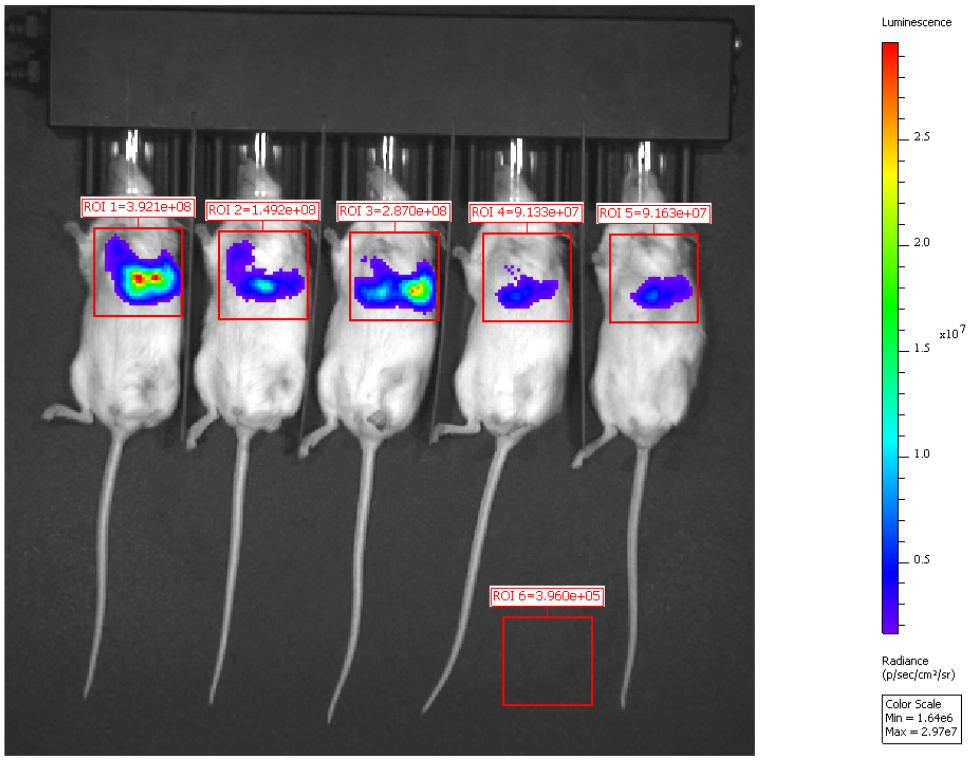

Figure 3.4: BLI acquisition: Final scan for Study - 3 showing the ROIs applied for measurements.

3.2.3.2 Micro-CT Imaging

For micro-CT imaging the mice were scanned using the Quantum GX2 micro-CT Imaging System (PerkinElmer). All acquisitions were conducted as 4 min breathing gated scans and their details can be seen in table 3.2.

Parameter	Value
Voltage (kV)	90
Current (µA)	88
FOV (mm)	36
Voxel size (µm)	72
Dose (mGy)	912

Table 3.2: Micro-CT acquisition details for the four Studies.

The breathing gating method utilised for the micro-CT acquisitions was DDG,

provided by the micro-CT system. DDG methods were introduced in section 1.11. For the DDG method applied in this work, a ROI was positioned over the diaphragm of the mouse before the start of the acquisition. The software recorded the respiratory signal with the trace spikes representing the diaphragm movements. Once the scan was completed the recorded inspiration and expiration signals could be viewed and reconstructed separately. The gating parameters used for the reconstructions were chosen based on the manufacturer's recommendations as per the following:

1. Threshold: The threshold was applied to the entire waveform, to separate the relaxed state of the diaphragm (baseline) from the diaphragm motion (peaks). This allowed for an initial separation of the baseline from the inspiration/expiration phases. The value chosen was 30%.
2. Inspiratory threshold: This was a secondary threshold that further refined the point selection above the initial threshold. This threshold affects the number of points on the waveform selected as 'end inspiration' points. Reducing this number can help to identify the transition point in diaphragm motion between the inspiration and expiration phases. The value chosen was 10%.
3. Expiratory threshold: This was another secondary threshold that further refined the point selection below the initial threshold. This threshold affects the number of points on the waveform selected as 'end expiration' points. Reducing this number can help refine the selection of the resting phase from the inspiration/expiration phases. The value chosen was 70%.
4. Rising invalid frames: This was the number of invalid frames to ignore on the inspiration side of the peak. The value chosen was 3.
5. Falling invalid frames: This was the number of invalid frames to ignore on the expiration side of the peak. The value chosen was 2.

The reconstruction method used was FBP. All micro-CT scans presented and analysed were the expiration phase reconstructions.

The whole lung volume analysis of the acquisitions was done using the Analyze 14.0 software (AnalyzeDirect) [100] by applying the image processing method published by Zaw Thin et al. with modification [101]. The baseline and final scans of each mouse were analysed in order to calculate the percentage change in total lung parenchyma, at the end of the study, compared to before the injection of the cancer cells. The average signal intensity (HU) within the trachea, for the measurement of air, and the average signal intensity (HU) of the heart, for the measurement of tissue (including blood), were used as calibrators. To perform the semi-automatic segmentation of lung parenchyma from the background, the image processing method applied was the following:

1. The scans were cropped to reduce the file size and to keep only the area of interest that is the lung.
2. A median spatial filter (kernel size: 3 x 3 x 3) was applied, that dampens noise and smoothed the volume, by replacing the value of each voxel with the average value of the neighbourhood. The neighbourhood around each voxel is defined by the kernel size selected. A 3 x 3 x 3 kernel has 27 voxels and the larger that the kernel size is, the more computationally intensive the filter becomes.
3. The trachea was segmented by using the semi-automatic segmentation method "Region Grow" with a threshold of -1000 to -700 HU. The "Region Grow" method limits the segmentation to voxels that are connected to the user-defined seed point that falls within the specified threshold range. Part of the heart was segmented manually based on the transverse slices of the scan. A representative segmentation of the trachea and the heart can be seen at the following figure 3.5.

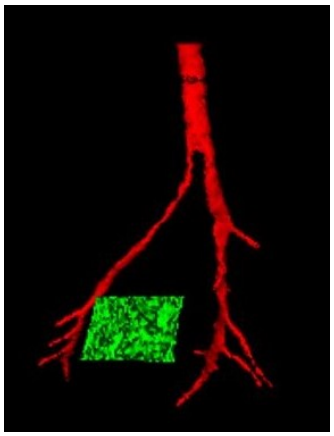

Figure 3.5: Representative segmentation of the trachea (in red) and part of the heart (in green), used for the calibration of the images for air and tissue (including blood) respectively.

4. The mean signal intensity of the trachea and the heart were measured. A linear HU calibration curve was created by using the known signal intensity of air (-1000 HU) and tissue (0 HU) and the mean signal intensities measured for each mouse.
5. The equation calculated was then applied to the scan of each mouse, to correct the image for air and tissue (including blood), that will be mentioned as modified scan.
6. In the modified scan the semi-automatic segmentation method "Object Extractor" was applied to segment the lung. The Object Extractor tool utilises a seed point that was manually set on the lung parenchyma. Then, a threshold range was set from absolute minimum to -300, to define the structure. The algorithm first applies a global threshold to the data set, using the minimum and maximum values specified. Next a 3D binary erosion is performed on the binary result of the global threshold. The erosion attempts to break connections between the target structure and neighbouring regions which have similar "Object Extractor" intensity values. The erosion is followed by a 3D 6-neighbour region grow, which uses the initial seed point. The processed target slice on which the initial seed point was set is compared to the initial auto trace from the user-defined seed point and threshold range. The erosion and region growing steps are repeated until the set of voxels on

the processed target slice are a subset of the initial auto trace. Next, the processed data is conditionally dilated until 99% of the voxels in the auto traced region on the processed target slice are recovered. Once the extraction process is complete, the resulting object is rendered and displayed over the 2D slice data.

7. The volume of the segmented lung was measured for each mouse.
8. To determine the lung volume, corrected for air and tissue (including blood), the following equations were utilised, using the mean HU and the lung volume (mm^3) measured.

$$\%change = Mean\ HU \times (-0.001) \tag{3.1}$$

$$Corrected\ lung\ volume = Measured\ Volume\ (mm^3) \times \%change \tag{3.2}$$

For individual tumour analysis the Analyze 14.0 software [100] was utilised to perform the semi-automatic segmentation of the tumour from the background. The image processing method applied was the following:

1. The scans were cropped to reduce the file size and to keep only the area of interest that is the lung.
2. A median spatial filter (kernel size: 3 x 3 x 3) was applied, as explained in the whole lung volume analysis.
3. The tumour was segmented by using the semi-automatic segmentation method "Region Grow" with a threshold of -260 to 580 HU [102].
4. The tumours were segmented individually and they were measured for each mouse.

3.2.3.3 PET/CT Imaging

For the mice of Studies - 3 and 4 an ^{18}F-FDG PET/CT scan was acquired prior to sacrifice and histological characterisation. Mice in Study - 3 were scanned on a Mediso nanoScan® PET/CT scanner (Mediso, Hungary), whereas mice in Study - 4 were scanned on a newer Mediso nanoScan® PET/CT system (PET122S/CT1512). For Studies - 1 and 2, no

^{18}F-FDG PET/CT scan was conducted, as the same cancer cell lines were utilised with Studies - 3 and 4. The mice were fasted for 12 h and they were injected 50-60 min before the start of acquisition, to allow for uptake and clearance of the radiopharmaceutical. The mice were under anaesthesia during the uptake period and they were placed on a heating pad at a set temperature of 37 °C. The activities at the time of injection and at the time of acquisition can be visualised in table 3.3.

Study	**Mouse**	**Injected Activity (MBq)**	**Acquisition Activity (MBq)**
3	1	5.78	4.01
	2	6.77	5.19
	3	10.45	8.12
	4	8.18	6.43
	5	9.25	6.92
4	1	9.48	6.91
	2	10.42	7.60
	3	10.88	7.93
	4	10.29	7.50
	5	9.28	6.77

Table 3.3: Activities in MBq, for Studies - 3 and 4, at the time of injection and at the start of acquisition.

For Study - 3, PET was acquired as a 20 min static scan and CT was acquired at 50 kVp with 300 ms exposure time (semicircular). Mice were monitored for breathing using an external breathing pad. For all acquisitions the mice were in supine position with the breathing pad taped on their upper stomach, centred on their diaphragm. PET data was reconstructed in 1 - 3 coincidence mode using the Tera-Tomo iterative algorithm (8 iterations, 6 subsets), in 0.4 mm isotropic voxels and CT data was reconstructed using the FBP reconstruction method, in 0.13 mm isotropic voxels. The analysis was done using the VivoQuant software (Version 2022 - Invicro). The identification of tumour (including oedema) and lung parenchyma in this model was not feasible on the PET/CT acquisitions, as the tumours could not be identified on the CT images. VOIs were drawn

manually in the whole chest cavity and the heart, to compare the difference in uptake in heart and whole lung (including tumour and oedema).

For Study - 4, PET was acquired as a 20 min static scan with breathing gating and CT was acquired at 70 kVp with 90 ms exposure time (zigzag). PET was reconstructed as both breathing gated and non-breathing gated that will be mentioned as breathing gated and static reconstruction respectively. The breathing gated signal was recorded again by utilising an external breathing pad, which was positioned on the mouse. For all acquisitions the mice were in supine position with the breathing pad taped on their upper stomach, centred on their diaphragm. The breathing pad tracks the movement of the chest and the respiration acquisition parameters were chosen based on the manufacturer's recommendations as per the following:

- The number of bins, that defines the number of intervals of the respiration histogram was set at 25.
- The minimum and maximum frequency, which are the lowest and the highest values shown on the histogram were set at 0 and 200 breaths per minute (bpm) respectively.

The breathing gated reconstruction parameters chosen were adapted to each mouse acquisition, based on the manufacturer's recommendations, as per the following:

- Nominal Respiration Rate: It was set at the middle of the desired range in the histogram. This value determines the length of the gated frames.
- Lower and Upper Acceptance windows: These windows determine the range of the data used for reconstruction. It was set at $\pm 10\%$ of double the value of the nominal rate. The data acquired during cycles outside of this rate window were excluded from the reconstruction.
- Backward and Forward Hold-Off: The desired time intervals before and after the trigger signal. Data collected during these periods were excluded from the reconstruction. Both these intervals were set at 0.20 sec for all mice.

The PET data was reconstructed in 1 - 3 coincidence mode using the Tera-Tomo iterative algorithm (4 iterations, 6 subsets), in 0.4 mm isotropic voxels. CT was reconstructed using the FBP reconstruction method, in 0.13 mm isotropic voxels. The analysis was done using the VivoQuant software. The identification of tumour (including oedema) and lung parenchyma in this model was feasible. VOIs were drawn manually on the areas of interest based on the CT scan. Then the connected thresholding algorithm was applied to segment the tumour and normal lung areas, avoiding the heart to minimise the spill-over effect. The algorithm utilises a seed point and a threshold range to classify all voxels of the input VOI (that was manually drawn) to an output VOI. The ranges used were -700 to -100 HU for the lung segmentation and -100 to 500 HU for the tumour (including oedema) segmentation.

3.2.3.4 Histology

As a final time point for all four studies, the mice were culled by i.v. injection of 100 µL of pentobarbital (pentobarbitone) (Pentoject® 200 mg/ml - Animalcare Limited), to keep the trachea intact for lung inflation and extraction. Ideally perfusion would be conducted to remove the blood from the lung sample, however due to the risk of puncturing the lung which would not allow lung inflation, perfusion was not conducted.

The chest of the animal was opened and the trachea was exposed. An opening was created in the trachea to insert a cannula for the inflation of the lungs. Once the lungs were inflated the cannula was removed, the trachea was sealed using a string and the lungs were extracted. For Studies - 1, 2 and 4 the lungs were inflated with 10% formalin, extracted and then stored in 10% formalin for 24 h. After that they were stored in 10% ethanol at 4 °C. Finally, the samples were transferred to 70% ethanol right before the paraffin embedding process was initiated. The embedding process started with an automated tissue processor (HistoCore PEARL - Leica Biosystems). The protocol applied by the tissue processor can be seen at the following table 3.4.

Reagent	Time (h:min)	Temperature (°C)
70% IMS	02:00	37
80% IMS	01:30	37
90% IMS	01:30	37
Absolute Ethanol	01:00	37
Absolute Ethanol	01:15	37
Absolute Ethanol	01:15	37
Xylene	01:00	37
Xylene	01:00	37
Xylene	01:00	40
Paraffin Wax	01:00	58
Paraffin Wax	01:00	58
Paraffin Wax	01:30	58

Table 3.4: The tissue processor system protocol used for the lung samples. IMS stands for Industrial Methylated Spirits (IMS), and it is ethanol that has been denatured with methanol.

Next, the samples were embedded in paraffin blocks and trimmed prior to sectioning. Contiguous 5 µm sections were cut on a microtome (Microm HM 325). The sections were picked up with tweezers and transferred to the surface of a pre-warmed 37 °C water bath. Then the sections were collected at a 30° angle on slides (Epredia - Polysine) and they were left to dry at room temperature for 24 h. A standard H&E staining process was conducted using an automated tissue staining system (Sakura Tissue-Tek DRS). The H&E process conducted was the following:

1. Start station, where the slides are initially put into the system.
2. Dryer station for 30 secs.
3. Xylene for 5 min (with mixing).
4. Xylene for 5 min (with mixing).
5. Ethanol: 100% for 3 min (with mixing).
6. Ethanol: 100% for 3 min (with mixing).
7. Ethanol: 70% for 2 min (with mixing).
8. Ethanol: 30% for 2 min (with mixing).

9. Distilled water for 1 min (with mixing).
10. Hematoxylin for 5 min (with mixing).
11. Tap water for 20 secs (with mixing).
12. 1% HCl acid in 70% Ethanol solution for 6 secs (with mixing).
13. Tap water for 2.5 min (with mixing).
14. Eosin for 4 min (with mixing).
15. Tap water for 2 min (with mixing).
16. Ethanol: 70% for 30 secs (with mixing).
17. Ethanol: 100% for 2 min (with mixing).
18. Ethanol: 100% for 2 min (with mixing).
19. Xylene for 2 min (with mixing).
20. Xylene for 3 min (with mixing).
21. End station where the slides are taken out of the system.

The slides were taken out of the automated tissue staining system and they were put in an automated film coverslipper (Sakura Tissue-Tek SCA), where a drop of xylene was added onto the tissue sample and a coverslip (IPI Pathotape® Coverslipping film) was put onto the slide and cut. The sections were left to dry for at least 24 h before imaging. The sections were imaged on a NanoZoomer 2.0-HT microscope (Hamamatsu Photonics) for Studies - 1 and 2. For Study - 4 the Nanozoomer S360 microscope (Hamamatsu Photonics) was used. All H&E images were analysed using the NDP.view2 Image viewing software [103].

The H&E staining utilised can demonstrate different tissue structures clearly by imaging. Hematoxylin stains the cell nuclei purple, showing clear intranuclear detail, whilst eosin stains cell cytoplasm and most connective tissue fibres in varying shades and intensities of pink and red [104].

For Study - 3 the mice were injected i.v. with 15 mg/kg of Hoechst 33342, 1-5 min before culling. The mice were culled using pentobarbital and prepared for lung inflation

as for the 10% formalin inflation of the lung, but in this study the lungs were inflated using Optimal Cutting Temperature (OCT) compound (CellPath) with DPBS (Gibco™) in 1:1 dilution. Then the extracted lung samples were embedded and frozen in OCT compound using a mould. Frozen OCT blocks were trimmed and then contiguous 10 µm frozen sections were cut using a cryostat (CM3050 S - Leica). The sections were collected on slides (Thermo Scientific™ - Superfrost®) and kept frozen at -20 °C, without adding a coverslip. They were imaged for Hoechst 33342 uptake utilizing an EVOS FL Cell Imaging System (Thermo Fisher Scientific) and the analysis was done using the Fiji software [105].

Hoechst 33342 intravenous injection, before euthanasia, provides vascular perfusion information. The intravenous injection delivers Hoechst 33342 via the bloodstream, allowing it to rapidly label nuclei of cells that are accessible via the vasculature. Hoechst 33342 is cell-permeant, therefore it crosses cell membranes and binds to the DNA of cells. Only well-perfused tissues will show strong nuclear staining, allowing the distinction between perfused (viable) tissue and non-perfused or ischaemic tissue [106]. Hoechst 33342 staining was utilised to assess how well a lung tumour is vascularized.

3.2.4 Statistical analysis

Statistical analysis was performed with GraphPad Prism version 8.0. Data are presented as mean ± standard deviation (SD). Paired samples two-tailed t test was conducted for the lung and tumour comparisons of each PET/CT reconstruction, as well as for the comparisons between breathing gated and static PET/CT for both tumour and lung. Statistical significance was identified for *$p \leq 0.05$, **$p \leq 0.01$, ***$p \leq 0.001$.

3.3 Results

3.3.1 Animal adverse effects

All methods utilised in this chapter were minimally invasive. For cancer cell implantation, the mice were under isoflurane anaesthesia for a few minutes and they recovered quickly after the injection of the cancer cells. No analgesia was needed and the mice did not show any signs of stress or discomfort. No adverse effects were observed for any study and all the mice survived until the end point of their respective study, with their body weight monitored throughout the studies and not reducing more than 10%.

3.3.2 Bioluminescent Imaging

The analysis of BLI data was done using ROIs as explained in section 3.2.3.1. The average Total Flux (p/s), corrected for background, per group (n = 5) was plotted versus the days post-injection. In figure 3.6 the results for all four studies conducted can be visualised. The two studies that the A549 cell line was utilised can be seen in red colour and the two studies that the MSTO-211H cell line was used can be seen in blue colour.

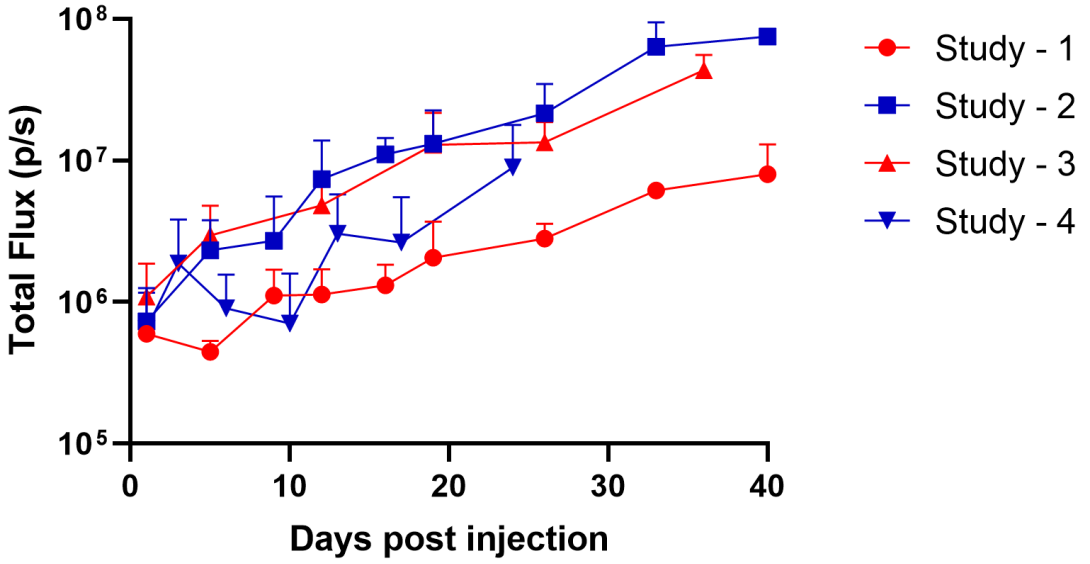

Figure 3.6: Thoracic region measurements of Total Flux (p/s), corrected for background, versus days post-injection for the four studies. Study - 1: i.v. injection of A549 cells, Study - 2: i.pl. injection of MSTO-211H cells, Study - 3: i.l. injection of A549 cells and Study - 4: i.l. injection of MSTO-211H cells. Day 0 is the day of injection. The data are plotted as mean ± SD, n = 5. For visual clarity only the upper error bar is shown.

In Study - 1 the A549 cell line was administered by i.v. injection, while in Study - 3 by i.l. injection into the left lung parenchyma. There is an initial decrease in signal for the i.v. injection that could be attributed to cell death due to the cell remodelling phase for tumour formation. Nevertheless, the signal for both administration methods increases over time, with the signal from the i.l. injection being lower, which could be explained by the deeper injection of the cancer cells. In Study - 2 the MSTO-211H cell line was injected by i.pl. injection in the right intrapleural space, while in Study - 4 by i.l. injection into the right lung parenchyma. There is a steady signal increase for the i.pl. injection over time, while for the i.l. injection there is an initial decrease in signal up to day 10, something that could be attributed to cancer cell death due to the cell remodelling phase for tumour formation of a pleural mesothelioma cell line within lung

parenchyma. Then the signal for both administration methods increases over time, with the signal from the i.l. injection being lower, something that can be explained again by the deeper injection of the cancer cells. Since the behaviour of the i.l. injection matched the i.pl. one, less acquisitions were conducted to subject the mice to less procedures.

3.3.3 Micro-CT Imaging

For every mouse a baseline 4 min breathing gated micro-CT scan was acquired before the injection of the cancer cells. In figure 3.7 a representative baseline micro-CT scan can be visualised, which shows a healthy mouse lung.

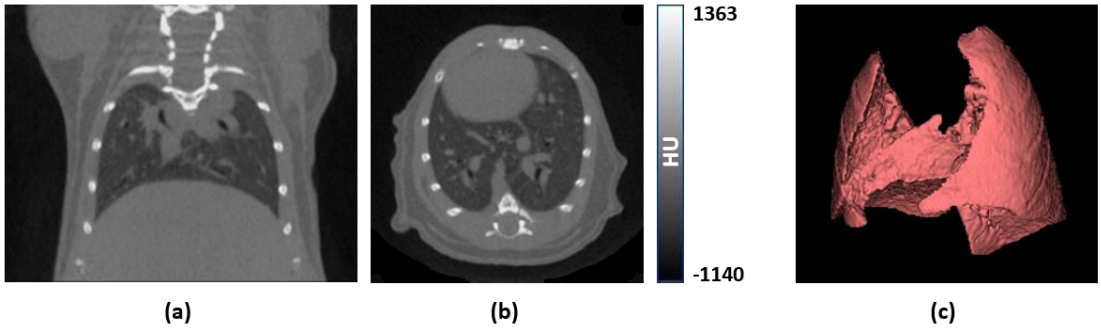

Figure 3.7: Baseline micro-CT scan: (a) Coronal slice, (b) Transverse slice, (c) Segmentation of the normal lung parenchyma - 3D render.

In Study - 1 the i.v. injection of the A549 human lung adenocarcinoma cells resulted in multiple tumours growing in the whole lung parenchyma. The largest tumour that could be clearly identified and individually segmented was 0.76 mm^3. The clear delineation of tumour tissue and normal lung parenchyma was challenging in this model, as the tumours grew throughout the whole lung. The identification of tumours smaller than 0.1 mm^3 was difficult as they could be misinterpreted as vessels and vice versa. The average tumour burden was 15.86 $\pm$ 7.77% (SD) based on the final micro-CT acquisitions, conducted 54 days post cancer cell implantation, compared to the baseline scans. A final micro-CT scan of Study - 1 can be visualised in figure 3.8. The tumours can be seen as indentations in the segmentation of the lung parenchyma in figure 3.8 (c).

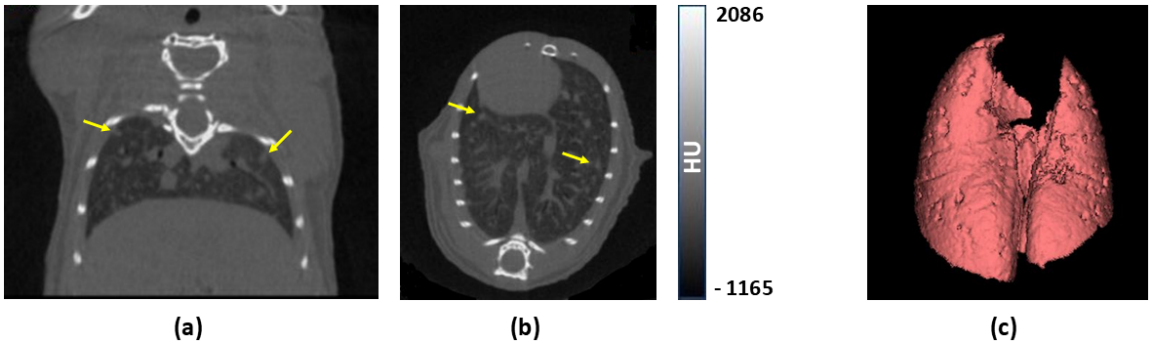

Figure 3.8: Final micro-CT acquisition of Study - 1: (a) Coronal slice, (b) Transverse slice, (c) Segmentation of the lung parenchyma - 3D render. The yellow arrows point to tumour formation.

In Study - 2 the i.pl. injection of the MSTO-211H malignant mesothelioma cells resulted in tumour formation in the pleura. Micro-CT imaging showed gradual compression of the lungs as the tumours grew in the intrapleural and between the lung lobes spaces. On average the tumour burden was 25.25 ± 7.41% (SD) based on the final micro-CT acquisitions, conducted 54 days post cancer cell implantation, compared to the baseline scans. A final micro-CT imaging acquisition of Study - 2 can be visualised in figure 3.9. The segmentation of the lung parenchyma in figure 3.9 (c) shows the compression and deformity of the lungs due to the pleural tumour and pleural effusion formation.

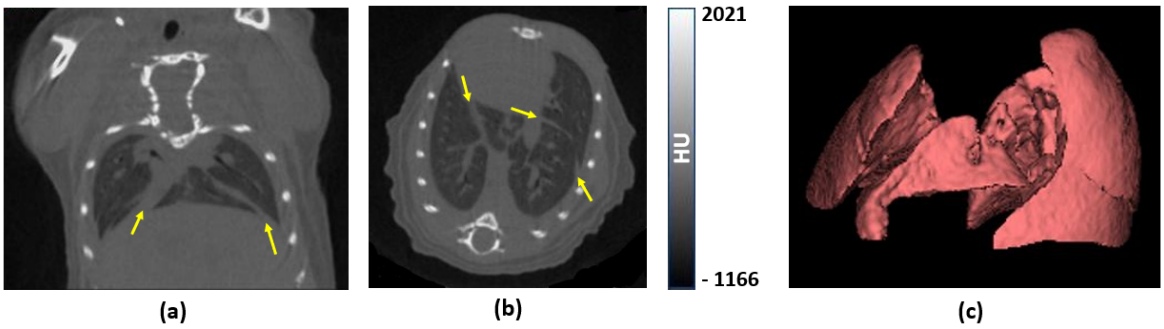

Figure 3.9: Final micro-CT acquisition of Study - 2: (a) Coronal slice, (b) Transverse slice, (c) Segmentation of the lung parenchyma - 3D render. The yellow arrows point to areas of pleural tumour and pleural effusion formation.

In 1/5 mice of Study - 2 the i.pl. injection was accidentally done deeper than intended, thus piercing the lung parenchyma and resulting in part of the cell suspension to be injected into the lung. Micro-CT imaging showed that there was tumour formation into the lung parenchyma at the site of injection and that there was gradual compression of the lungs as tumours grew in the intrapleural and between the lung lobes spaces, as was the case for the other four mice of Study - 2. The final micro-CT imaging acquisition for the mouse with cancer cell seeding into the lung, can be seen in figure 3.10. The segmentation of the lung parenchyma in figure 3.10 (c) shows the compression of the lungs due to the tumour and pleural effusion formation outside the lung parenchyma.

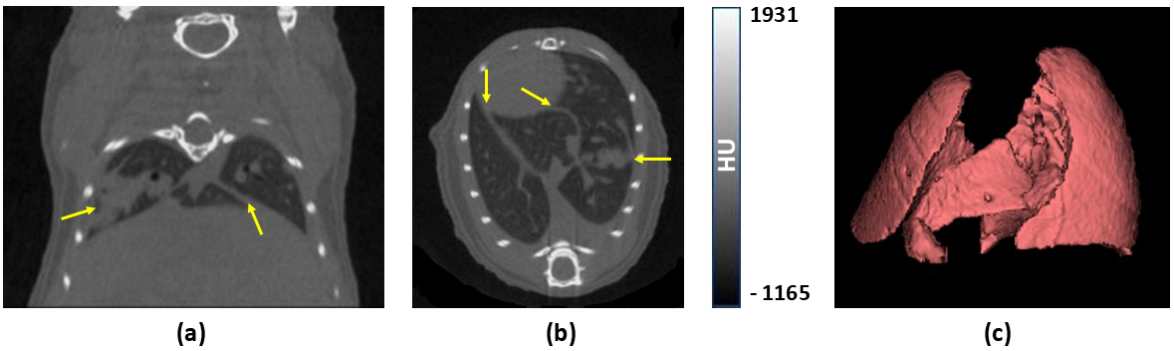

Figure 3.10: Final micro-CT acquisition of Study - 2 where the i.pl. injection pierced the lung parenchyma: (a) Coronal slice, (b) Transverse slice, (c) Segmentation of the lung parenchyma - 3D render. The yellow arrows point to areas of tumour formation.

In Study - 3, the i.l. injection of the A549 human lung adenocarcinoma cells resulted in tumour and effusion formation in the intrapleural and between the lung lobes spaces, but not into the lung parenchyma. Pleural tumours and pleural effusions gradually compressed the lungs. On average the normal lung parenchyma volume reduced by 39.83 $\pm$ 6.97% (SD), based on the final micro-CT acquisitions, conducted 67 days post cancer cell implantation, compared to the baseline scans. A final micro-CT scan of Study - 3 can be visualised in figure 3.11. The segmentation of the lung parenchyma in figure 3.11 (c) shows the compression and deformity of the lungs due to the pleural tumour and pleural effusion formation.

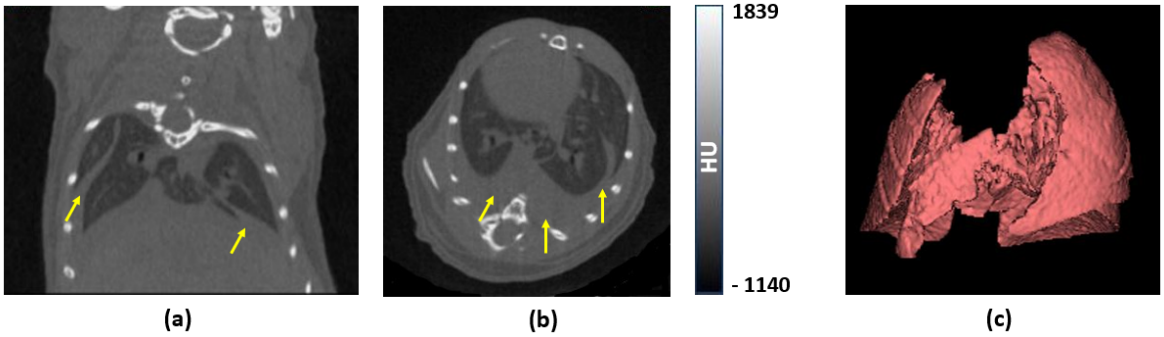

Figure 3.11: Final micro-CT acquisition of Study - 3: (a) Coronal slice, (b) Transverse slice, (c) Segmentation of the lung parenchyma - 3D render. The yellow arrows point to areas of pleural tumour and pleural effusion formation outside the lungs.

Due to the fact that in Study - 2 the deeper injection of MSTO-211H cells into the lung parenchyma formed a single tumour mass, MSTO-211H cells were evaluated as an i.l. injection model. In Study - 4 the i.l. injection of the MSTO-211H human malignant pleural mesothelioma cells resulted in distinct tumour formation in the lung parenchyma. A final micro-CT scan of Study - 4 can be visualised in the following figure 3.12.

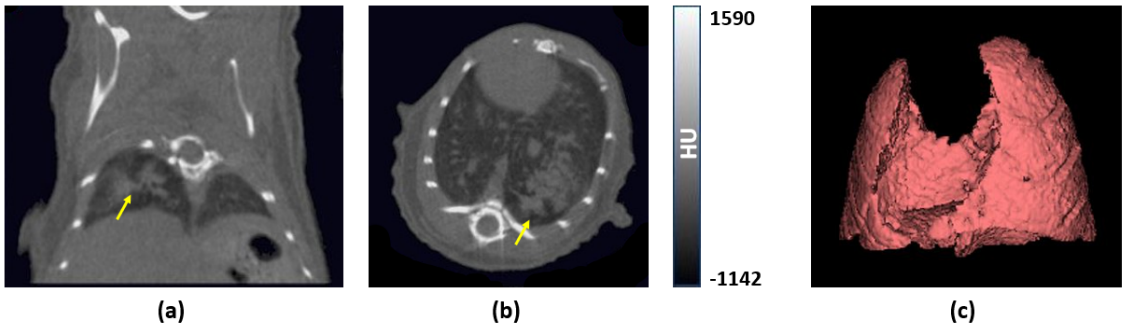

Figure 3.12: Final micro-CT acquisition of Study - 4: (a) Coronal slice, (b) Transverse slice, (c) Segmentation of the lung parenchyma - 3D render. The yellow arrows point to tumour formation.

Due to a fault in the micro-CT system during the course of the study, the final CT acquisitions of Study - 4 were done using the CT compartment of the PET/CT system. The acquisitions, reconstructions and analysis were done as explained in section 3.2.3.3. The average tumour volume was 47.71 $\pm$ 27.31% (SD) based on the final CT acquisitions,

conducted 56 days post cancer cell implantation.

Despite the localised tumour formation in healthy lung parenchyma by intralobular injection of the MSTO-211H cells, there were cases (2/5) that tumours grew in the intrapleural spaces as well as within the right lung parenchyma. This was caused by seeding of cancer cells in the right intrapleural space during injection and the imaging representation of those mice was as seen in figure 3.10.

3.3.4 PET/CT Imaging

In figure 3.13 an ^{18}F-FDG scan of Study - 3 can be visualised. The tumour formation (including oedema) and the normal lung parenchyma cannot be distinguished using the CT. The study was conducted on an old generation PET/CT system and despite reconstructing the data as 0.13 mm isotropic voxels the images did not allow the distinction of tumours. The segmentation of the heart and the rest of the chest cavity (lung including tumour and oedema) was done manually.

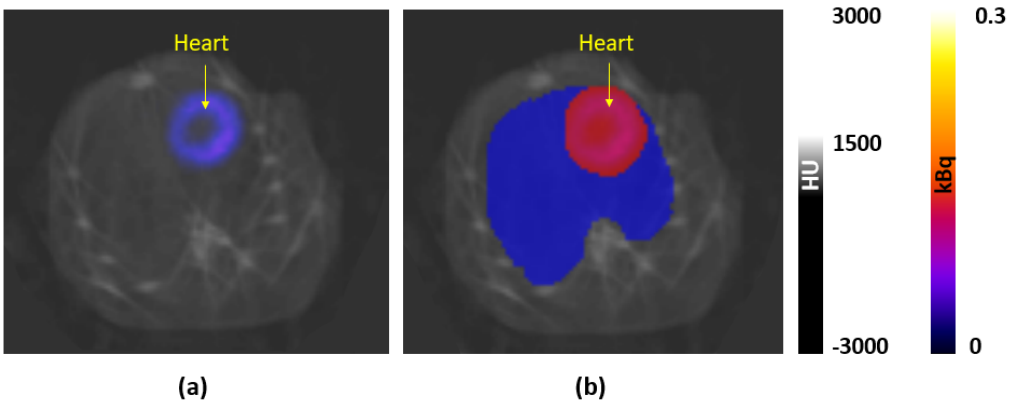

Figure 3.13: ^{18}F-FDG PET/CT imaging for Study - 3: (a) Transverse slice, (b) Transverse slice with segmentations. The heart segmentation is in red colour and the lung, including tumour and oedema is in blue.

^{18}F-FDG-PET imaging showed high cardiac uptake with no distinct uptake in the rest of the thoracic wall. On average 73.78 ± 7.46% (SD) of the activity in the whole thoracic wall was within the heart.

In figure 3.14 an ^{18}F-FDG scan of Study - 4 can be visualised. The tumour formation and the normal lung parenchyma can be clearly distinguished using the CT, as this study was done at a new state of the art PET/CT system. The segmentation of the tumour and lung was done as was explained in section 3.2.3.3.

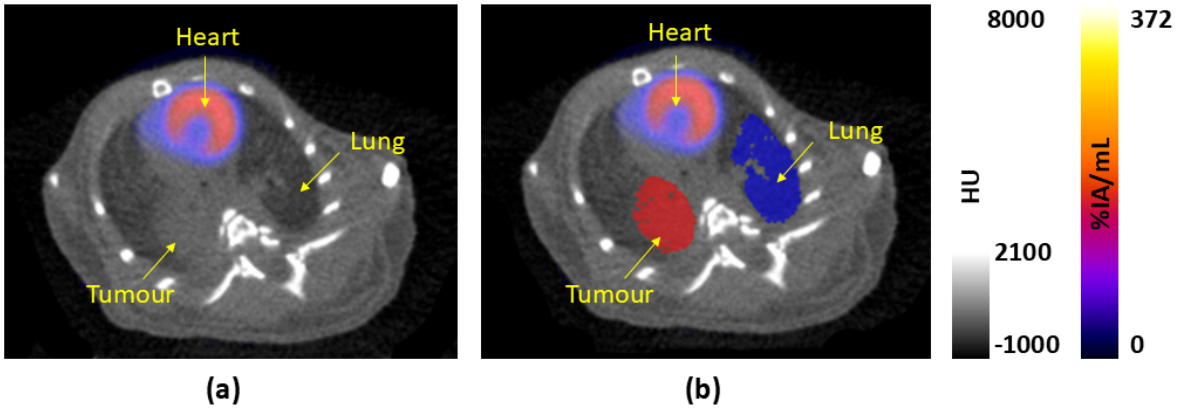

Figure 3.14: ^{18}F-FDG PET/CT imaging for Study - 4. Breathing gated reconstruction: (a) Transverse slice, (b) Transverse slice with segmentations. The tumour segmentation is in red colour and the normal lung is in blue.

^{18}F-FDG-PET imaging showed for the breathing gated reconstructions, an uptake of 5.72 ± 1.44 %IA/mL for the tumour and 4.20 ± 0.29 %IA/mL for the lung, which was not statistically different ($p = 0.13$). For the static reconstructions, an uptake of 5.67 ± 1.36 %IA/mL for the tumour and 4.22 ± 0.31 %IA/mL for the lung was found, which again was not statistically different ($p = 0.14$). No difference was shown between the breathing gated and static reconstruction methods for the tumour ($p = 0.31$) and for the lung ($p = 0.63$).

3.3.5 Histology

During extraction of the lung samples for histology, effusion formation was observed in the intrapleural space of mice of Studies - 3 and 4.

In Study - 1 the H&E sections showed multiple tumour formation in the whole lung, which is in agreement with micro-CT imaging. In figure 3.15 a section can be visualised.

The tumours can be seen as small areas of densely packed cells with irregular boundaries. Haematoxylin stains cell nuclei in purple colour and this indicates higher cell numbers. There are also areas of eosin staining with no evidence of alveoli within these dense lesions which indicates areas of necrosis. In the zoomed in image on the right-hand side the tumour lesions are highlighted by black arrows.

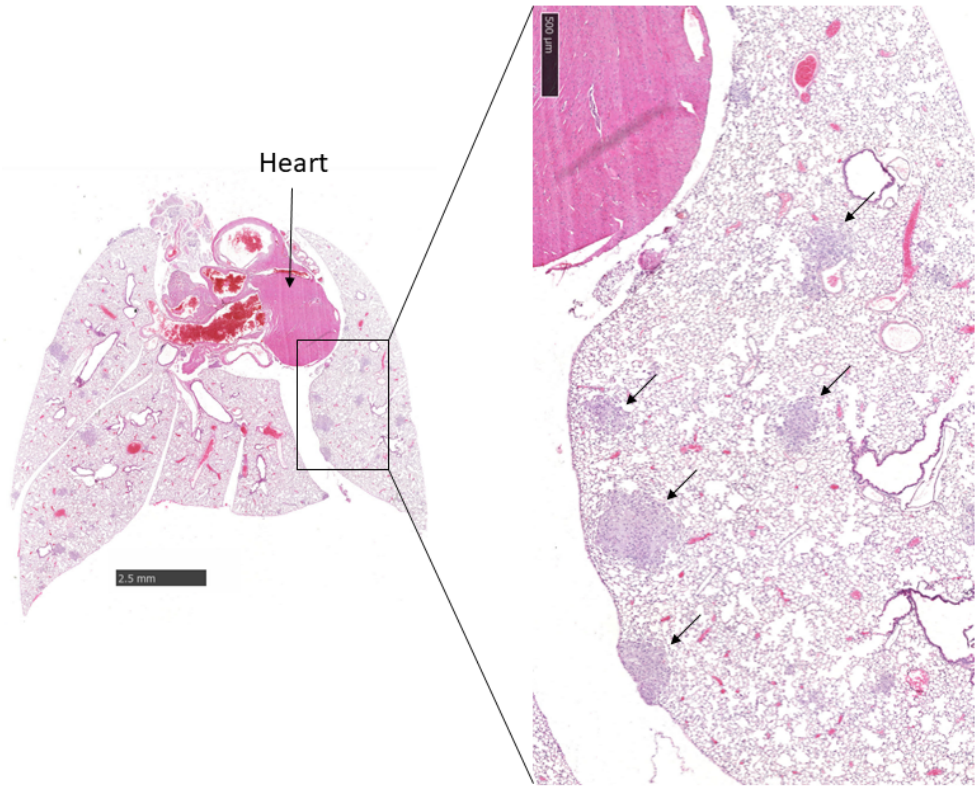

Figure 3.15: Study - 1: H&E section of a lung sample. In this section the heart can be visualised. Tumours can be seen throughout the whole lung parenchyma as densely packed cells in purple colour and are highlighted by black arrows.

Red blood cells can be identified within the lung vessels, in red colour, as the samples were not perfused.

In Study - 2 the H&E sections showed multiple tumour formation in the intrapleural and between the lung lobes spaces but not within the lung parenchyma, which is in agreement with micro-CT imaging. In figure 3.16 a section can be visualised. The tumours can be seen as formations of densely packed cells in purple colour (haematoxylin) around the lungs. In the zoomed in image on the right-hand side the tumours that grew in the pleura and between the lung lobes are highlighted by black arrows. In the zoomed in image on the left-hand side the tumours that grew in the space between the right and left lung and between the lung and the diaphragm are highlighted by black arrows. Tumours that attached to the diaphragm resulted in pieces of the diaphragm being extracted with the sample and visualised in the histology sections.

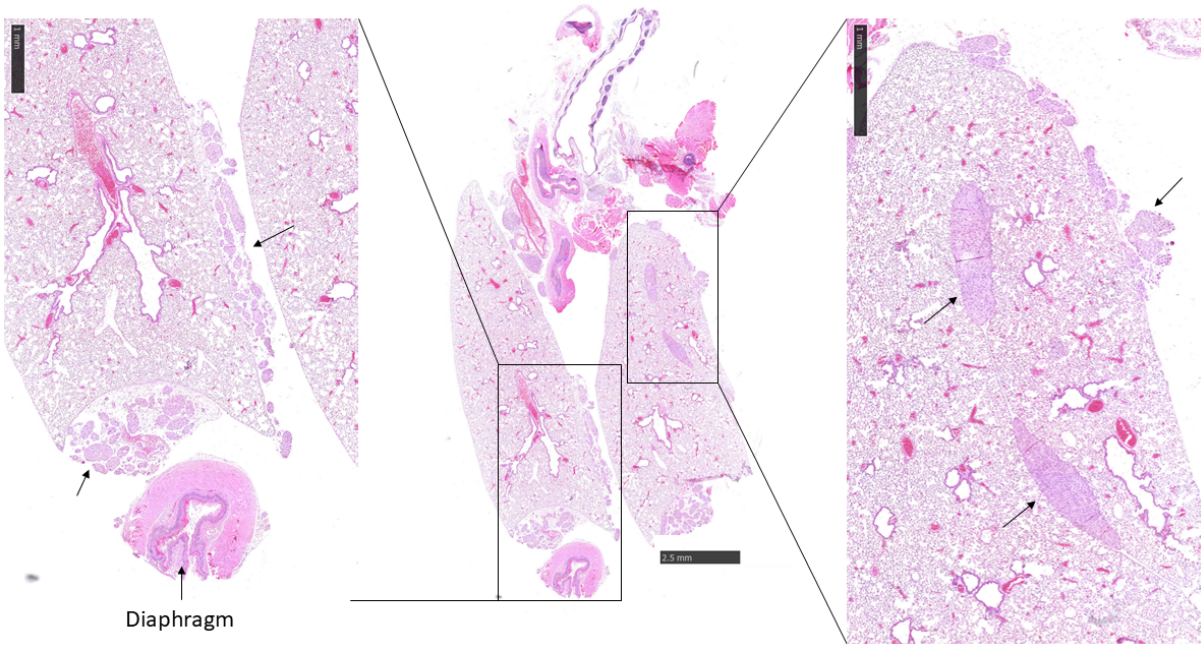

Figure 3.16: Study - 2: H&E section of a lung sample. There is tumour formation in the intrapleural and between the lung lobes spaces. The tumours can be seen as densely packed cells in purple colour and are highlighted by black arrows.

Red blood cells can again be identified within the lung vessels, in red colour, as the samples were not perfused.

The one mouse of Study - 2 where there was MSTO-211H cell seeding within the lung parenchyma and resulted in tumour formation both within and outside the lung can be seen in the following figure 3.17. The tumours can be seen as formations of densely packed cells in purple colour (haematoxylin). Tumours that grew around the lungs are highlighted by black arrows and in the zoomed in image on the right-hand side the tumours that grew between the lung lobes and within the lung parenchyma are again highlighted by black arrows.

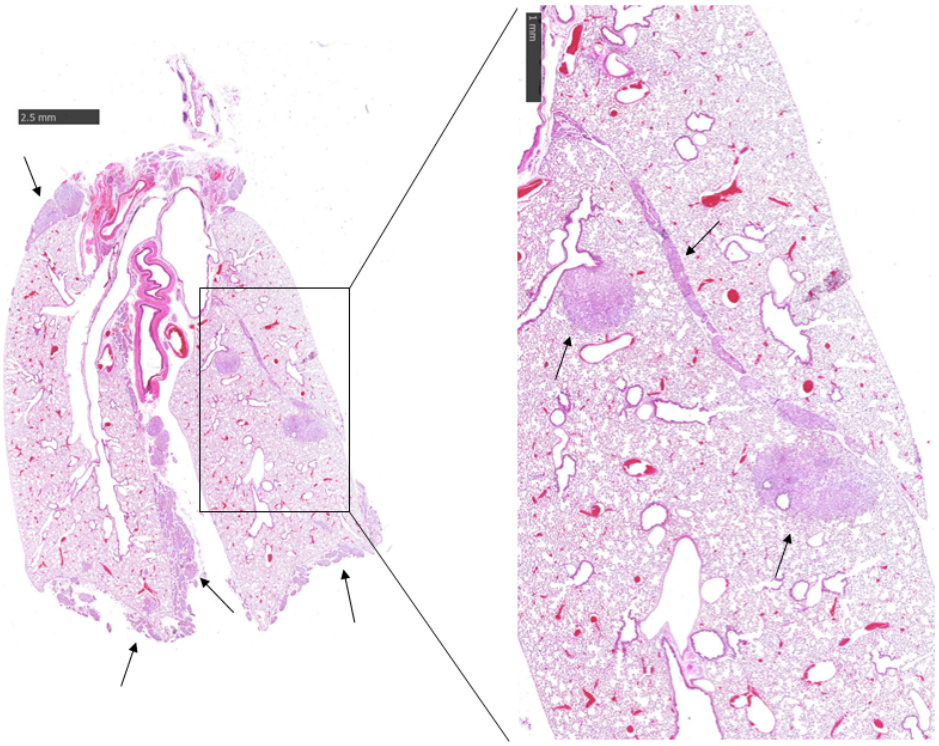

Figure 3.17: Study - 2: H&E section of a lung sample. There is tumour formation in the intrapleural and between the lung lobes spaces as well as within the lung parenchyma. The tumours can be seen as densely packed cells in purple colour and are highlighted by black arrows.

Red blood cells can again be identified within the lung vessels, in red colour, as the samples were not perfused.

In Study - 3, micro-CT imaging showed tumour formation only in the intrapleural and between the lung lobes spaces but not within the lung parenchyma. ^{18}F-FDG-PET imaging showed high cardiac uptake with no distinct uptake in the rest of the thoracic wall. The injection of Hoechst 33342 was used to specifically stain the nuclei of cells in vascularised areas and assess whether the tumour tissue was well vascularised or necrotic. In figure 3.18 lung sections of Study - 3 can be visualised. The lung parenchyma had uniform blue staining while the tumours, that are highlighted by the yellow arrows, did not. The fact that no blue staining was imaged inside the tumour tissue means that there were no perfused vessels within the tumour lesion and is therefore necrotic which explains the absence of ^{18}F-FDG uptake.

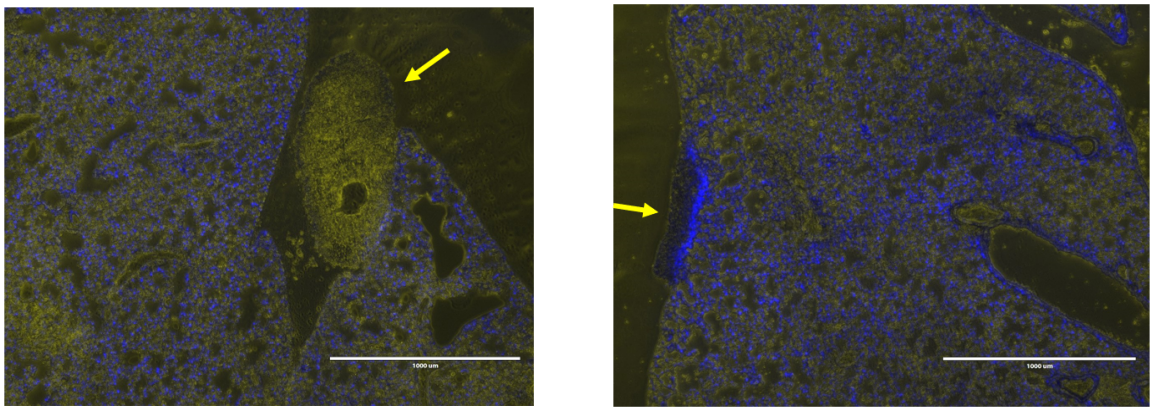

(a) **(b)**

Figure 3.18: Study - 3: (a) The tumour, highlighted by the yellow arrow, grows in the space between the lung lobes, (b) The tumour, highlighted by the yellow arrow, is attached on the lung and grows between the lung and the pleura.

In Study - 4, micro-CT imaging showed localised tumour formation within lung parenchyma, something that was confirmed by H&E, as can be seen in the following figure 3.19. The tumour can be seen as a localised area of densely packed cells in purple colour (haematoxylin). However, micro-CT imaging showed cases that tumours grew in the intrapleural and between the lung lobe spaces, as well as in the lung parenchyma, something that was confirmed by H&E, as can be seen in the following figure 3.20. The tumours are highlighted by black arrows and can be seen as areas of densely packed cells.

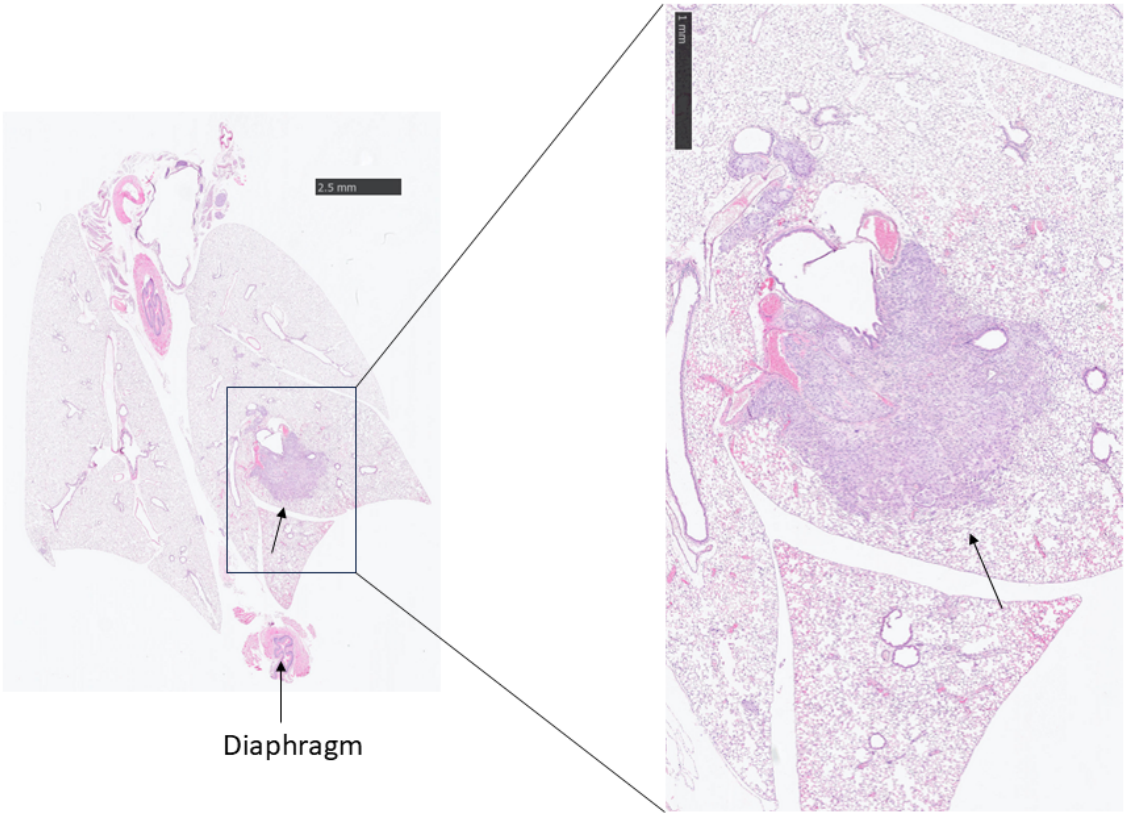

Figure 3.19: Study - 4: H&E section of a lung sample. There is localised tumour formation in the right lung parenchyma that can be seen as densely packed cells in purple colour. The tumour is highlighted by the black arrow.

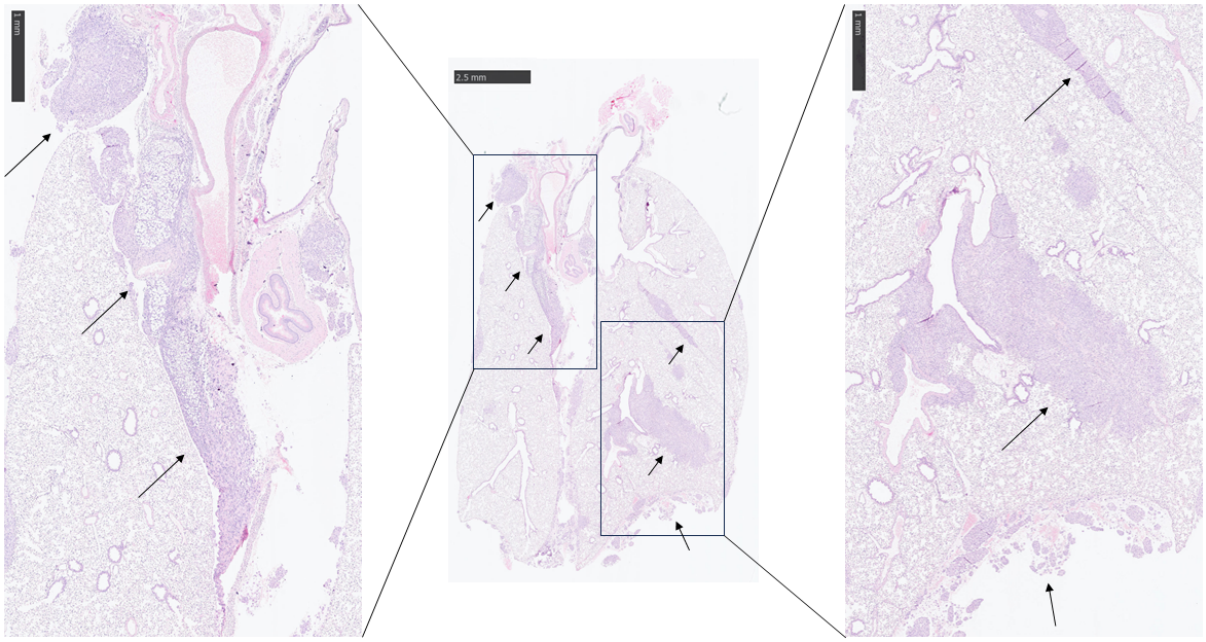

Figure 3.20: Study - 4: H&E section of a lung sample. There is localised tumour formation in the right lung parenchyma. However, there is also tumour formation in the intrapleural and between the lung lobes spaces. The tumours can be identified as densely packed cells in purple colour and are highlighted by black arrows.

Red blood cells can again be identified within the lung vessels, in red colour, as the samples were not perfused.

3.4 Discussion

Numerous different types of animal models have been developed and used in the literature for studying all major types of lung cancer. All models have their individual strengths and weaknesses, which need to be carefully evaluated in order to maximise the information obtained from the studies. PDX models are crucial in personalised treatment strategies, as they require tumour tissue or cells from patients, however their use is challenging for studies where no patient samples are available and orthotopic models are needed for accurate assessment of therapeutic cell distribution and uptake. GEMMs are crucial

for studying gene interactions and alongside chemogenic models they can represent the clinical cancer progression, however, the inter cohort growth can be variable and the tumour presentation can be complex in both of these models. Therefore their use for the tracking of radiolabelled cell therapies *in vivo* would be challenging, as not all mice may be suitable for imaging due to their multiple tumour presentation.

The most appropriate, easily applicable and time efficient models, for *in vivo* cell tracking by imaging, are the orthotopic models developed by cancer cell administration. This is because they have less variability between tumour growth rates and tumour presentation within a cohort than PDX, GEMM and chemogenic models.

The intravenous administration method of cancer cells has been employed in the literature for studying the antitumour effects of drugs like chemotherapy [107], microRNA therapy [108], and for studying tumour invasion and metastasis [109]. The venous blood flows directly from the tail vein of a mouse to the lungs via the right side of the heart, ensuring that the lungs are the first organ reached by the cells that have been injected intravenously. The pulmonary capillaries are narrow, trapping the cancer cells in the lung, thus creating an orthotopic model of lung cancer.

In Study - 1 the A549 human lung adenocarcinoma cell line was administered intravenously, resulting in widespread distribution of the cancer cells in the lung. BLI monitoring in figure 3.6 showed an initial slight decrease in signal from day 1 to day 5. This can be explained by the fact that not all cancer cells survive after injection and implantation within the lung. Those that do survive produce colonies of cells which result in solid tumour masses over time, providing a steady signal increase over time. BLI offered information on the cell proliferation until the tumour formation could be identified by micro-CT imaging. Micro-CT imaging showed multiple tumour lesions throughout the whole lung parenchyma, something that was confirmed by H&E histological analysis. Jarry et al. had reported that for intravenous injection of the human lung cancer PC-9 and A549 cell lines there was multiple tumour formation in the lung tissue. In their

study, they had utilised BLI and H&E histological analysis, which are in agreement with this work, however there was no micro-CT imaging to provide high resolution *in vivo* 3D images [107]. In a study by Janker et al., they administered the Lewis lung carcinoma cell line intravenously and they found that tumours were homogenously distributed in the lung. However, in their work they only utilised histology and no *in vivo* imaging was conducted [110]. In this chapter, the formation of multiple small tumours by intravenous injection of cancer cells made the identification and delineation of tumour tissue within normal lung parenchyma using imaging challenging. Therefore, it would not be suitable for the acquisition of quantitative measurements for the understanding of the *in vivo* distribution of radiolabelled [^{89}Zr]Zr-oxine MSCTRAIL cells.

The intravenous administration method of breast cancer cells for orthotopic lung cancer mouse model development, according to the Seed and Soil Hypothesis [111] was not assessed in this thesis. With this method the cancer cell distribution would be widespread, resulting in multiple tumour formation in the lung, as well as possible metastasis in other organs, something not advantageous for tracking radiolabelled MSCTRAIL cells, as discussed for the intravenous administration of A549 cells.

Another method used in the literature for orthotopic lung cancer mouse model development is the intratracheal administration of cancer cells. Mice are anaesthetised and placed in supine position on a platform or in an upright position using an intubation standard for ventilation. The tongue is gently pulled out with forceps to visualise the trachea using a small light source or a fiber-optic laryngoscope. A micropipette tip, an intratracheal cannula, or a catheter is inserted into the trachea through the mouth and the cell suspension is slowly injected directly into the trachea. This method is invasive, can cause discomfort to the animal and there is the possibility of surgical trauma. The tumours can easily be implanted in the upper airways [107, 112] or there can be widespread distribution of the cancer cells over the lung, resulting in multiple tumour formation, which is not advantageous for tracking radiolabelled MSCTRAIL cells, as

discussed for the intravenous model. Finally, misplaced injection via the oesophagus into the stomach can result in tumour formation in the stomach, thus creating an ectopic model [112].

In Study - 2 the MSTO-211H human malignant pleural mesothelioma cell line was administered by intrapleural injection. BLI monitoring in figure 3.6 showed a steady increase in signal over time. Micro-CT imaging showed gradual compression of the lungs as there was tumour formation in the pleural space around the lung and between the lobes of the lung, which was confirmed by histological analysis. Therefore, this model provided distinct tumour formation outside the healthy lung parenchyma that can be identified and quantified by CT imaging. Nevertheless, this model did not provide tumour formation within normal lung parenchyma, except from the one case where there was cancer cell seeding within the lung. This model has the clinical representation of malignant pleural mesothelioma that is a rare but aggressive type of cancer that develops in the pleura. In the work of Sage et al., they conducted an incision on the right chest wall, and a right anterolateral thoracotomy was performed in the fourth intercostal space, followed by installation of MSTO-211H cells to develop a malignant pleural mesothelioma model. In their work they only assessed their tumour model by BLI and they found increasing signal over 21 days, which is in agreement with this work [31].

An alternative method that has been developed to produce an orthotopic model of lung cancer is via a surgical incision on the posterior medial line of the right thorax and dissects the soft tissue to expose the thoracic ribs and intercostal space. Then transthoracic injection of cells can be performed directly into the upper lobe of the right lung through the exposed ribs. This method is invasive as it requires wound stitches and analgesia. According to Madero-Visbal et al., lung cancer tumours formed in 90% of the animals with no adverse effects observed, however there was the risk of lung collapse during incision. Furthermore, this method was assessed only with BLI and histology (H&E) and no micro-CT or CT imaging was conducted, meaning that there is no 3D

imaging data showing the localisation of the tumour formation [113].

In Study - 3 the A549 human lung adenocarcinoma cell line was administered directly into the left lung parenchyma by intralobular injection. The left lung was chosen as it is a single lobe and this would reduce the risk of injection into the space between the lung lobes. BLI monitoring in figure 3.6 showed a steady increase in signal over time. Micro-CT imaging showed gradual compression of the lungs, as there was an increase in the high CT signal around the lung lobes, suggestive of tumour and effusion formation in the intrapleural space. ^{18}F-FDG PET/CT imaging showed high background cardiac uptake but no distinct tumour uptake, and histological analysis confirmed that the tumour tissue was necrotic due to the absence of Hoechst 33342 staining. The goal of this model was to generate a distinct lung adenocarcinoma tumour within healthy lung parenchyma. However, upon lung extraction it was observed that this model generated effusion and tumour formation within the intrapleural space. This added tumour burden would be problematical for studying MSCTRAIL distribution in mice as the addition of MSC cells in a compressed lung could be detrimental for the animal and may not allow full characterisation of the MSCTRAIL biodistribution over multiple time points. Jarry et al. had reported that for intercostal implantation of A549 cells there was tumour growth for 5/5 mice mostly around the lung and not inside the tissue. In their study they had utilised BLI and H&E histological analysis, which are in agreement with this work, however there was no micro-CT *in vivo* imaging showing the tumour formation [107]. In a study by Liu et al. intralobular injections of the A549 cell line (5 x 10^5) were conducted to the right lung of nude BALB/c nu/nu mice. In their study they found a 90% success rate of tumour implantation. They used spiral CT for *in vivo* imaging and H&E histology for *ex-vivo* validation and they found an intrathoracic tumour metastasis rate of 100% [114]. This finding was confirmed in the work of this chapter as 5/5 mice had intrapleural tumour formation as well as pleural effusion. The micro-CT imaging conducted in this work provided higher resolution images than the spiral CT, allowing

for clear identification of lung compression. The model of Study - 3 did not provide tumour formation within lung parenchyma and it was deemed not suitable for *in vivo* cell tracking studies in the diseased lung.

In Study - 4 the MSTO-211H human malignant pleural mesothelioma cell line was administered directly into the right lung parenchyma by intralobular injection. The right lung was chosen as it is larger in size than the left, thus minimising the chance of miss-injection, as no incision is done and the mice breathe normally under anaesthesia. BLI monitoring in figure 3.6 showed an initial decrease in signal that can be justified by initial cell death due to the cell remodelling phase for tumour formation, as discussed previously for the intravenous injection in Study - 1. Micro-CT imaging showed localised tumour formation within normal lung parenchyma. In 2 out of 5 mice there was cell seeding in the intrapleural space during injection that resulted in tumour formation in the intrapleural space and between the lung lobes. ^{18}F-FDG PET/CT imaging showed high background cardiac uptake and there was no statistically significant difference of uptake between tumour and healthy lung parenchyma. Histological analysis confirmed that there was localised tumour formation within healthy lung parenchyma. In the case that tumours grew in the intrapleural space this was confirmed by H&E as well. H&E showed tumour areas of densely packed cells with absence of alveoli and vasculature, which explains the non significant difference of ^{18}F-FDG uptake between lung and tumour tissue. The goal of this model was a distinct lung tumour formation in healthy lung parenchyma for the prospective use of the model in *in vivo* cell tracking studies. The model was deemed suitable as in all cases tumour formation was created in the lung parenchyma. For the cases that there was tumour outside the lung as well, this could be easily identified and quantified due to the lung compression.

A final alternative method that has been assessed in the literature for orthotopic lung cancer model development is the intranasal administration of cancer cells. The intranasal administration method has been commonly used in the literature for establishing

infectious models of influenza virus and rhinovirus [115, 116, 117] and it is not commonly used for cancer cell administration. In a study by Tanaka et al. the tumour presentation derived from the intranasal administration of Lewis lung carcinoma murine cells was compared with the tumour presentation derived from the intralobular by incision and the intratracheal administration methods of the same cell line. They only assessed their models by histology (H&E) and they observed tumour formation in the left lung lobe and in the thoracic cavity for all three administration methods. Intralobular and intratracheal administration methods resulted in tumour growth in the entire left lung lobe and thoracic cavity broadly, but intranasal injection showed limited growth in the thoracic cavity and primarily formed tumours around bronchioles and alveoli. By conducting intranasal administration of cancer cells they developed a minimally invasive method for producing an orthotopic model of lung cancer, however, their model provided multiple tumour formation within and outside lung parenchyma. Furthermore, they only assessed their models by histology (H&E) and no *in vivo* imaging was conducted [91] for the understanding of tumour presentation *in vivo* and whether tumour formation could be clearly identified by imaging. The intranasal cancer cell implantation method was not assessed in this thesis as the method could lead to widespread cell distribution within the lung, resulting in multiple tumour formation, something not advantageous for tracking radiolabelled MSCTRAIL cells, as discussed for the intravenous and intratracheal models.

For the mice that there was tumour and effusion formation in the intrapleural and between the lung lobes spaces, the distinction between tumour and effusion using micro-CT imaging was challenging as the HU values between the two overlap. A HU range of approximately 0 to 30 HU can encompass both effusion and tumour formation [118], therefore, for the work of this thesis, it was chosen to quantify the compression of the lung parenchyma due to tumour and pleural effusion formation outside the lung by quantifying the final micro-CT acquisitions and comparing them to the respective baseline scans.

The breathing gated micro-CT acquisitions conducted in this chapter exposed the

mice to ionising radiation, which over time, in longitudinal studies, could cause radiation-induced lung injury or affect the tumour formation. However, the dose of a breathing gated micro-CT scan (912 mGy) is an order of magnitude lower than the typical doses applied in the field of radiotherapy for lung treatment (4-20 Gy). In this work, no tumour volume reduction or adverse effects were observed, which is in agreement with the work of Zaw Thin et al. In their work, they assessed various lung tumour models utilising different micro-CT scanners and did not observe any radiation-induced adverse effects or tumour volume changes [101].

The cancer cell implantation methods utilised in this chapter were minimally invasive. For the cancer cell administration, the mice were under anaesthesia for a few minutes and they recovered quickly after the injection of the cancer cells. No analgesia was needed after the procedure and the mice did not exhibit any signs of stress or discomfort. No adverse effects were observed for any study and all mice survived until the end point of their respective study. It was chosen to not conduct a pleural incision for the intralobular administration method. The pleural incision allows the visualisation of the lung lobe, but it does not eliminate the possibility for seeding of cancer cells in the intrapleural space during injection and it causes pain and discomfort to the animals as it is a surgical procedure.

3.5 Conclusion

In this chapter, a minimally invasive orthotopic preclinical mouse model of lung cancer was developed to represent clear tumour formation within healthy lung parenchyma for application in *in vivo* cell tracking imaging studies. The model allows for the clear delineation of the different areas for the prospective cell tracking and quantification of [^{89}Zr]Zr-oxine radiolabelled MSCTRAIL cells in both tumour and healthy lung tissue, as well as other organs, as will be explained in Chapter 5.

CHAPTER 4

Preclinical Phantom Imaging Using ^{89}Zr

4.1 Introduction

Preclinical PET/CT systems are a well-established non-invasive imaging tool used for the development and validation of novel radiotracers, the investigation of molecular mechanisms of disease in animal models, as well as the testing of drug safety, efficacy and response to treatments for their prospective clinical translation [119]. Preclinical PET/CT imaging is commonly performed in rodents and non-human primates [119] and quantitative measurements are used to quantify the uptake of radioactivity in different organs of interest, to understand disease progression, treatment response or to track cells *in vivo*, as is the aim of this thesis.

The regular quality control (QC) and assessment of the systems for their quantitative accuracy are highly important, as it has been highlighted by a recent procedure guideline programme by the European Association of Nuclear Medicine (EANM) and the European Society for Molecular Imaging (ESMI) [56]. When novel radionuclides such as ^{89}Zr are used for preclinical imaging studies, the systems need to be assessed for their performance, with phantom studies, before the animal studies commence.

In this thesis, longitudinal imaging of immunocompromised mice for the *in vivo* cell tracking of a [^{89}Zr]Zr-oxine direct radiolabelled human mesenchymal stem cell product will be conducted. The range of activities that will be utilised for injection per mouse will be between 150 and 300 kBq, as was discussed in section 2.4, meaning that the injected radioactivity will decay as low as 0.03 MBq over the planned 7 day longitudinal *in vivo* imaging window. The NSG immunocompromised mice required for these studies are susceptible to anaesthesia, as it was discussed in section 3.2.3 and therefore the total

acquisition time should not exceed 1 h, something that limits increasing sensitivity by increasing scan times.

In this chapter, a preclinical PET/CT system was assessed for its performance using a phantom, for the prospective *in vivo* imaging protocol that will be utilised for the *in vivo* cell tracking of [^{89}Zr]Zr-oxine radiolabelled MSCTRAIL cells in longitudinal preclinical mouse studies in Chapter 5. Aside from the *in vivo* imaging protocol, phantom acquisitions were conducted using the standard acquisition imaging protocol, set by the manufacturer, for the quality control of the PET/CT system. The standard phantom imaging protocol was acquired for both ^{89}Zr and ^{18}F, as ^{18}F is the radionuclide that all the standard QC measurements and the calibration of the system are conducted for. Finally, a comparison of the results was conducted between the two radionuclides.

4.2 Materials and Methods

The preclinical phantom utilised was the National Electrical Manufacturers Association (NEMA) IQ phantom, which has a main body that is fillable with a total volume of 20.5 mL, of a homogenous concentration of radioactivity. The radioactive solution was injected via one port so that it filled all of the different compartments, that are the uniform area and five rods, which vary in diameter from 1 to 5 mm. The lid to the large homogenous volume also contained two chambers of 0.8 mL each, one was filled with air and the other with non-radioactive water. With these compartments different measurements were conducted for the uniformity, recovery coefficient (RC) and spill-over ratio (SOR) of a preclinical PET scanner, to assess its performance for imaging with ^{89}Zr.

The preclinical NEMA IQ phantom utilised and its different compartments can be seen at the following figure 4.1. The preclinical system utilised was a Mediso nanoScan® PET/CT (PET122S/CT1512) system. The details of the system can be seen at the following table 4.1.

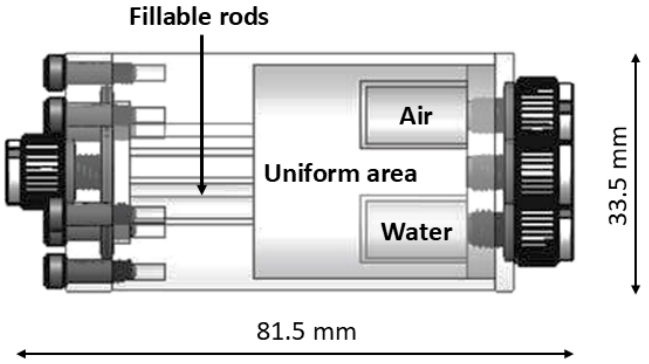

Figure 4.1: Preclinical NEMA IQ phantom and its different compartments. Image adapted from Phantech [120].

Parameter	Value
Detector crystal	Lutetium Oxyorthosilicate (LSO)
Number of detectors	12
Number of detector rings	2
Crystal dimensions	1.12 x 1.12 x 13 mm
Coincidence modes	1 - 1, 1 - 3, 1 - 5
Axial FOV	94.7 mm
Transaxial FOV	1 - 1: 44x44 mm, 1 - 3: 85x85 mm, 1 - 5: 102x102 mm
Energy window	400-600 keV

Table 4.1: Specifications of the preclinical Mediso nanoScan® PET/CT system.

4.2.1 Preparation of the radionuclide formulation and filling of the phantom

^{89}Zr was purchased from Revvity as [^{89}Zr]Zr-oxalate in 1 M oxalic acid. The [^{89}Zr]Zr-oxalate complex, $[^{89}Zr(C_2O_4)_4]^{4-}$, has a negative charge of -4 and is only stable, fully soluble, at low pH (pH $<$ 2) conditions. In order to ensure an even distribution of radioactivity within the phantom and prevent precipitation, [^{89}Zr]Zr-oxalate was chelated with Diethylenetriamine pentaacetate (DTPA), which reduced the negative charge to -1. Moreover, the MOPS (3-(N-morpholino)propanesulfonic acid) buffering agent was added to ensure that the pH of the solution would be neutral.

The phantom was first partially filled with non-radioactive water. For all ^{89}Zr

phantom experiments, a total volume of 3 ml of DTPA (10 mM) and MOPS (40 mM) in HPLC water (pH = 7.4) was thoroughly mixed with the supplied activity and it was used for the filling of the phantom. For the ^{18}F phantom experiments, the ^{18}F-FDG radiopharmaceutical was used without adding DTPA/MOPS and again it was injected in a 3 ml volume of purified water. Finally, the phantom was filled completely with non-radioactive water making sure that no bubbles were present and no radioactivity leaked from the phantom. The phantom was mixed gently once sealed to ensure even distribution of radioactivity through all compartments.

The activity injected to the phantom was measured on a CRC-55tR calibrator. For the longitudinal *in vivo* imaging protocol the injected activity to the phantom was 1.08 MBq and 18 consecutive acquisitions were conducted in total, one per day for 18 days, until the activity had decayed to 0.03 MBq. For the standard phantom imaging protocol, three separate acquisitions were conducted for each radionuclide, and the injected activities were 3.2 ± 0.3 MBq (SD) for ^{89}Zr and 3.9 ± 0.2 MBq (SD) for ^{18}F, to compare the two radionuclides under same conditions.

4.2.2 Acquisition process and image processing

The phantom was placed on the single mouse bed of the PET/CT system and scanned using list-mode for all acquisitions. For the *in vivo* imaging protocol, the phantom was scanned longitudinally for 18 consecutive days, to assess the performance of the system for different activity values, as the activity in the phantom decayed. The *in vivo* imaging protocol was set to the same imaging parameters that will be used for all future [^{89}Zr]Zr-oxine labelled MSC *in vivo* applications. PET was acquired as static for 40 min in 1 - 3 coincidence mode, and a whole phantom CT acquisition was acquired at 70 kVp with 90 ms exposure (zigzag). As discussed previously, the total acquisition time chosen was the longest possible to increase sensitivity and improve image quality, while still taking into consideration the high sensitivity of the NSG mice to anaesthesia. The standard

quantitative corrections in preclinical imaging were applied, which are Normalization, Randoms correction, Dead time correction, Decay correction, Attenuation correction and Scatter correction.

For the standard phantom imaging protocol, for both ^{89}Zr and ^{18}F studies, PET was acquired as static for 20 min in 1 - 3 coincidence mode and a whole phantom CT acquisition was acquired at 50 kVp with 170 ms exposure (helical). The standard quantitative corrections in preclinical imaging were applied as before.

All PET data was reconstructed in 1 - 3 coincidence mode using the Tera-Tomo iterative algorithm with 4 iterations and 6 subsets in 0.4 mm isotropic voxels. The CT was reconstructed using the FBP reconstruction method in 0.13 mm isotropic voxels for the *in vivo* imaging protocol and in 0.25 mm isotropic voxels for the standard phantom imaging protocol.

4.2.3 Analysis and data processing

All phantom acquisitions were analysed according to the NEMA NU 4-2008 [121] protocol using the MATLAB analysis software provided on the PET/CT system by the manufacturer. The analysis acquired measurements for uniformity, RC and SOR. For the uniformity measurements, the MATLAB programme draws a 22.5 mm diameter by 10 mm long cylindrical VOI in the uniform area of the phantom and the average activity concentration is measured in Bq/mL. The percentage standard deviation (%SD) is also calculated according to the following equation:

$$\%SD_{uniformity} = \frac{SD_{uniform}}{Mean_{uniform}} \times 100 \tag{4.1}$$

where $\mathrm{SD}_{uniform}$ is the standard deviation of pixel values in the uniform region and $\mathrm{Mean}_{uniform}$ is the average activity concentration measured in the uniform region.

For the RC the following procedure was followed for its calculation. First, the

reconstructed transverse image slices along the central 10 mm of the hot rods were averaged to reduce noise. Next cylinder ROIs with diameters twice the physical diameters of the rods were drawn around each rod. Linear profiles were drawn along the rods in the axial direction. Assuming that the RC of the homogeneous region is equal to 1, the average pixel values of the linear profiles were divided by the average pixel value of the uniform region, to determine the recovery coefficients, as can be seen at the following equation:

$$RC = \frac{Mean_{line\ profile}}{Mean_{uniform}} \tag{4.2}$$

where $\text{Mean}_{line\ profile}$ is the mean value from each of the hot rods (1, 2, 3, 4 and 5 mm) and $\text{Mean}_{uniform}$ is the average activity concentration measured in the uniform region. Thereafter, the %SD of the RC ($\%\text{SD}_{RC}$) for each rod was determined using the following equation:

$$\%SD_{RC} = \sqrt{(\frac{SD_{line\ profile}}{Mean_{line\ profile}})^2 + (\frac{SD_{uniform}}{Mean_{uniform}})^2} \times 100 \tag{4.3}$$

where $\text{SD}_{line\ profile}$ and $\text{Mean}_{line\ profile}$ are the standard deviation and mean measurements for each rod and $\text{SD}_{uniform}$ and $\text{Mean}_{uniform}$ corresponds to the standard deviation and the mean activity concentration in the uniform region.

For the SOR, ROIs were drawn on each water and air chamber with the SOR values calculated as ratios between the water or air chamber mean value, divided by the mean measurement of the uniform region, as can be seen at the equation below:

$$SOR = \frac{Mean_{chamber}}{Mean_{uniform}} \tag{4.4}$$

The percentage standard deviation (%SD) was also calculated according to the following equation:

$$\%SD_{SOR} = \sqrt{(\frac{SD_{chamber}}{Mean_{chamber}})^2 + (\frac{SD_{uniform}}{Mean_{uniform}})^2} \times 100 \tag{4.5}$$

where $\text{SD}_{chamber}$ is the standard deviation of pixel values in the water or air chamber and

$\text{Mean}_{chamber}$ is the mean value from each individual water or air chamber respectively. $\text{SD}_{uniform}$ and $\text{Mean}_{uniform}$ corresponds to the standard deviation and the mean activity concentration in the uniform region, as before.

Representative images of the Mediso MATLAB analysis software for the NEMA IQ phantom, displaying the regions utilised for the analysis (uniformity, RC and SOR), as well as the placements of ROIs are shown in the following figure 4.2.

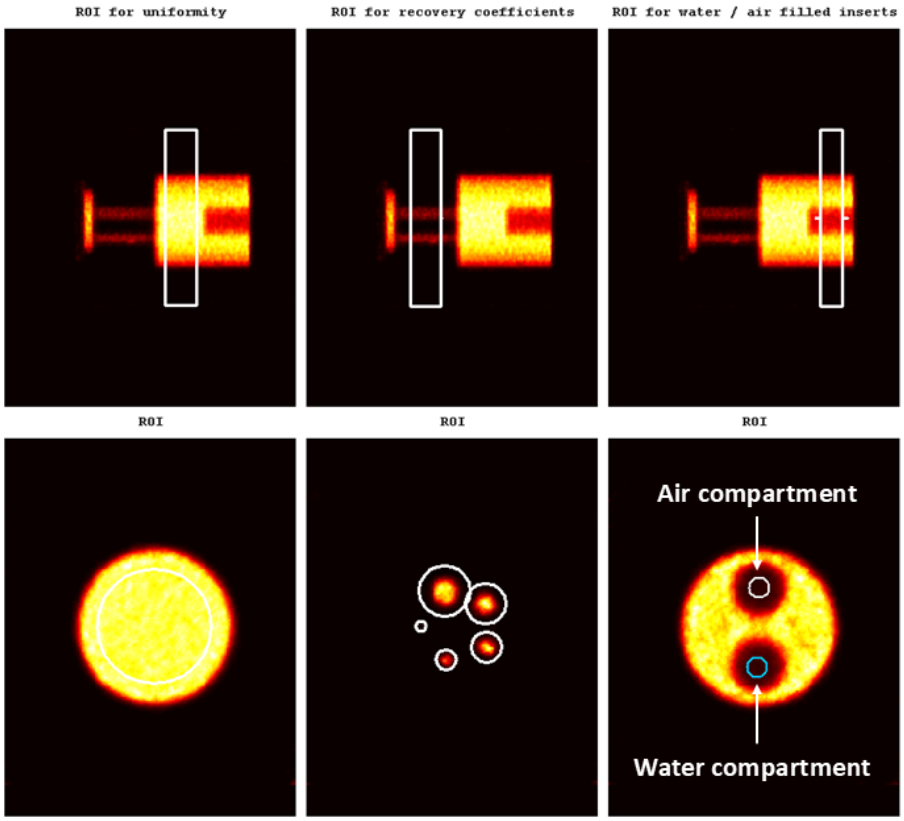

Figure 4.2: MATLAB analysis software: Preclinical NEMA IQ phantom and the different ROIs applied to the compartments for the analysis.

For the longitudinal *in vivo* imaging protocol acquisitions, the VivoQuant software (Version 2022 - Invicro) was used to calculate the percentage difference between the measured and expected activities. To measure the total activity of the phantom at each acquisition, a VOI that contained the whole phantom was applied. The expected activity

for each acquisition was calculated based on the measurement from the calibrator and equation 1.5. The value was decay corrected based on the time difference from the time of measurement at the calibrator and the time of acquisition at the system. The percentage difference between the measured values and the expected ones, was calculated according to the following equation:

$$\%Diff_m = \frac{|measured\ value - expected\ value|}{\frac{(measured\ value\ +\ expected\ value)}{2}} \times 100 \tag{4.6}$$

4.2.4 Statistical analysis

Statistical analysis was performed with GraphPad Prism version 8.0. For the standard phantom imaging protocol, data are presented as mean ± standard deviation (SD). Unpaired samples two-tailed t test was conducted for the comparison of ^{18}F and ^{89}Zr measurements, conducted using the standard phantom imaging protocol. Statistical significance was identified for *p ≤ 0.05, **p ≤ 0.01, ***p ≤ 0.001.

4.3 Results

4.3.1 *In vivo* imaging protocol

For the *in vivo* imaging protocol, the %SD calculated for the uniformity was plotted alongside the total number of coincidence events accumulated, versus the consecutive 18 acquisitions acquired, as can be seen in the following figure 4.3. The %SD increased as the radioactivity decayed and the total number of coincidence events detected decreased.

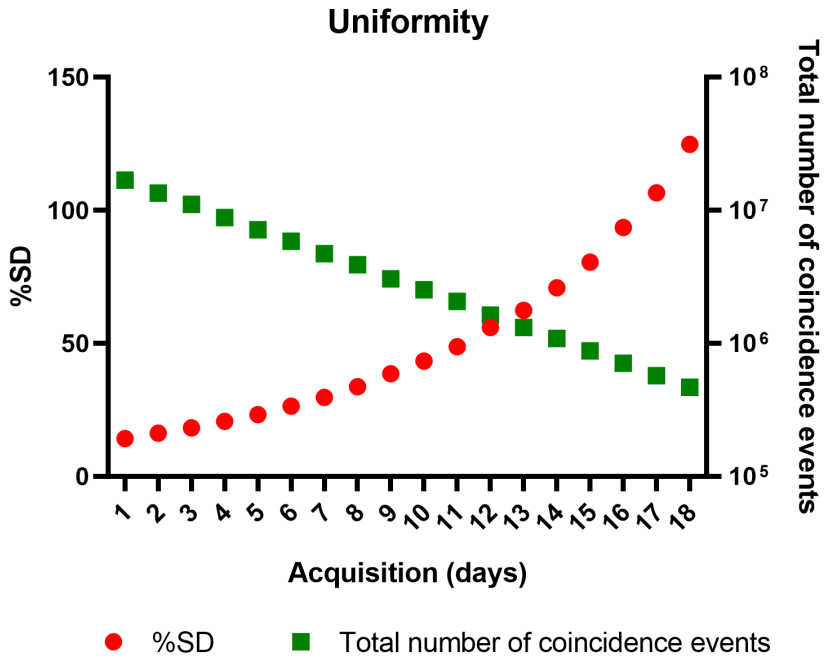

Figure 4.3: *In vivo* imaging protocol using ^{89}Zr: %SD of uniformity plotted alongside the total number of coincidence events accumulated, versus the 18 consecutive acquisitions conducted.

The RC for all acquisitions of the *in vivo* imaging protocol, using ^{89}Zr, versus the rod diameter can be seen at figure 4.4. Three graphs were plotted for different expected activity ranges. For rod diameter more than 3 mm the RC values are generally above 1. This means that for structures larger than 3 mm there is an overestimation of radioactivity within the structure. As the total activity decreases there is a slight increase in RC values for the larger rods.

The $\%SD_{RC}$ for all acquisitions of the *in vivo* imaging protocol, using ^{89}Zr, versus the rod diameter can be seen at figure 4.5. Again three graphs were plotted as before. The %SD values decrease as the rod diameter increases, as for larger structures more counts are included into the ROI analysis and therefore there is less noise in the measurement. However, as radioactivity decays the %SD values increase, due to the increase in noise in agreement with the findings of figure 4.3.

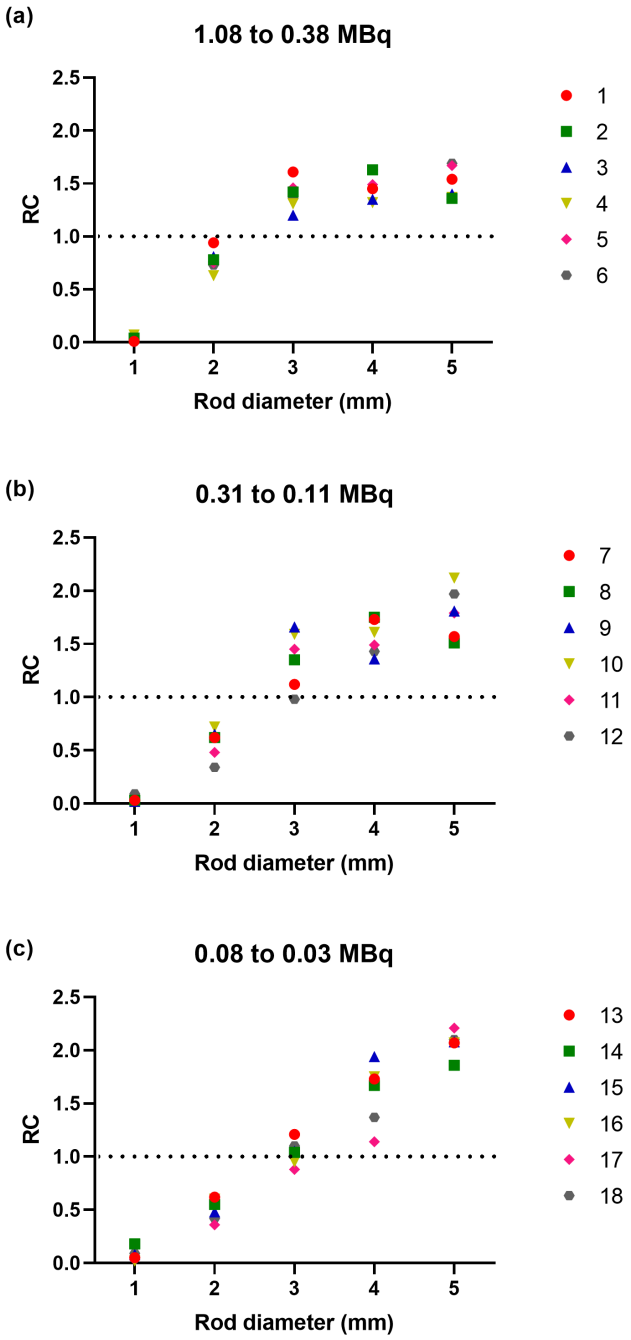

Figure 4.4: *In vivo* imaging protocol using ^{89}Zr: Recovery coefficient (RC) versus rod diameter for the 18 consecutive acquisitions conducted. Expected activities (a) 1.08 to 0.38 MBq, (b) 0.31 to 0.11 MBq and (c) 0.08 to 0.03 MBq.

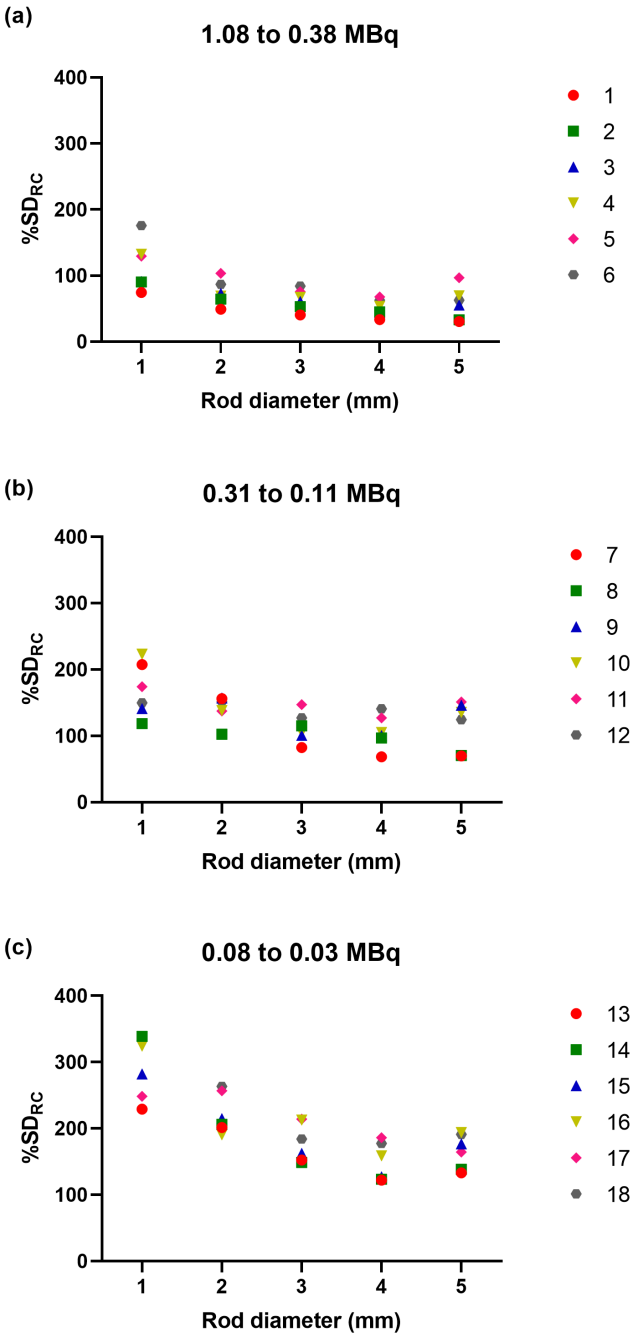

Figure 4.5: *In vivo* imaging protocol using ^{89}Zr: $\%SD_{RC}$ versus rod diameter for the 18 consecutive acquisitions conducted. Expected activities (a) 1.08 to 0.38 MBq, (b) 0.31 to 0.11 MBq and (c) 0.08 to 0.03 MBq.

The SOR for each acquisition of the *in vivo* imaging protocol can be seen at the following table 4.2 for both the water and air chambers. The SOR values generally remain similar for both chambers as the activity decays.

Acquisition (days)	**SOR Water**	**SOR Air**
1	0.09	0.08
2	0.09	0.08
3	0.09	0.08
4	0.09	0.08
5	0.09	0.08
6	0.09	0.08
7	0.07	0.08
8	0.08	0.07
9	0.10	0.07
10	0.10	0.08
11	0.10	0.08
12	0.09	0.08
13	0.07	0.09
14	0.10	0.09
15	0.10	0.09
16	0.10	0.08
17	0.09	0.07
18	0.09	0.12

Table 4.2: *In vivo* imaging protocol using ^{89}Zr: SOR values for the water and air chambers of the NEMA IQ phantom for the 18 consecutive acquisitions conducted.

The %SD of SOR versus the acquisitions conducted for the *in vivo* imaging protocol, using ^{89}Zr, can be seen in the following figure 4.6. The %SD values increase for both the water and air chambers as the radioactivity decays. The expected activity versus the measured activity for the *in vivo* imaging protocol can be seen in figure 4.7. A strong positive correlation was identified ($R^2 = 0.9997$) between expected and measured activities.

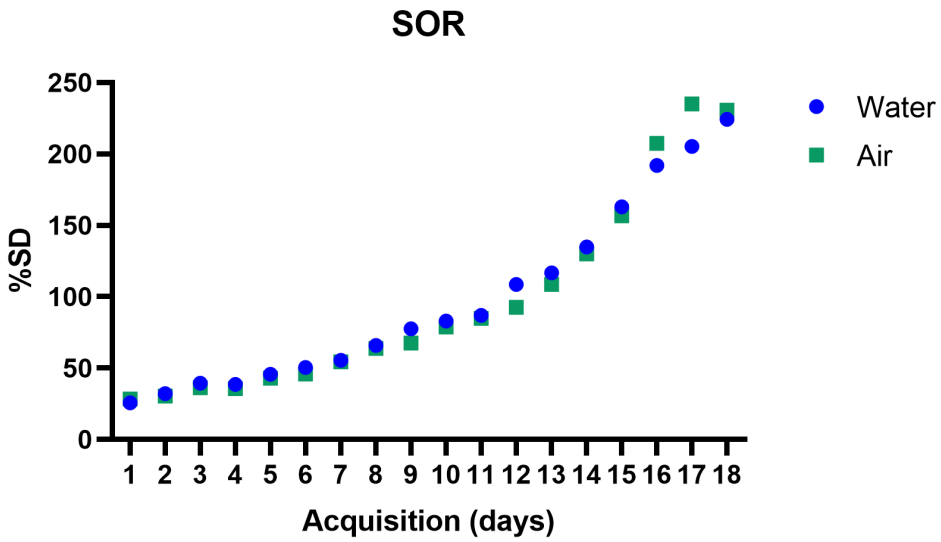

Figure 4.6: *In vivo* imaging protocol using ^{89}Zr: %SD of SOR versus the 18 consecutive acquisitions conducted, for both the water and air chambers.

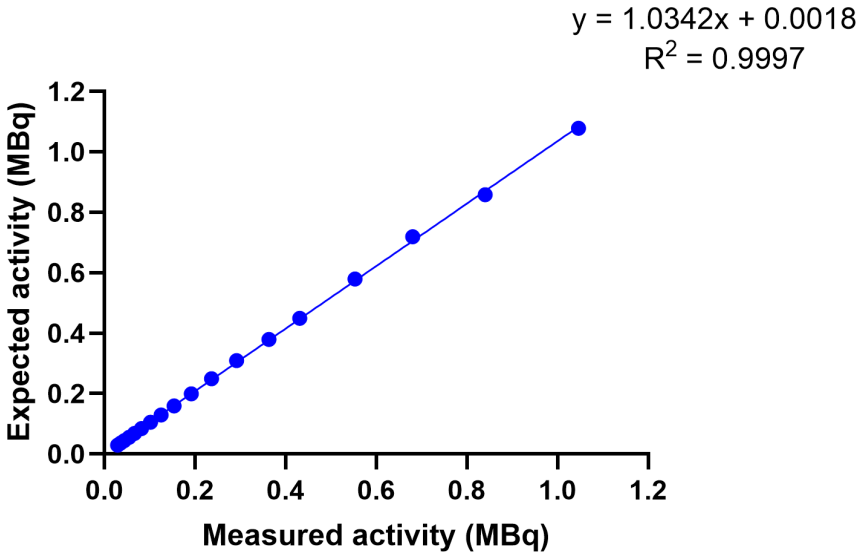

Figure 4.7: *In vivo* imaging protocol using ^{89}Zr: the expected activity versus the measured activity for every acquisition conducted.

4.3.2 Standard phantom imaging protocol

For the standard imaging protocol of the NEMA IQ phantom, the %SD of uniformity can be seen in figure 4.8 and the RC versus the rod diameter can be seen in figure 4.9 for both ^{18}F and ^{89}Zr.

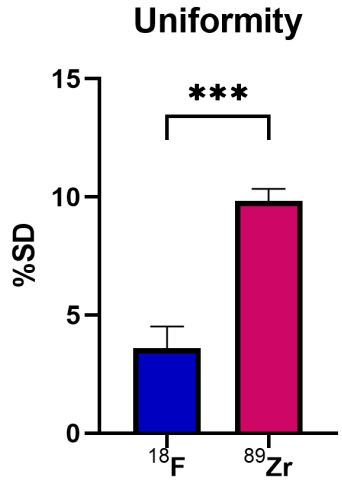

Figure 4.8: Standard phantom imaging protocol: %SD of uniformity for ^{18}F and ^{89}Zr.

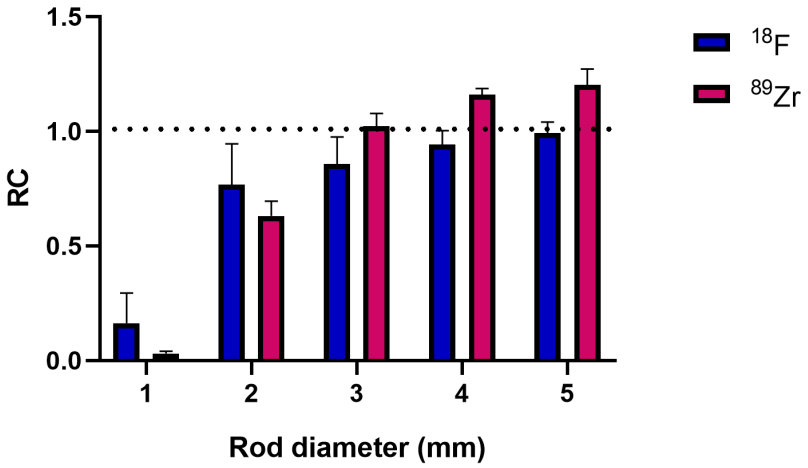

Figure 4.9: Standard phantom imaging protocol: RC versus rod diameter for ^{18}F and ^{89}Zr.

For ^{18}F the RC values increase as the rod diameter increases and for the largest rod the RC is approximately 1. The increase in RC for larger structures is expected, as the effect of PVE is less prominent and for a calibrated system the RC for larger structures should be 1. However, for ^{89}Zr the overestimation of values identified in figure 4.4 is seen again.

The %SD of SOR for the water and air chambers for both ^{18}F and ^{89}Zr can be seen at the following figure 4.10.

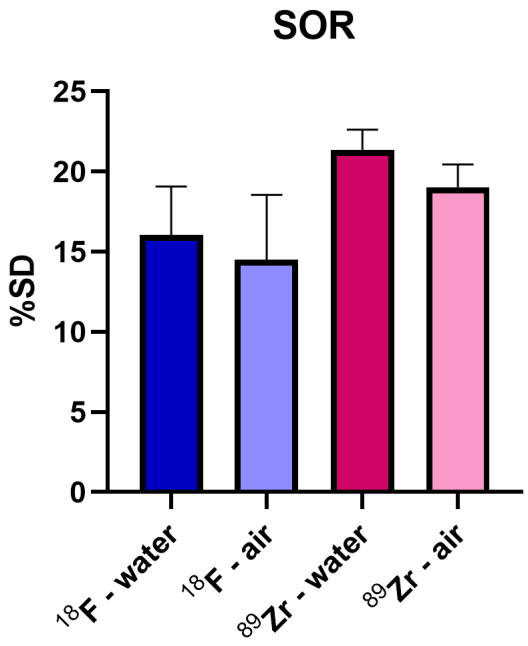

Figure 4.10: Standard phantom imaging protocol: %SD of SOR for the water and air chambers for both ^{18}F and ^{89}Zr.

Statistical analysis showed a significant difference for the %SD of uniformity between ^{18}F and ^{89}Zr ($p = 0.0005$), while no significant difference ($p > 0.05$) was identified between the ^{18}F and ^{89}Zr %SD results of the SOR, for both the water and air chambers.

4.4 Discussion

The importance of standardisation for preclinical PET/CT imaging has been highlighted in the literature, and a publication by McDougald et al. assessed the variability of five different commercial preclinical PET/CT systems using ^{18}F, for their acquisition and reconstruction protocols. In their study, they highlighted the need for standardised protocols, as well as the calibration and regular QC of the systems. Nevertheless, ^{89}Zr imaging was not assessed in their study [122].

In this chapter, the performance of a preclinical PET/CT system was assessed using a NEMA IQ phantom, containing comparable activity and scanned using the same acquisition parameters, as will be used for the longitudinal imaging of mice, injected with a [^{89}Zr]Zr-oxine labelled mesenchymal stem cell product (longitudinal *in vivo* imaging protocol). The standard imaging protocol for a NEMA IQ phantom, set by the manufacturer to be used for QC, was also conducted for both ^{18}F and ^{89}Zr, for comparison between the two radionuclides.

For the *in vivo* imaging protocol, the %SD of uniformity increased as the radioactivity decayed and the total number of coincidence events detected decreased, as was seen in figure 4.3. The %SD is a metric of noise in the reconstructed PET images, and it shows that noise increases as the total radioactivity in the phantom decreases, and thus the total number of coincidence events available for reconstruction decrease, something that was expected, as reduced sensitivity increases noise.

The RC values for the *in vivo* imaging protocol, versus the rod diameter were seen in figure 4.4. For rod diameter more than 3 mm the RC values are generally above 1. This means that for structures larger than 3 mm there is an overestimation of radioactivity within the structure. As the total activity decreases there is a slight increase in RC values for the larger rods. The overestimation in RC values could be due to an overcorrection applied by the image reconstruction, as an overcompensation could be applied for partial

volume effects, leading to artificially high RC values. Furthermore, the increased noise present in ^{89}Zr imaging could be another factor influencing the RC values being above 1. The %SD values of RC were seen in figure 4.5. The %SD values decrease as the rod diameter increases, as for larger structures more counts are included into the ROI analysis and therefore there is less noise in the measurement. However, as radioactivity decays the %SD values increase, due to the increase in noise in agreement with the findings of figure 4.3. In the work of Vanhove et al., they highlight the importance of noise as they state that RCs can be overestimated in cases of high variance and noise and thus the RC values can be above 1 even though there can be good recovery [56].

The SOR values for the water and air chambers measured for the *in vivo* imaging protocol were seen in table 4.2. The SOR values generally remain similar for both chambers as the activity decays, something that can be explained by the fact that this measurement is a ratio and both the numerator and denominator are affected proportionally by the decrease in radioactivity and thus the reduction in the total coincidence events accumulated. However, the %SD values increase for both the water and air chambers, as can be seen in figure 4.6, showing an increase in noise in agreement with the finding of figures 4.3 and 4.5.

For the *in vivo* imaging protocol, the expected activity values at the time of scanning ranged from 1.08 to 0.03 MBq. In figure 4.7 no plateau area created due to dead time was shown, therefore the activity values assessed in this experiment are in the linear area, which indicates that the administered activities should be properly assessed given the measured activity value that is acquired by the PET/CT system. The overestimation in activity measurements shown in the RC values was not reflected in the total phantom measurements. This could be explained by the following reasons. ^{89}Zr longer positron range, compared to ^{18}F, can affect image quality, creating blurring and leading to spill-over between regions. Furthermore, its high energy photons (909.9 keV) increase the random events, which increase noise. The increased spill-over can amplify the signal in

larger spheres, leading to RC values larger than 1. The increased noise can affect image reconstruction especially for iterative reconstruction methods, as noise fluctuations in larger regions can cause positive bias due to edge-enhancing effects in reconstruction, leading to an overestimation of RC. On the other hand, spill-out from smaller spheres, the increase in background variability and the overall increased noise can cause the total activity to be underestimated.

For the standard phantom imaging protocol the conditions between the two radionuclide acquisitions were kept consistent, a significant difference was shown between the $\%SD_{uniformity}$ of ^{18}F and ^{89}Zr (figure 4.8). This highlights the significantly larger noise present in ^{89}Zr studies, that can be attributed to the larger positron range and lower branching ratio for positron decay of ^{89}Zr compared to ^{18}F and the high energy photons (909.9 keV) of ^{89}Zr.

In figure 4.9 the RC values for ^{18}F and ^{89}Zr were seen. For ^{18}F the RC values increase as the rod diameter increases and for the largest rod the RC was approximately 1, as expected. However, for ^{89}Zr the overestimation of values identified in figure 4.4 was seen again.

For the SOR, the %SD seen in figure 4.10, was not significantly different between ^{18}F and ^{89}Zr for both the water and air chambers. This can be explained by the fact that the %SD measures the relative noise in the cold regions, so it is a normalised measure that shows the noise in the cold region relative to its own mean, and not the noise in the whole image. Therefore, even though ^{89}Zr images are globally noisier, compared to ^{18}F, the cold regions scale proportionally thus leading to a similar %SD value.

Preclinical NEMA IQ phantom studies have been published for various isotopes including ^{89}Zr. In the work of Bradshaw et al., they compared the image quality of ^{18}F and ^{89}Zr in a preclinical PET/CT scanner using different reconstruction methods and different phantoms, including the NEMA IQ phantom. They found that ^{89}Zr had greater image noise compared to ^{18}F, in agreement with this work [123].

In the work of Teuho et al., they applied the NEMA NU 4-2008 protocol to compare different preclinical systems using different radionuclides. They adapted the imaging acquisition time to record a similar amount of total coincidence events as ^{18}F for all other radionuclides, including ^{89}Zr. In their work, they did not find RC values above 1 for ^{89}Zr. However, they highlight that the %RC values are affected by the counting statistics, that reflect image noise and system sensitivity, the image reconstruction algorithm applied, as well as the differences in positron range, physical half-life and positron fraction of the radionuclide used. They also identified that increased noise results in increase of $\%SD_{RC}$. For the $\%SD_{uniformity}$ they identified that it remains relatively stable between radionuclides as long as sufficient amount of counting statistics is collected and the same reconstruction algorithm is applied. However, if the total activity or the counting statistics is too low, the standard deviation in the uniform region and other phantom regions are affected. Their results for the $\%SD_{SOR}$ showed no radionuclide-specific differences in agreement with this work [124].

In a study by Chomet et al., longitudinal NEMA IQ phantom experiments were conducted on a Mediso nanoScan® PET/CT scanner until the radioactivity in the phantom decayed, using different radionuclides including ^{18}F and ^{89}Zr. They determined the SOR and the RCs and for the RCs they utilised two analysis methods. First, the ROIs were defined with their size matching the contours of the rods, to closely match the *in vivo* tumour analysis strategy applied in their animal work. Second, ROI analysis according to the standardized NEMA protocol was performed using the Mediso NEMA analysis software, in which the ROI sizes in the rods are double their actual size. They found higher RC values using the Mediso NEMA analysis software, that agree with the results of this chapter, compared to their first analysis method. For the SOR they reported values in air and water that ranged between 12 and 17% for all isotopes which are similar to the ones reported in this work [125].

The performance of a preclinical PET/CT scanner should be assessed for tracer

quantification ahead of *in vivo* studies, especially when radionuclides such as ^{89}Zr are used for longitudinal *in vivo* cell tracking. The increased noise identified in this work highlights the importance of assessing a protocol ahead of *in vivo* implementation. For the prospective imaging study of Chapter 5, the acquisition time cannot be extended as radioactivity decays, to keep the total number of coincidence events constant and thus mitigate the effect of noise, due to the sensitivity of NSG mice to anaesthesia. Since quantitative measurements of different organs need to be acquired, the appropriate quantitative measure that will be used is the percentage of the injected activity, decay corrected to the time of each acquisition, per the volume of the VOI applied in mL (%IA/mL), which takes into account the total activity in the animal and is not affected by the volume of the different organ segmentations or by differences in injected activities between animals. The *in vivo* imaging protocol can be applied for the *in vivo* cell tracking of ^{89}Zr radiolabelled MSCTRAIL cells, for the range of activities assessed, however for studies that require even lower range of activities or different radionuclides need to be used and compared, extra care must be taken in the acquisition and reconstruction protocols, as the reduced sensitivity and the inherent differences of the different radionuclides can affect the quantitative measurements and thus the deductions made.

4.5 Conclusion

In this chapter, a preclinical NEMA IQ phantom was utilised to assess the performance of a preclinical PET/CT system for the *in vivo* tracking of cells using ^{89}Zr. It was deemed that the *in vivo* imaging protocol can be applied for the prospective *in vivo* tracking of [^{89}Zr]Zr-oxine MSCTRAIL cells, for the range of activities assessed, by applying relative measurements to mitigate the effect of noise and keep the measurements consistent between different organs and animals.

CHAPTER 5

In vivo Tracking of [^{89}Zr]Zr-oxine Radiolabelled Stem Cells in a Mouse Model of Lung Cancer

5.1 Introduction

Cell therapies are developed for a vast range of pathologies, including cancer, cardiovascular and neurological diseases and regenerative medicine. Mesenchymal stem cell therapies are of particular interest for the treatment of cancer, as stem cells can be used as carriers to deliver a treatment to the cancer site. Multiple *in vivo* cell tracking methods for stem cells have previously been developed and evaluated in preclinical models, using various imaging modalities, to understand the *in vivo* stem cell distribution and assess delivery to the target tissue as well as off-target delivery [126].

Cell engineering for the expression of firefly luciferase and BLI have been used to track human bone marrow-derived MSCs in mouse models of breast cancer [127, 128], thyroid cancer [128] and murine large cell lung carcinoma [129], as well as human umbilical cord tissue-derived MSCs in a mouse model of breast cancer [130]. PET imaging has been utilised to track human bone marrow-derived MSCs in mouse models of murine colon carcinoma using indirect labelling with ^{18}F-labelled 9-(4-fluoro-3-hydroxymethylbutyl)-guanine ([^{18}F]-FHBG) [131], human hepatocellular carcinoma using indirect labelling of NIS expressing MSCs with ^{124}I [132], as well as human umbilical cord tissue-derived MSCs in a mouse model of lung cancer using direct labelling with [^{89}Zr]Zr-oxine [46]. SPECT imaging has been utilised to track NIS expressing human bone marrow-derived MSCs, by indirect labelling with ^{123}I in mouse models of human hepatocellular carcinoma [132, 133, 134] and by indirect labelling with ^{99m}Tc in mouse models of breast cancer [135] and human cervical cancer [136]. MRI has been used to track human bone marrow-

derived MSCs in mouse models of human cervical cancer [136], human glioma [137] and metastatic lung cancer [138], using SPIONs.

Nevertheless, not all preclinically used cell tracking methods can be applied to patients. BLI is widely used in the preclinical setting for *in vivo* cell tracking, however, the luciferase reporter proteins needed for imaging are of non-mammalian origin, so BLI cannot be translated to the clinic due to safety concerns and regulatory constraints. Furthermore, the attenuation and scatter of light within the tissue means that BLI allows imaging up to a few cm depth, which is a limitation for imaging in large animals and patients [33]. PET, SPECT and MRI cell tracking imaging methods can be clinically translated as long as they are safe for patients and can be conducted under GMP standards. For example, the method developed by Ferris et al. [77] has been used in the preclinical setting for PET/CT cell tracking using [^{89}Zr]Zr-oxine, however, the method is not suitable for clinical translation as was discussed in Chapter 2.

Clinical trials are conducted to assess the safety and therapeutic efficacy of cell therapies, however, imaging is rarely used during a clinical trial to understand the *in vivo* distribution of the therapeutic cells [33]. This is due to the limited available options of *in vivo* cell tracking methods, that are safe for humans and can be easily implemented in the clinical setting. Furthermore, the increase in cost and the lack of technical expertise of cell tracking among clinicians also hinder the application of cell tracking methods as part of clinical trials. Consequently, there is the need for the validation of clinically translatable cell tracking methods, that can be easily applied in the clinical setting, for their application in clinical trials.

In this chapter, the clinically translatable method of direct [^{89}Zr]Zr-oxine radiolabelling for MSCs, explained in Chapter 2, was assessed *in vivo* in an orthotopic mouse model of lung cancer, as well as in naïve mice, using PET/CT imaging. The orthotopic model of lung cancer was developed to represent clear delineation of tumour versus healthy lung parenchyma, allowing for their segmentation as was discussed in

Chapter 3. Moreover, segmentations of the heart, liver, spleen, left kidney, brain and skeleton were performed for each animal to understand the *in vivo* distribution in those organs. The segmentations provided quantitative measurements of activity and the imaging was longitudinal for up to 7 days. *Ex vivo* measurements of the organs as well as autoradiography and histology were conducted to verify the imaging findings.

5.2 Materials and Methods

Thirty one female mice with severe combined immunodeficiency (NOD-SCID Gamma, strain NOD.CB17-Prkdc^{scid}/NCrCrl; Charles River, UK), aged 6-8 weeks and weighing 20-24 g, were used in total. Procedures were carried out under the authority of project and personal licences issued by the Home Office, UK, and were approved by local Animal Welfare and Ethical Review Bodies at University College London. Out of the 31 female mice, 24 were injected with the MSTO-211H cell line to produce an orthotopic model of lung cancer. The cancer cell implantation was conducted as explained in section 3.2.2 for the intralobular injection in the right lung parenchyma (Study - 4). Briefly, a small patch of fur was shaved over the right hand side of the rib cage. Under isoflurane anaesthesia (2% - 2.5% isoflurane in oxygen 1 L/min), 1 x 10^5 MSTO-211H cells (previously transduced to express firefly luciferase [31]) were injected into the right intralobular space, in 20 µL of DPBS (Gibco™). Out of the 31 female mice, 7 control mice had their right pleura area shaved but no injection of cancer cells was conducted.

5.2.1 Bioluminescence Imaging

Tumour growth was initially followed by BLI for 15 days, to validate successful cancer cell implantation. The acquisition and analysis method was conducted as explained in section 3.2.3.1. Briefly, mice were anaesthetised with isofluorane and kept at 37 °C. Mice were injected intraperitoneally with 150 mg/kg of D-Luciferin solution, and

imaged at 10 min post-injection. The automatic acquisition setting was chosen to ensure exposure times were optimised and sufficient signal was obtained without saturation. The acquisition times were between 1 to 2 min. The light output was quantified using ROI analysis as Total Flux in photons/second (p/s) and corrected for background signal.

5.2.2 Micro-CT imaging

Baseline breathing gated micro-CT scans were acquired before any procedures took place, using the Quantum GX2 micro-CT Imaging System (PerkinElmer). Further weekly micro-CT imaging acquisitions were acquired at 1 month post cancer cell implantation up to the day before the injection of the radiolabelled MSCTRAIL cells, to assess tumour growth. All acquisitions were conducted as was explained in section 3.2.3.2. Lung tumour volume segmentation was conducted using the final micro-CT scans and the VivoQuant software (Version 2022 - Invicro). VOIs were manually drawn for the tumour area and then the connected thresholding algorithm was applied to segment the tumour from the lung parenchyma. The range applied was -100 to 500 HU for the tumour (including oedema) as explained in section 3.2.3.3. The time difference between the micro-CT and the CT scans was between 1 and 6 days, due to the micro-CT acquisitions conducted the day before the intravenous injections of the radiolabelled MSCTRAIL cells, while PET/CT imaging was conducted for different time points.

5.2.3 Stem cell radiolabelling and injection

The radiolabelling method was explained in section 2.2.3. Briefly, the MSCTRAIL cells were defrosted in a water bath at 37 °C and mixed with MEM a, GlutaMAX™ Supplement, no nucleosides (Gibco™) with 10% FBS (Gibco™), in a 1:1 ratio (cells to media). Then the cells were washed twice with DPBS (Gibco™) and counted by mixing a 10 µL aliquot of cell suspension with 10 µL of Trypan Blue, which was then pipetted onto a haemocytometer and viewed on an inverted microscope. The cells were then

resuspended in DPBS for radiolabelling. The [^{89}Zr]Zr-oxine, prepared by utilising the kit formulation, was added to the cells. The cells were left for 20 min behind shielding, gently swirling every 5 min. Finally, the cells were washed, first, with MEM a GlutaMAX™ Supplement, no nucleosides with 10% FBS and then twice with DPBS. The complete radiolabelling process was conducted in a Class II Microbiological Safety Cabinet using aseptic tissue culture procedures. Five separate radiolabelling batches were conducted in total for mouse injections, 3 for the tumour bearing cohort and 2 for the controls. The final radiolabelling activities for the injections ranged from 167 to 331 kBq/million cells.

The mice were injected intravenously, under isofluorane anaesthesia (1.5% - 2.0% isoflurane in oxygen 1 L/min), with 1 x 10^6 [^{89}Zr]Zr-oxine radiolabelled MSCTRAIL cells in 200 µL DPBS. The activities at the time of injection were calculated by measuring the syringe before and after injection, using a CRC-55tR calibrator and the values ranged from 150 to 300 kBq.

To reduce the risk of embolism, a different syringe was used for each mouse and the radiolabelled cell suspension was mixed well, using a pipette, before each injection. The volume of injection was chosen as the maximum volume allowed for intravenous injection (10 mL/kg, approximating 200 µL) and the administration was done very slowly, with constant monitoring of the animal's breathing. Once injected, the mice were put in a heated recovery chamber and were monitored closely until righting reflex had returned. In the event that mice exhibited significant evidence of embolism as identified on the PET images, then these mice would be excluded from the study, as emboli lead to significant uptake of radioactivity in the points of occlusion, thus affecting the biodistribution of cells throughout the whole body and therefore affecting the quantitative measurements of the different organs.

5.2.4 PET/CT imaging

The imaging time points for the tumour bearing and control mice after the i.v. injection of [^{89}Zr]Zr-oxine radiolabelled MSCTRAIL cells were Day 0 (1-2 h), 1, 2, 4, and 7. The scanner used was a PET/CT (nanoScan® PET/CT - PET122S/CT1512 - Mediso) system. PET was acquired as static, with breathing gating, for 40 min in 1 - 3 coincidence mode, and a whole body CT acquisition was conducted at 70 kVp with 90 ms exposure time (zigzag). The total acquisition time was chosen taking into consideration the high sensitivity of the NSG mice to anaesthesia, as well as the image quality. The PET data was reconstructed as both breathing gated and non-breathing gated that will be mentioned as breathing gated and static reconstructions respectively. The breathing gated acquisition method was explained in section 3.2.3.3.

Six mice from the tumour bearing cohort were scanned at two time points and the 7 mice of the control cohort were imaged at all time points, except from Day 0, that 5 of the control mice were imaged. Due to a fault in the breathing gating hardware, the breathing gated signal was not recorded correctly for 4 mice of the tumour bearing cohort, therefore the data could only be reconstructed as static. In 2 out of the 7 mice of the control cohort a significant uptake of radioactivity was identified as emboli within the heart, and thus these mice were excluded from the study. The final numbers of mice utilised in the analysis for each imaging time point and reconstruction method can be seen at the following table 5.1.

All PET data was reconstructed in 1 - 3 coincidence mode using the Tera-Tomo iterative algorithm (4 iterations, 6 subsets) in 0.4 mm isotropic voxels. The CT was reconstructed using the FBP reconstruction method, in 0.13 mm isotropic voxels.

Imaging time point	Static Reconstruction		Breathing Gated Reconstruction	
	Lung Cancer	Control	Lung cancer	Control
Day 0	5	3	4	3
Day 1	7	5	4	5
Day 2	6	5	6	5
Day 4	6	5	6	5
Day 7	6	5	6	5

Table 5.1: The numbers of mice for each imaging time point, for both static and breathing gated PET reconstructions.

The analysis was done using the VivoQuant software. VOIs were acquired for the left normal lung, tumour, heart, liver, spleen, left kidney, brain and skeleton. The VOIs for the normal lung and tumour were drawn as explained in section 3.2.3.3. Briefly, VOIs were drawn manually on the areas of interest based on the CT scan. Then the connected thresholding algorithm was applied to segment the parenchymal tumour and the whole left lung parenchyma, that was normal. The ranges applied were -100 to 500 HU for the tumour, including oedema, segmentation and -700 to -100 HU for the normal lung parenchyma segmentation. For the heart, liver, spleen, left kidney and brain segmentations, these were done manually based on the CT for each mouse. The right part of the heart was segmented, as that was the area of high uptake of radioactivity based on the PET images, while the other organs were segmented as whole. For the skeleton segmentations the connected thresholding algorithm was used with a range of 1000 to 7000 HU.

An example segmentation of all the organs can be seen at the following figure 5.1. The colours used are: left normal lung in dark blue, tumour in red, heart in orange, liver in yellow, spleen in light blue, left kidney in pink, brain in light green and skeleton in white.

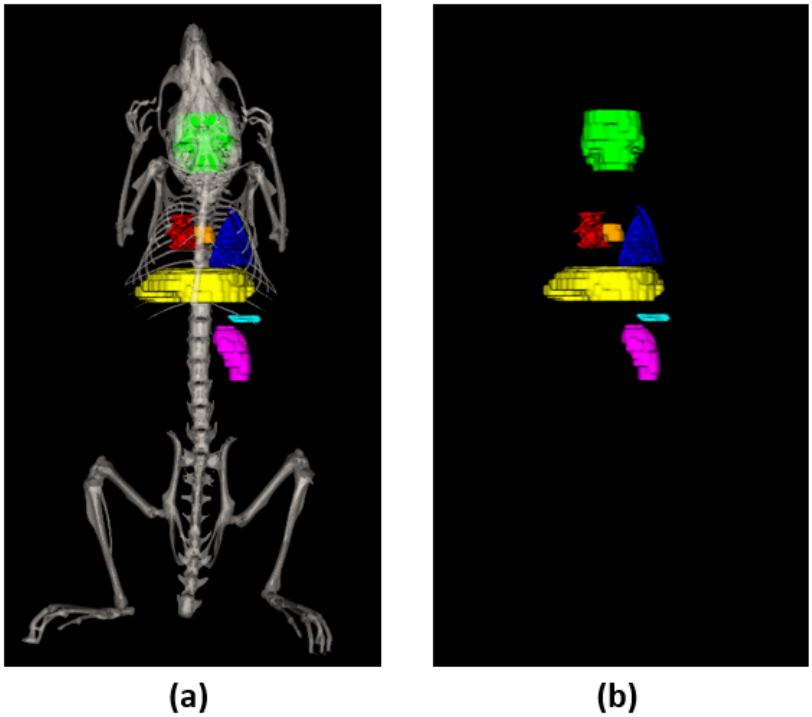

Figure 5.1: Organ Segmentations: (a) Segmentations of all the organs and the skeleton, (b) Segmentations of all the organs without the skeleton.

The measurements acquired from the VOI segmentations were calculated as the percentage of the injected activity, decay corrected to the time of each acquisition, per the volume of the VOI in mL (%IA/mL). It was assumed that the biological half-life was negligible, as no notable excretion of radioactivity was expected from the body by natural processes. According to literature the free ^{89}Zr and the activity lost from cells is accumulated in the liver, spleen and bone and is not excreted from the body [46].

For measurements acquired in lung PET/CT imaging, a correction needs to be applied for the TFE, as has been shown by Lambrou et al. [139] and Holman et al. [47] and it was discussed in section 1.9.6. According to Lambrou et al. and Holman et al, a lung voxel contains only 2 components, that are air and tissue. Tissue is considered to be the combination of lung parenchyma and blood. With this assumption, the HU of

a CT voxel can be considered according to the following equation:

$$HU_L = V_a \times HU_a + V_t \times HU_t \tag{5.1}$$

where HU_L, HU_a, and HU_t are the HU values of the CT lung, air, and tissue voxel respectively. V_a and V_t are the fractional air and tissue volumes in the voxel respectively and $V_a + V_t = 1$. This means that V_a can be calculated according to the following equation:

$$V_a = \frac{HU_L - HU_t}{HU_a - HU_t} \tag{5.2}$$

Then, the activity concentration can be corrected according to the following equation:

$$C_{AFC} = \frac{C_{measured}}{1 - V_a} \tag{5.3}$$

where $C_{measured}$ is the measured activity concentration and C_{AFC} is the activity concentration in the tissue after the application of Air Fraction Correction (AFC). With the application of AFC the voxel values represent only the tissue component [47], [139].

To calculate the V_a value, the HU_L, HU_a, and HU_t were measured using the VivoQuant software on the downsampled CT acquisition of each mouse. The CT was downsampled to 0.4 mm isotropic voxels using the nearest neighbour interpolation. For the HU_L value the normal left lung segmentation was used and for the HU_t the heart segmentation was used, for each mouse. For the HU_a value, the trachea of each mouse was segmented by manually drawing a VOI on the area of interest and then applying the connected thresholding algorithm with a range of -1000 to -600 HU. The HU_L, HU_a, and HU_t values utilised in the analysis were the average HU measurements of the respective segmentations for each mouse.

According to the preclinical phantom work conducted in Chapter 4 for the longitudinal *in vivo* imaging protocol, the average SOR value for the water chamber, for acquisitions 7 to 18 (activities between 300 to 30 kBq) was 0.09 (table 4.2). Given

that the lung tumour was surrounded by lung tissue, to apply a correction for the SOR of a hot area (lung tissue) to a cold area (tumour tissue) the following equation was used:

$$C_{SOC} = C_{measured} - SOR \times C_{AFC} \tag{5.4}$$

where $C_{measured}$ is the measured activity concentration in the tumour, SOR is 0.09 which is the average value calculated for acquisitions 7 to 18 in table 4.2, and C_{AFC} is the activity concentration in the lung tissue after the application of the AFC. C_{SOC} is the activity concentration in the tumour after the application of the spill over correction (SOC).

5.2.5 Cohorts for *ex-vivo* measurements

After their final imaging time point mice were culled by i.v. injection of 100 µL of pentobarbital (Pentoject® 200 mg/mL - Animalcare Limited), to conduct *ex-vivo* measurements. The number of tumour bearing mice culled at each time point were Day 0 (n = 5), Day 1 (n = 4), Day 2 (n = 5), Day 4 (n = 4), and Day 7 (n = 6). The total number of mice for the tumour bearing cohort was 24. The numbers of mice at each imaging time point are different from the numbers of mice used at each *ex-vivo* time point as 6 mice were scanned at two imaging time points and they were culled at the second imaging time point. For the control mice, 7 mice were utilised in total, with 2 being excluded from the study, due to emboli leading to significant uptake of radioactivity in the heart and thus affecting the distribution of cells throughout the whole body. All control mice were culled at the final imaging time point acquisition at Day 7.

5.2.6 *Ex-vivo* gamma counter measurements

Prior to gamma counting measurements, the lungs were inflated with either OCT (CellPath) with DPBS in 1:1 dilution or 10% formalin (Thermo Scientific Chemicals),

to later conduct either OCT or paraffin embedding respectively, as discussed in section 3.2.3.4. The tumour was not extracted from the lung sample, as the removal would deflate the lung, thus affecting the quality of the histology and the *ex-vivo* autoradiography imaging. Therefore, the *ex-vivo* gamma counter lung measurements were conducted as normal lung parenchyma with tumour and no comparison between normal lung parenchyma and tumour was done for these measurements. The heart was removed from the lung sample and it was measured separately. The liver, spleen, left kidney, brain and tibia (for bone measurement) were extracted as well. All organs were weighed using a precision scale (VWR®). Due to the lung inflation there was great variability between the weight of the lung samples, as the amount of inflation compound would be different for each mouse. To try to resolve this issue, 5 control lungs of a separate cohort of adult female NSG mice were extracted and weighed without inflation and the average weight was calculated. This average weight was then used as the lung weight of all lung samples for all calculations. All samples were measured in a Wizard 2480 automated gamma counter (PerkinElmer).

The measurements were acquired as counts and they were corrected for background. The acquisition time was 1 min for each sample. To convert the measurements in counts to activity, a standard curve was created, using known amounts of activity, that were measured in both the CRC-55tR calibrator and the gamma counter. The total activity in the mouse at the time of the *ex-vivo* measurements was calculated, by decay correcting the injected activity. As with the *in vivo* measurements, it was assumed that the biological half-life was negligible due to the fact that no significant excretion of radioactivity from the body was expected by natural processes. Finally, by knowing the weight of the samples, the %IA/g values were calculated for each sample.

5.2.7 Sample processing

The lung samples of both tumour bearing and control mice were kept for autoradiography and histology, as well as the hearts of the mice that showed distinct uptake of radioactivity on PET imaging. The lung samples inflated with the OCT/DPBS compound and the heart samples were embedded in OCT blocks and they were kept frozen at -20 °C. The lung samples inflated with 10% formalin were processed and embedded in paraffin blocks, as was explained in section 3.2.3.4.

For the OCT embedded samples, contiguous 10 µm frozen sections were cut using a cryostat (CM3050 S - Leica). Then the sections were collected on slides (Thermo Scientific™ - Superfrost®) and they were kept frozen at -20 °C. For the paraffin embedded samples, contiguous 5 µm sections were cut on a microtome (Microm HM 325). The sections were picked up with tweezers and transferred to the surface of a pre-warmed 37 °C water bath. Then the sections were collected at a 30° angle on slides (Epredia - Polysine) and they were stored at room temperature.

5.2.8 Autoradiography

For autoradiography, the lung and heart samples embedded in the OCT compound were utilised. To quantify the amount of radioactivity in the samples, serial dilutions of known activity were created. Filter paper and double sided tape were used to attach filter paper circles onto a microscope slide, and the known amounts of radioactivity were added on the circles using a pipette. The range of activities was from 10 to 0.2 kBq, which was based on the highest possible activity within the sample, to the lowest that could be achieved by pipetting a volume of 1 µL. The slides with the samples and the slide with the serial dilutions were put in an autoradiography cassette containing a phosphor screen (GE Healthcare). The cassette was left in a shielded - low environmental background area for 4 days. Then the samples were taken out of the cassette and the phosphor screen

was imaged using a Typhoon™ FLA 7000 Biomolecular Imager (GE Healthcare) system. A 650 nm excitation laser beam was used, the acquisition time was 4 min and the image resolution was 25 µm.

The analysis was done using the Fiji software [105]. Background ROI measurements were acquired (n = 3) and the average value was used to correct all measurements. A standard curve was created using the known activities and the measurements acquired for each filter paper circle. All measurements were acquired as Mean Grey Values (MGV) per area, in cm^2, and they were converted to kBq/cm^2 using the standard curve.

For the tumour bearing cohort, measurements of normal lung parenchyma (n = 3) and tumour (n = 3) were acquired for each time point. For the control mice measurements of normal lung parenchyma (n = 3) and heart (n = 3) were acquired for the final time point (Day 7).

5.2.9 Histology

The histology of the lung samples was conducted with two aims. The first aim was the identification of the injected MSCTRAIL cells and the second was the identification of emboli. The reason behind identifying the distribution of the MSCTRAIL cells *ex vivo* was for the validation of the *in vivo* imaging findings, for the confirmation of presence or absence of MSCTRAIL cells within lung parenchyma and tumour. The reason for the need of identification of emboli was that for 5/6 patients that took part in the TACTICAL clinical trial occlusions were identified in their CT acquisitions. The groups for both aims, for the lung samples, were tumour bearing and control mice that MSCTRAIL cells were administered, as well as tumour bearing control mice that no MSCTRAIL cells were injected. Histology for the identification of emboli was also conducted to the heart samples of the 2 mice, that occlusions were identified in their hearts using PET/CT. The Immunofluorescence (IF) staining method was employed for both aims, using different antibodies.

For the identification of MSCTRAIL cells in lung samples, TRAIL was used as the cell marker to identify the MSCTRAIL cells. As human cancer cells (MSTO-211H) were utilised for the lung cancer mouse model development, TRAIL was chosen as a cell marker to distinguish between MSCs and cancer cells. The antibodies that were utilised were the following:

- Primary antibodies: Rat MoAb to Integrin aIIb (BD Pharmingen 553847 clone MWReg30) in 1/100 dilution and Anti-TRAIL antibody - Rabbit Polyclonal TRAIL antibody (ab2056 - Abcam) in 1/100 dilution.
- Secondary antibodies: Alexa Fluor™ 488 donkey antirat IgG and Alexa Fluor™ 555 Donkey antirabbit IgG (Thermo Fisher Scientific). The order of the secondary antibodies is respective of the primary.

For the identification of embolism, in lung and heart samples, the antibodies that were utilised were the following:

- Primary antibodies: Rat MoAb to Integrin aIIb (BD Pharmingen 553847 clone MWReg30) in 1/100 dilution, Rabbit PoAb to Fibrin (ab34269 - Abcam) in 1/300 dilution and CD31/PECAM-1 (AF3628 - Bio-Techne) in 1/100 dilution.
- Secondary antibodies: Alexa Fluor™ 488 donkey antirat IgG, Alexa Fluor™ 555 Donkey antirabbit IgG and Alexa Fluor™ plus 647 Donkey anti-goat IgG (Thermo Fisher Scientific). The order of the secondary antibodies is respective of the primary.

The IF staining process was conducted under the same conditions for all samples and it was the following:

1. For the paraffin embedded samples the sections were washed 3 times, for 5 min each, in xylene (Thermo Scientific Chemicals). Then they were washed 3 times, for 5 min each, in absolute ethanol (Thermo Scientific Chemicals) and finally, they were rinsed in tap water. For the OCT embedded samples, the sections were fixed in 10% formalin (Thermo Scientific Chemicals) for 15 min.

2. The solution PBS (Gibco™) 0.05% Tween20 (Thermo Scientific™) was prepared and it will be called as PBS.T.
3. The sections were rinsed for 10 min in PBS.
4. The sections were incubated for 15 min in PBS.T 0.5% TritonX100 (Thermo Scientific™) and then washed for 5 min in PBS.T.
5. A hydrophobic pen (ImmEdge® Hydrophobic Barrier PAP Pen - Bio-Techne) was used to circle the section and delineate the incubation area.
6. The sections were incubated in PBS.T 5% Bovine Serum Albumin (BSA) (Thermo Scientific™) for 30 min in a moist chamber at room temperature, to block non-specific binding sites. The moist chamber was positioned on a wave rocker (Stuart) for the whole incubation period.
7. The primary antibodies were diluted in PBS.T 1% BSA and the solution was centrifuged for 5 min at 16000 g, to remove aggregates.
8. The blocking reagent was removed, and the sections were incubated with the primary antibodies in a moist chamber in the refrigerator (4 °C) overnight. The moist chamber was positioned on a wave rocker for the whole incubation period.
9. The sections were washed 3 times for 5 min each in PBS.T.
10. The secondary antibodies were diluted in PBS.T 1% BSA and the solution was centrifuged for 5 min at 16000 g, to remove aggregates. The dilution of all the secondary antibodies was 1/1000.
11. The sections were incubated with the secondary antibodies for 1 h at room temperature in a moist chamber, in the dark. The moist chamber was positioned on a wave rocker for the whole incubation period.
12. The sections were washed 3 times for 5 min each in PBS.T.
13. The sections were incubated for 5 min in DAPI (nucleus staining, D3571 - Invitrogen™) diluted in PBS.T (1/1000 dilution), and then washed for 5 min in PBS.

14. The excess amount of liquid was removed and 50 µL of ProLong™ Gold Antifade Mountant (Invitrogen™) was added using a pipette. The cover slip (Menzel-Gläser, 22x50 mm, thickness No. 1.5) was carefully added on the section, to avoid excessive air bubbles.
15. The mounting medium was left to polymerize overnight at room temperature in the dark.
16. The cover slip was sealed on the edges using clear nail polish.
17. The slides were kept at 4 °C for preservation before imaging.

Imaging was conducted using a Zeiss Fluorescence Microscope (Axiovert 5 - Carl Zeiss). The imaging acquisition settings utilised were the default settings set by the microscope manufacturer for the Alexa Fluor™ antibodies and the DAPI nucleus staining. The acquisition details can be seen at the following table 5.2. For the paraffin embedded samples of tumour bearing mice with (n = 4) and without (n = 4) the administration of MSCTRAIL cells, the number of occluded vessels were counted.

Dye	Excitation (nm)	Emission (nm)
AlexaFluor™ 488	499	520
AlexaFluor™ 555	553	568
AlexaFluor™ 647	653	668
DAPI	358	463

Table 5.2: The excitation and emission wavelengths for the dyes utilised for the staining of the samples

5.2.10 Statistical analysis

Statistical analysis was performed with GraphPad Prism version 8.0. Data are presented as mean ± standard deviation (SD). Paired samples two-tailed t test was conducted for the micro-CT - CT comparison. Two-way ANOVA with Tukey's multiple comparisons was conducted for the same organ comparisons between static and breathing gated reconstructions and between tumour bearing and control cohorts. Two-way ANOVA

with Dunnett's multiple comparisons test versus the left normal lung was conducted for the longitudinal *in vivo* comparisons of the different organs. After the application of corrections the comparisons of the organs were versus the AFC lung values, except for the comparison between tumour values before and after SOC, that the test was versus tumour. Dunnett's multiple comparisons test versus the whole lung (including tumour) was conducted for the longitudinal *ex vivo* gamma counter measurements. Unpaired samples two-tailed t test was conducted for the rest of the experiments. Statistical significance was identified for *p $\leq$ 0.05, **p $\leq$ 0.01, ***p $\leq$ 0.001.

5.3 Results

5.3.1 Bioluminescent Imaging

BLI was conducted to ensure the successful cancer cell implantation in the thoracic cage after injection. The mice were imaged from 1 day up to 15 days after implantation, and the average total flux value (p/s), corrected for background, increased from 1.45 x 10^6 $\pm$ 0.96 x 10^6 to 1.90 x 10^7 $\pm$ 0.64 x 10^7, confirming cancer cell growth as previously seen in Chapter 3.

5.3.2 Comparison of micro-CT and CT imaging tumour identification

Breathing gated micro-CT imaging was conducted to assess the tumour localisation and volume ahead of the injection of the radiolabelled MSCTRAIL cells, and to aid the identification of the tumours on the CT images. The range of values for the tumour segmentations were from 6.5 to 56.3 mm^3 for the micro-CT and from 5.0 to 53.9 mm^3 for the CT. The maximum absolute difference between the micro-CT and the CT segmentation volumes was 5.2 mm^3 and the results of the micro-CT and CT analysis can

be seen in the following figure 5.2. Two-tailed paired samples t-test showed no significant difference between the micro-CT and CT tumour volume measurements (p = 0.09).

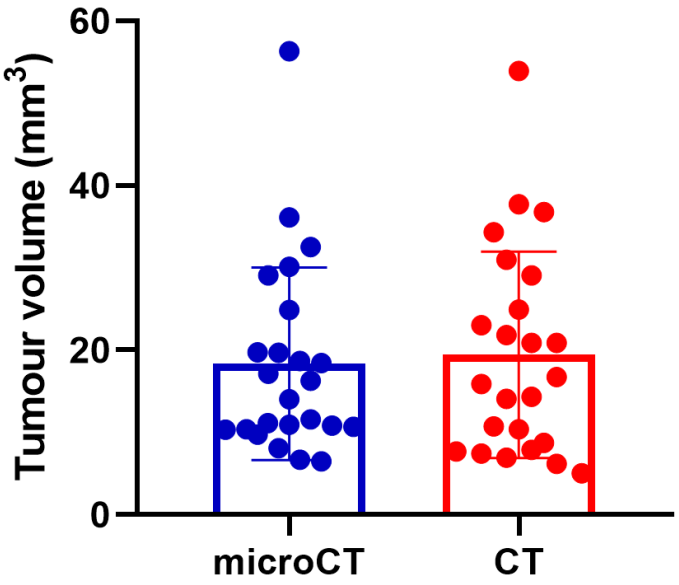

Figure 5.2: Tumour volume segmentations, in mm^3, for the micro-CT and CT data, for all the animals of the tumour bearing cohort (n = 24). The individual values can be seen alongside the mean (box) and SD.

5.3.3 PET/CT imaging

Longitudinal PET/CT imaging was conducted to assess the distribution of the radiolabelled MSCTRAIL cells *in vivo*. In figure 5.3 the whole-body distribution of [^{89}Zr]Zr-oxine radiolabelled MSCTRAIL cells, followed up to 7 days post-injection, can be visualised for the tumour bearing cohort and in figure 5.4 for the control cohort. Figure 5.5 shows a control mouse that was found to have an embolism within the heart, as indicated by high signal, which affected the overall distribution of the ^{89}Zr-MSCTRAIL cells and thus excluded the mouse from the study.

For the tumour bearing cohort, the longitudinal distribution of radioactivity that can be seen in figure 5.3, shows that the vast majority of radioactivity is within the lung for Day 0, while after Day 0 the signal in the liver, spleen and skeleton increase. The signal

in liver, spleen and bone is indicative of free ^{89}Zr uptake [46], as was discussed earlier in section 5.2.4.

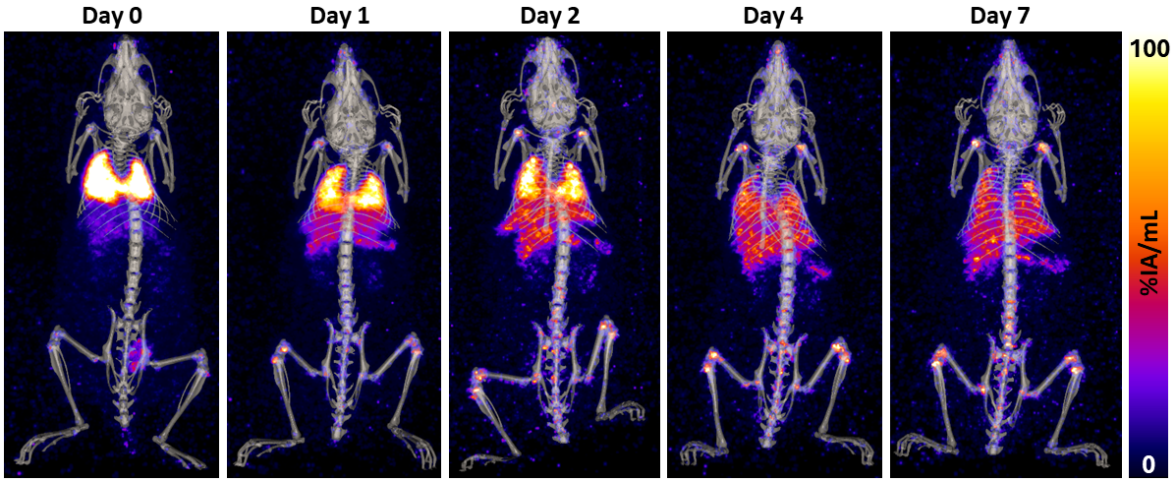

Figure 5.3: Maximum intensity-projection PET showing the ^{89}Zr signal, overlaid onto the skeleton segmentation, based on the CT, at days 0, 1, 2, 4 and 7 post intravenous injection, for the tumour bearing mice.

For the control cohort, the longitudinal distribution of radioactivity (figure 5.4) shows the same *in vivo* distribution as was seen in figure 5.3 for the tumour bearing cohort.

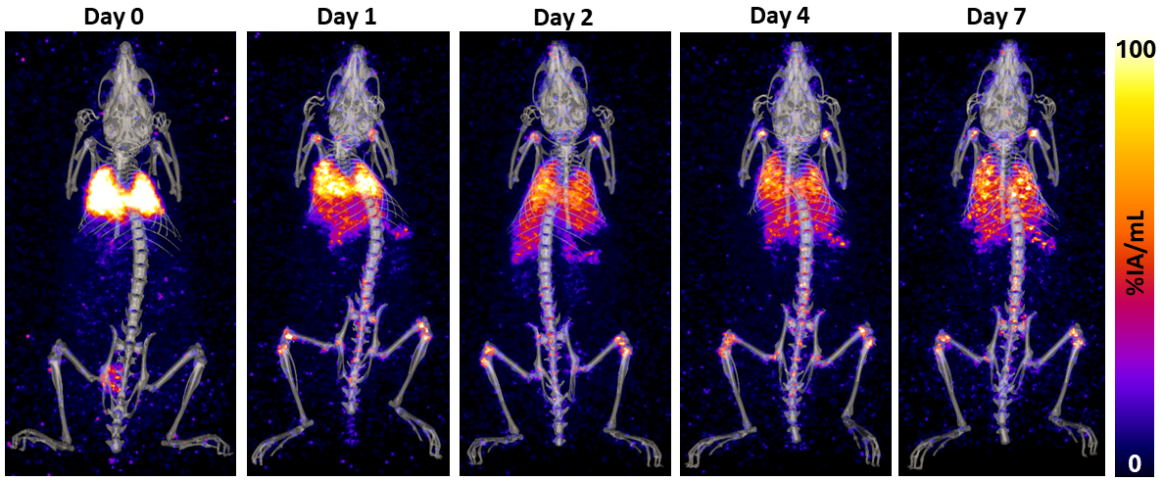

Figure 5.4: Maximum intensity-projection PET showing the ^{89}Zr signal, overlaid onto the skeleton segmentation, based on the CT, at days 0, 1, 2, 4 and 7 post intravenous injection, for the control mice.

For the control mouse that an embolism was identified within the heart (figure 5.5), the heart signal did not change throughout the 7 day period. However, the signal in the lung decreased from Day 1 to Day 2 until there was almost no visual identification in Day 7. The signal in the liver, spleen and bone increased after Day 0 as was identified before.

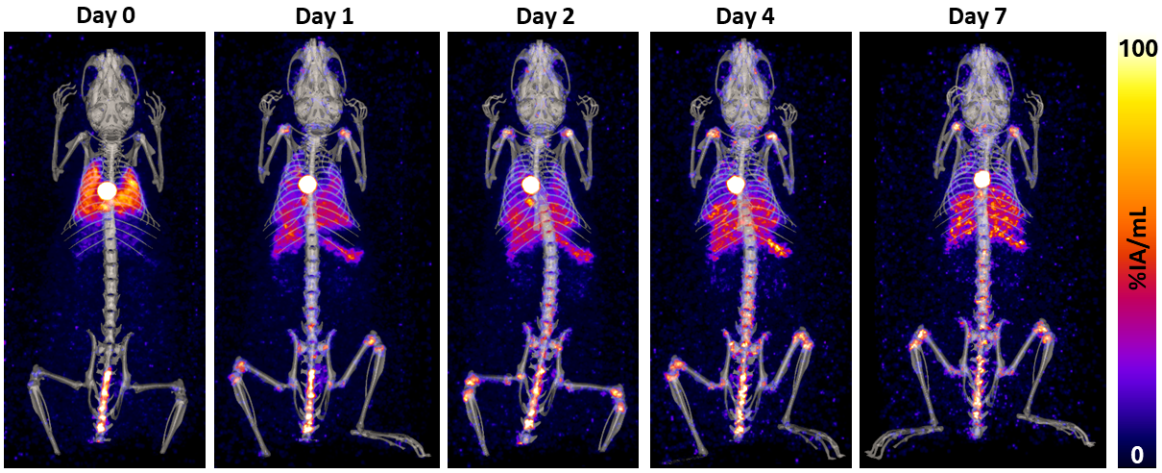

Figure 5.5: Maximum intensity-projection PET showing the ^{89}Zr signal, overlaid onto the skeleton segmentation, based on the CT, at days 0, 1, 2, 4 and 7 post intravenous injection, for a control mouse with significant uptake of radioactivity in the heart, that was excluded from the study.

Measurements were acquired, in %IA/mL, for the tumour, healthy left lung, liver, spleen, kidney, brain and skeleton in the tumour bearing cohort and for the same organs, except the tumour in the control cohort.

In figure 5.6 the results for the tumour bearing cohort can be visualised for static and breathing gated reconstructions. In figure 5.7 the results for the control cohort can be seen, again, for static and breathing gated reconstructions.

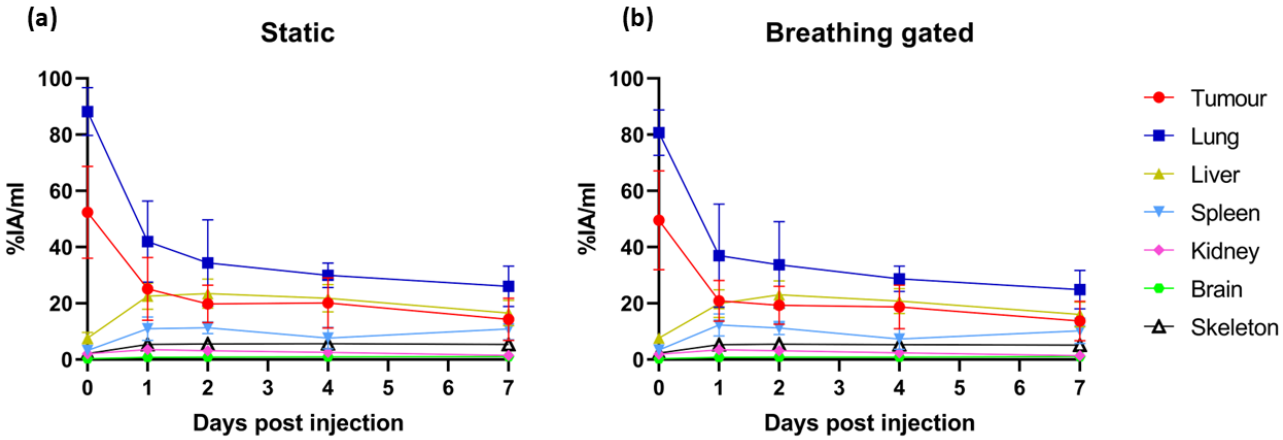

Figure 5.6: *In vivo* longitudinal results, in %IA/mL, plotted as mean ± SD for the different organs of the tumour bearing cohort. (a) Static reconstruction, (b) Breathing gated reconstruction.

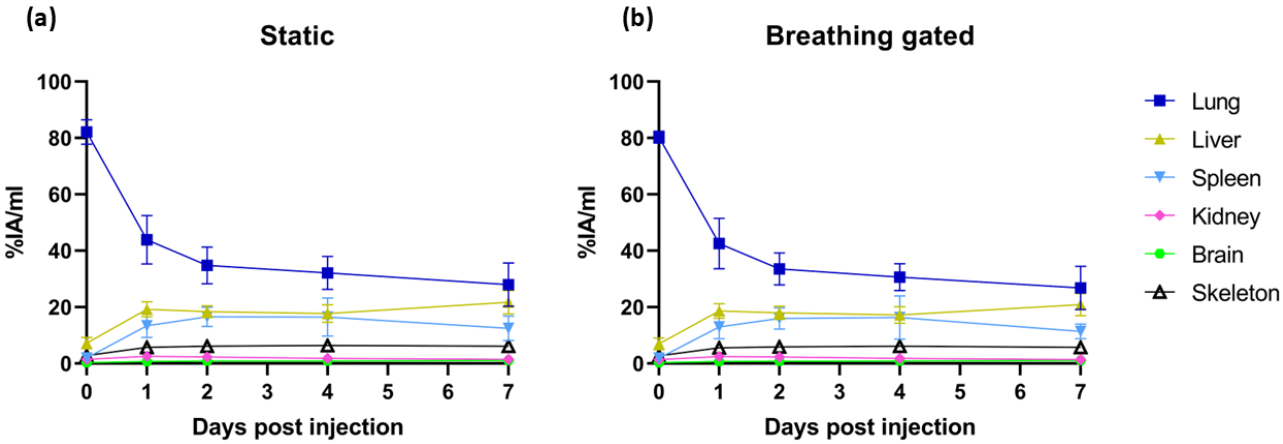

Figure 5.7: *In vivo* longitudinal results, in %IA/mL, plotted as mean ± SD for the different organs of the control cohort. (a) Static reconstruction, (b) Breathing gated reconstruction.

Two-way ANOVA showed a significant effect of time for all the tests conducted ($p < 0.001$). Multiple comparisons showed no differences between static and breathing gated results for the same organs and time points ($p > 0.05$), of both the tumour bearing and control cohorts. Furthermore, there was no difference between the same organs of tumour bearing and control mice, for any time points ($p > 0.05$).

For the tumour bearing cohort, multiple comparisons showed that the healthy left lung was significantly higher than all the other organs, except tumour and liver from Day 1 onwards, as can be seen in the following figure 5.8, for static reconstruction.

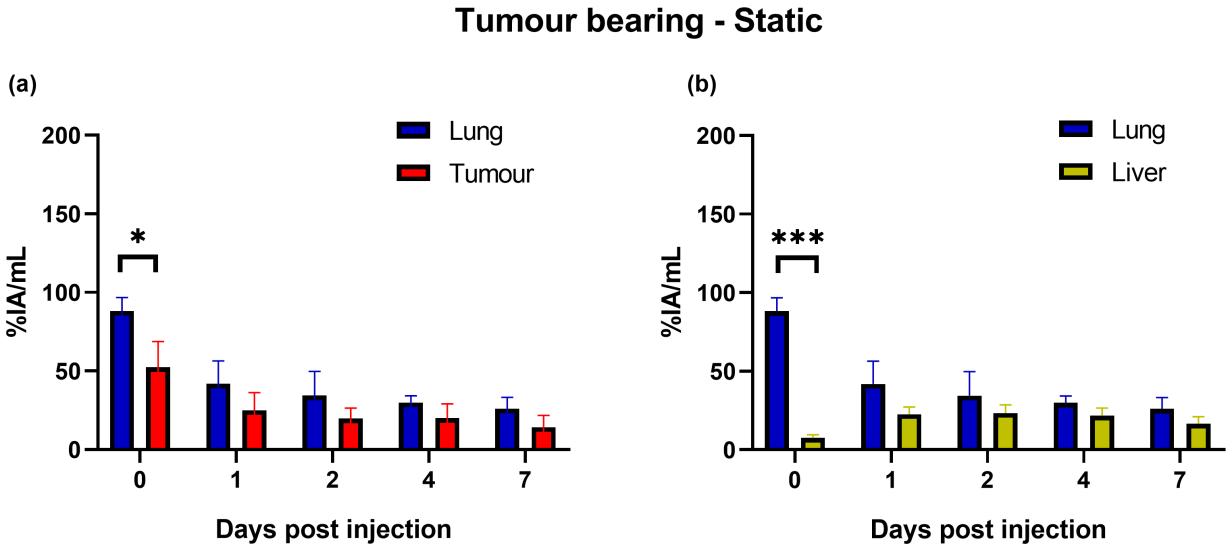

Figure 5.8: *In vivo* longitudinal results, in %IA/mL, plotted as mean ± SD for the static reconstruction of the tumour bearing cohort: (a) Lung and tumour measurements, (b) Lung and liver measurements.

For the control cohort the lung was significantly higher than all the other organs, except the liver for Day 7, as can be seen in the following figure 5.9, for static reconstruction.

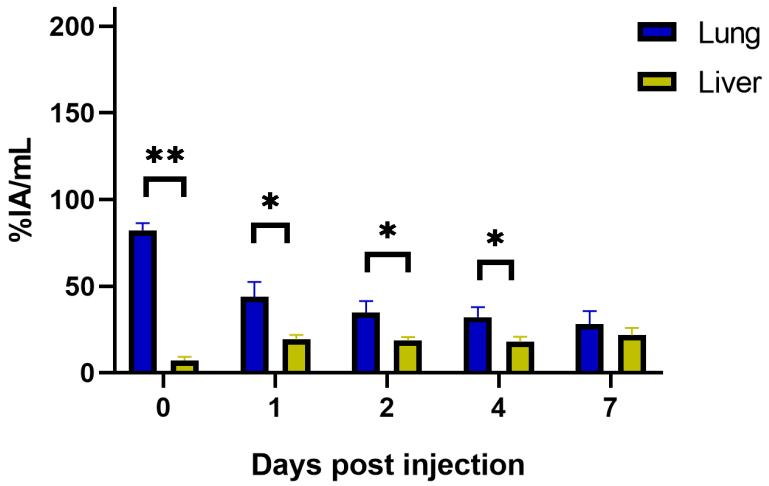

Figure 5.9: *In vivo* longitudinal results, in %IA/mL, plotted as mean ± SD for the static reconstruction of the control cohort: Lung and liver measurements

The values for the healthy left lung before and after the application of AFC can be seen at the following figure 5.10, for both static and breathing gated reconstructions as well as for both tumour bearing and control mice. The application of AFC increased the values in all cases, however not all differences were significant as indicated on the graphs of figure 5.10.

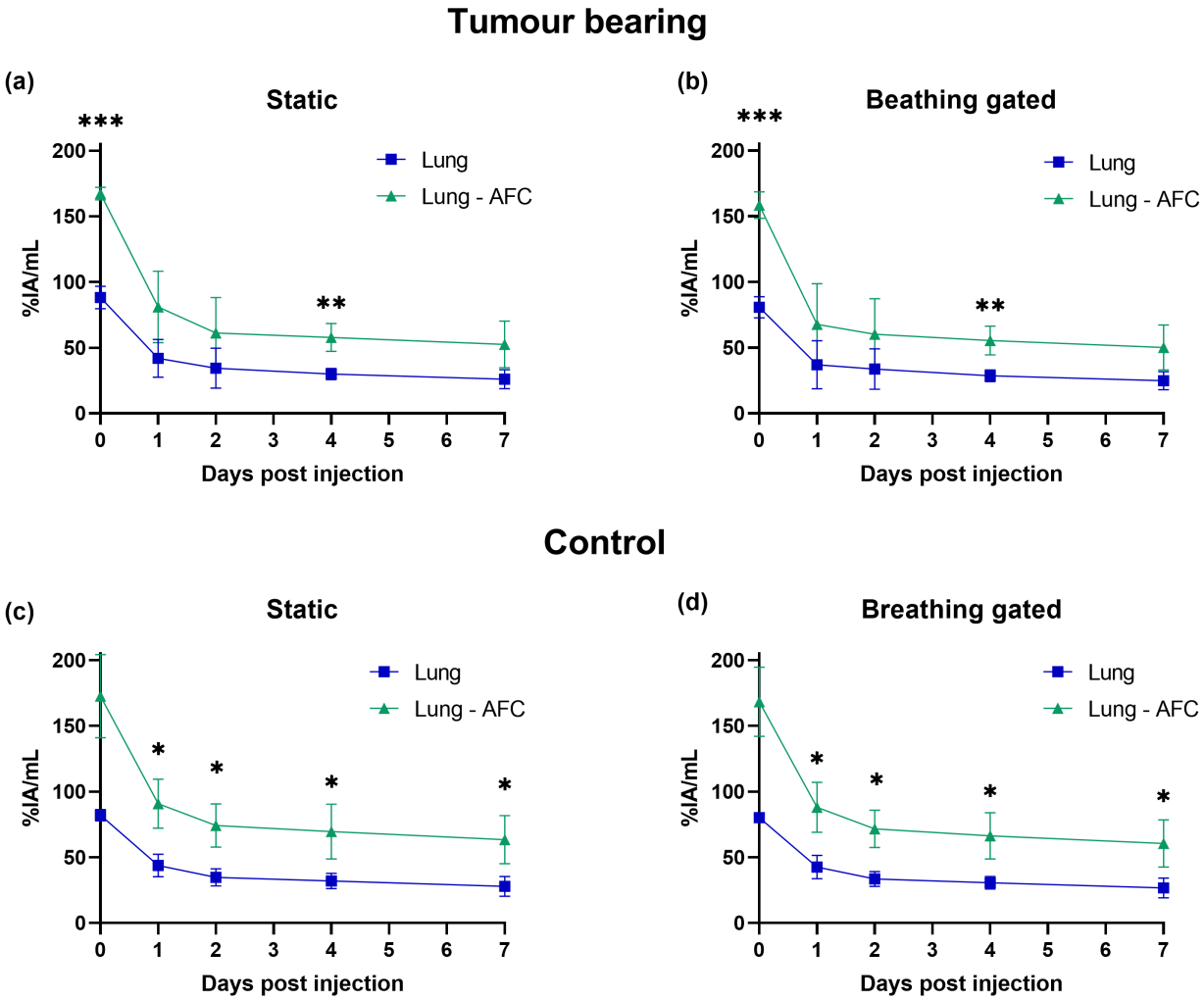

Figure 5.10: *In vivo* longitudinal results, in %IA/mL, plotted as mean ± SD, for the left lung before and after the application of AFC. Tumour bearing cohort: (a) Static reconstruction, (b) Breathing gated reconstruction. Control cohort: (c) Static reconstruction, (d) Breathing gated reconstruction.

In figure 5.11 the tumour values of the tumour bearing cohort can be seen before and after the application of spill over correction (SOC), for both static and breathing gated reconstructions. No differences were found between the values for all time points and reconstruction methods ($p > 0.05$).

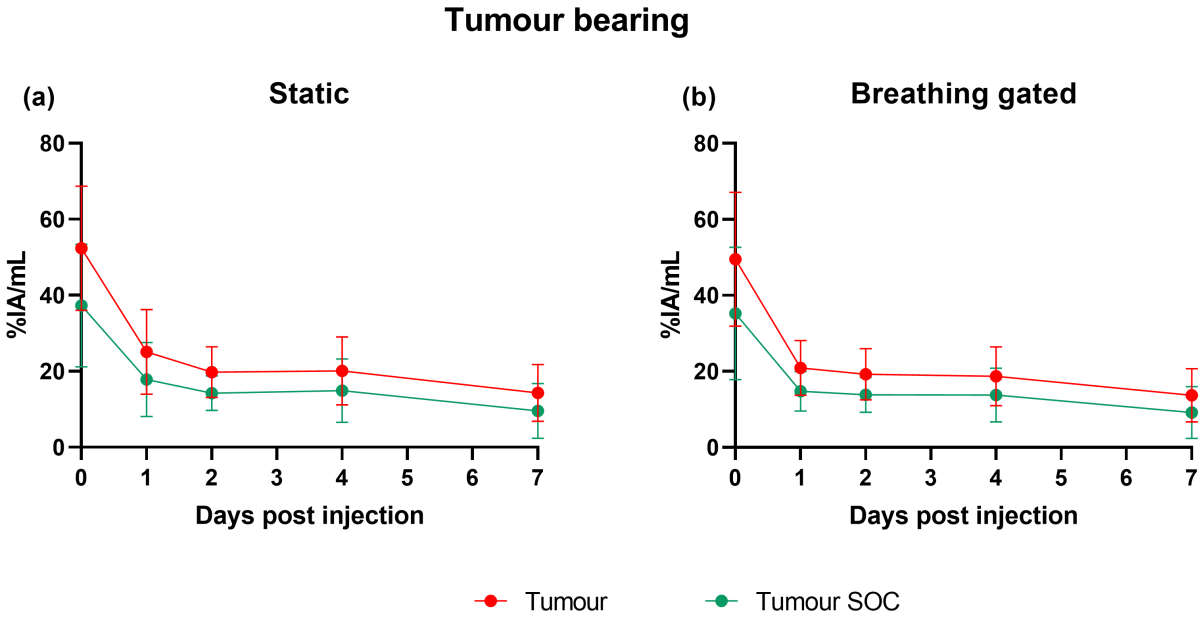

Figure 5.11: *In vivo* longitudinal results, in %IA/mL, plotted as mean ± SD for the tumour before and after the application of spill over correction (SOC). (a) Static reconstruction, (b) Breathing gated reconstruction.

After the application of AFC the difference between lung and all other organs was significant, for both control and tumour bearing mice. For the tumour bearing cohort, after the application of corrections the difference between lung and tumour was significant for all time points, as can be seen in figure 5.12 (a). Furthermore, the lung values after the application of AFC were significantly higher than the liver as can be seen in figure 5.12 (b).

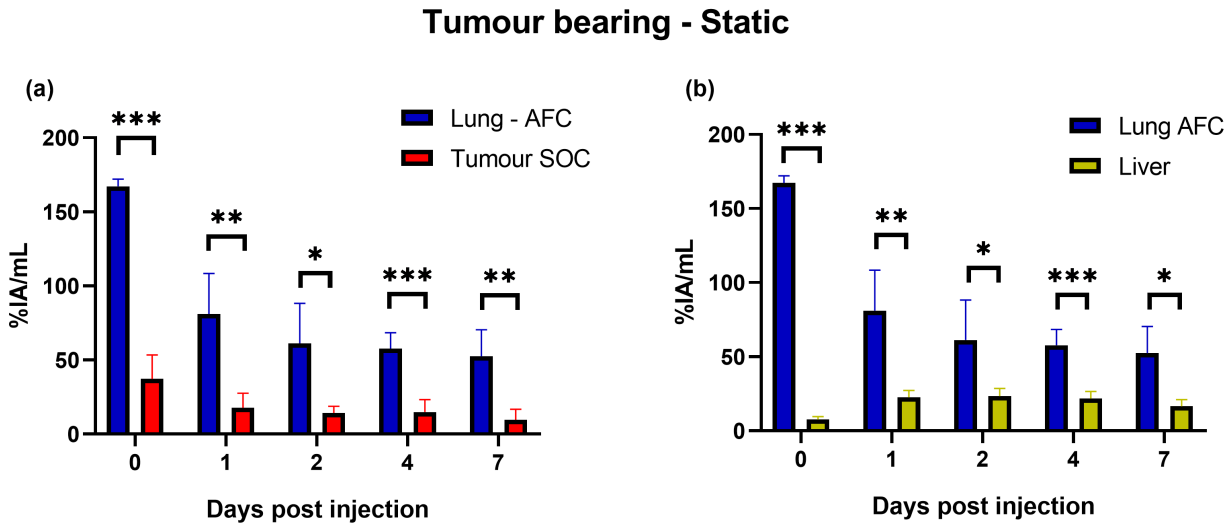

Figure 5.12: *In vivo* longitudinal results, in %IA/mL, plotted as mean ± SD for the static reconstruction of the tumour bearing cohort: (a) Lung and tumour measurements after the application of corrections, (b) Lung and liver measurements after the application of AFC to the lung.

For the control cohort, the lung values after the application of AFC were significantly higher than the liver for all time points as can be seen in the following figure 5.13.

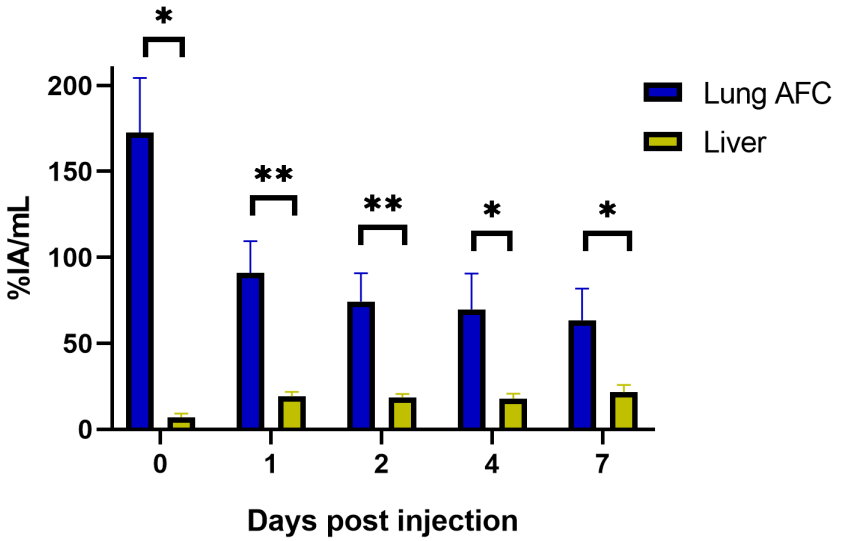

Figure 5.13: *In vivo* longitudinal results, in %IA/mL, plotted as mean ± SD for the static reconstruction of the control cohort: Lung and liver measurements after the application of AFC to the lung.

5.3.4 *Ex vivo* gamma counter measurements

The *ex vivo* gamma counter measurements were conducted for the same organs as the *in vivo* analysis. For the lung, the measurements were conducted for the whole organ, both right and left lungs, including tumour, as was explained in section 5.2.6. In figure 5.14 the %IA/g for the different organs, except the heart, can be seen for up to 7 days post ^{89}Zr-MSCTRAIL injection. The %IA/g value for the lungs with tumour decreases from Day 0 to Day 1, while it remains generally stable from Day 1 onwards.

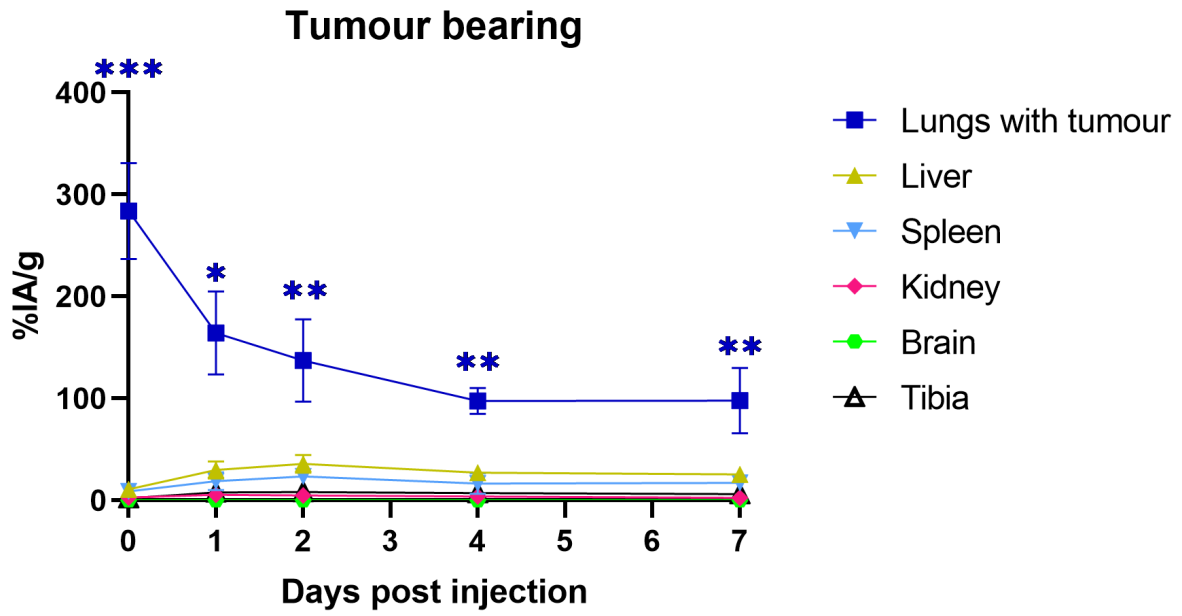

Figure 5.14: *Ex vivo* gamma counter measurements, in %IA/g, plotted as mean ± SD for the different organs of tumour bearing mice, up to 7 days post ^{89}Zr-MSCTRAIL injection.

Dunnett's multiple comparisons showed a significant difference between the lungs and all of the other organs for all time points. Day 0: $p \leq 0.001$, Day 1: $p \leq 0.05$, Day 2: $p \leq 0.01$, Day 4: $p \leq 0.01$ and Day 7: $p \leq 0.01$.

In figure 5.15, the %IA/g for the different organs, except the heart, of tumour bearing and control mice can be seen for day 7 post ^{89}Zr-MSCTRAIL injection.

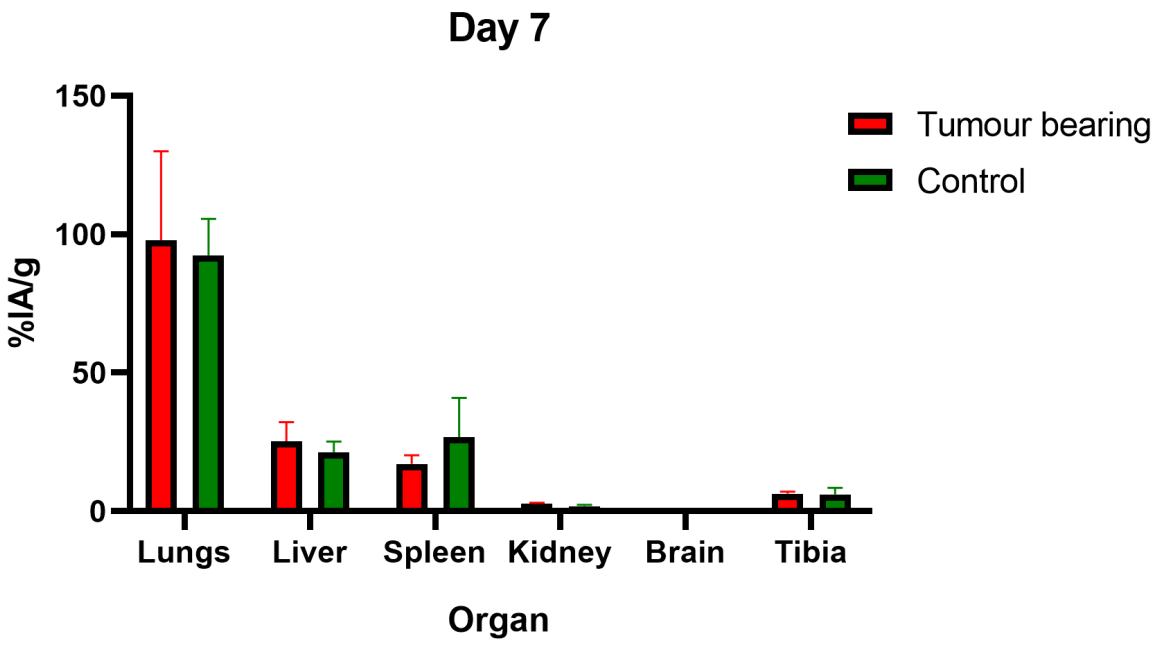

Figure 5.15: *Ex vivo* gamma counter measurements, in %IA/g, plotted as mean ± SD for the different organs of tumour bearing and control mice, at Day 7 post ^{89}Zr-MSCTRAIL injection.

For the comparison between tumour bearing and control mice no statistical difference was found for any organ (unpaired samples two-tailed t test, $p > 0.05$).

In figure 5.16, the %IA/g for the heart of tumour bearing and control mice, at day 7 post ^{89}Zr-MSCTRAIL injection can be seen. As validation for excluding the mice which exhibited high signal within the heart due to emboli, the heart values of the two control mice, when included in the grouping, can be clearly identified in figure 5.16 as the two highest values.

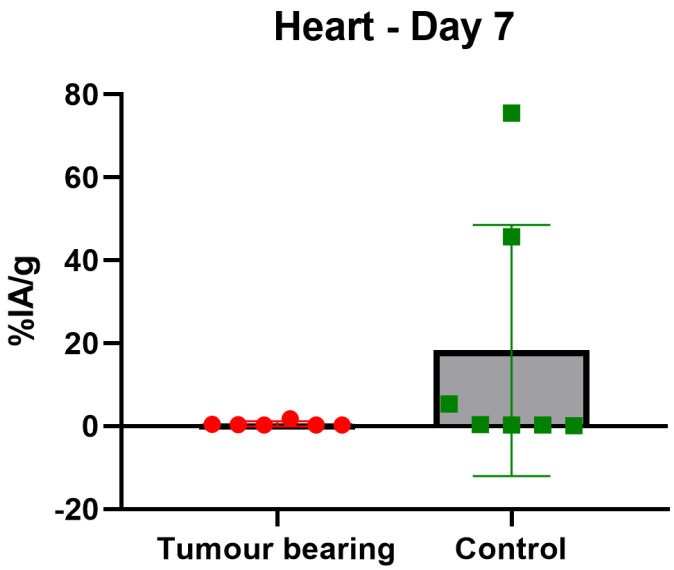

Figure 5.16: *Ex vivo* gamma counter measurements, in %IA/g, plotted as mean ± SD, for the heart of tumour bearing and control mice, at Day 7 post ^{89}Zr-MSCTRAIL injection, showing the 2 mice that were excluded from the study for having significant uptake of radioactivity in the heart.

5.3.5 Autoradiography

In figure 5.17, the autoradiography results for lung and tumour tissue of the tumour bearing cohort can be seen over time. At Day 7 the values for tumour were below the limit of detection, making the %IA/g value 0. In figure 5.18 a representative autoradiography image can be seen for the tumour bearing and the control cohort, as well as for the heart of a mouse that showed significant uptake of radioactivity in PET imaging.

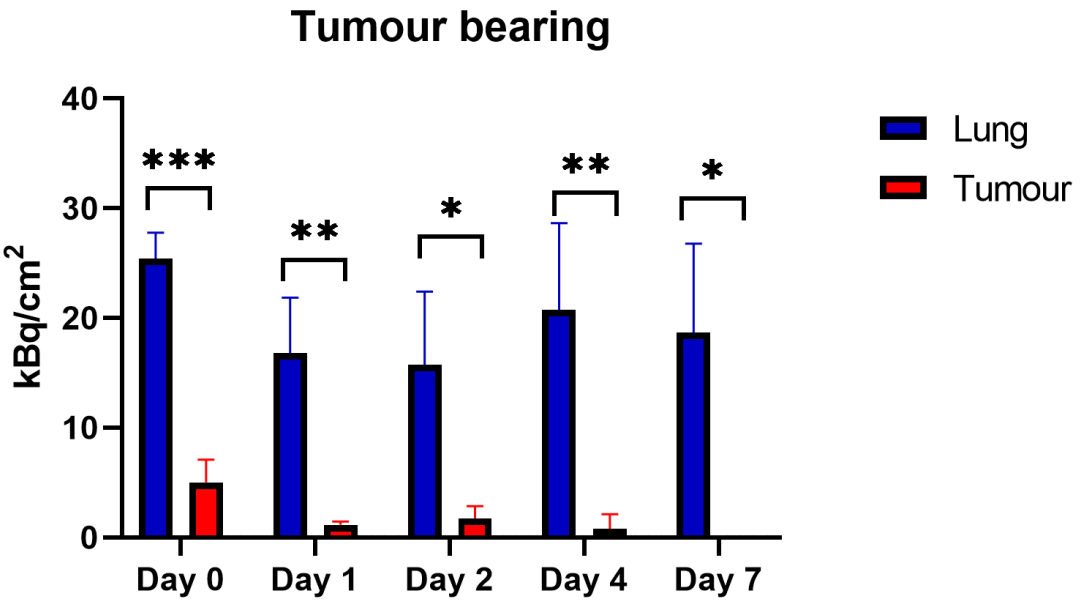

Figure 5.17: *Ex vivo* autoradiography values, in kBq/cm^2, plotted as mean ± SD, from Day 0 to Day 7 for normal lung and lung tumour of the tumour bearing cohort.

Ex vivo autoradiography showed significantly higher uptake of radioactivity in the lung compared to the tumour, for all time points (unpaired samples two-tailed t test). Day 0: p = 0.0004, Day 1: p = 0.0058, Day 2: p = 0.0237, Day 4: p = 0.0125 and Day 7: p = 0.0165.

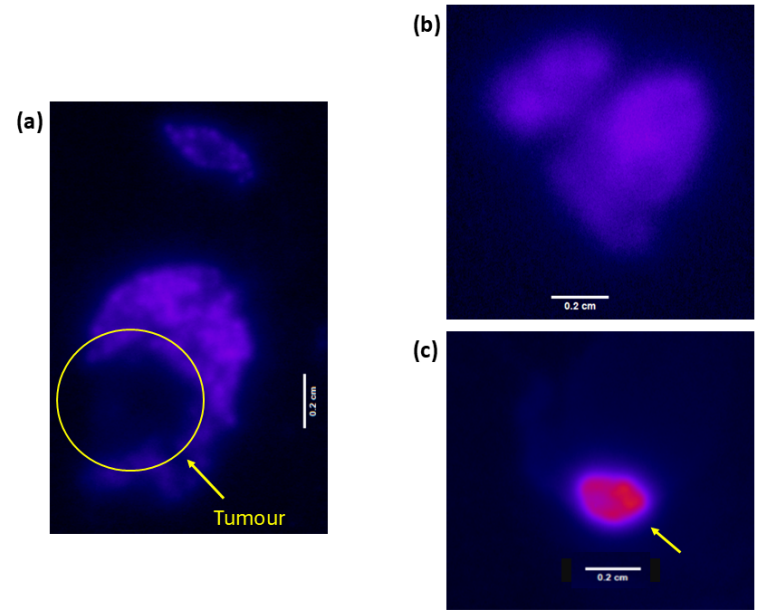

Figure 5.18: Autoradiography images: (a) Lung section of a tumour bearing mouse with the tumour area highlighted by a circle, (b) Lung section of a control mouse (c) Heart section of a control mouse, that was excluded from the study for significant uptake of radioactivity in the heart. The area of radioactivity uptake is highlighted by a yellow arrow. All sections were 10 µm.

For the control cohort autoradiography confirmed the uniform distribution of radioactivity in the lung. The activity distribution in the normal lung was 5.5 ± 2.7 kBq/cm^2 on average. In the case of the mice that *in vivo* PET imaging showed uptake in the heart, autoradiography confirmed the finding. The activity distribution for the heart was 3.1 ± 0.6 kBq/cm^2 on average.

5.3.6 Histology

IF staining was conducted for the identification of MSCTRAIL cells, in lung samples and for the identification of emboli, in lung and heart samples. For the stem cell identification staining, the results can be seen from figure 5.19 to figure 5.21. In figure 5.19 the lung sample of a tumour bearing mouse, that had been injected with MSCTRAIL cells can be seen. The area imaged is the upper lungs and trachea.

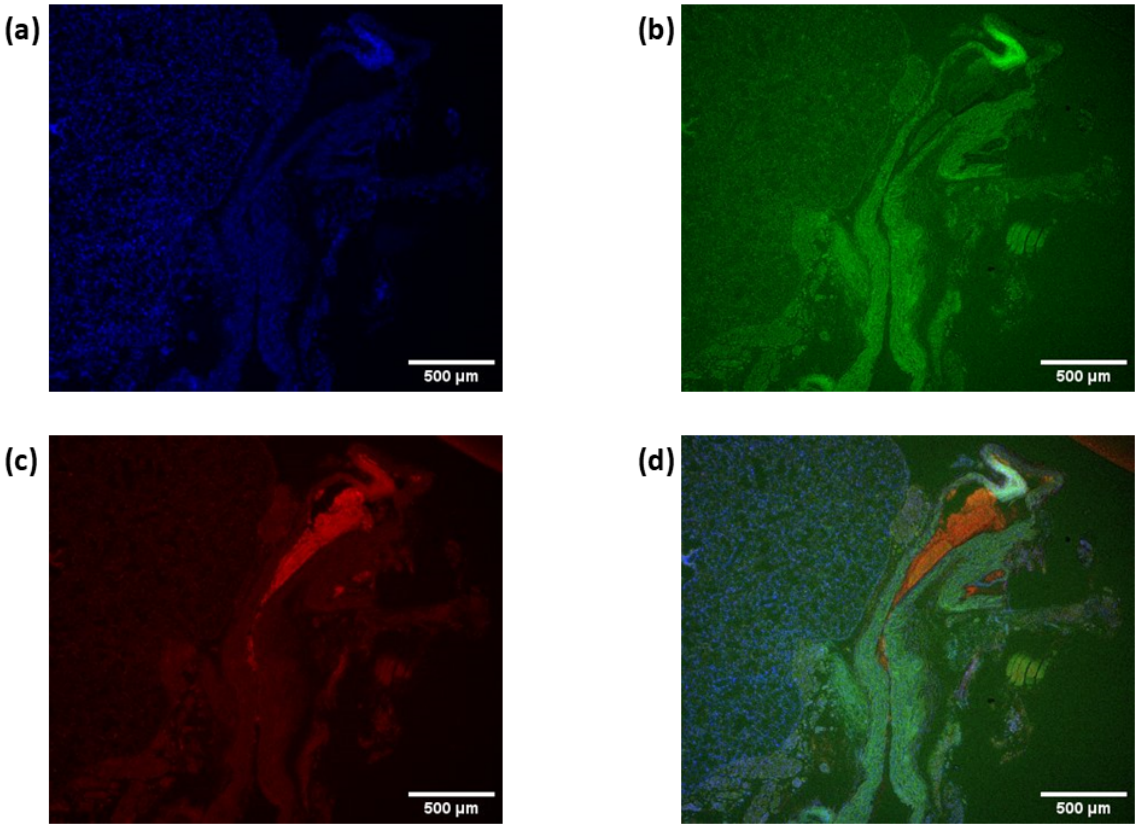

Figure 5.19: Fluorescence staining for the identification of MSCTRAIL cells in a tumour bearing mouse lung sample that MSCTRAIL cells were administered: (a) DAPI, (b) Platelets, (c) anti-TRAIL, (d) Composite.

In figure 5.20 the lung sample of a control mouse that had been injected with MSCTRAIL cells can be visualised. The area imaged is a lung vessel.

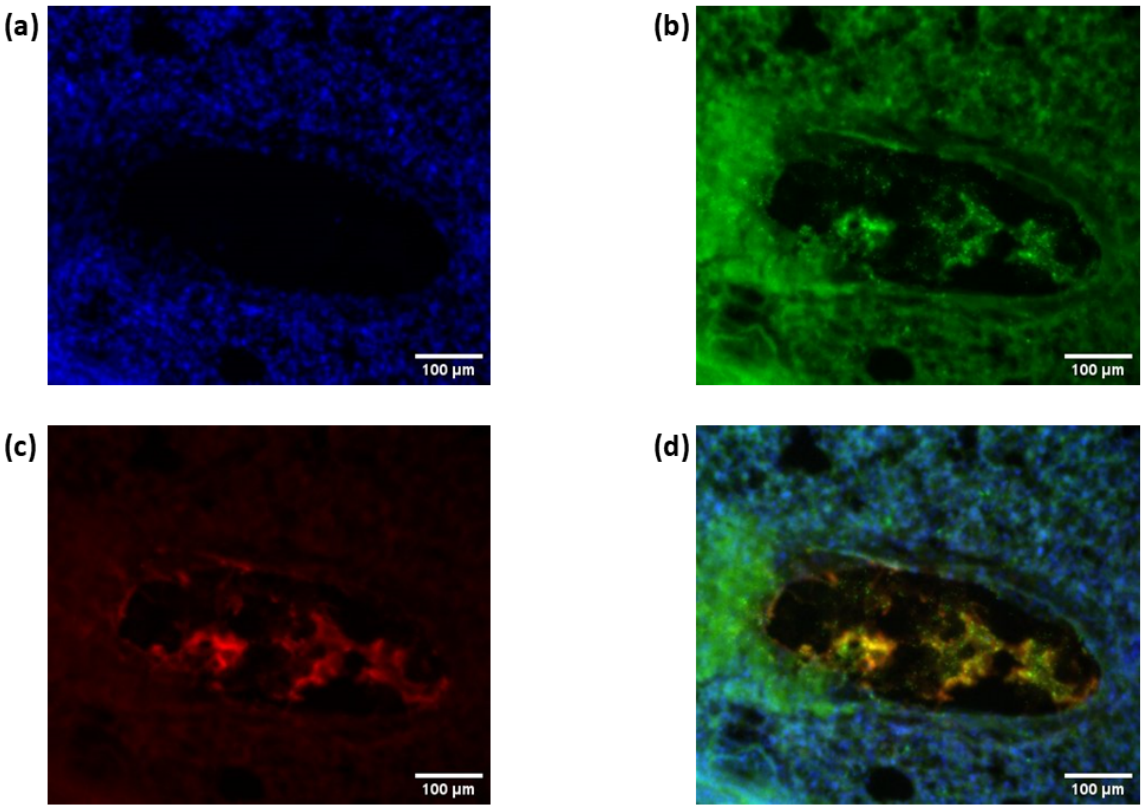

Figure 5.20: Fluorescence staining for the identification of MSCTRAIL cells in a control mouse lung sample that MSCTRAIL cells were administered: (a) DAPI, (b) Platelets, (c) anti-TRAIL, (d) Composite.

In figure 5.21 the lung sample of a tumour bearing control mouse that no MSCTRAIL cells were administered can be seen. The area imaged is lung parenchyma with tumour tissue that is highlighted by the yellow circle.

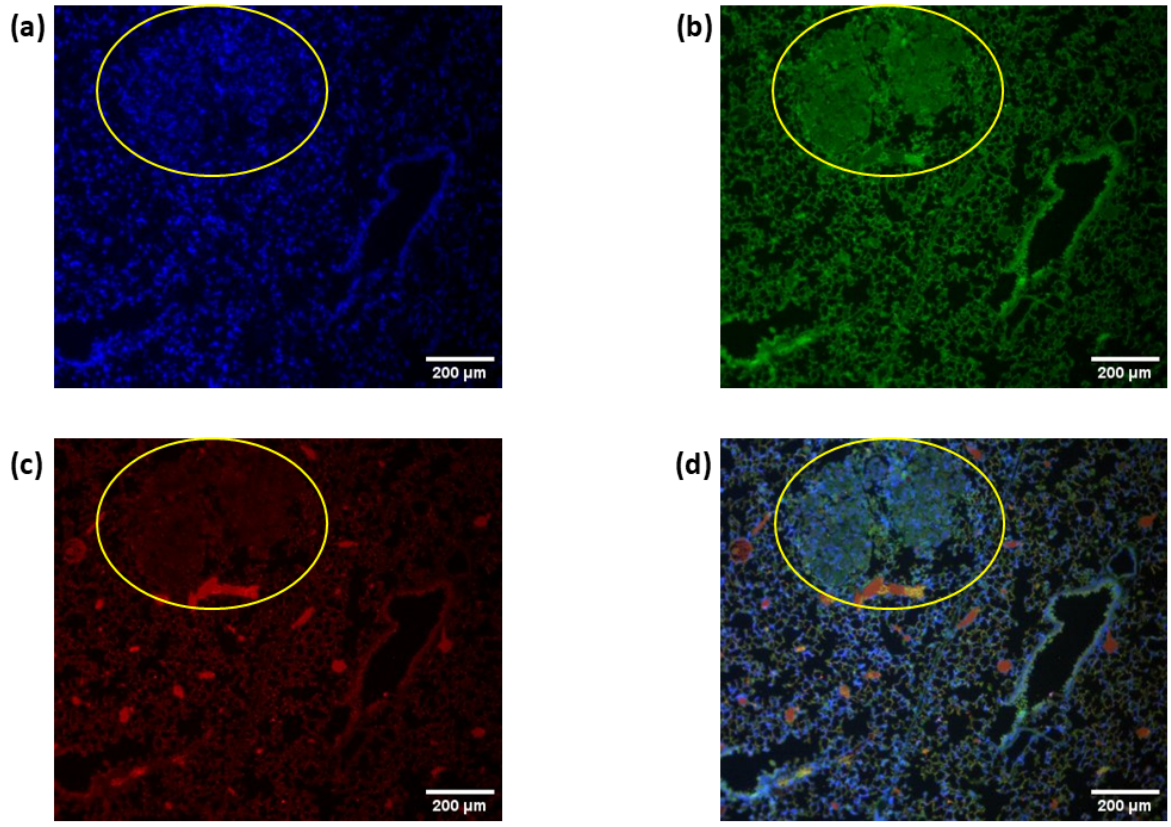

Figure 5.21: Fluorescence staining for the identification of MSCTRAIL cells in a tumour bearing control mouse lung sample, that no MSCTRAIL cells were administered. The tumour can be seen inside the yellow circle: (a) DAPI, (b) Platelets, (c) anti-TRAIL, (d) Composite.

In all three groups the anti-TRAIL antibody showed non-specific binding. Based on the fact that the lung samples were not perfused, the anti-TRAIL antibody showed preferential staining for the blood of the mouse. In figure 5.19 there was blood in the trachea, due to the cannulation process for the lung inflation and extraction, that can be clearly identified in figure 5.19 (c). In figures 5.20 (c) and 5.21 (c) the preferential staining of the blood in the lung vessels can again be clearly identified.

For the identification of occluded vessels in the lung samples the results can be seen from figure 5.22 to figure 5.24. In figure 5.22 the lung sample of a tumour bearing mouse, that had been injected with MSCTRAIL cells can be seen. The area imaged is a lung vessel that is positive for both platelets and fibrin staining, figure 5.24 (b) and (c) respectively.

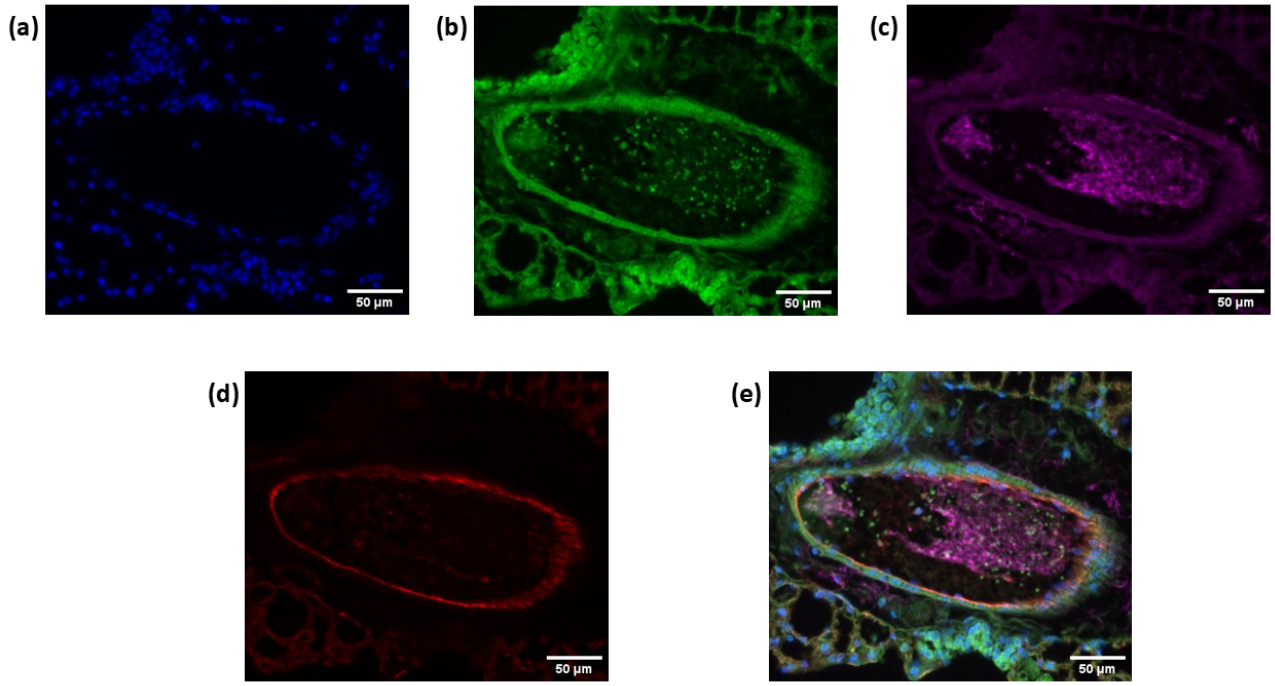

Figure 5.22: Fluorescence staining for the identification of embolism in a tumour bearing lung sample that MSCTRAIL cells were administered: (a) DAPI, (b) Platelets, (c) Fibrin, (d) CD31, (e) Composite.

In figure 5.23 the lung sample of a control mouse, which had been injected with MSCTRAIL cells can be seen. The area imaged are lung vessels and lung parenchyma. The vessels are positive for both platelets and fibrin staining, figure 5.23 (b) and (c) respectively.

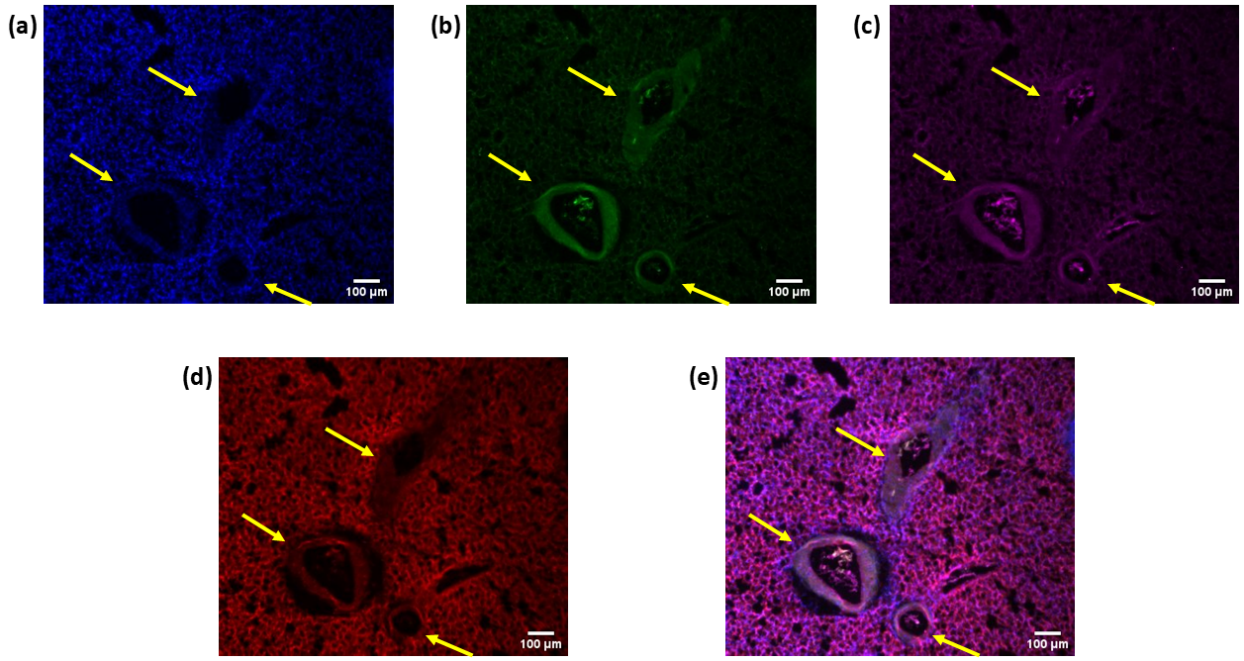

Figure 5.23: Fluorescence staining for the identification of embolism in a control lung sample that MSCTRAIL cells were administered: (a) DAPI, (b) Platelets, (c) Fibrin, (d) CD31, (e) Composite. The vessels are highlighted by yellow arrows.

In figure 5.24 the lung sample of a tumour bearing control mouse, that no MSCTRAIL cells were administered, can be visualised. The area imaged are lung vessels and lung parenchyma. The vessels are positive for both platelets and fibrin staining, figure 5.24 (b) and (c) respectively.

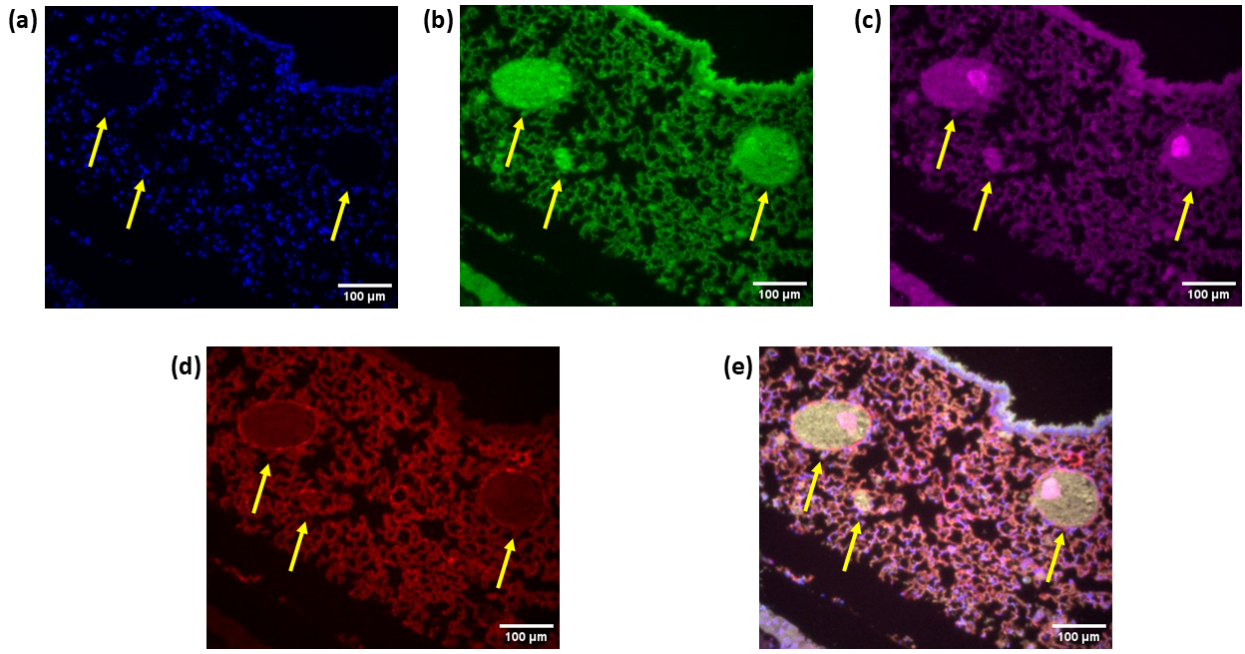

Figure 5.24: Fluorescence staining for the identification of embolism in a tumour bearing lung sample that no MSCTRAIL cells were administered: (a) DAPI, (b) Platelets, (c) Fibrin, (d) CD31, (e) Composite. The vessels are highlighted by yellow arrows.

Occluded vessels were identified in all three groups, as all three groups had vessels positive for both platelets and fibrin. A comparison between the tumour bearing mice, injected with MSCTRAIL cells to the ones that had no MSCTRAIL cells administered, showed no statistically significant difference between them (unpaired samples two-tailed t test, $p = 0.9$).

IF staining showed no staining of CD31 for the vasculature inside the lung tumours. A characteristic image can be seen at the following figure 5.25. The tumour is highlighted by the yellow arrow. It is positive for DAPI staining but not for CD31, figure 5.25 (a) and (d) respectively.

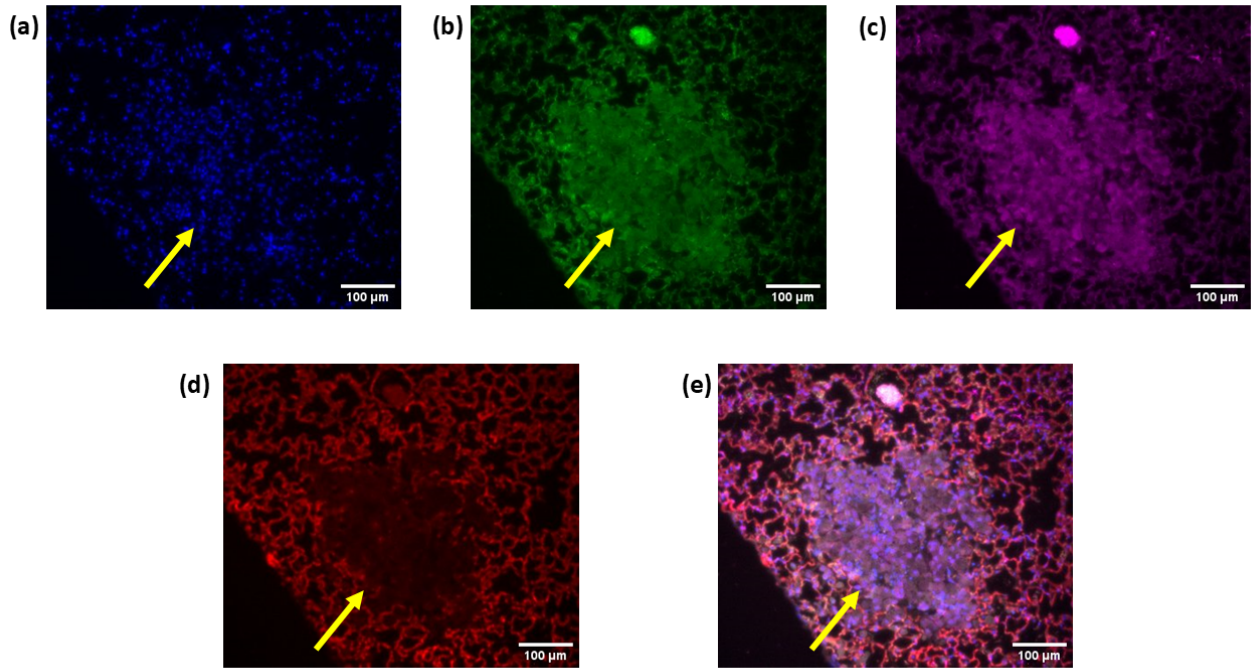

Figure 5.25: Fluorescence staining for the identification of embolism in a tumour bearing lung sample that no MSCTRAIL cells were administered. The tumour is highlighted by the yellow arrow: (a) DAPI, (b) Platelets, (c) Fibrin, (d) CD31, (e) Composite.

For the heart, IF staining was used for the identification of emboli in the heart chambers. As can be seen at the following figure 5.26 a structure was identified in a heart chamber. The structure is DAPI positive on the outside but not in the centre, making it a cell structure that contains red blood cells. Furthermore, the structure is positive for platelets and fibrin making it likely to be an embolus. The sample was cut coronally and due to the orientation no definitive identification could be made that the chamber was the right atrium.

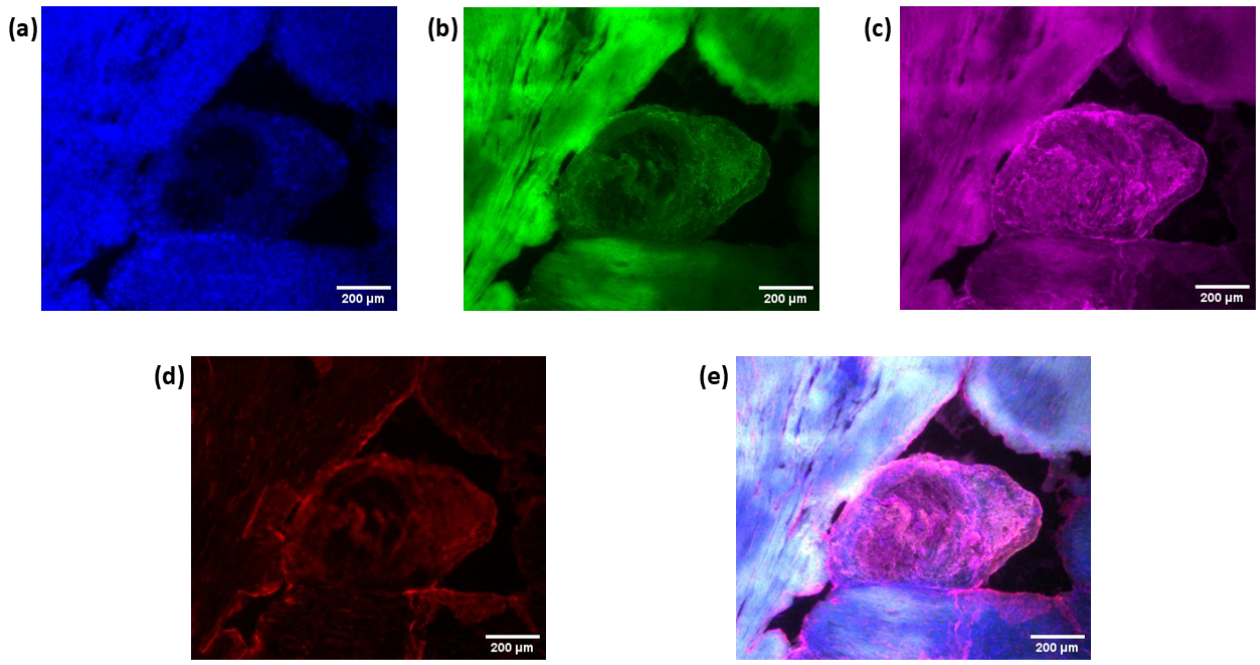

Figure 5.26: Fluorescence staining for the identification of embolism in a control mouse heart that MSCTRAIL cells were administered: (a) DAPI, (b) Platelets, (c) Fibrin, (d) CD31, (e) Composite.

5.4 Discussion

Mesenchymal stem cell therapies have been developed for different fields of medical care, including cancer treatment, neurological, cardiological and immunological disorders [140]. Clinical trials are conducted to assess the stem cell therapies for their safety and efficacy, however, imaging is rarely utilised to assess the *in vivo* biodistribution of the therapeutic cells, due to the lack of widely established and easily clinically applicable methods of cell tracking.

Out of the 1535 clinical trials registered on clinicaltrials.gov on April 2025, that utilise mesenchymal stem cells, only 154 have applied any type of imaging for the evaluation of patients and no clinical trials were found utilising ^{89}Zr PET imaging for *in vivo* stem cell tracking [18]. Nevertheless, there are clinical trials that have applied imaging for *in vivo* cell tracking of stem cells. ^{18}F-FDG PET has been applied for tracking peripheral hematopoietic stem cells in patients with myocardial infarction [141], [^{111}In]In-oxine SPECT has been applied to track MSCs in patients with advanced cirrhosis [142], and SPIO - MRI of MSCs has been applied for multiple sclerosis and amyotrophic lateral sclerosis [143], as well as for chronic ischaemic heart disease [144].

Despite examples of clinical *in vivo* cell tracking studies already existing, there is still the need for the development, assessment and validation of more cell tracking options that can be clinically applied. As the imaging needs depend on the research question, the type of cell therapy used and the pathology and target organ of interest, different imaging modalities and methods need to be available.

In this chapter, the clinically translatable [^{89}Zr]Zr-oxine direct radiolabelling method for MSCs, developed in Chapter 2, was applied to a mouse model of lung cancer, that was developed in Chapter 3. ^{89}Zr PET/CT was utilised for longitudinal *in vivo* imaging up to 7 days post MSCTRAIL cell injection. Whereas, *ex vivo* measurements, such as organ gamma counting, autoradiography and fluorescence immunohistochemistry were

applied to validate the imaging findings.

Micro-CT imaging was conducted before the commencement of the PET/CT studies, to assess tumour progression and localisation and to assist the identification of tumours on the lower resolution CT images. Despite the difference in resolution, micro-CT resolution was 0.072 mm, while CT resolution was 0.13 mm, there was no difference between the final volume segmentations of the two systems. The higher resolution micro-CT images can allow for the identification of small tumours (1 mm^3), thus making possible the identification of a tumour earlier than CT would allow. However, for tumour sizes larger than 5 mm^3, that were utilised in this chapter, no difference was found between the two systems. In the work of Zaw Thin et al., they utilised two micro-CT systems and one PET/CT system to identify the optimal image acquisition and analysis protocols, to successfully track lung tumours of sizes 0.06 to 0.08 mm^3 [101]. The tumours utilised in this works were localised and at least 5 times larger than the work of Zaw Thin et al., thus making the identification and segmentation clear.

Longitudinal PET/CT imaging showed that [^{89}Zr]Zr-oxine umbilical cord tissue-derived MSCs can be tracked *in vivo* in a preclinical mouse model of lung cancer and in control mice, up to 7 days post-injection. It is not feasible to determine whether the PET signal comes from labelled viable stem cells, or from endogenous cells that have taken up leaked radioactivity, or labelled debris from dead stem cells, something that is a common issue for all direct cell labelling techniques. Nevertheless, it has been shown in literature, by the application of *in vivo* BLI imaging, that the stem cell viability decreases over time *in vivo* over the course of 1 week for both umbilical cord tissue-derived MSCs [46] and adipocyte-derived stem cells (ADSCs) [145]. It has also been shown that the BLI distribution follows the same distribution changes over time, as was seen in the PET imaging of this thesis, and therefore this would suggest that there is a component of live cells within the lung PET distribution of this work [46, 145].

The longitudinal *in vivo* PET/CT imaging showed no significant differences between

static and breathing gated reconstructions, thus making the application of breathing gating not a factor of interest for this work. Furthermore, no significant differences were found between the organs of tumour bearing and control cohorts, showing the same distribution of radioactivity *in vivo* for both the presence and absence of disease.

Before the application of corrections to the imaging data (AFC and SOC), there was no difference between tumour and healthy lung, for the tumour bearing cohort, for all time points except Day 0. Furthermore, the lung was significantly higher than all other organs, except the liver from Day 1 onwards. For the controls, the lung values were significantly higher than all the other organs, except the liver for Day 7. After the application of corrections the difference between tumour and lung was found to be significant for all time points, which is in agreement with the *ex-vivo* measurements of autoradiography. The AFC lung values had a significant difference with all other organs, for both tumour bearing and control cohorts, which again is in agreement with the *ex vivo* findings. The application of SOC to the tumour measurements did not significantly alter the tumour measurements for any time point. The findings of this work highlight the importance of applying corrections for the TFE in *in vivo* lung imaging data, as well as accounting for the SOR, in order to properly interpret the imaging results.

In the work of Patrick et al., *in vivo* PET/CT imaging showed a similar distribution of radioactivity with the work of this thesis for tumour bearing mice. In Patrick et al., they found the majority of radioactivity to be in the lung at 1 h post-injection, and then it decreased over time as the liver signal increased. They also identified spleen, kidney and bone uptake. However, no quantification of the different organs of control mice was conducted in their work, no dedicated tumour measurements were acquired *in vivo* and no corrections were applied for the TFE [46].

The autoradiography conducted in this chapter confirmed the uniform distribution of radioactivity in controls, identified in the *in vivo* PET images and the presence of radioactivity in the hearts of the two mice that were excluded from the study.

Autoradiography is an established method used in the literature for different studies. For example, it has been used to compare between different radiolabelled cell suspensions [34], and as a bridge between immunohistochemical staining and *in vivo* imaging, as it provides both high sensitivity and resolution images that can be quantified [146]. Autoradiography has been applied in preclinical *in vivo* immune cell tracking studies, for the *ex vivo* validation of the imaging findings [147]. In the *in vivo* stem cell tracking work of Patrick et al., autoradiography was conducted alongside fluorescence microscopy and DAPI staining to confirm the presence of intravenously injected ZsGreen-expressing umbilical cord tissue-derived MSCs in the lungs. However, in their work no quantitative analysis of the autoradiography images was conducted to compare between lung and tumour uptake of radioactivity [46].

The fluorescence immunohistochemistry staining conducted in this chapter did not provide information on the localisation of MSCTRAIL cells within the lung samples. Both the cancer and the stem cell lines were of human origin and the MSCTRAIL cells were the GMP clinical product developed for the patients taking part in the TACTICAL clinical trial. The TACTICAL clinical trial umbilical cord tissue-derived MSCs were genetically engineered to express TRAIL and not another reporter gene that could be utilised for preferential staining. In the work of Patrick et al., the stem cells were identified on the lung sample sections by green fluorescence microscopy, having utilised ZsGreen-expressing cord-derived MSCs [46]. In the work of Zaw Thin et al., human ADSCs were identified in lung and breast tumour sections by utilising human specific vimentin, however, in their work they had not utilised a human cancer cell line for their model development, thus the only cell line of human origin was the ADSCs [145].

The tissue samples utilised for histology were both OCT and paraffin embedded. The OCT embedded samples were OCT inflated and flash frozen in OCT, while fresh. During the washing process it was identified that they were detaching from the slide, so it was decided to initially flash fixate the slides in 10% formalin for 15 min. The paraffin

embedded samples were inflated and fixed in 10% formalin. No antigen retrieval was conducted to the samples, to keep the protocol consistent. Antigen retrieval is needed for paraffin embedded samples to enhance the signal and avoid non-specific binding, however, the same finding was identified in the OCT samples, thus it can be concluded that the unsuccessful staining for the identification of MSCTRAIL cells is more likely to be attributed to the anti-TRAIL antibody used than the immunohistochemical method applied. In future studies the antigen retrieval step needs to be taken into consideration, for paraffin embedded samples, as well as the exploration of other antibodies that could differentiate the human stem cells.

The fluorescence immunohistochemistry staining for emboli showed the presence of occluded vessels in all samples. This finding could be attributed to the sample processing method. The lung samples were not perfused prior to extraction, as the perfusion posed the risk of damage to the lung, that would not allow for lung inflation. Perfusion also posed the risk of removing any possible emboli during the process, and so providing misleading results. For the identification of occlusions in vessels, dedicated studies should be conducted, for example by using Evans Blue intravenous injections to the mice before culling, and by avoiding all sample handling to minimise the chances of creating occlusions post-mortem. The CD31 staining conducted in the tumour bearing cohort showed the lung vascularisation clearly, but no vascularisation was shown inside the tumours. This is a limitation of the study, as the tumour vascularisation could be a factor for the fact that the uptake of radioactivity was significantly lower for the tumour compared to the lung.

Ex-vivo identification of occlusions was also conducted in the hearts of the 2 mice that were excluded from the *in vivo* PET/CT imaging study, to provide validation for exclusion. The significant uptake of radioactivity that was identified in the heart area of the PET images is most likely due to an occlusion caused by a bolus of radiolabelled stem cells in the right atrium of the heart. Cells when injected via the tail vein go up the

vena cava and enter the right atrium of the heart, are then passed into the right ventricle before being pumped into the respiratory circulation system of the lungs. For the 2 mice the radioactivity that was measured in the lung parenchyma was insignificant compared to the heart uptake, and significantly lower than all other mice. Therefore, the occlusion must have happened within the first pass into the heart within either the atrium or ventricle prior to passing into the respiratory circulation of the lungs. Although, both mice had significant heart uptake of radioactivity, they did not show any adverse effects and were scanned without any issues up to Day 7 post MSCTRAIL injection.

The lung uptake and retention of MSCs following intravenous injection, shown in this work, is consistent with previous reports in small [46, 148] and large [149] animal imaging studies, as well as patients [142]. Though intravenously injected MSCs have also been shown to subsequently migrate from the lungs to tumours [31, 150], this finding has not been universal and it was not found in the work of this thesis. Other studies have shown that MSCs sometimes remained trapped in the lungs after intravenous injection, where they progressively lost viability, before clearance of labelled cell debris to the liver and spleen [150, 151]. This variability between findings could be attributed to a range of complex interacting factors that differ between studies, including the source, species, dose and preparation of the MSCs, the species and type of animal model, and the disease state of the animal [150]. For the orthotopic mouse tumour model of this work, IF staining by CD31 proved the absence of tumour vasculature, that is an important factor for the cell migration inside the tumour. Though the results of this thesis do not support the lung delivery and retention of MSCs to a specific tumour homing effect, they support the intravenous route as an effective means of delivering and retaining MSCs in the lung for up to one week.

The blood fraction correction (BFC) developed in the literature was not applied to the *in vivo* imaging data of this work. The BFC can be applied by either blood sampling or by estimating the blood concentration directly from the PET images, by dynamic imaging

of a large vessel during injection. In this work, the distribution of the radiolabelled cells was of interest and not the pharmacokinetics of a tracer. Thus, it was expected that the radioactivity present in the blood circulation would be insignificant. Therefore, the option of blood sampling was discarded, as it is a highly invasive procedure that could put the well-being of the animals at risk, and it would not offer useable information. Imaging is a non-invasive option but due to the very slow intravenous injection of the cells and the fact that there was fast accumulation in the lungs, imaging would not offer usable information to allow for the measurement of blood concentration by imaging [152].

5.5 Conclusion

In this chapter, a clinically translatable [^{89}Zr]Zr-oxine direct radiolabelling method for MSCs was applied to a preclinical mouse model of lung cancer. The work of this chapter showed that imaging is achievable preclinically up to a week without any adverse effects for the mice. The majority of radioactivity accumulated in the lungs and no differences were identified between tumour bearing and control mice. After the application of corrections a statistically significant difference was identified between lung and tumour, in agreement with the *ex vivo* measurements, highlighting the importance of applying corrections for the interpretation of *in vivo* imaging findings.

CHAPTER 6

Imaging of Clinical Phantoms Using ^{89}Zr

6.1 Introduction

^{89}Zr-based PET imaging studies have been conducted during clinical trials for pembrolizumab, a programmed cell death 1 (PD-1) monoclonal antibody in NSCLC patients [153], and in NSCLC patients as well as patients with advanced or metastatic melanoma [154]. PET imaging of ^{89}Zr-Df-IAB22M2C, an anti-CD8 radiolabelled minibody, has been utilised to detect whole-body and tumour CD8^{+} leukocyte distribution in patients with metastatic solid tumours, as part of a clinical trial [155]. PET imaging of ^{89}Zr-VRC01, a radiolabelled HIV Env-specific broadly neutralizing antibody, has been utilised to identify and characterise the tissue-wide burden of HIV, in HIV-infected individuals as well as uninfected controls, as part of a clinical trial [156]. The vast range of clinical applications that longitudinal ^{89}Zr PET imaging could offer valuable information for, makes the use of ^{89}Zr in standard clinical practice increasingly interesting, and thus the acquisition of accurate quantitative measurements of ^{89}Zr on clinical PET/CT systems becomes imperative, as it is for all clinical studies.

Currently, the gold standard isotope of use in clinical practice is ^{18}F, which is the reason why PET scanners are calibrated for it and the validation studies are generally performed only for this isotope [157]. Imaging with ^{89}Zr is appealing due to its half-life that allows for longitudinal imaging, but there are also challenges due to its much lower true count statistics, compared to ^{18}F, its high energy 909.9 keV γ rays and its relatively long positron range, all of which could result in a deterioration of spatial resolution and contrast of PET images, especially in lung imaging [44].

In this work, the *in vivo* distribution of ^{89}Zr radiolabelled MSCs in patients as a

treatment option for lung cancer is of interest. The target organ of the stem cell therapy assessed in this thesis is the lung, however, for all intravenously injected cell therapies the lung is an organ of interest. For intravenous administration the first organ of passage is the heart, specifically the right atrium and ventricle, and then the blood is pumped to the lungs for oxygenation, before being distributed to the systemic circulation via the left side of the heart, making the heart and the lungs organs of interest for any cell treatment infusion. For the clinical translation of *in vivo* stem cell tracking using ^{89}Zr, *in vitro* studies were conducted to assess the viability of the [^{89}Zr]Zr-oxine radiolabelled MSCs (Chapter 2) and preclinical PET/CT imaging was conducted for the *in vivo* distribution of the MSCs in naïve and lung tumour bearing mice (Chapter 5). Before clinical imaging of patients commences, phantom studies need to be conducted first, to understand the quantitative accuracy of the clinical PET/CT systems for ^{89}Zr, to identify the optimal clinical imaging protocol that can be used and the corrections that are needed.

In this chapter, three different clinical phantoms were utilised for imaging with ^{89}Zr, the uniform cylinder phantom, the NEMA IEC body phantom and the anthropomorphic torso phantom. The phantoms were scanned at both LAFOV and SAFOV clinical PET/CT systems, to compare the findings between the systems. The uniform cylinder phantom is utilised with ^{18}F, to calibrate the systems to provide a Standardized Uptake Value (SUV) of 1, for areas of uniformly distributed radioactivity, regardless of the total amount of radioactivity that has been injected [158]. The SUV standardisation is a critical step for quantitative imaging to ensure accurate and standardised SUV measurements across different PET scanners and centres. However, SUV is not standardised for imaging with ^{89}Zr, thus an understanding of the SUV values across the FOV of LAFOV systems and a comparison with SAFOV systems is needed. The image quality of clinical PET systems is assessed using the NEMA IEC body phantom for ^{18}F, thus a comparative study for imaging with ^{89}Zr is needed, across the FOV of LAFOV systems and a comparison with SAFOV systems. Finally, the anthropomorphic torso

phantom utilised has different compartments that allow for different concentrations of radioactivity to be injected, including lung compartments that simulate the human lung density, making possible the application of the different ratios of radioactivity identified in the *in vivo* preclinical studies, on clinical systems.

6.2 Materials and Methods

The uniform cylinder phantom (Model Number: 10221061 REV03), the NEMA IEC body phantom (Model Number: ECT/IEC-BODY/P) and the anthropomorphic torso phantom (Model Number: ECT/TOR/P) were utilised, as a surrogate to patient imaging, to assess the quantitative accuracy of imaging with ^{89}Zr on clinical PET/CT systems. The uniform cylinder phantom and the NEMA IEC body phantom can be seen in figure 6.1 (a) and (b), respectively. The anthropomorphic torso phantom and its different compartments can be seen in figure 6.2.

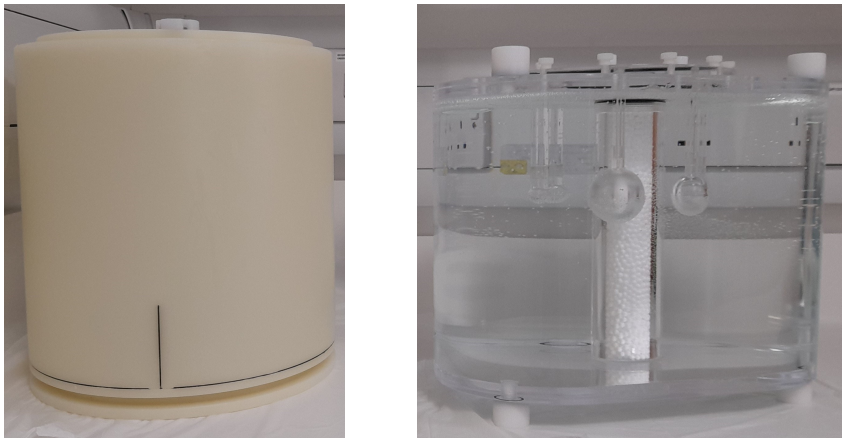

(a) **(b)**

Figure 6.1: Clinical phantoms: (a) Uniform cylinder phantom and (b) NEMA IEC body phantom.

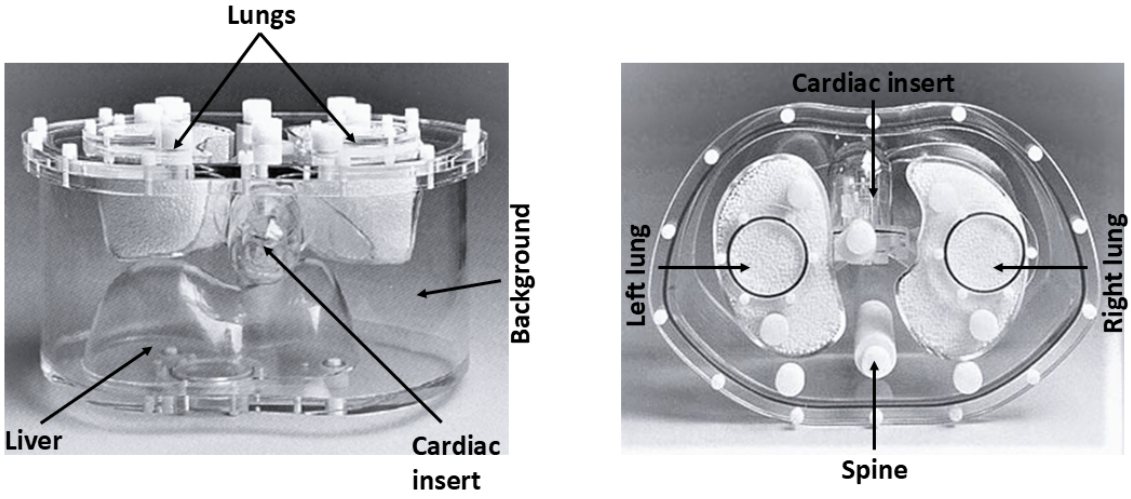

Figure 6.2: Anthropomorphic torso phantom and its different compartments.

The NEMA IEC body phantom contains a cylindrical insert, filled with a low atomic number material, that has an average density of 0.30 ± 0.10 g/mL, to simulate the attenuation of lung. The cylindrical insert has an outside diameter of 50 ± 2 mm, a wall thickness of 4 mm and it is centred inside the body phantom, extending through the entire axial extent of the phantom. No radioactivity was added to the cylindrical insert.

The anthropomorphic torso phantom simulates an average to large, life size, human torso and it has different compartments that can be filled separately. The torso regions of the phantom are the lower chest and upper abdomen, approximately the lower third of the lungs and upper half of the liver. The fillable compartments are the background, lungs, liver, and heart and they are isolated to allow for different concentrations of radioactivity to be injected, while the spine is solid and cannot be filled. The lung and liver compartments are modelled from human subjects and the lung compartments are filled with polystyrene beads, to simulate the human lung density. The heart has two compartments that can be filled separately, an inner and an outer. The spine insert has an attenuation coefficient similar to human bone [159].

To calculate the activity concentration in each phantom compartment, the volumes of the compartments need to be known. Due to variations in manufacturing, the volumes

of the same phantom type might be slightly different, therefore the volumes of each phantom compartment need to be determined individually before the start of the study. The volumes were determined by weighing the phantoms with and without water, except for the NEMA IEC body phantom spheres and the lung compartments. The volumes of the spheres were determined by adding water via syringe and the lung compartments were first filled with the polystyrene beads and then the volumes were determined by adding water via syringe. The volume of the uniform cylinder phantom was 6.28 L. The specifications and the different volumes for the compartments of the NEMA IEC body phantom can be seen in tables 6.1 and 6.2 respectively. The dimensions of the anthropomorphic torso phantom can be seen in table 6.3. The volumes of the different anthropomorphic torso phantom compartments can be seen in table 6.4.

Parameter	**Value (mm)**
Interior length of phantom	194
Fillable spheres (6) inner diameter	10, 13, 17, 22, 28 and 37
Distance from sphere plane to bottom plate	70
Sphere wall thickness	1
Diameter of sphere opening	2
External length of lung insert	203

Table 6.1: Specifications of the NEMA IEC Body Phantom.

Compartment	**Volume (mL)**
10 mm Sphere	0.5
13 mm Sphere	1.2
17 mm Sphere	2.6
22 mm Sphere	5.7
28 mm Sphere	11.5
37 mm Sphere	27.0
Lung Insert	194.0
Torso Cavity	9784.8

Table 6.2: Volumes of the NEMA IEC body phantom compartments.

Compartment	Dimensions (cm)
Lateral outside	38
Lateral inside	36
Anterior-posterior outside	26
Anterior-posterior inside	24
Wall thickness	1

Table 6.3: Dimensions of the anthropomorphic torso phantom.

Compartment	Volume (L)
Right lung (with Polystyrene beads)	0.41
Left lung (with Polystyrene beads)	0.32
Liver	1.20
Background	9.95
Whole Phantom	11.88

Table 6.4: Volumes of the different compartments of the anthropomorphic torso phantom.

The PET/CT systems utilised were the Biograph Vision Quadra and the Biograph Vision 600 (Siemens Healthineers). The three phantoms were scanned at both systems. The anthropomorphic torso phantom was also acquired at a Biograph mCT system (Siemens Healthineers). All three PET/CT systems were located at the Royal Free Hospital in London - United Kingdom. The characteristics of the three clinical PET/CT systems can be seen in table 6.5.

Parameter	Biograph Vision Quadra	Biograph Vision 600	Biograph mCT
Detector material	LSO	LSO	LSO
Crystal dimensions	3.2x3.2x20 mm	3.2x3.2x20 mm	4x4x20 mm
Detector elements per module	200	200	169
Total number of detector elements	243,200	60,800	32,448
Axial FOV	106 cm	26 cm	21.8 cm
Plane spacing	1.65 mm	1.65 mm	2 mm
Coincidence time window	4.7 ns	4.7 ns	4.1 ns
Energy window	435-585 keV	435-585 keV	435-650 keV
Time of flight performance	$<$ 228 ps*	214 ps	540 ps
Photodetectors	SiPMs	SiPMs	PMTs

Table 6.5: Specifications of the Biograph Vision Quadra, Biograph Vision 600 and Biograph mCT PET/CT clinical systems. *depending on acceptance angle.

6.2.1 Preparation of the radionuclide formulation and filling of the phantoms

^{89}Zr was supplied by Revvity as [^{89}Zr]Zr-oxalate. In order to achieve an even distribution across the different compartments of the phantoms, as explained in section 4.2.1, ^{89}Zr-oxalate was chelated with DTPA (10 mM) and the MOPS (3-(N-morpholino) propanesulfonic acid) (40 mM) buffering agent was added to ensure that the pH of the solution would be neutral. A total volume of 10 mL of DTPA/MOPS was thoroughly mixed with the supplied activity for the filling of each phantom compartment, which will be mentioned as radioactive solution.

In order to calculate the injected activity for each compartment, the syringe used was measured before and after the injection of the radioactive solution, on a CRC-55tR calibrator and the date and time was recorded. Each syringe used was flushed using the water of the compartment to ensure that the vast majority of radioactivity in the syringe was injected into the compartment. By knowing the injected activities and the

final volumes of the different compartments, the activity concentrations were calculated.

For the uniform cylinder phantom, the phantom was filled with water and the radioactive solution was added. The injected activity was 37.5 MBq at the time of injection.

For the NEMA IEC body phantom, two radioactive solutions were prepared, one for the filling of the spheres and one for the filling of the torso compartment (background). The torso compartment was initially filled with cold water and the top insert with the empty spheres was attached. A syringe was used to fill all 6 spheres (10, 13, 17, 22, 28 and 37 mm) of the phantom, using the prepared radioactive solution for the spheres. Then the radioactive solution, prepared for the torso compartment, was added into it and more cold water was added, until the torso compartment was completely full. The spheres were filled with an activity concentration of 7.78 kBq/mL and the background with an activity concentration of 1.90 kBq/mL. The activity concentration of the spheres was 4.09 times that of the background, which is in agreement with the recommendation of 4 times by the NEMA NU 2-2018 protocol [160].

For the anthropomorphic torso phantom, the phantom was first acquired on the Biograph mCT system. The acquisition was conducted before the Biograph Vision Quadra and Biograph Vision 600 experiments. Due to the fact that the Biograph mCT system was going to be decommissioned and removed from the Royal Free Hospital and due to the *in vivo* preclinical work of this thesis not being completed, the ratios of the different phantom compartments were based on the published work of Patrick et al. The preclinical *in vivo* PET/CT results of Day 1, post MSCTRAIL injection, reported on figure 4 (B) for the lungs, liver and skeleton were utilised. The skeleton was chosen for the background compartment of the phantom and no values were reported for the heart, as the heart was not an area of interest in their work [46]. The background compartment is not an area of interest, however activity was added into it, to better simulate a patient, as based on the preclinical results, a patient will have uptake of radioactivity on their

skeleton, which will contribute to an increase in scattered and random counts. For the filling of the different compartments of the anthropomorphic torso phantom, the inner and outer parts of the heart compartment were filled with cold water, and the heart was included in the phantom. Activity was added in the lung compartments, the liver and the background, by preparing a radioactive solution for each one and the activity concentrations at the time of filling can be seen at table 6.6.

For the anthropomorphic torso phantom acquisitions on the Biograph Vision Quadra and Biograph Vision 600 systems, the different compartment ratios were based on the *in vivo* preclinical work conducted in Chapter 5 and they were chosen as the *in vivo* preclinical PET/CT results of Day 1, that can be seen in figures 5.6 and 5.7. For Day 1 the values for both the diseased and normal control cohorts were approximately 40 %IA/mL for the lungs, 20 %IA/mL for the liver and 5 %IA/mL for the skeleton, that will be used as the background. This means that the activity concentration of the lungs was 2 times that of the liver and 8 times that of the skeleton, which was replicated in the torso phantom. The inner and outer parts of the heart compartment were filled with cold water, and the heart compartment was included in the phantom. It was chosen to not add activity in the heart, as the heart uptake seen in the *in vivo* experiments was an irregular finding, attributed to the mechanism of intravenous injection, and the mice that exhibited this finding were excluded from the study, as was explained in Chapter 5. Activity was added in the lung compartments, the liver and the background, by preparing a radioactive solution for each one. The phantom was filled once and it was acquired on both the LAFOV and SAFOV systems. The activity concentrations of each compartment, at the time of filling, can be seen in table 6.6.

Activity Concentrations (kBq/mL)		
Compartment	**Biograph mCT**	**Biograph Vision Quadra and Biograph Vision 600**
Right Lung	19.03	7.22
Left Lung	22.02	7.93
Liver	6.36	3.72
Background	0.04	0.92

Table 6.6: The activity concentrations of the different compartments, at the time of filling, for the anthropomorphic torso phantom, acquired on the Biograph mCT, Biograph Vision Quadra and Biograph Vision 600 systems.

6.2.2 Acquisition process and data reconstruction

The phantoms were placed on the imaging table and scanned using list-mode acquisition for all PET/CT systems and all phantom studies conducted. The standard quantitative corrections were applied for all studies, which are Normalization, Randoms correction, Dead time correction, Decay correction, Attenuation correction and Scatter correction. The decay correction was applied for each acquisition time and all corrections were discussed in section 1.10.5.

For the Biograph Vision Quadra system, the uniform cylinder and the NEMA IEC body phantoms were scanned at 5 different positions of the FOV. The phantoms were centred along the axial axis at 1/4, 1/3, 1/2, 2/3 and 3/4 of the axial FOV, as recommended by the EARL accreditation protocol [161]. The anthropomorphic torso phantom was centred in the tranverse FOV and placed axially where the same anatomical region of an adult person would be. The data for all phantom studies were acquired in UHS mode, with the maximum ring distance (MRD 322). Then, in addition to the UHS mode, images were also reconstructed using the HS mode (MRD 85), which is comparable to the Biograph Vision 600 MRD of 80 crystal rings, as was explained in section 1.13. Static and CBM acquisitions were acquired for all three phantoms. For the static acquisitions the imaging times were 5 min for the uniform cylinder, 10 min

for the NEMA and 10 min for the anthropomorphic torso phantom. For the CBM, the speed of acquisitions was 2.2 mm/sec for the uniform cylinder, 1.1 mm/sec for the NEMA and 1.1 mm/sec for the anthropomorphic torso phantom. The static acquisition times were chosen based on what would be used in clinical practice and what has been used in published literature for human studies [61]. The CBM speeds were chosen in order to match the static count statistics and image quality, according to the manufacturer's recommendation. CT acquisitions were conducted as helical (pitch = 0.8). For the uniform cylinder and NEMA phantoms, CT was acquired at 80 kVp with 500 ms exposure time and for the anthropomorphic torso phantom at 100 kVp with 500 ms exposure time.

For the Biograph Vision 600 system all three phantoms were centred in the transverse plane and Step-and-Shoot (SS) and CBM acquisitions were acquired for all of them. For the SS acquisitions, 2 bed positions were needed for all three phantoms. The time per bed position was 5 min for the uniform cylinder, 10 min for the NEMA and 10 min for the anthropomorphic torso phantom. For CBM the speed of acquisitions was 0.8 mm/sec for the uniform cylinder, 0.6 mm/sec for the NEMA and 0.6 mm/sec for the anthropomorphic torso phantom. The SS acquisition times were chosen based on what would be used in clinical practice and to match the time per bed position used for the Biograph Vision Quadra system. The CBM speeds were chosen to match the SS count statistics and image quality, according to the manufacturer's recommendation. CT acquisitions were conducted as helical (pitch = 0.8). For the uniform cylinder phantom, CT was acquired at 80 kVp with 500 ms exposure time and for the NEMA and anthropomorphic torso phantoms at 120 kVp with 500 ms exposure time.

For all PET studies of both the Biograph Vision Quadra and Biograph Vision 600 systems, the image matrix size was 440x440, with pixel size of 1.65 mm and slice thickness of 3 mm. For all reconstructions the relative scatter correction method was applied and the filter used was the all pass filter. For the Biograph Vision Quadra system, all phantom data were reconstructed using an iterative reconstruction of 4 iterations and 5 subsets,

using TOF for both UHS and HS, as well as TOF with PSF for both UHS and HS. For the Biograph Vision 600 system, all phantom data were reconstructed using an iterative reconstruction of 4 iterations and 5 subsets, using TOF, as well as TOF with PSF. The values for iterations and subsets were chosen based on what is used in clinical practice for all whole and half-body studies on the Biograph Vision Quadra and Biograph Vision 600 systems. CT was reconstructed using the FBP reconstruction method.

For the Biograph mCT system, the anthropomorphic torso phantom was acquired as a SS acquisition for 2 bed positions, of 10 min each. The image matrix size was 200x200, with pixel size of 4.07 mm and slice thickness of 3 mm. An iterative reconstruction of 3 iterations and 21 subsets was applied using TOF and TOF with PSF. The values for iterations and subsets were chosen based on what was used in clinical practice for whole and half-body ^{18}F-FDG studies and what has been used in publications of ^{89}Zr phantom studies for the Biograph mCT system [157, 162, 163]. A Gaussian filter with a value of 2 mm was applied, because it was applied in clinical practice for whole and half-body ^{18}F-FDG studies and has also been used in published work for ^{89}Zr [162]. CT was acquired as helical (pitch = 0.8) at 100 kVp with 500 ms exposure time and reconstructed using the FBP reconstruction method.

6.2.3 Analysis and data processing

For the uniform cylinder phantom analysis, the VivoQuant software (Version 2022 - Invicro) was used. A cylindrical VOI was applied to the centre of the phantom, avoiding the edges, as can be seen in the following figure 6.3, in order to calculate the Standardized Uptake Value (SUV). The SUV can be calculated according to the following equation:

$$SUV = \frac{r}{a'/w} \tag{6.1}$$

where r is the activity concentration (kBq/mL) measured within the VOI, a′ is the injected activity (kBq) decay-corrected to the time of acquisition, and w is the weight of the phantom (g). SUV is dimensionless under the assumption that 1 mL of soft tissue is equivalent to 1 g [158].

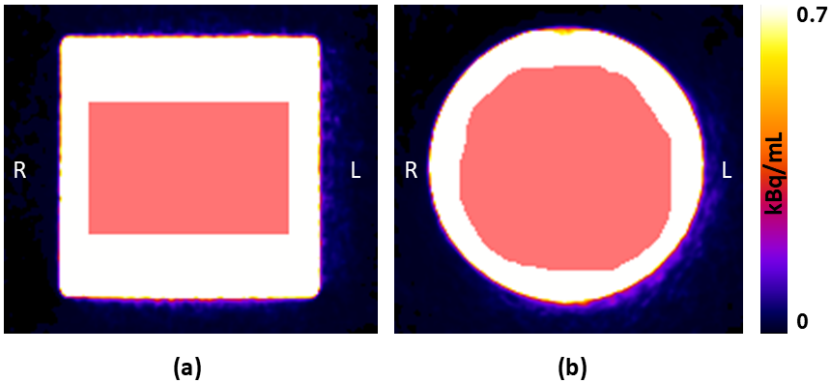

Figure 6.3: Uniform cylinder phantom analysis: representative images showing the VOI applied: (a) coronal slice, (b) transverse slice.

For the NEMA IEC body phantom the analysis was conducted according to the NEMA NU 2-2018 protocol [160], by utilising the analysis software provided on the PET/CT systems by Siemens Healthineers. A transverse image centred on the hot spheres was chosen and ROIs were positioned on each hot sphere. The ROIs had a diameter equal to the inner diameter of the sphere being measured. ROIs of the same sizes as the ROIs of the hot spheres were positioned in the background of the phantom on the slice centred on the spheres. Twelve 37 mm diameter ROIs were positioned throughout the background at a distance of 15 mm from the edge of the phantom but no closer than 15 mm to any sphere, as can be seen at the following figure 6.4. ROIs of the smaller sizes (10, 13, 17, 22, and 28 mm) were positioned concentric to the 37 mm background ROIs. The background ROIs were also positioned on the slices as close as possible to +2 cm, +1 cm, -1 cm and -2 cm on either side of the central slice. A total of 60 background ROIs of each size, 12 ROIs on each of five slices were drawn and the average counts in each background ROI were recorded.

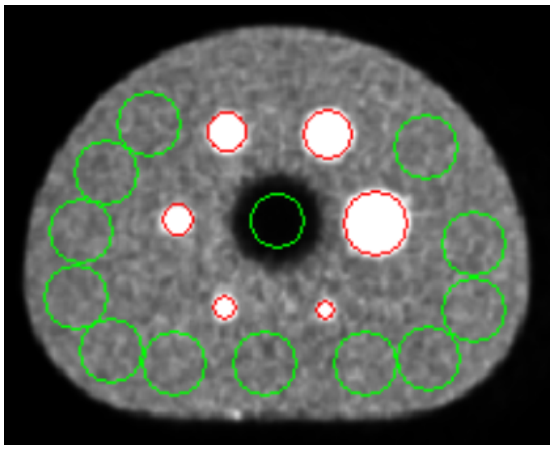

Figure 6.4: NEMA IEC body phantom analysis: Representative image showing the ROIs applied on the central slice. The ROIs applied on the hot spheres can be seen in red. The twelve 37 mm diameter ROIs of the background can be seen in green. The central ROI in green colour is the one applied to the lung insert.

The percent contrast Q_j, for each sphere j, was calculated by the following equation:

$$Q_j = \frac{(C_{S,j}/C_{B,j}) - 1}{(a_S/a_B) - 1} \times 100\% \tag{6.2}$$

where $C_{S,j}$ is the average counts in the ROI for sphere j, $C_{B,j}$ is the average of the background ROI counts for sphere j, a_S is the activity concentration in the spheres and a_B is the activity concentration in the background.

The percent background variability N_j, for each sphere j, was calculated as:

$$N_j = \frac{SD_j}{C_{B,j}} \times 100\% \tag{6.3}$$

where SD_j is the standard deviation of the background ROI counts for sphere j, calculated as:

$$SD_j = \sqrt{\frac{\sum_{k=1}^{K}(C_{B,j,k} - C_{B,j})^2}{(K-1)}} \tag{6.4}$$

where the sum is taken over the K = 60 background ROIs.

For the accuracy of attenuation and scatter corrections a circular ROI of 30 mm

in diameter was centred on the lung insert, as can be seen in figure 6.4. To measure the residual error in scatter and attenuation corrections, the relative error $\Delta C_{lung,i}$ was calculated as:

$$\Delta C_{lung,i} = \frac{C_{lung,i}}{C_{B,37mm}} \times 100\% \tag{6.5}$$

where $C_{lung,i}$ is the average counts in the lung insert ROI and $C_{B,37mm}$ is the average of the sixty 37 mm background ROIs.

For the analysis of the anthropomorphic torso phantom, VOIs were manually drawn on the two lung compartments and the liver, based on the CT acquisition, using the VivoQuant software. The VOIs contained the whole compartments, as it can be seen at the following figure 6.5 and they were applied to all of the reconstructions of all acquisitions. For the background compartment no VOIs were applied. In figure 6.6 a PET acquisition of the anthropomorphic torso phantom, on the Biograph Vision 600 system can be seen.

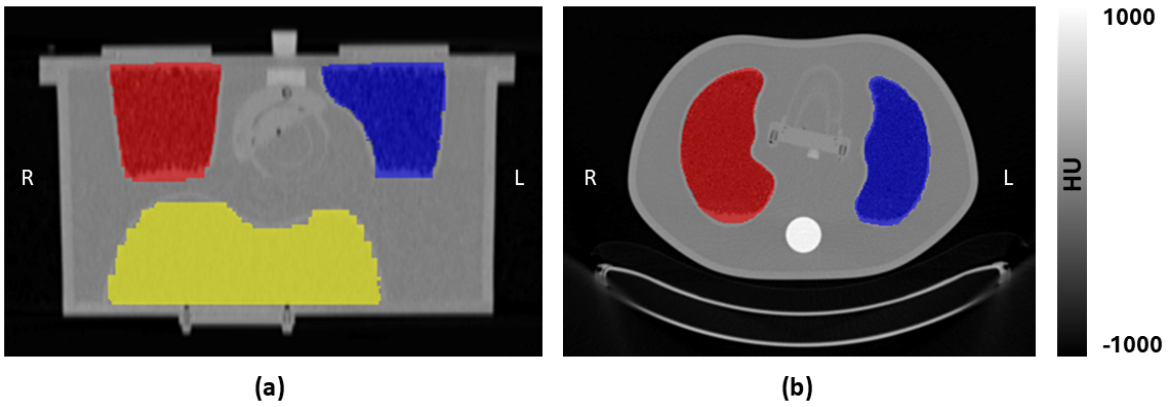

Figure 6.5: Representative CT slices showing the ROIs applied at the different compartments for the analysis. The left lung is in blue, the right lung is in red and the liver is in yellow. (a) Coronal slice, (b) Transverse slice showing the lung compartments.

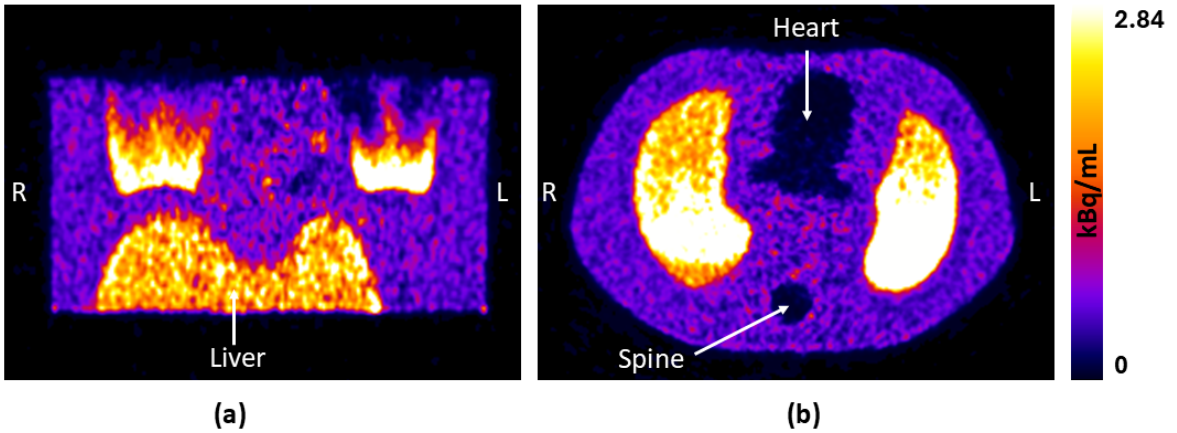

Figure 6.6: Representative PET slices of the anthropomorphic torso phantom, acquired on the Biograph Vision 600 system. (a) Coronal slice, (b) Transverse slice showing the lung compartments.

The expected activity concentrations of the anthropomorphic torso compartments were calculated based on the measurement from the calibrator, the known volumes of the compartments, and equation 1.5. The value was decay corrected for the time difference between the time of measurement at the calibrator and the time of acquisition at the system. The expected activity concentrations were considered to not have an error. The measured activity concentrations were the mean values of the VOIs applied to the whole compartments. The percentage difference ($\%\text{Diff}_m$) between the measured and expected values was calculated according to equation 4.6. A limitation of the anthropomorphic phantom study was that the distribution of beads and water was not uniform throughout the lung compartments. The beads did not absorb the radioactive water and they rose to the top of the compartment, while the bottom of the compartment contained mostly water. Despite the non uniform distribution of beads and water in the compartment, it was chosen to acquire measurements for the whole lung compartments, as the true distribution of beads and water throughout the compartment could not be known, while the true activity concentration in the whole compartment was known.

The AFC method applied to the preclinical *in vivo* imaging data as explained in

section 5.2.4, was also applied to the lung compartments of the anthropomorphic torso phantom. The lung compartments of the phantom contained polystyrene beads to simulate human lung density. The only components of the lung compartments were water and polystyrene beads. The water represents the tissue component, that contains the radioactivity, and the polystyrene beads represent the air component. In order to apply the AFC, according to the previous analysis, the HU_t, HU_a and HU_L values needed to be known. The HU value of water, which is the HU_t value, is by definition 0. The HU value for the polystyrene beads was identified by applying ROIs of the pixel size on the highest resolution CT images acquired for the phantom (pixel size 0.74x0.74 mm). Twenty ROIs were applied in total, 10 ROIs on each lung compartment. The mean value of the 20 ROIs, in HU, was the HU_a value utilised in the calculations (HU_a = - 944). For the HU_L value the CT acquisitions were downsampled to match the PET resolution, using the VivoQuant software and applying the nearest neighbour interpolation. For the Biograph Vision Quadra and Biograph Vision 600 systems the CT was downsampled to 1.65 mm pixel size and for the Biograph mCT system the CT was downsampled to 4.07 mm pixel size. The HU_L value was the mean HU value measured for each whole lung compartment, utilising the same VOIs as the PET analysis. Therefore, the value of V_a was calculated according to equation 5.2 and the values can be seen in the following table 6.7.

System	Acquisition	Compartment	V_a
Biograph Vision Quadra	Static	Right Lung	0.55
		Left Lung	0.57
	CBM	Right Lung	0.55
		Left Lung	0.58
Biograph Vision 600	SS	Right Lung	0.53
		Left Lung	0.56
	CBM	Right Lung	0.53
		Left Lung	0.56
Biograph mCT	SS	Right Lung	0.54
		Left Lung	0.55

Table 6.7: The correction factor, V_a, utilised for the AFC of each lung compartment, for each acquisition mode and PET/CT system.

The percentage increase (%Incr) of the measured values after the application of AFC was calculated according to equation 6.6 and the percentage difference between the AFC values and the expected ones ($\%Diff_{AFC}$) was calculated according to equation 6.7.

$$\%Incr = \frac{AFC\ value - measured\ value}{measured\ value} \times 100 \tag{6.6}$$

$$\%Diff_{AFC} = \frac{|AFC\ value - expected\ value|}{\frac{(AFC\ value\ +\ expected\ value)}{2}} \times 100 \tag{6.7}$$

6.3 Results

6.3.1 Uniform cylinder phantom

For the uniform cylinder phantom, the SUV results presented are the average values measured in the VOIs, rounded to two decimal places. The results for the Biograph Vision Quadra system can be seen at table 6.8 and for the Biograph Vision 600 system at table 6.9, for all reconstructions of both static or SS and CBM acquisitions.

Position	Reconstruction method	Static	CBM
1/4	TOF HS	0.92	0.92
	TOF UHS	0.92	0.92
	TOFPSF HS	0.92	0.92
	TOFPSF UHS	0.92	0.92
1/3	TOF HS	0.92	0.92
	TOF UHS	0.92	0.92
	TOFPSF HS	0.92	0.92
	TOFPSF UHS	0.92	0.92
1/2	TOF HS	0.92	0.92
	TOF UHS	0.92	0.92
	TOFPSF HS	0.92	0.92
	TOFPSF UHS	0.92	0.92
2/3	TOF HS	0.92	0.92
	TOF UHS	0.92	0.92
	TOFPSF HS	0.92	0.92
	TOFPSF UHS	0.92	0.92
3/4	TOF HS	0.92	0.92
	TOF UHS	0.92	0.92
	TOFPSF HS	0.92	0.92
	TOFPSF UHS	0.92	0.92

Table 6.8: SUV results, using a uniform cylinder phantom, for the Biograph Vision Quadra system, for 5 different positions of the FOV. Ultra-high sensitivity (UHS), High sensitivity (HS).

Reconstruction method	SS	CBM
TOF	0.97	0.97
TOFPSF	0.97	0.97

Table 6.9: SUV results, using a uniform cylinder phantom, for the Biograph Vision 600 system.

The SUV values remained consistent at each system, for all reconstructions and for both static or SS and CBM acquisitions.

6.3.2 NEMA IEC body phantom

For the NEMA IEC body phantom, the results for both static and CBM acquisitions of the Biograph Vision Quadra system can be seen at the following figures 6.7 to 6.10.

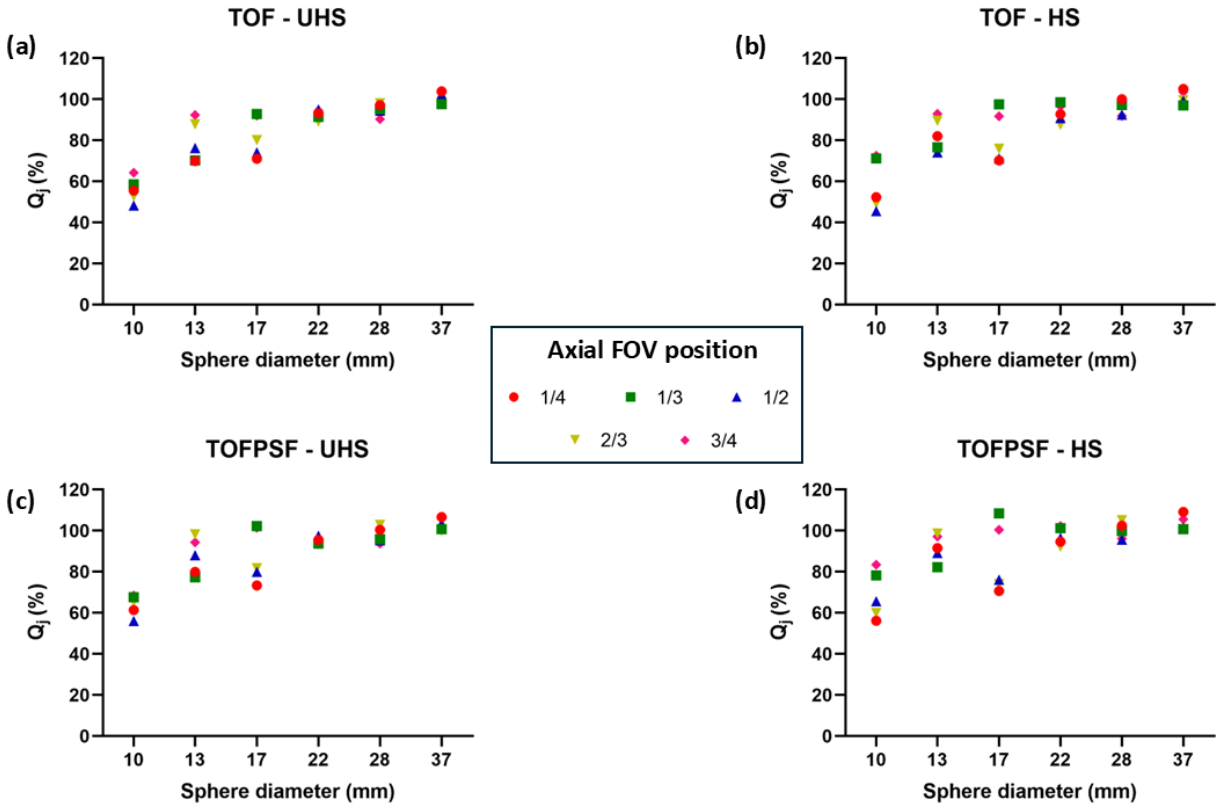

Figure 6.7: Percent contrast, Q_j, versus sphere diameter, for the 5 different acquisition positions in the FOV, of the Biograph Vision Quadra system, for the static acquisition: (a) TOF with UHS reconstruction, (b) TOF with HS reconstruction, (c) TOF and PSF with UHS reconstruction, (d) TOF and PSF with HS reconstruction.

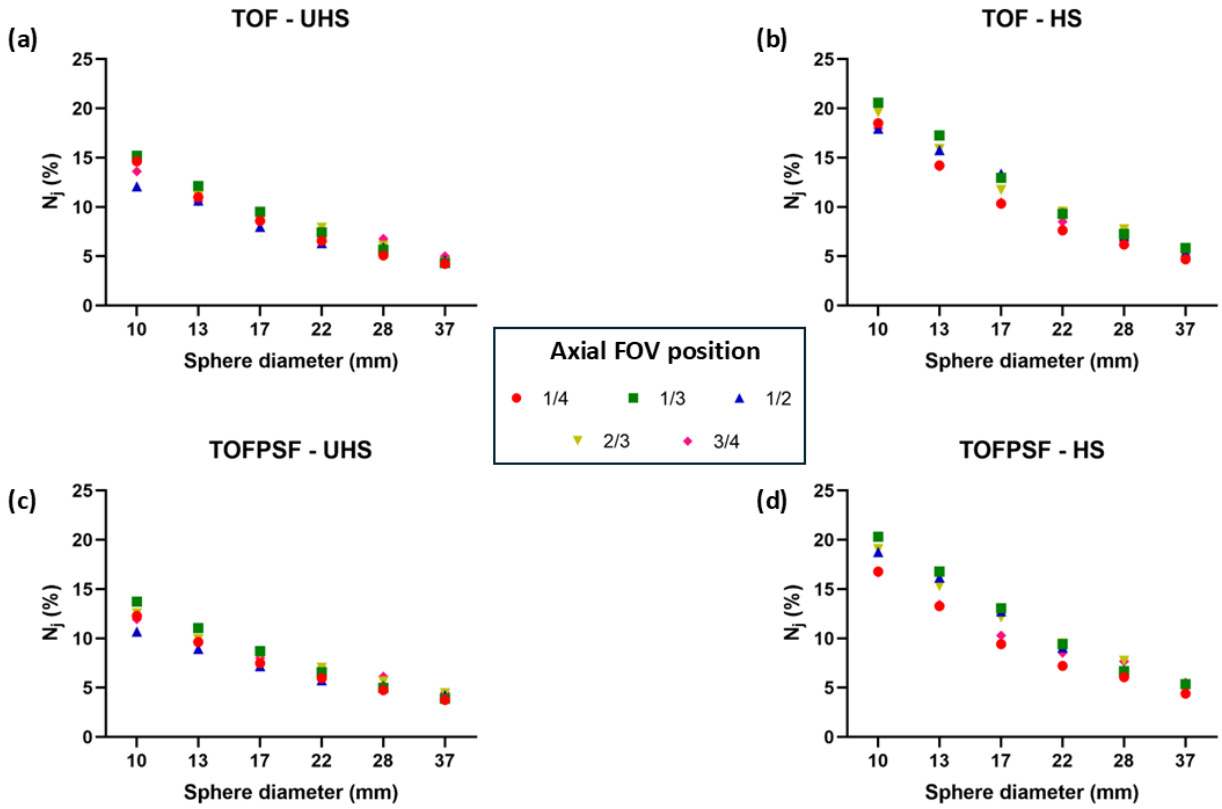

Figure 6.8: Percent background variability, N_j, versus sphere diameter, for the 5 different acquisition positions in the FOV, of the Biograph Vision Quadra system, for the static acquisition: (a) TOF with UHS reconstruction, (b) TOF with HS reconstruction, (c) TOF and PSF with UHS reconstruction, (d) TOF and PSF with HS reconstruction.

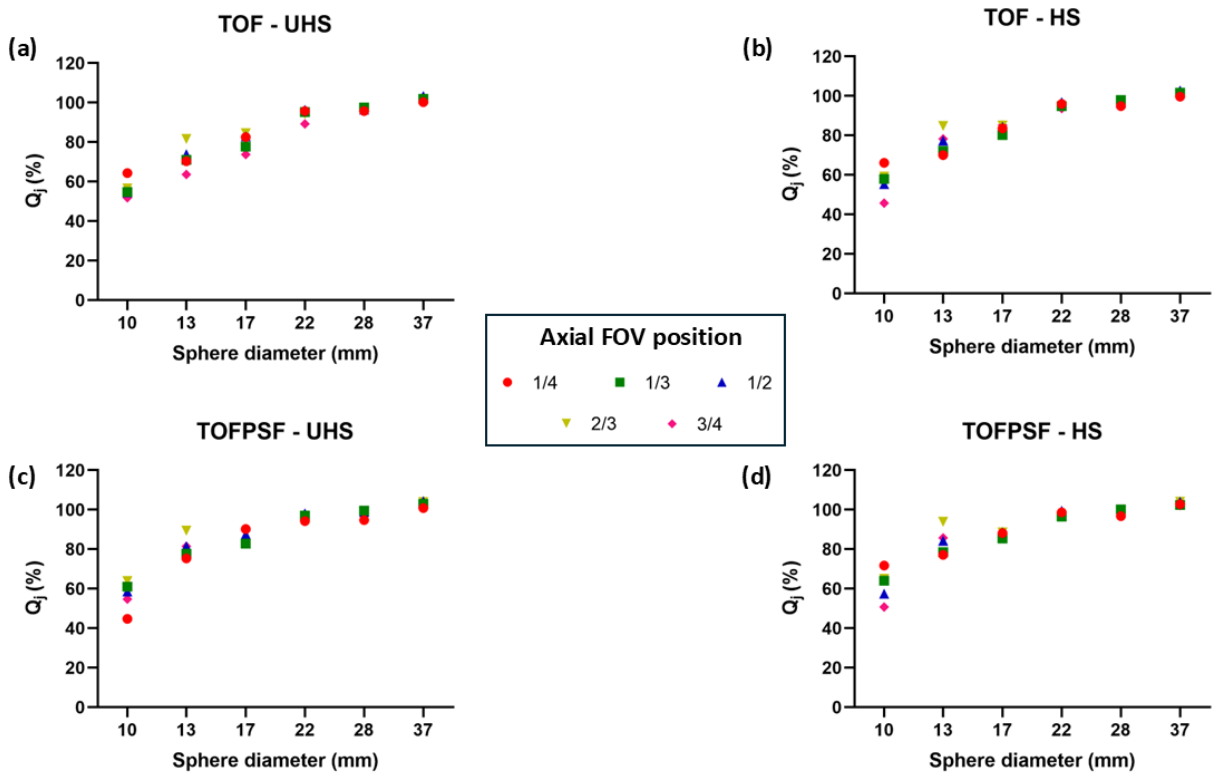

Figure 6.9: Percent contrast, Q_j, versus sphere diameter, for the 5 different acquisition positions in the FOV, of the Biograph Vision Quadra system, for the CBM acquisition: (a) TOF with UHS reconstruction, (b) TOF with HS reconstruction, (c) TOF and PSF with UHS reconstruction, (d) TOF and PSF with HS reconstruction.

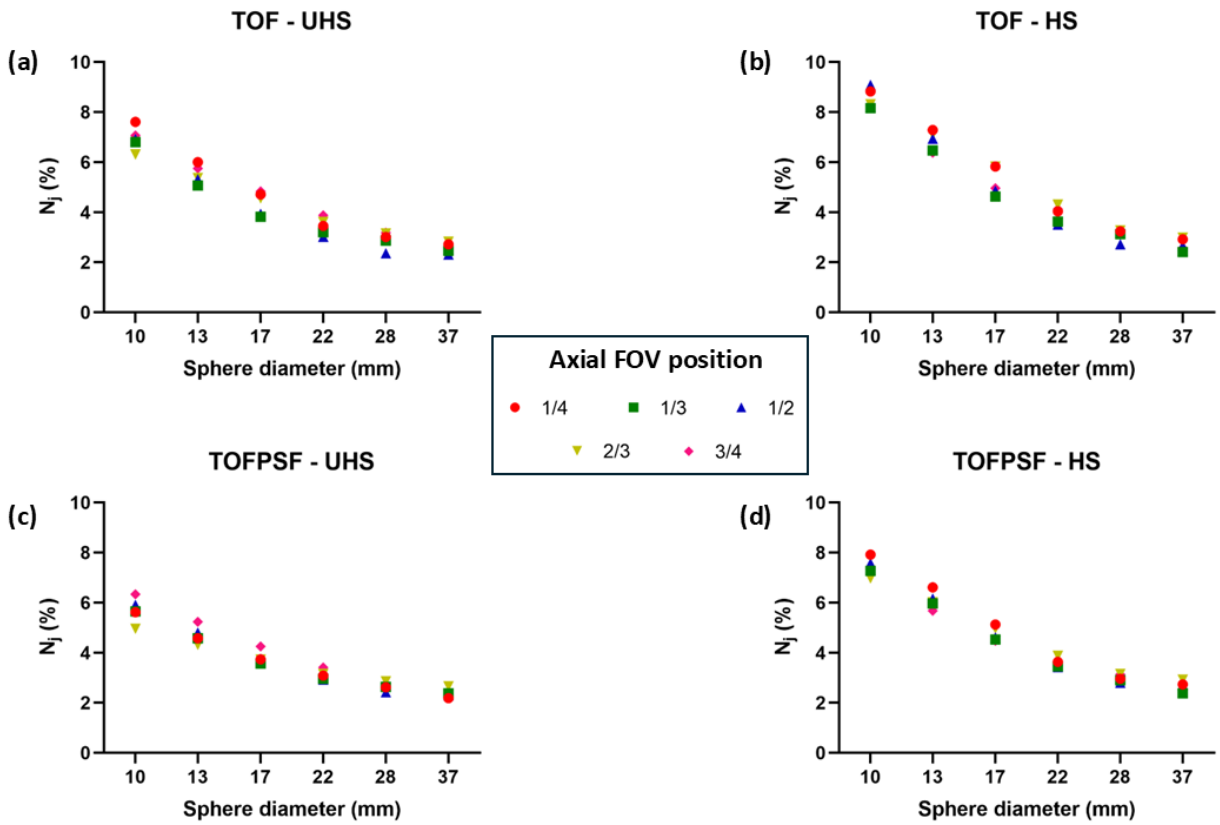

Figure 6.10: Percent background variability, N_j, versus sphere diameter, for the 5 different acquisition positions in the FOV, of the Biograph Vision Quadra system, for the CBM acquisition: (a) TOF with UHS reconstruction, (b) TOF with HS reconstruction, (c) TOF and PSF with UHS reconstruction, (d) TOF and PSF with HS reconstruction.

For the percent contrast, Q_j, the values between the two acquisition modes are similar and as the sphere diameter increases, the percent contrast values increase as well. For spheres larger than 22 cm the values are similar between the different FOV points.

For the percent background variability, N_j, as the sphere diameter increases the values decrease for both static and CBM acquisitions. The background variability results were lower for the CBM acquisition compared to the static, and lower for the UHS reconstruction compared to the HS reconstruction, for the smaller sphere sizes (10, 13 and 17 mm).

The relative error, $\Delta C_{lung,i}$, for all reconstructions applied for the five different FOV positions, of both static and CBM acquisitions for the Biograph Vision Quadra system can be seen at the following table 6.10.

Position	Reconstruction method	Static	CBM
1/4	TOF HS	6.57	4.48
	TOF UHS	5.65	4.30
	TOFPSF HS	4.24	4.12
	TOFPSF UHS	4.09	4.06
1/3	TOF HS	6.70	4.50
	TOF UHS	5.19	4.23
	TOFPSF HS	4.22	4.17
	TOFPSF UHS	3.85	4.03
1/2	TOF HS	6.78	4.30
	TOF UHS	4.65	3.99
	TOFPSF HS	4.37	4.01
	TOFPSF UHS	3.59	3.82
2/3	TOF HS	7.63	4.42
	TOF UHS	5.80	4.14
	TOFPSF HS	5.15	4.10
	TOFPSF UHS	4.47	3.94
3/4	TOF HS	7.17	4.71
	TOF UHS	5.90	4.54
	TOFPSF HS	4.71	4.27
	TOFPSF UHS	4.43	4.26

Table 6.10: The relative error, $\Delta C_{lung,i}$, for the different reconstructions used for the 5 different FOV positions, for both static and CBM acquisitions on the Biograph Vision Quadra system.

The relative error values reduced after the application of PSF for all positions of the FOV for the static acquisition, while for the CBM acquisition the values remained similar.

For the Biograph Vision 600 system, the results for both SS and CBM acquisitions, for the NEMA IEC body phantom, can be seen at the following figure 6.11.

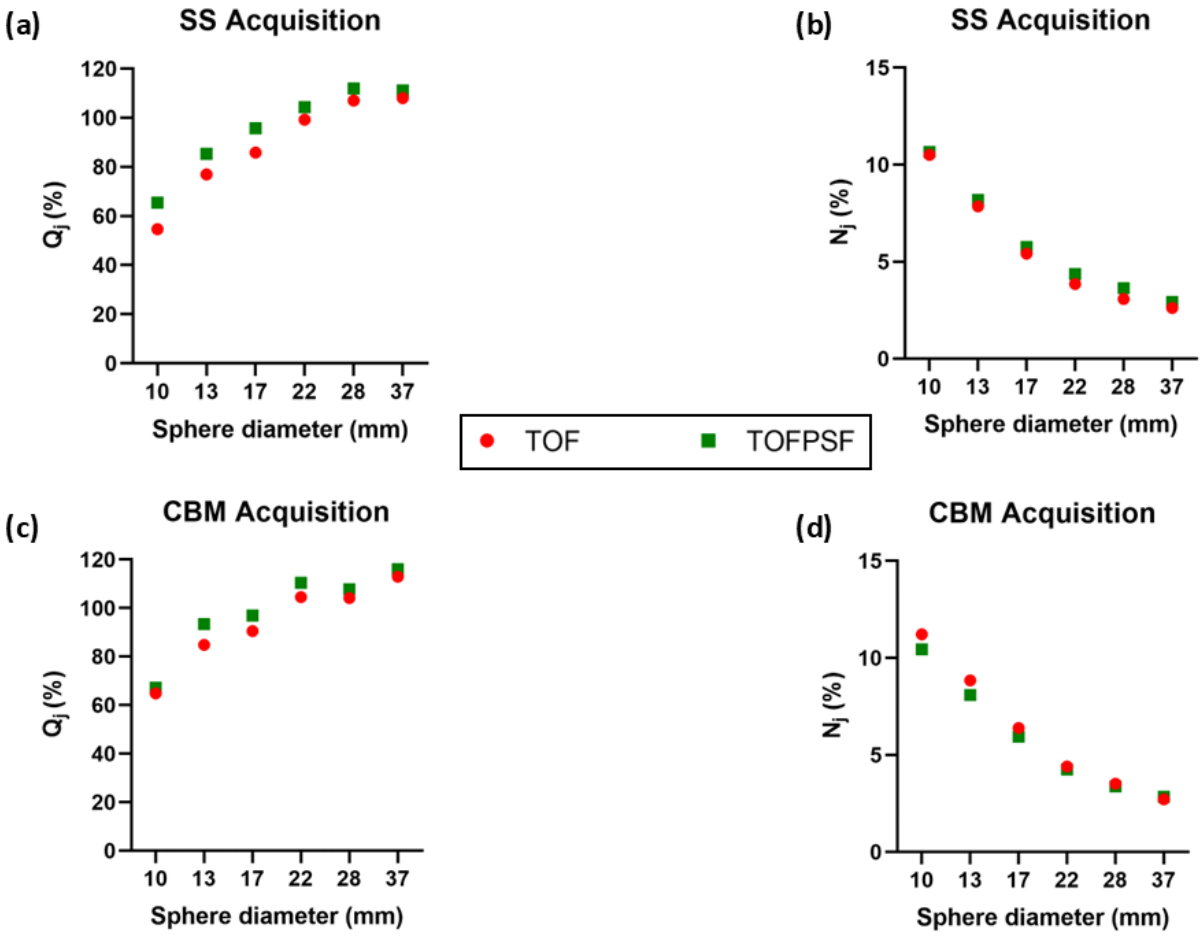

Figure 6.11: Results for the Biograph Vision 600 system using TOF and TOF with PSF reconstructions: (a) Percent contrast, Q_j, versus sphere diameter for SS acquisition, (b) Percent background variability, N_j, versus sphere diameter for SS acquisition, (c) Percent contrast, Q_j, versus sphere diameter for CBM acquisition, (d) Percent background variability, N_j, versus sphere diameter for CBM acquisition.

The percent contrast and background variability results between the two acquisition modes are similar for both reconstructions utilised. As the sphere diameter increases, the percent contrast values increase, while the background variability decreases.

The relative error, $\Delta C_{lung,i}$, results for the two reconstructions applied, for both SS

and CBM acquisitions for the Biograph Vision 600 system can be seen at the following table 6.11.

Reconstruction method	**SS**	**CBM**
TOF	6.88	6.13
TOFPSF	4.98	4.86

Table 6.11: The relative error, $\Delta C_{lung,i}$, for both SS and CBM acquisitions on the Biograph Vision 600 system.

The relative error values reduced after the application of PSF for both SS and CBM acquisitions.

6.3.3 Anthropomorphic torso phantom

For the anthropomorphic torso phantom the results for the different compartments can be seen at figure 6.12 for the Biograph Vision Quadra system, at figure 6.13 for the Biograph Vision 600 system and at figure 6.14 for the Biograph mCT system.

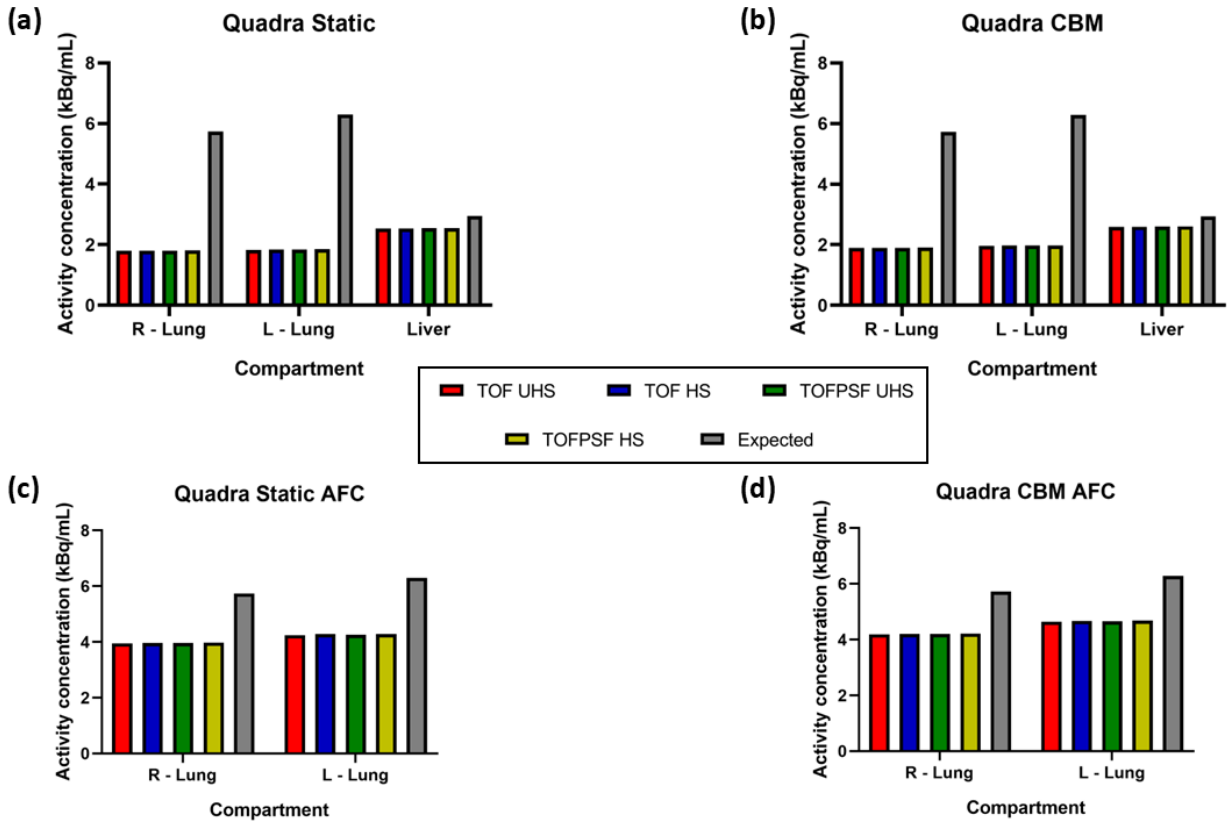

Figure 6.12: Activity concentration results, in kBq/mL, for the different compartments of the anthropomorphic torso phantom acquired on the Biograph Vision Quadra system. The results for every reconstruction method are plotted alongside the expected value of activity concentration for the compartment. (a) Static acquisition, (b) CBM acquisition, (c) Application of AFC to the lung compartments for the static acquisition, (d) Application of AFC to the lung compartments for the CBM acquisition.

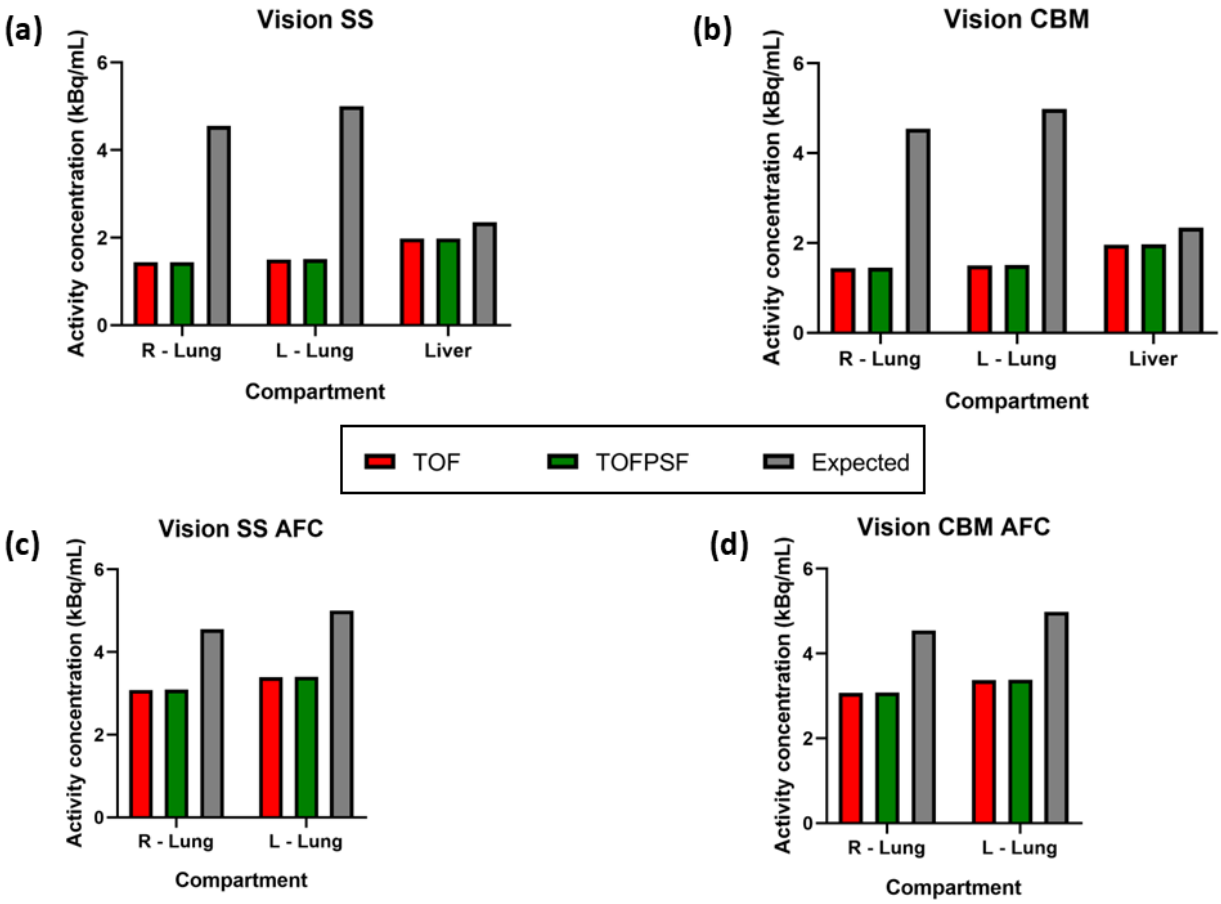

Figure 6.13: Activity concentration results, in kBq/mL, for the different compartments of the anthropomorphic torso phantom acquired on the Biograph Vision 600 system. The results for every reconstruction method are plotted alongside the expected value of activity concentration for the compartment. (a) SS acquisition, (b) CBM acquisition, (c) Application of AFC to the lung compartments for the SS acquisition, (d) Application of AFC to the lung compartments for the CBM acquisition.

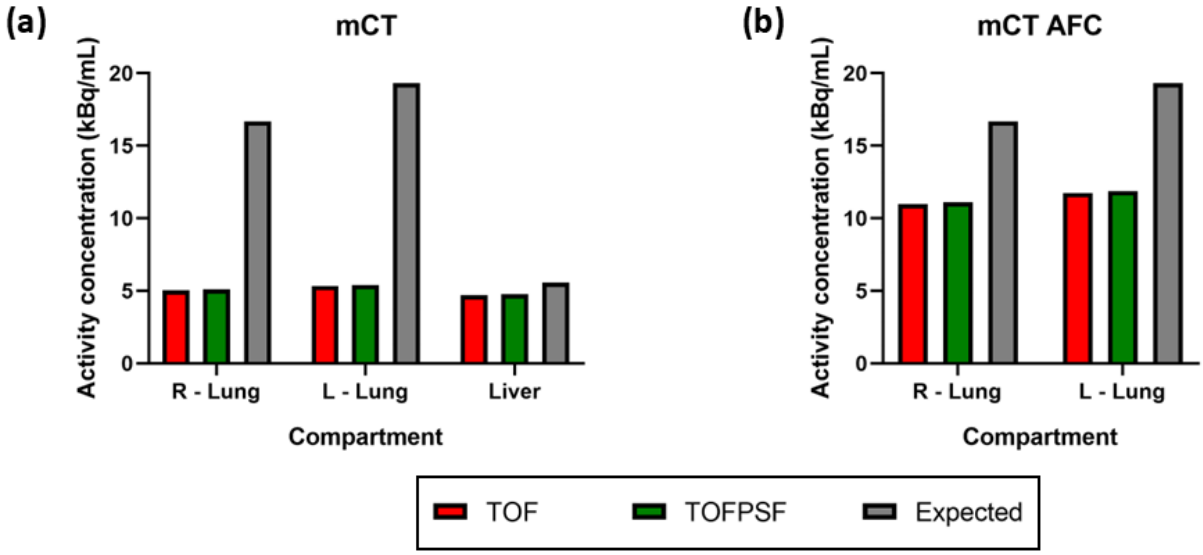

Figure 6.14: Activity concentration results, in kBq/mL, for the different compartments of the anthropomorphic torso phantom acquired on the Biograph mCT system. The results for every reconstruction method are plotted alongside the expected value of activity concentration for the compartment. (a) SS acquisition, (b) Application of AFC to the lung compartments for the SS acquisition.

The different reconstruction methods provided quite similar results in all three PET/CT systems. The application of AFC in the lung compartments increased the activity concentration values. In the following table 6.12 the maximum percentage differences between the measured and expected activity concentrations for the different compartments (%Diff$_m$), as well as the maximum percentage increase after the application of AFC (%Incr) and the maximum percentage differences between the AFC and expected activity concentrations (%Diff$_{AFC}$) for the two lung compartments can be seen.

System	Acquisition	Compartment	%Diff$_m$	%Incr	%Diff$_{AFC}$
Biograph Vision Quadra	Static	Right Lung	105%	120%	36%
		Left Lung	110%	132%	38%
		Liver	15%	-	-
	CBM	Right Lung	101%	122%	31%
		Left Lung	105%	137%	30%
		Liver	13%	-	-
Biograph Vision 600	SS	Right Lung	104%	114%	38%
		Left Lung	108%	126%	38%
		Liver	17%	-	-
	CBM	Right Lung	103%	113%	38%
		Left Lung	107%	125%	38%
		Liver	17%	-	-
Biograph mCT	SS	Right Lung	108%	118%	41%
		Left Lung	113%	120%	48%
		Liver	17%	-	-

Table 6.12: Percentage difference and increase results for the different compartments of the anthropomorphic torso phantom.

6.4 Discussion

In this chapter, three phantoms were utilised to assess the image quality and quantitative accuracy of LAFOV and SAFOV clinical PET/CT systems for imaging with ^{89}Zr. The uniform cylinder phantom provided SUV measurements across the FOV of the LAFOV Biograph Vision Quadra system and a comparison with the SUV of the SAFOV Biograph Vision 600 system. The NEMA IEC body phantom provided image quality measurements across the FOV of the Biograph Vision Quadra system and a comparison with the Biograph Vision 600. The anthropomorphic torso phantom was utilised to simulate the different activity concentrations identified in the preclinical *in vivo* PET imaging studies of intravenously injected mesenchymal stem cells, and assess the differences between measured and expected values, as well as the application of AFC. Finally, different acquisition and reconstruction methods were explored to identify the optimal imaging

parameters that can be utilised in clinical trials for *in vivo* cell tracking studies using ^{89}Zr.

For the uniform cylinder phantom, the average SUV value of the Biograph Vision Quadra system was 0.92, for all reconstructions across the FOV, of both static and CBM acquisitions. For the Biograph Vision 600 system the average SUV value was 0.97 for all reconstructions, of both SS and CBM acquisitions. The SUV results show that there are no differences across the FOV of a LAFOV system and the acquisition and reconstruction method does not change the SUV values in both systems. For the LAFOV system the values are lower compared to the SAFOV system. The lower results could be explained by the lower image noise present in LAFOV studies. SUV measurements are sensitive to noise and can result in upward bias, as it has been highlighted in the literature [164, 165].

In a study by Mohr et al., they assessed the SUV values of ^{89}Zr immuno-PET scans between the Biograph Vision Quadra and the Biograph Vision 600 systems, by scanning metastatic breast cancer patients injected with 37 MBq of ^{89}Zr-trastuzumab, 4 days after injection. For tumours, the SUV_{max} and SUV_{peak} values were compared between the 2 PET/CT systems, whereas for healthy tissues the SUV_{max}, SUV_{peak}, and SUV_{mean} values were compared. SUV_{max} is the highest voxel value identified within a VOI, SUV_{peak} is the average SUV within a small, typically spherical region of approximately 1 cm^3, centred on the highest uptake area within a lesion, and SUV_{mean} is the average SUV within a VOI. In their work, they identified that the SUV_{max} and SUV_{peak} values of the lesions were lower for the LAFOV system than for the SAFOV. For healthy tissues the SUV_{max}, SUV_{peak} and SUV_{mean} values were again lower for the LAFOV system compared to the SAFOV [165].

For the NEMA IEC body phantom the percent contrast, Q_j, and background variability, N_j, were assessed across the FOV of the Biograph Vision Quadra system, for both static and CBM acquisitions. In figures 6.7 and 6.9 the percent contrast results can be seen for static and CBM acquisitions respectively. The values between the two

acquisition modes are similar and as the sphere diameter increases, the percent contrast values increase as well. For spheres larger than 22 cm the values are similar between the different FOV points. The fact that percent contrast increases as the sphere diameter increases can be explained by the limitations of the spatial resolution of the PET system and its ability to represent larger areas better (PVE) [166]. The percent contrast is similar between static and CBM acquisitions due to the same acquisition time used, as this ensures that the total number of detected events remains similar, thus leading to comparable image contrast. Moreover, for the CBM and static acquisitions the same reconstruction methods and corrections were utilised, meaning that both acquisitions maintained similar spatial resolution.

On the other hand, as the sphere diameter increases the percent background variability decreases, as it can be seen in figures 6.8 and 6.10 for the static and CBM acquisitions respectively. This is because the background ROIs were the same size as their respective spheres sizes and the larger that the background ROI is, the larger the number of counts measured, meaning that there is less noise. The background variability results were lower for the CBM acquisition compared to the static, and the background variability was lower for the UHS reconstruction. The fact that the CBM acquisition leads to lower percent background variability compared to the static acquisition can be explained by the following reasons. In CBM, the bed moves continuously through the scanner, thus allowing each voxel to be sampled from multiple angles and at different times, which results in a more uniform count distribution and smoother statistical noise across the image [167]. Moreover, in LAFOV PET systems, the sensitivity is highest at the centre of the FOV and lower near the edges [168] and with CBM the bed motion helps smooth out these sensitivity differences, leading to more uniform background noise characteristics. On the contrary, for static acquisitions, regions might receive disproportionately higher or lower count statistics, leading to more variable background noise. The background variability decreasing with UHS can be explained by the fact that MRD 322 mode

increases the sensitivity and it reduces the statistical noise thus contributing to lower background variability [169].

In the work of Prenosil et al., they assessed a Biograph Vision Quadra system according to the NEMA NU 2-2018 protocol [160], by conducting ^{18}F imaging of a NEMA IEC body phantom. They acquired measurements with all spheres filled with a concentration of 4 times that of the background as was done in this work, and they positioned the phantom in the centre of the FOV, utilising the static acquisition for 30 min in list-mode. The data were corrected for decay, normalization, scatter, randoms, and attenuation. The images were reconstructed in HS mode using TOF and TOF with PSF, with 4 iterations and 5 subsets, with no post-reconstruction filtering applied. Their results for the percent contrast were similar to the ones reported in this work, however for the background variability their results were lower, something that could be explained by the greater noise of ^{89}Zr compared to ^{18}F [61].

In the work of Mannheim et al., they utilised a cylindrical preclinical micro hollow sphere phantom equipped with a single fillable sphere for ^{89}Zr with a ratio of 8:1, on the Biograph Vision Quadra system. The phantom was measured at multiple positions along the FOV. All acquisitions were performed as list-mode with MRD 322 and reconstructed as TOF with PSF with 4 iterations and 5 subsets. For ^{89}Zr they identified increased noise compared to ^{18}F and ^{89}Zr noise levels in the centre of the FOV significantly decreased when reconstructing the data with MRD 322 compared to MRD 85, as was identified in this work [170].

For the Biograph Vision 600 system, the percent contrast, Q_j, and background variability, N_j, were again assessed for both SS and CBM acquisitions, as can be seen in figure 6.11. The values between the two acquisition modes are similar for both reconstructions utilised and as the sphere diameter increases, the percent contrast values increase, while the background variability decreases. The percent contrast and background variability behaviour can be explained by the same reasons as before, for

the Biograph Vision Quadra system. However, the results for the background variability are now similar for both SS and CBM acquisitions, which can be explained by the fact that the Biograph Vision 600 system has a smaller AFOV, that reduces the sensitivity variation. Unlike the LAFOV Biograph Vision Quadra, where sensitivity can vary across the extended axial FOV, the SAFOV Biograph Vision 600 has a more uniform sensitivity profile over each bed position. Furthermore, both SS and CBM acquisitions, of the Biograph Vision 600, sample the data with similar sensitivity, thus leading to comparable noise characteristics. Since both methods have similar sensitivity, the noise characteristics remain alike, making CBM less impactful in further reducing background noise [171].

The percent contrast, Q_j, results between the Biograph Vision Quadra and Biograph Vision 600 systems were similar, something that could be explained by the fact that the two systems have the same specifications, except from the AFOV, and the fact that the same reconstruction methods were used, thus leading to similar percent contrast results. Nevertheless, the background variability was higher for the static acquisition of the Biograph Vision Quadra system, something that could be explained by the non-uniform sensitivity across the FOV of the LAFOV system and the high energy photons of ^{89}Zr (909.9 keV) that increase the random counts and lead to an increase in noise. The effect was not observed for the CBM acquisition as the bed motion helps smooth out the sensitivity differences, leading to more uniform background noise characteristics, as was explained before.

For the Biograph Vision Quadra system the relative error values, $\Delta C_{lung,i}$, reduced after the application of PSF, for all positions of the FOV for the static acquisition, while for the CBM acquisition remained similar. This can be explained by the fact that in static acquisition, PSF reduces residual scatter and attenuation correction errors by improving spatial resolution and compensating for sensitivity variations across the FOV [172]. In CBM acquisition, these residual errors are already lower due to uniform data sampling and smoother count distribution, meaning that the impact of PSF is less pronounced

compared to the static acquisition. For the Biograph Vision 600 system the relative error values, $\Delta C_{lung,i}$, reduced after the application of PSF for both SS and CBM acquisitions. As was explained before, PSF improves spatial resolution and compensates for sensitivity variations across the FOV. The SAFOV systems have a more uniform axial sensitivity profile than LAFOV systems and in LAFOV systems CBM reduces sensitivity variations naturally, thus diminishing the impact of PSF, while in SAFOV PET the sensitivity profile is already relatively uniform in both SS and CBM acquisitions, which means that PSF provides similar benefits for scatter and attenuation corrections in both modes.

For the anthropomorphic torso phantom the measured activity concentrations for every compartment were consistently lower than the expected activities, for all systems, acquisition modes and reconstruction methods applied. The different acquisition and reconstruction methods provided almost identical results. For the liver the differences between measured and expected values were about 15%. For the lung compartments, before the application of AFC, the differences between measured and expected values were greater than 100%. However, after the application of AFC the activity concentration values for the lung compartments increased by at least 118%, making the differences with the expected values from 30% up to 48%. The change in differences of the lung values with the expected ones after the application of AFC highlights the importance of applying corrections for the TFE when quantitative measurements are acquired in the lung. The difference of the lung values after the application of AFC with the expected ones was more than double compared to the liver values. This can be justified by the limitations of the experiment, as within the lung compartments the distribution of beads and radioactivity was non-uniform and the analysis was conducted based on VOIs instead of voxel-wise analysis. The percentage of underestimation in the values of the lung and liver compartments could be attributed to the high energy 909.9 keV photopeak of ^{89}Zr that causes an increase in random counts and noise leading to overcompensation of the corrections applied, as well as the reduced total number of accumulated events due to

the low branching ratio for positron decay of ^{89}Zr.

It is important to note that despite the fact that the anthropomorphic torso phantom has polystyrene beads in the lung compartments that simulate lung density, there is no breathing motion as happens in patient's studies. When there is breathing motion the results will be further affected as motion artifacts can be present. Furthermore, in the case of lung cancer patients, solid tumours are present in the lung parenchyma and patients have a variable disease representation, meaning that in order to apply corrections for the TFE voxel based analysis would be needed to account for the different areas in the lung and a different Va value would need to be identified for different regions.

No comparable anthropomorphic torso phantom studies were found in the literature for the assessment of LAFOV and SAFOV systems, for prospective ^{89}Zr cell tracking studies, and the effect of the application of corrections for the TFE. However, clinical imaging studies of patients have been conducted comparing the two systems for ^{18}F and ^{68}Ga [173] as well as for ^{89}Zr [165]. In the work of Alberts et al., they found improved image quality, lesion quantification, and SNR resulting from higher sensitivity, for a LAFOV system in a head-to-head comparison of the systems under clinical conditions. The LAFOV system provided images of comparable quality and lesion quantification in under 2 min, compared to routine SAFOV acquisition of 16 min for equivalent FOV coverage. Alternatively, the LAFOV system allowed for low-dose examination protocols of adequate quality with respect to target lesion identification, suggesting that ultra-fast or low-dose acquisitions can be acceptable in selected settings [173]. In the work of Mohr et al., as was discussed before, they found that LAFOV ^{89}Zr immuno-PET provided lower SUV values due to the lower image noise [165].

Based on the phantom studies conducted in this chapter, the optimal acquisition method for imaging with ^{89}Zr on a LAFOV system would be CBM. For a SAFOV system there were no differences in image quality between SS and CBM acquisitions, however CBM acquisitions can reduce the overall scan time, thus leading to a more comfortable

experience for patients [174]. Therefore, the CBM method should be preferred for whole-body longitudinal *in vivo* cell tracking studies on both LAFOV and SAFOV systems. For the reconstruction method the TOF with PSF modelling should be preferred on both LAFOV and SAFOV systems, and for LAFOV systems the UHS should be used.

6.5 Conclusion

This work assessed the image quality and quantitative accuracy of clinical PET imaging with ^{89}Zr for its prospective application in *in vivo* cell tracking clinical studies. A comparison between LAFOV and SAFOV systems was conducted, to identify the limitations and the optimal parameters for imaging on each system. The limitations of this work were that only phantoms were utilised, and the only correction applied for the TFE was the AFC, conducted based on VOIs instead of voxel-wise analysis.

CHAPTER 7

Discussion, Main Conclusions and Future Work

Stem cell therapies have been developed for a vast range of pathologies including lung cancer. Clinical trials are conducted to assess the stem cell therapies for their safety and therapeutic efficacy, however, imaging is rarely utilised during a clinical trial to assess the *in vivo* biodistribution of the therapeutic cells, due to the lack of established and easily clinically applicable methods of cell tracking.

In this thesis, a clinically translatable [^{89}Zr]Zr-oxine direct radiolabelling method was developed for a GMP stem cell therapy (MSCTRAIL) for metastatic lung adenocarcinoma. The radiolabelling method was first assessed *in vitro*, for cell viability and toxicity, and then in preclinical *in vivo* studies for the validation of the imaging method and the understanding of cell distribution in naïve and lung cancer mouse models. Finally, the preclinical *in vivo* imaging findings were translated to a clinical phantom, and phantom studies were conducted on both SAFOV and LAFOV clinical PET/CT systems, for the understanding of imaging with ^{89}Zr and the identification of optimal imaging parameters in the clinical setting.

7.1 Main conclusions and limitations

In Chapter 2 the [^{89}Zr]Zr-oxine radiolabelling method was developed and assessed using different radioactivity levels and controls by applying viability assays. The effect of radiation on cell viability, identified in this work, has also been highlighted in the literature. The kit formulation assessed in this thesis provides a one-step method for the production of [^{89}Zr]Zr-oxine, and it was shown that the kit formulation was non-toxic to the cells. Nevertheless, care must be taken in the cell radiolabelling process, as the kit contains polysorbate 80, which can be toxic to the cells. Furthermore, only one stem cell

product was assessed, meaning that for other cell type therapies *in vitro* studies need to be conducted.

To apply the radiolabelling method in *in vivo* preclinical imaging studies, an orthotopic mouse model of lung cancer was developed in Chapter 3. Different minimally invasive methods were assessed, to develop a model with clear tumour and lung parenchyma areas, that would allow for the *in vivo* cell tracking of the MSCTRAIL cell therapy in the diseased lung. The model was successfully developed by intralobular injection, without conducting an incision, of a human malignant pleural mesothelioma cell line into the right lung lobe. The model represented areas of tumour tissue and healthy lung parenchyma that could be clearly identified by micro-CT and CT imaging. However, tumours grew in the intrapleural space as well for 2/5 mice, due to cancer cell seeding in the intrapleural space during injection. Furthermore, the lung tumours were not well vascularised as indicated by histology (H&E in Chapter 4 and CD31 staining in Chapter 5).

Since low ^{89}Zr injected activities were needed for longitudinal *in vivo* imaging studies, as was identified in Chapter 2, the preclinical PET/CT system was assessed ahead of the *in vivo* imaging studies by preclinical phantom studies (Chapter 4). A significant effect of noise was identified for ^{89}Zr that can affect image quality. However, due to the sensitivity of NSG mice to anaesthesia, the acquisition time could not be extended as the radioactivity decayed. Therefore, it was chosen to acquire relative measurements to mitigate the effects of noise and the differences in injected activities between animals.

In Chapter 5, [^{89}Zr]Zr-oxine radiolabelled MSCTRAIL cells were successfully tracked *in vivo* in naïve and tumour bearing mice for up to 1 week. *In vivo* PET/CT imaging showed a significant difference between lung parenchyma and the other organs except for tumour and liver from Day 1 onwards. Nonetheless, the application of corrections for the TFE (AFC) and the SOR (SOC) showed that the activity concentration was significantly higher in the lung compared to the tumour and liver for all time points, something

that was validated by *ex vivo* measurements. The limitations of this chapter were that the corrections applied were simplified and derived from either the mice themselves or phantoms, and they were conducted based on VOIs instead of voxel-wise analysis. Nevertheless, they highlighted the importance of applying corrections in preclinical *in vivo* imaging data, to properly interpret the results ahead of clinical translation. Furthermore, the histology conducted did not provide answers on the presence or absence of MSCTRAIL cells in the lung or tumour tissue.

Finally, in Chapter 6 clinical phantom studies were conducted to assess LAFOV and SAFOV clinical PET/CT systems for imaging with ^{89}Zr. Results showed that SUV measurements are lower for LAFOV systems compared to SAFOV systems. Furthermore, percent contrast results between the two systems were similar with the background variability being higher in the Biograph Vision Quadra system only for the static acquisition. The anthropomorphic torso phantom showed an underestimation between the measured and the expected results, with the application of AFC making the differences with the expected values from 30% up to 48%. Nevertheless, the anthropomorphic torso phantom was a simplified version that did not represent disease. Also AFC could only be applied, which was done based on VOIs instead of voxel-wise analysis. In patient studies, the disease representation might be complex and voxel based analysis will be needed to apply corrections for the TFE, as was explored previously for idiopathic pulmonary fibrosis [47].

7.2 Future directions - Clinical translation

The radiolabelling method developed and assessed in this thesis can be clinically translated for application in clinical trials. The cell therapy assessed in this work was a mesenchymal stem cell therapy, however, the direct radiolabelling method can be applied to any cell therapy, given that *in vitro* studies are first conducted, to assess the cell viability and the tolerated dose limits for the specific cell type. The direct [^{89}Zr]Zr-oxine

radiolabelling method can be used for imaging the *in vivo* biodistribution of the cell therapy in patients, however, for its successful implementation the following steps need to be undertaken.

7.2.1 Scale up of radiolabelling method for the clinic

In the clinical setting the complete radiolabelling process needs to be done under sterile GMP conditions, in a class A environment of a radio-pharmacy department. The [^{89}Zr]Zr-oxine/kit formulation can be prepared as was explained in this thesis, and the washing process can be done by centrifugation, as was done in this work. However, washing by centrifugation poses challenges due to the fact that the centrifuge needs to fit in the safety cabinet, lead shielding is needed for the front of the cabinet and the exposure and dose to the radio-pharmacists is increased. Filtration based methods, like tangential flow filtration, are less common but would reduce the exposure of a radio-pharmacist. The washing process method needs to be tested ahead of the clinical trial and the cells need to be tested for bacterial contamination at the end of the radiolabelling process to ensure no contamination. Finally, care must be taken in keeping the discarded radioactive liquid in leak proof containers in shielded boxes until it decays.

The complete radiolabelling process conducted in this work for one activity level was less than 1 h. The time needed for the complete radiolabelling process is critical in the clinical setting, as the viability of the cells is of the outmost importance. Viability decreases the longer the cells are handled and dedicated studies need to be conducted for the viability of each individual cell therapy product ahead of the radiolabelling process and the administration to the patients.

7.2.2 Imaging of patients

As highlighted in Chapter 2 the activity per million cells is highly important not only for the cell viability of the cell therapy but also for the administered activity, as this affects

the effective dose to the patient as well as the image quality.

For the TACTICAL clinical trial the number of cells administered to the patients was up to 5 x 10^6 MSCTRAIL cells/kg, meaning that for an 80 kg patient up to 400 x 10^6 MSCTRAIL cells were administered. During Phase I of the trial a dose de-escalation was decided to 200 x 10^6 MSCTRAIL cells per patient.

Clinical PET imaging of ^{89}Zr antibodies on SAFOV systems has been reported up to 5 days post-injection with an injected activity of 37 MBq and imaging times of 5 to 12 min per bed position [175, 176] and up to 6 days using an injected activity of 70 to 75 MBq and imaging times of 7 min per bed position [177, 178]. Immuno-PET/CT patient studies of ^{89}Zr have been acquired on LAFOV systems with an injected activity of 37 MBq and imaging times of 30 and 32 min acquired 4 days post-injection [165, 179].

For a total injected activity of 37 MBq, for the TACTICAL clinical trial, 92.5 kBq per million cells would be needed for the 400 x 10^6 MSCTRAIL administered cell dose and 185 kBq per million cells would be needed for the 200 x 10^6 MSCTRAIL administered cell dose. These activity ranges are achievable from a radiolabelling and cell viability perspective, as was shown in Chapter 2.

7.2.3 Dosimetry considerations for patients and staff

As was discussed in section 1.12, for an administered activity of 37 to 74 MBq of ^{89}Zr, the effective doses to patients range from 20 to 40 mSv, which is about 2 to 4 times higher than the effective dose of an ^{18}F-FDG PET scan [73]. The effective dose is an important factor for imaging patients with ^{89}Zr. Due to the high effective doses of ^{89}Zr the acceptable injected activity to patients is limited for radiation protection reasons. This can make imaging on SAFOV systems challenging, as longer acquisition times would be required, especially for longitudinal whole-body *in vivo* cell tracking studies that require multiple bed positions. The extended FOV of a LAFOV scanner and its increased sensitivity would allow for lower injected activities without increasing the acquisition time. A reduction of

the injected activity by a factor of 3 would give a radiation dose well below 10 mSv and therefore would allow ^{89}Zr-immuno-PET applications in non-oncologic diseases and young patients. Furthermore, the increased sensitivity can be exploited to acquire longitudinal studies with reasonable scan durations, as were applied before, allowing for longitudinal *in vivo* cell tracking of cell therapies [165].

For the effective doses to staff, a study by Alzimami et al. conducted Monte Carlo simulations to calculate the effective dose distribution in a PET/CT facility for ^{89}Zr imaging. In their work, they found that the high-energy photons of ^{89}Zr (909.9 keV) cause a significantly higher effective dose to the staff than ^{18}F outside the patient room, such as corridors and control rooms. On the other hand, despite the low administered activity of ^{89}Zr, compared to ^{18}F, the dose to staff near the patient is comparable or lower than ^{18}F [180]. Their findings raise important radiation protection considerations for a PET/CT facility, as careful examination and evaluation of the shielding installation needs to be done for the department, ahead of the incorporation of ^{89}Zr into clinical practice, to ensure staff safety and compliance with radiation protection standards. Possible outcomes can be that additional shielding of areas may be necessary to protect staff adequately, especially in areas adjacent to patient rooms. Moreover, a re-evaluation of the use of control rooms and adjacent corridors might be necessary to minimise exposure from high-activity areas. Finally, operational protocols need to be implemented for imaging with ^{89}Zr, to limit staff time spent near patients post-injection and during imaging.

Bibliography

[1] Global Cancer Observatory, International Agency for Research on Cancer - World Health Organisation. https://gco.iarc.fr/.

[2] Cancer Research UK. https://www.cancerresearchuk.org/.

[3] American Cancer Society, "What Causes Lung Cancer?." https://www.cancer.org/cancer/types/lung-cancer/causes-risks-prevention/what-causes.html.

[4] National Health Service (NHS), "Lung cancer causes." https://www.nhs.uk/conditions/lung-cancer/causes/.

[5] B. Järvholm, L. Hedman, M. Landström, P. Liv, A. Burdorf, and K. Torén, "Changing smoking habits and the occurrence of lung cancer in Sweden - a population analysis," *European Journal of Public Health*, vol. 34, no. 3, pp. 566–571, 2024.

[6] C. Poon, A. Haderi, A. Roediger, and M. Yuan, "Should we screen for lung cancer? A 10-country analysis identifying key decision-making factors," *Health Policy*, vol. 126, no. 9, pp. 879–888, 2022.

[7] R. Nooreldeen and H. Bach, "Current and future development in lung cancer diagnosis," *International Journal of Molecular Sciences*, vol. 22, no. 16, p. 8661, 2021.

[8] C. M. Rudin, E. Brambilla, C. Faivre-Finn, and J. Sage, "Small-cell lung cancer," *Nature Reviews Disease Primers*, vol. 7, no. 1, pp. 1–20, 2021.

[9] C. Zappa and S. A. Mousa, "Non-small cell lung cancer: current treatment and future advances," *Translational lung cancer research*, vol. 5, no. 3, p. 288, 2016.

[10] G. S. Jones and D. R. Baldwin, "Recent advances in the management of lung cancer," *Clinical Medicine*, vol. 18, no. Suppl 2, p. s41, 2018.

[11] T. P. Diwanji, P. Mohindra, M. Vyfhuis, J. W. Snider III, C. Kalavagunta, S. Mossahebi, J. Yu, S. Feigenberg, and S. N. Badiyan, "Advances in radiotherapy

techniques and delivery for non-small cell lung cancer: benefits of intensity-modulated radiation therapy, proton therapy, and stereotactic body radiation therapy," *Translational lung cancer research*, vol. 6, no. 2, p. 131, 2017.

[12] M. Araghi, R. Mannani, A. Heidarnejad maleki, A. Hamidi, S. Rostami, S. H. Safa, F. Faramarzi, S. Khorasani, M. Alimohammadi, S. Tahmasebi, *et al.*, "Recent advances in non-small cell lung cancer targeted therapy; an update review," *Cancer cell international*, vol. 23, no. 1, p. 162, 2023.

[13] M. Miller and N. Hanna, "Advances in systemic therapy for non-small cell lung cancer," *Bmj*, vol. 375, 2021.

[14] Y. T. Lee, Y. J. Tan, and C. E. Oon, "Molecular targeted therapy: Treating cancer with specificity," *European journal of pharmacology*, vol. 834, pp. 188–196, 2018.

[15] H. Guo, W. Li, L. Qian, and J. Cui, "Clinical challenges in neoadjuvant immunotherapy for non-small cell lung cancer," *Chinese Journal of Cancer Research*, vol. 33, no. 2, p. 203, 2021.

[16] J. A. Barta, C. A. Powell, and J. P. Wisnivesky, "Global epidemiology of lung cancer," *Annals of global health*, vol. 85, no. 1, 2019.

[17] A. E.-H. El-Kadiry, M. Rafei, and R. Shammaa, "Cell Therapy: Types, Regulation, and Clinical Benefits," *Frontiers in Medicine*, vol. 8, 2021.

[18] ClinicalTrials.gov - U.S. National Library of Medicine. https://clinicaltrials.gov/.

[19] R. C. Sterner and R. M. Sterner, "CAR-T cell therapy: current limitations and potential strategies," *Blood cancer journal*, vol. 11, no. 4, pp. 1–11, 2021.

[20] J. Qu, Q. Mei, L. Chen, and J. Zhou, "Chimeric antigen receptor (CAR)-T-cell therapy in non-small-cell lung cancer (NSCLC): current status and future perspectives," *Cancer immunology, immunotherapy*, vol. 70, no. 3, pp. 619–631, 2021.

[21] C. Lonez and E. Breman, "Allogeneic CAR-T therapy technologies: has the promise

been met?," *Cells*, vol. 13, no. 2, p. 146, 2024.

[22] Z. Tian, T. Yu, J. Liu, T. Wang, and A. Higuchi, "Introduction to stem cells," *Progress in Molecular Biology and Translational Science*, vol. 199, pp. 3–32, 2023.

[23] E. K. Sage, R. M. Thakrar, and S. M. Janes, "Genetically modified mesenchymal stromal cells in cancer therapy," *Cytotherapy*, vol. 18, no. 11, pp. 1435–1445, 2016.

[24] MSCTRAIL for lung cancer. https://gtr.ukri.org/project/A08EAD8D-0EC5-4B7C-A12C-2ECC02D4E7D3.

[25] K. K. Kolluri, G. J. Laurent, and S. M. Janes, "Mesenchymal stem cells as vectors for lung cancer therapy," *Respiration*, vol. 85, no. 6, pp. 443–451, 2013.

[26] Z. Yuan, K. K. Kolluri, K. H. Gowers, and S. M. Janes, "TRAIL delivery by MSC-derived extracellular vesicles is an effective anticancer therapy," *Journal of extracellular vesicles*, vol. 6, no. 1, p. 1265291, 2017.

[27] R. S. Herbst, S. G. Eckhardt, R. Kurzrock, S. Ebbinghaus, P. J. O'Dwyer, M. S. Gordon, W. Novotny, M. A. Goldwasser, T. M. Tohnya, B. L. Lum, *et al.*, "Phase I dose-escalation study of recombinant human Apo2L/TRAIL, a dual proapoptotic receptor agonist, in patients with advanced cancer," *Journal of Clinical Oncology*, vol. 28, no. 17, pp. 2839–2846, 2010.

[28] A. Mohr, S. M. Albarenque, L. Deedigan, R. Yu, M. Reidy, S. Fulda, and R. M. Zwacka, "Targeting of XIAP combined with systemic mesenchymal stem cell-mediated delivery of sTRAIL ligand inhibits metastatic growth of pancreatic carcinoma cells," *Stem cells*, vol. 28, no. 11, pp. 2109–2120, 2010.

[29] L. G. Menon, K. Kelly, H. W. Yang, S.-K. Kim, P. M. Black, and R. S. Carroll, "Human bone marrow-derived mesenchymal stromal cells expressing S-TRAIL as a cellular delivery vehicle for human glioma therapy," *Stem cells*, vol. 27, no. 9, pp. 2320–2330, 2009.

[30] L. Kucerova, V. Altanerova, M. Matuskova, S. Tyciakova, and C. Altaner, "Adipose tissue–derived human mesenchymal stem cells mediated prodrug cancer gene

therapy," *Cancer research*, vol. 67, no. 13, pp. 6304–6313, 2007.

[31] E. Sage, K. Kolluri, K. McNulty, S. Lourenco, T. Kalber, K. Ordidge, D. Davies, Y. C. G. Lee, A. Giangreco, and S. Janes, "Systemic but not topical TRAIL-expressing mesenchymal stem cells reduce tumour growth in malignant mesothelioma," *Thorax*, vol. 69, no. 7, pp. 638–647, 2014.

[32] ClinicalTrials.gov - U.S. National Library of Medicine., "Targeted Stem Cells Expressing TRAIL as a Therapy for Lung Cancer (TACTICAL)." https://clinicaltrials.gov/ct2/show/NCT03298763.

[33] M. Iafrate and G. O. Fruhwirth, "How non-invasive in vivo cell tracking supports the development and translation of cancer immunotherapies," *Frontiers in Physiology*, vol. 11, p. 154, 2020.

[34] P. J. Gawne, F. Man, P. J. Blower, and R. TM de Rosales, "Direct cell radiolabeling for in vivo cell tracking with PET and SPECT imaging," *Chemical reviews*, vol. 122, no. 11, pp. 10266–10318, 2022.

[35] A. Sato, B. Klaunberg, and R. Tolwani, "In vivo bioluminescence imaging," *Comparative medicine*, vol. 54, no. 6, pp. 631–634, 2004.

[36] L. Mezzanotte, M. van't Root, H. Karatas, E. A. Goun, and C. W. Löwik, "In vivo molecular bioluminescence imaging: new tools and applications," *Trends in biotechnology*, vol. 35, no. 7, pp. 640–652, 2017.

[37] H.-L. M. Cheng, "A primer on in vivo cell tracking using MRI," *Frontiers in Medicine*, vol. 10, p. 1193459, 2023.

[38] N. J. Stewart, L. J. Smith, H.-F. Chan, J. A. Eaden, S. Rajaram, A. J. Swift, N. D. Weatherley, A. Biancardi, G. J. Collier, D. Hughes, *et al.*, "Lung MRI with hyperpolarised gases: current & future clinical perspectives," *The British Journal of Radiology*, vol. 95, no. 1132, p. 20210207, 2022.

[39] P. Charoenphun, L. K. Meszaros, K. Chuamsaamarkkee, E. Sharif-Paghaleh, J. R. Ballinger, T. J. Ferris, M. J. Went, G. E. Mullen, and P. J. Blower, "[^{89}Zr]oxinate$_4$

for long-term in vivo cell tracking by positron emission tomography," *European journal of nuclear medicine and molecular imaging*, vol. 42, no. 2, pp. 278–287, 2015.

[40] C. Ashmore-Harris, M. Iafrate, A. Saleem, and G. O. Fruhwirth, "Non-invasive reporter gene imaging of cell therapies, including T cells and stem cells," *Molecular Therapy*, vol. 28, no. 6, pp. 1392–1416, 2020.

[41] G. Severin, J. Engle, T. Barnhart, and J. Nickles, "^{89}Zr Radiochemistry for Positron Emission Tomography," *Medicinal Chemistry*, vol. 7, no. 5, pp. 389–394, 2011.

[42] Y. Zhang, H. Hong, and W. Cai, "PET tracers based on Zirconium-89," *Current radiopharmaceuticals*, vol. 4, no. 2, pp. 131–139, 2011.

[43] J. Posner, P. Barrington, T. Brier, and A. Datta-Mannan, "Monoclonal antibodies: past, present and future," *Concepts and principles of pharmacology*, pp. 81–141, 2019.

[44] S. Alanazi, K. Alzimami, M. Ghannam, I. Aljammaz, F. Alrumayan, and S. Sassi, "Quantitative imaging characteristics of zirconium-89 on Gemini Time-Of-Flight PET/CT," *Nuclear medicine communications*, vol. 37, pp. 1238–1245, 2016.

[45] B. M. Zeglis and J. S. Lewis, "The bioconjugation and radiosynthesis of ^{89}Zr-DFO-labeled antibodies," *Journal of visualized experiments: JoVE*, no. 96, p. 52521, 2015.

[46] P. S. Patrick, K. Kolluri, M. Zaw Thin, A. Edwards, E. Sage, T. Sanderson, B. Weil, J. Dickson, M. Lythgoe, M. Lowdell, S. Janes, and T. Kalber, "Lung delivery of MSCs expressing anti-cancer protein TRAIL visualised with ^{89}Zr-oxine PET-CT," *Stem Cell Research & Therapy*, vol. 11, no. 1, p. 256, 2020.

[47] B. Holman, V. Cuplov, L. Millner, B. Hutton, T. Maher, A. Groves, and K. Thielemans, "Improved correction for the tissue fraction effect in lung PET/CT imaging," *Physics in medicine and biology*, vol. 60, pp. 7387–7402, 2015.

[48] S. Cherry, J. Sorenson, and M. Phelps, *Physics in Nuclear Medicine*. Elsevier Inc.,

2012.

[49] T. Jones and D. Townsend, "History and future technical innovation in positron emission tomography," *Journal of Medical Imaging*, vol. 4, no. 1, p. 011013, 2017.

[50] I. A. E. AGENCY, *Quality Assurance for PET and PET/CT Systems*. No. 1 in Human Health Series, Vienna: INTERNATIONAL ATOMIC ENERGY AGENCY, 2009.

[51] M. Amirrashedi, H. Zaidi, and M. R. Ay, "Advances in preclinical PET instrumentation," *PET clinics*, vol. 15, no. 4, pp. 403–426, 2020.

[52] Z.-g. Chu, Y. Zhang, W.-j. Li, Q. Li, Y.-n. Zheng, and F.-j. Lv, "Primary solid lung cancerous nodules with different sizes: computed tomography features and their variations," *BMC cancer*, vol. 19, no. 1, pp. 1–8, 2019.

[53] D. Clark and C. Badea, "Advances in micro-CT imaging of small animals," *Physica Medica*, vol. 88, pp. 175–192, 2021.

[54] G. B. Saha, PhD, *Basics of PET Imaging Physics, Chemistry, and Regulations*. Springer International Publishing, 3rd ed., 2016.

[55] S. Tong, A. Alessio, and P. Kinahan, "Image reconstruction for PET/CT scanners: past achievements and future challenges.," *Imaging in medicine*, vol. 2, no. 5, pp. 529–545, 2010.

[56] C. Vanhove, M. Koole, P. Fragoso Costa, M. Schottelius, J. Mannheim, C. Kuntner, G. Warnock, W. McDougald, A. Tavares, and M. Bernsen, "Preclinical SPECT and PET: Joint EANM and ESMI procedure guideline for implementing an efficient quality control programme," *European journal of nuclear medicine and molecular imaging*, vol. 51, no. 13, pp. 3822–3839, 2024.

[57] M. M. Khalil, *Basic Science of PET Imaging*. Springer International Publishing, 1st ed., 2017.

[58] I. Rausch, J. Cal-González, D. Dapra, H. J. Gallowitsch, P. Lind, T. Beyer, and G. Minear, "Performance evaluation of the Biograph mCT Flow PET/CT system

according to the NEMA NU2-2012 standard," *EJNMMI physics*, vol. 2, pp. 1–17, 2015.

[59] S. Surti and J. S. Karp, "Update on latest advances in time-of-flight PET," *Physica Medica*, vol. 80, pp. 251–258, 2020.

[60] M. G. Bisogni, A. Del Guerra, and N. Belcari, "Medical applications of silicon photomultipliers," *Nuclear instruments and methods in physics research section A: accelerators, spectrometers, detectors and associated equipment*, vol. 926, pp. 118–128, 2019.

[61] G. A. Prenosil, H. Sari, M. Fürstner, A. Afshar-Oromieh, K. Shi, A. Rominger, and M. Hentschel, "Performance characteristics of the Biograph Vision Quadra PET/CT system with a long axial field of view using the NEMA NU 2-2018 standard," *Journal of nuclear medicine*, vol. 63, no. 3, pp. 476–484, 2022.

[62] Z. Sarnyai, K. Nagy, G. Patay, M. Molnár, G. Rosenqvist, M. Tóth, A. Takano, B. Gulyás, P. Major, C. Halldin, *et al.*, "Performance evaluation of a high-resolution nonhuman primate PET/CT system," *Journal of Nuclear Medicine*, vol. 60, no. 12, pp. 1818–1824, 2019.

[63] B. Knäusl, A. Hirtl, G. Dobrozemsky, H. Bergmann, K. Kletter, R. Dudczak, and D. Georg, "PET based volume segmentation with emphasis on the iterative TrueX algorithm," *Zeitschrift für medizinische Physik*, vol. 22, no. 1, pp. 29–39, 2012.

[64] O. Jacobson, D. Kiesewetter, and X. Chen, "Fluorine-18 Radiochemistry, Labeling Strategies and Synthetic Routes," *Bioconjugate Chemistry*, vol. 26, no. 1, pp. 1–18, 2015.

[65] D. Trani, A. Yaromina, L. Dubois, M. Granzier, S. G. Peeters, R. Biemans, G. Nalbantov, N. Lieuwes, B. Reniers, E. E. Troost, *et al.*, "Preclinical Assessment of Efficacy of Radiation Dose Painting Based on Intratumoral FDG-PET UptakeFDG Dose Painting and Tumor Response," *Clinical Cancer Research*, vol. 21, no. 24, pp. 5511–5518, 2015.

[66] J. Holland, Y. Sheh, and J. Lewis, "Standardized methods for the production of high specific-activity zirconium-89," *Nuclear medicine and biology*, vol. 36, no. 7, pp. 729–739, 2009.

[67] M. Conti and L. Eriksson, "Physics of pure and non-pure positron emitters for PET: A review and a discussion," *EJNMMI Physics*, vol. 3, no. 1, p. 8, 2016.

[68] A. Pepin, J. Daouk, P. Bailly, S. Hapdey, and M.-E. Meyer, "Management of respiratory motion in PET/computed tomography: the state of the art," *Nuclear medicine communications*, vol. 35, no. 2, p. 113, 2014.

[69] S. A. Nehmeh and Y. E. Erdi, "Respiratory motion in positron emission tomography/computed tomography: a review," *Seminars in nuclear medicine*, vol. 38, no. 3, pp. 167–176, 2008.

[70] L. M. Burk, Y. Z. Lee, J. M. Wait, J. Lu, and O. Z. Zhou, "Non-contact respiration monitoring for in-vivo murine micro computed tomography: characterization and imaging applications," *Physics in Medicine & Biology*, vol. 57, no. 18, p. 5749, 2012.

[71] F. Büther, I. Ernst, L. J. Frohwein, J. Pouw, K. P. Schäfers, and L. Stegger, "Data-driven gating in PET: influence of respiratory signal noise on motion resolution," *Medical physics*, vol. 45, no. 7, pp. 3205–3213, 2018.

[72] R. Martin, A. Rubinstein, M. Ahmad, L. Court, and T. Pan, "Evaluation of intrinsic respiratory signal determination methods for 4D CBCT adapted for mice," *Medical physics*, vol. 42, no. 1, pp. 154–164, 2015.

[73] J.-K. Yoon, B.-N. Park, E.-K. Ryu, Y.-S. An, and S.-J. Lee, "Current perspectives on ^{89}Zr-PET imaging," *International Journal of Molecular Sciences*, vol. 21, no. 12, p. 4309, 2020.

[74] Graphics created in BioRender.com. https://biorender.com/.

[75] R. J. Hicks, R. E. Ware, and J. Callahan, "Total-body PET/CT: pros and cons," in *Seminars in Nuclear Medicine*, Elsevier, 2024.

[76] F. Man, A. A. Khan, A. Carrascal-Miniño, P. J. Blower, and R. T. de Rosales, "A kit

formulation for the preparation of [^{89}Zr]Zr(oxinate)$_4$ for PET cell tracking: White blood cell labelling and comparison with [^{111}In]In(oxinate)$_3$," *Nuclear medicine and biology*, vol. 90, pp. 31–40, 2020.

[77] T. J. Ferris, P. Charoenphun, L. K. Meszaros, G. E. Mullen, P. J. Blower, and M. J. Went, "Synthesis and characterisation of zirconium complexes for cell tracking with Zr-89 by positron emission tomography," *Dalton transactions*, vol. 43, no. 39, pp. 14851–14857, 2014.

[78] M. R. Weist, R. Starr, B. Aguilar, J. Chea, J. K. Miles, E. Poku, E. Gerdts, X. Yang, S. J. Priceman, S. J. Forman, *et al.*, "PET of adoptively transferred chimeric antigen receptor T cells with ^{89}Zr-oxine," *Journal of Nuclear Medicine*, vol. 59, no. 10, pp. 1531–1537, 2018.

[79] F. Man, L. Lim, A. Volpe, A. Gabizon, H. Shmeeda, B. Draper, A. C. Parente-Pereira, J. Maher, P. J. Blower, G. O. Fruhwirth, *et al.*, "In vivo PET tracking of ^{89}Zr-labeled Vγ9Vδ2 T cells to mouse xenograft breast tumors activated with liposomal alendronate," *Molecular Therapy*, vol. 27, no. 1, pp. 219–229, 2019.

[80] K. O. Asiedu, S. Koyasu, L. P. Szajek, P. L. Choyke, and N. Sato, "Bone marrow cell trafficking analyzed by ^{89}Zr-oxine positron emission tomography in a murine transplantation model," *Clinical Cancer Research*, vol. 23, no. 11, pp. 2759–2768, 2017.

[81] K. O. Asiedu, M. Ferdousi, P. T. Ton, S. S. Adler, P. L. Choyke, and N. Sato, "Bone marrow cell homing to sites of acute tibial fracture: ^{89}Zr-oxine cell labeling with positron emission tomographic imaging in a mouse model," *EJNMMI research*, vol. 8, pp. 1–11, 2018.

[82] N. Sato, H. Wu, K. O. Asiedu, L. P. Szajek, G. L. Griffiths, and P. L. Choyke, "^{89}Zr-oxine complex PET cell imaging in monitoring cell-based therapies," *Radiology*, vol. 275, no. 2, pp. 490–500, 2015.

[83] Promega. https://www.promega.co.uk/resources/guides/cell-biology/

atp-assays/.

[84] Roche: Cell Proliferation Kit II (XTT). https://www.sigmaaldrich.com/GR/en/product/roche/11465015001.

[85] RealTime-Glo^{TM} Annexin V Apoptosis and Necrosis Assay. https://worldwide.promega.com/products/cell-health-assays/apoptosis-assays/realtime-glo-annexin-v-apoptosis-assay/?catNum=JA1011.

[86] T. T. Pham, A. Chenoweth, N. Patel, A. Banu, G. Osborn, P. J. Blower, S. N. Karagiannis, and M. T. Ma, "In Vivo PET Imaging of ^{89}Zr-Labeled Natural Killer Cells and the Modulating Effects of a Therapeutic Antibody," *Journal of Nuclear Medicine*, vol. 65, no. 7, pp. 1035–1042, 2024.

[87] N. S. Sta Maria, L. A. Khawli, V. Pachipulusu, S. W. Lin, L. Zheng, D. Cohrs, X. Liu, P. Hu, A. L. Epstein, and R. E. Jacobs, "Spatio-temporal biodistribution of ^{89}Zr-oxine labeled huLym-1-A-BB3z-CAR T-cells by PET imaging in a preclinical tumor model," *Scientific Reports*, vol. 11, no. 1, p. 15077, 2021.

[88] H. Sun, R. Yang, J. Wang, X. Yang, J. Tu, L. Xie, C. Li, Q. Lao, and C. Sun, "Component-based biocompatibility and safety evaluation of polysorbate 80," *RSC advances*, vol. 7, no. 25, pp. 15127–15138, 2017.

[89] Z. Yuan, S. D. S. Lourenco, E. K. Sage, K. K. Kolluri, M. W. Lowdell, and S. M. Janes, "Cryopreservation of human mesenchymal stromal cells expressing TRAIL for human anti-cancer therapy," *Cytotherapy*, vol. 18, no. 7, pp. 860–869, 2016.

[90] A. F. Gazdar, F. R. Hirsch, and J. D. Minna, "From mice to men and back: an assessment of preclinical model systems for the study of lung cancers," *Journal of Thoracic Oncology*, vol. 11, no. 3, pp. 287–299, 2016.

[91] R. Tanaka, S. Yoshinouchi, K. Karouji, Y. Tanaka, T. Tominari, M. Hirata, C. Matsumoto, Y. Itoh, C. Miyaura, and M. Inada, "A mouse model of lung cancer induced via intranasal injection for anticancer drug screening and evaluation of pathology," *FEBS Open Bio*, vol. 13, no. 1, pp. 51–59, 2023.

[92] G. A. Elder, M. A. Gama Sosa, and R. De Gasperi, "Transgenic mouse models of Alzheimer's disease," *Mount Sinai Journal of Medicine: A Journal of Translational and Personalized Medicine: A Journal of Translational and Personalized Medicine*, vol. 77, no. 1, pp. 69–81, 2010.

[93] G. Lozano, "Mouse models of p53 functions," *Cold Spring Harbor Perspectives in Biology*, vol. 2, no. 4, p. a001115, 2010.

[94] M. Kovalenko, A. Milnerwood, J. Giordano, J. St. Claire, J. R. Guide, M. Stromberg, T. Gillis, E. Sapp, M. DiFiglia, M. E. MacDonald, *et al.*, "$Htt^{Q111/+}$ Huntington's disease knock-in mice exhibit brain region-specific morphological changes and synaptic dysfunction," *Journal of Huntington's Disease*, vol. 7, no. 1, pp. 17–33, 2018.

[95] M.-c. Kwon and A. Berns, "Mouse models for lung cancer," *Molecular oncology*, vol. 7, no. 2, pp. 165–177, 2013.

[96] Y. Liu, T. Yin, Y. Feng, M. M. Cona, G. Huang, J. Liu, S. Song, Y. Jiang, Q. Xia, J. V. Swinnen, *et al.*, "Mammalian models of chemically induced primary malignancies exploitable for imaging-based preclinical theragnostic research," *Quantitative imaging in medicine and surgery*, vol. 5, no. 5, p. 708, 2015.

[97] G.-Z. Ge, T.-R. Xu, and C. Chen, "Tobacco carcinogen NNK-induced lung cancer animal models and associated carcinogenic mechanisms," *Acta Biochim Biophys Sin*, vol. 47, no. 7, pp. 477–487, 2015.

[98] C. Xu, L. Zhou, L. Lu, T. Chen, S. Wei, X. Lin, and X. Lian, "Inflammation has a role in urethane-induced lung cancer in C57BL/6J mice," *Molecular medicine reports*, vol. 14, no. 4, pp. 3323–3328, 2016.

[99] M. R. Loebinger, A. Eddaoudi, D. Davies, and S. M. Janes, "Mesenchymal stem cell delivery of trail can eliminate metastatic cancer," *Cancer research*, vol. 69, no. 10, pp. 4134–4142, 2009.

[100] Analyze 14.0 - Visualization and Analysis Software for Medical Imaging. https:

//analyzedirect.com/analyze14/.

[101] M. Zaw Thin, C. Moore, T. Snoeks, T. Kalber, J. Downward, and A. Behrens, "Micro-CT acquisition and image processing to track and characterize pulmonary nodules in mice," *Nature Protocols*, vol. 18, no. 3, pp. 990–1015, 2023.

[102] K. H. Barck, H. Bou-Reslan, U. Rastogi, T. Sakhuja, J. E. Long, R. Molina, A. Lima, P. Hamilton, M. R. Junttila, L. Johnson, *et al.*, "Quantification of tumor burden in a genetically engineered mouse model of lung cancer by micro-CT and automated analysis," *Translational oncology*, vol. 8, no. 2, pp. 126–135, 2015.

[103] Hamamatsu Photonics. https://www.hamamatsu.com/eu/en.html.

[104] S. K. Suvarna, C. Layton, and J. D. Bancroft, *Bancroft's Theory and Practice of Histological Techniques*. Elsevier, 8th ed., 2019.

[105] J. Schindelin, I. Arganda-Carreras, E. Frise, V. Kaynig, M. Longair, T. Pietzsch, S. Preibisch, C. Rueden, S. Saalfeld, B. Schmid, *et al.*, "Fiji: an open-source platform for biological-image analysis," *Nature methods*, vol. 9, no. 7, pp. 676–682, 2012.

[106] M. Trotter, P. Olive, and D. Chaplin, "Effect of vascular marker hoechst 33342 on tumour perfusion and cardiovascular function in the mouse," *British journal of cancer*, vol. 62, no. 6, pp. 903–908, 1990.

[107] U. Jarry, M. Bostoën, R. Pineau, L. Chaillot, V. Mennessier, P. Montagne, E. Motte, M. Gournay, A. Le Goff, T. Guillaudeux, *et al.*, "Orthotopic model of lung cancer: isolation of bone micro-metastases after tumor escape from Osimertinib treatment," *BMC cancer*, vol. 21, no. 1, pp. 1–10, 2021.

[108] S.-M. Son, J. Yun, D.-W. Kim, Y.-S. Jung, S.-B. Han, Y. H. Lee, H. S. Han, C. G. Woo, H.-C. Lee, and O.-J. Lee, "MicroRNA 29a therapy for CEACAM6-expressing lung adenocarcinoma," *BMC cancer*, vol. 23, no. 1, p. 843, 2023.

[109] Y. Wang, J. Zhang, Y.-J. Li, N.-N. Yu, W.-T. Liu, J.-Z. Liang, W. W. Xu, Z.-H. Sun, B. Li, and Q.-Y. He, "MEST promotes lung cancer invasion and metastasis

by interacting with VCP to activate NF-κB signaling," *Journal of Experimental & Clinical Cancer Research*, vol. 40, pp. 1–20, 2021.

[110] F. Janker, W. Weder, J.-H. Jang, and W. Jungraithmayr, "Preclinical, non-genetic models of lung adenocarcinoma: a comparative survey," *Oncotarget*, vol. 9, no. 55, p. 30527, 2018.

[111] S. Paget, "The distribution of secondary growths in cancer of the breast," *The Lancet*, vol. 133, no. 3421, pp. 571–573, 1889.

[112] T. Buckle and F. W. Van Leeuwen, "Validation of intratracheal instillation of lung tumour cells in mice using single photon emission computed tomography/computed tomography imaging," *Laboratory animals*, vol. 44, no. 1, pp. 40–45, 2010.

[113] R. A. Madero-Visbal, J. F. Colon, I. C. Hernandez, A. Limaye, J. Smith, C. M. Lee, P. A. Arlen, L. Herrera, and C. H. Baker, "Bioluminescence imaging correlates with tumor progression in an orthotopic mouse model of lung cancer," *Surgical Oncology*, vol. 21, no. 1, pp. 23–29, 2012.

[114] X. Liu, J. Liu, Y. Guan, H. Li, L. Huang, H. Tang, and J. He, "Establishment of an orthotopic lung cancer model in nude mice and its evaluation by spiral CT," *Journal of thoracic disease*, vol. 4, no. 2, p. 141, 2012.

[115] R. M. Wadowsky, S. M. Mietzner, D. P. Skoner, W. J. Doyle, and P. Fireman, "Effect of experimental influenza A virus infection on isolation of Streptococcus pneumoniae and other aerobic bacteria from the oropharynges of allergic and nonallergic adult subjects," *Infection and immunity*, vol. 63, no. 4, pp. 1153–1157, 1995.

[116] N. W. Bartlett, R. P. Walton, M. R. Edwards, J. Aniscenko, G. Caramori, J. Zhu, N. Glanville, K. J. Choy, P. Jourdan, J. Burnet, *et al.*, "Mouse models of rhinovirus-induced disease and exacerbation of allergic airway inflammation," *Nature medicine*, vol. 14, no. 2, pp. 199–204, 2008.

[117] M. D. Tate, D. L. Pickett, N. van Rooijen, A. G. Brooks, and P. C. Reading,

"Critical role of airway macrophages in modulating disease severity during influenza virus infection of mice," *Journal of virology*, vol. 84, no. 15, pp. 7569–7580, 2010.

[118] Y. Abramowitz, N. Simanovsky, M. S. Goldstein, and N. Hiller, "Pleural effusion: characterization with CT attenuation values and CT appearance," *American Journal of Roentgenology*, vol. 192, no. 3, pp. 618–623, 2009.

[119] A. Miranda, D. Bertoglio, S. Stroobants, S. Staelens, and J. Verhaeghe, "Translation of preclinical PET imaging findings: Challenges and motion correction to overcome the confounding effect of anesthetics," *Frontiers in Medicine*, vol. 8, p. 753977, 2021.

[120] Phantech: Preclinical Nuclear Medicine Phantoms - NEMA Standard Phantoms. https://www.phantechmedical.com/preclinnm_nema.html.

[121] National Electrical Manufacturers Association, "Performance measurements of small animal positron emission tomographs," *NEMA Standards Publication, NU 4-2008*, pp. 1–23, 2008.

[122] W. McDougald, C. Vanhove, A. Lehnert, B. Lewellen, J. Wright, M. Mingarelli, C. A. Corral, J. E. Schneider, S. Plein, D. E. Newby, *et al.*, "Standardization of preclinical PET/CT imaging to improve quantitative accuracy, precision, and reproducibility: a multicenter study," *Journal of Nuclear Medicine*, vol. 61, no. 3, pp. 461–468, 2020.

[123] T. J. Bradshaw, M. J. Voorbach, D. R. Reuter, A. M. Giamis, S. R. Mudd, and J. D. Beaver, "Image quality of Zr-89 PET imaging in the Siemens microPET Focus 220 preclinical scanner," *Molecular imaging and biology*, vol. 18, pp. 377–385, 2016.

[124] J. Teuho, L. Riehakainen, A. Honkaniemi, O. Moisio, C. Han, M. Tirri, S. Liu, T. J. Grönroos, J. Liu, L. Wan, *et al.*, "Evaluation of image quality with four positron emitters and three preclinical PET/CT systems," *EJNMMI research*, vol. 10, no. 1, pp. 1–17, 2020.

[125] M. Chomet, M. Schreurs, R. Vos, M. Verlaan, E. J. Kooijman, A. J. Poot,

R. Boellaard, A. D. Windhorst, G. A. van Dongen, D. J. Vugts, *et al.*, "Performance of nanoScan PET/CT and PET/MR for quantitative imaging of ^{18}F and ^{89}Zr as compared with ex vivo biodistribution in tumor-bearing mice," *EJNMMI research*, vol. 11, no. 1, p. 57, 2021.

[126] R. L. Rajendran, M. P. Jogalekar, P. Gangadaran, and B.-C. Ahn, "Noninvasive in vivo cell tracking using molecular imaging: a useful tool for developing mesenchymal stem cell-based cancer treatment," *World Journal of Stem Cells*, vol. 12, no. 12, p. 1492, 2020.

[127] A. V. Meleshina, E. I. Cherkasova, M. V. Shirmanova, N. V. Klementieva, E. V. Kiseleva, L. Đ. Snopova, N. N. Prodanets, and E. V. Zagaynova, "Influence of mesenchymal stem cells on metastasis development in mice in vivo," *Stem cell research & therapy*, vol. 6, pp. 1–10, 2015.

[128] S. Kalimuthu, L. Zhu, J. M. Oh, P. Gangadaran, H. W. Lee, R. L. Rajendran, A. Gopal, S. Y. Jeong, S.-W. Lee, J. Lee, *et al.*, "Migration of mesenchymal stem cells to tumor xenograft models and in vitro drug delivery by doxorubicin," *International Journal of Medical Sciences*, vol. 15, no. 10, pp. 1051–1061, 2018.

[129] T. Hakkarainen, M. Särkioja, P. Lehenkari, S. Miettinen, T. Ylikomi, R. Suuronen, R. A. Desmond, A. Kanerva, and A. Hemminki, "Human mesenchymal stem cells lack tumor tropism but enhance the antitumor activity of oncolytic adenoviruses in orthotopic lung and breast tumors," *Human gene therapy*, vol. 18, no. 7, pp. 627–641, 2007.

[130] L. Leng, Y. Wang, N. He, D. Wang, Q. Zhao, G. Feng, W. Su, Y. Xu, Z. Han, D. Kong, *et al.*, "Molecular imaging for assessment of mesenchymal stem cells mediated breast cancer therapy," *Biomaterials*, vol. 35, no. 19, pp. 5162–5170, 2014.

[131] S.-C. Hung, W.-P. Deng, W. K. Yang, R.-S. Liu, C.-C. Lee, T.-C. Su, R.-J. Lin, D.-M. Yang, C.-W. Chang, W.-H. Chen, *et al.*, "Mesenchymal stem cell targeting

of microscopic tumors and tumor stroma development monitored by noninvasive in vivo positron emission tomography imaging," *Clinical cancer research*, vol. 11, no. 21, pp. 7749–7756, 2005.

[132] K. Knoop, M. Kolokythas, K. Klutz, M. J. Willhauck, N. Wunderlich, D. Draganovici, C. Zach, F.-J. Gildehaus, G. Böning, B. Göke, *et al.*, "Image-guided, tumor stroma-targeted ^{131}I therapy of hepatocellular cancer after systemic mesenchymal stem cell-mediated NIS gene delivery," *Molecular Therapy*, vol. 19, no. 9, pp. 1704–1713, 2011.

[133] M. Tutter, C. Schug, K. A. Schmohl, S. Urnauer, N. Schwenk, M. Petrini, W. J. Lokerse, C. Zach, S. Ziegler, P. Bartenstein, *et al.*, "Effective control of tumor growth through spatial and temporal control of theranostic sodium iodide symporter (NIS) gene expression using a heat-inducible gene promoter in engineered mesenchymal stem cells," *Theranostics*, vol. 10, no. 10, p. 4490, 2020.

[134] C. Schug, W. Sievert, S. Urnauer, A. M. Mueller, K. A. Schmohl, A. Wechselberger, N. Schwenk, K. Lauber, M. Schwaiger, G. Multhoff, *et al.*, "External beam radiation therapy enhances mesenchymal stem cell–mediated sodium–iodide symporter gene delivery," *Human gene therapy*, vol. 29, no. 11, pp. 1287–1300, 2018.

[135] R. M. Dwyer, J. Ryan, R. J. Havelin, J. C. Morris, B. W. Miller, Z. Liu, R. Flavin, C. O'Flatharta, M. J. Foley, H. H. Barrett, *et al.*, "Mesenchymal stem cell-mediated delivery of the sodium iodide symporter supports radionuclide imaging and treatment of breast cancer," *Stem cells*, vol. 29, no. 7, pp. 1149–1157, 2011.

[136] C. Belmar-Lopez, G. Mendoza, D. Oberg, J. Burnet, C. Simon, I. Cervello, M. Iglesias, J. C. Ramirez, P. Lopez-Larrubia, M. Quintanilla, *et al.*, "Tissue-derived mesenchymal stromal cells used as vehicles for anti-tumor therapy exert different in vivo effects on migration capacity and tumor growth," *Bmc Medicine*, vol. 11, pp. 1–16, 2013.

[137] Y. Qiao, J. Gumin, C. J. MacLellan, F. Gao, R. Bouchard, F. F. Lang, R. J.

Stafford, and M. P. Melancon, "Magnetic resonance and photoacoustic imaging of brain tumor mediated by mesenchymal stem cell labeled with multifunctional nanoparticle introduced via carotid artery injection," *Nanotechnology*, vol. 29, no. 16, p. 165101, 2018.

[138] M. R. Loebinger, P. G. Kyrtatos, M. Turmaine, A. N. Price, Q. Pankhurst, M. F. Lythgoe, and S. M. Janes, "Magnetic resonance imaging of mesenchymal stem cells homing to pulmonary metastases using biocompatible magnetic nanoparticles," *Cancer research*, vol. 69, no. 23, pp. 8862–8867, 2009.

[139] T. Lambrou, A. M. Groves, K. Erlandsson, N. Screaton, R. Endozo, T. Win, J. C. Porter, and B. F. Hutton, "The importance of correction for tissue fraction effects in lung PET: preliminary findings," *European journal of nuclear medicine and molecular imaging*, vol. 38, pp. 2238–2246, 2011.

[140] D. E. Rodríguez-Fuentes, L. E. Fernández-Garza, J. A. Samia-Meza, S. A. Barrera-Barrera, A. I. Caplan, and H. A. Barrera-Saldaña, "Mesenchymal stem cells current clinical applications: a systematic review," *Archives of medical research*, vol. 52, no. 1, pp. 93–101, 2021.

[141] W. J. Kang, H.-J. Kang, H.-S. Kim, J.-K. Chung, M. C. Lee, and D. S. Lee, "Tissue distribution of ^{18}F-FDG-labeled peripheral hematopoietic stem cells after intracoronary administration in patients with myocardial infarction," *Journal of Nuclear Medicine*, vol. 47, no. 8, pp. 1295–1301, 2006.

[142] A. Gholamrezanezhad, S. Mirpour, M. Bagheri, M. Mohamadnejad, K. Alimoghaddam, L. Abdolahzadeh, M. Saghari, and R. Malekzadeh, "In vivo tracking of ^{111}In-oxine labeled mesenchymal stem cells following infusion in patients with advanced cirrhosis," *Nuclear medicine and biology*, vol. 38, no. 7, pp. 961–967, 2011.

[143] D. Karussis, C. Karageorgiou, A. Vaknin-Dembinsky, B. Gowda-Kurkalli, J. M. Gomori, I. Kassis, J. W. Bulte, P. Petrou, T. Ben-Hur, O. Abramsky, *et al.*, "Safety

and immunological effects of mesenchymal stem cell transplantation in patients with multiple sclerosis and amyotrophic lateral sclerosis," *Archives of neurology*, vol. 67, no. 10, pp. 1187–1194, 2010.

[144] A. B. Mathiasen, A. A. Qayyum, E. Jørgensen, S. Helqvist, A. Ekblond, M. Ng, K. Bhakoo, and J. Kastrup, "In vivo MRI tracking of mesenchymal stromal cells labeled with ultrasmall paramagnetic iron oxide particles after intramyocardial transplantation in patients with chronic ischemic heart disease," *Stem Cells International*, vol. 2019, no. 1, p. 2754927, 2019.

[145] M. Z. Thin, H. Allan, R. Bofinger, T. D. Kostelec, S. Guillaume, J. J. Connell, P. S. Patrick, H. C. Hailes, A. B. Tabor, M. F. Lythgoe, *et al.*, "Multi-modal imaging probe for assessing the efficiency of stem cell delivery to orthotopic breast tumours," *Nanoscale*, vol. 12, no. 31, pp. 16570–16585, 2020.

[146] A. Moscoso, M. C. Wren, T. Lashley, E. Arstad, M. E. Murray, N. C. Fox, K. Sander, and M. Schöll, "Imaging tau pathology in Alzheimer's disease with positron emission tomography: lessons learned from imaging-neuropathology validation studies," *Molecular neurodegeneration*, vol. 17, no. 1, p. 39, 2022.

[147] Ł. Kiraga, P. Kucharzewska, S. Paisey, Ł. Cheda, A. Domańska, Z. Rogulski, T. P. Rygiel, A. Boffi, and M. Król, "Nuclear imaging for immune cell tracking in vivo–comparison of various cell labeling methods and their application," *Coordination chemistry reviews*, vol. 445, p. 214008, 2021.

[148] L. Scarfe, A. Taylor, J. Sharkey, R. Harwood, M. Barrow, J. Comenge, L. Beeken, C. Astley, I. Santeramo, C. Hutchinson, *et al.*, "Non-invasive imaging reveals conditions that impact distribution and persistence of cells after in vivo administration," *Stem cell research & therapy*, vol. 9, pp. 1–17, 2018.

[149] D. L. Kraitchman, M. Tatsumi, W. D. Gilson, T. Ishimori, D. Kedziorek, P. Walczak, W. P. Segars, H. H. Chen, D. Fritzges, I. Izbudak, *et al.*, "Dynamic imaging of allogeneic mesenchymal stem cells trafficking to myocardial infarction,"

Circulation, vol. 112, no. 10, pp. 1451–1461, 2005.

[150] J. Leibacher and R. Henschler, "Biodistribution, migration and homing of systemically applied mesenchymal stem/stromal cells," *Stem cell research & therapy*, vol. 7, pp. 1–12, 2016.

[151] E. Eggenhofer, V. Benseler, A. Kroemer, F. Popp, E. Geissler, H. Schlitt, C. Baan, M. Dahlke, and M. Hoogduijn, "Mesenchymal stem cells are short-lived and do not migrate beyond the lungs after intravenous infusion," *Frontiers in immunology*, vol. 3, p. 297, 2012.

[152] C. Kuntner and D. Stout, "Quantitative preclinical PET imaging: opportunities and challenges," *Frontiers in physics*, vol. 2, p. 12, 2014.

[153] A.-L. N. Niemeijer, D. E. Oprea-Lager, M. C. Huisman, O. S. Hoekstra, R. Boellaard, I. Bahce, D. J. Vugts, G. A. van Dongen, E. Thunnissen, E. F. Smit, *et al.*, "Study of ^{89}Zr-pembrolizumab PET/CT in patients with advanced-stage non–small cell lung cancer," *Journal of Nuclear Medicine*, vol. 63, no. 3, pp. 362–367, 2022.

[154] I. Kok, J. Hooiveld, P. Van De Donk, D. Giesen, E. Van Der Veen, M. Lub-de Hooge, A. Brouwers, T. Hiltermann, A. van der Wekken, L. Hijmering-Kappelle, *et al.*, "^{89}Zr-pembrolizumab imaging as a non-invasive approach to assess clinical response to PD-1 blockade in cancer," *Annals of Oncology*, vol. 33, no. 1, pp. 80–88, 2022.

[155] M. D. Farwell, R. F. Gamache, H. Babazada, M. D. Hellmann, J. J. Harding, R. Korn, A. Mascioni, W. Le, I. Wilson, M. S. Gordon, *et al.*, "CD8-targeted PET imaging of tumor-infiltrating T cells in patients with cancer: a phase I first-in-humans study of ^{89}Zr-Df-IAB22M2C, a radiolabeled anti-CD8 minibody," *Journal of Nuclear Medicine*, vol. 63, no. 5, pp. 720–726, 2022.

[156] D. R. Beckford-Vera, R. R. Flavell, Y. Seo, E. Martinez-Ortiz, M. Aslam, C. Thanh, E. Fehrman, M. Pardons, S. Kumar, A. N. Deitchman, *et al.*, "First-in-

human immunoPET imaging of HIV-1 infection using ^{89}Zr-labeled VRC01 broadly neutralizing antibody," *Nature communications*, vol. 13, no. 1, p. 1219, 2022.

[157] P. E. Christian, S.-P. Williams, L. Burrell, P. Castaneda, J. Albiani, N. Sandella, A. Iagaru, J. M. Hoffman, A. de Crespigny, and S. S. Bohorquez, "Optimization of ^{89}Zr PET Imaging for Improved Multisite Quantification and Lesion Detection Using an Anthropomorphic Phantom," *Journal of Nuclear Medicine Technology*, vol. 48, no. 1, pp. 54–57, 2020.

[158] J. Fletcher and P. Kinahan, "PET/CT standardized uptake values (SUVs) in clinical practice and assessing response to therapy," *NIH Public Access*, vol. 31, no. 6, pp. 496–505, 2010.

[159] Anthropomorphic Torso Phantom - Data Spectrum. https://www.spect.com/our-products/anthropomorphic-torso-phantom.

[160] N. E. M. Association, "NEMA standards publication NU 2–2018: performance measurements of Positron emission tomographs (PET)," *National Electrical Manufacturers Association*, 2018.

[161] EARL, "EARL PET/CT Accreditation User Manual - Version 4.3," *European Association of Nuclear Medicine (EANM)*, Feb 2024.

[162] T. A. Soderlund, J. Chaal, G. Tjio, J. J. Totman, M. Conti, and D. W. Townsend, "Beyond ^{18}F-FDG: Characterization of PET/CT and PET/MR scanners for a comprehensive set of positron emitters of growing application - ^{18}F, ^{11}C, ^{89}Zr, ^{124}I, ^{68}Ga and ^{90}Y," *Journal of Nuclear Medicine*, vol. 56, pp. 1285–1291, 2015.

[163] N. E. Makris, R. Boellaard, E. P. Visser, J. R. de Jong, B. Vanderlinden, R. Wierts, B. J. van der Veen, H. J. Greuter, D. J. Vugts, G. A. van Dongen, A. A. Lammertsma, and M. C. Huisman, "Multicenter Harmonization of ^{89}Zr PET/CT Performance," *Journal of Nuclear Medicine*, vol. 55, pp. 264–267, 2014.

[164] M. A. Lodge, M. A. Chaudhry, and R. L. Wahl, "Noise considerations for PET quantification using maximum and peak standardized uptake value," *Journal of*

Nuclear Medicine, vol. 53, no. 7, pp. 1041–1047, 2012.

[165] P. Mohr, J. van Sluis, L. Providência, J. H. van Snick, M. N. Lub-de Hooge, A. T. Willemsen, A. W. Glaudemans, R. Boellaard, A. A. Lammertsma, A. H. Brouwers, *et al.*, "Long versus short axial field of view immuno-PET/CT: semiquantitative evaluation for ^{89}Zr-trastuzumab," *Journal of Nuclear Medicine*, vol. 64, no. 11, pp. 1815–1820, 2023.

[166] M. Soret, S. L. Bacharach, and I. Buvat, "Partial-volume effect in PET tumor imaging," *Journal of nuclear medicine*, vol. 48, no. 6, pp. 932–945, 2007.

[167] D. R. Osborne, S. Acuff, S. Cruise, M. Syed, M. Neveu, A. Stuckey, and Y. Bradley, "Quantitative and qualitative comparison of continuous bed motion and traditional step and shoot PET/CT," *American Journal of Nuclear Medicine and Molecular Imaging*, vol. 5, no. 1, p. 56, 2014.

[168] M. E. Daube-Witherspoon and S. R. Cherry, "Scanner design considerations for long axial field-of-view PET systems," *PET clinics*, vol. 16, no. 1, p. 25, 2020.

[169] K. G. Zeimpekis, L. Mercolli, M. Conti, H. Sari, G. Prenosil, K. Shi, and A. Rominger, "Phantom-based evaluation of yttrium-90 datasets using biograph vision quadra," *European journal of nuclear medicine and molecular imaging*, vol. 50, no. 4, pp. 1168–1182, 2023.

[170] J. G. Mannheim, I. Rausch, M. Conti, C. la Fougère, and F. P. Schmidt, "Characterization of the partial volume effect along the axial field-of-view of the Biograph Vision Quadra total-body PET/CT system for multiple isotopes," *EJNMMI physics*, vol. 10, no. 1, p. 33, 2023.

[171] K. Kumamoto, H. Sato, Y. Tsutsui, S. Awamoto, Y. Yamashita, S. Baba, and M. Sasaki, "Continuous Bed Motion in a Silicon Photomultiplier–Based Scanner Provides Equivalent Spatial Resolution and Image Quality in Whole-Body PET Images at Similar Acquisition Times Using the Step-and-Shoot Method," *Journal of nuclear medicine technology*, vol. 50, no. 4, pp. 335–341, 2022.

[172] I. S. Armstrong, M. D. Kelly, H. A. Williams, and J. C. Matthews, "Impact of point spread function modelling and time of flight on FDG uptake measurements in lung lesions using alternative filtering strategies," *EJNMMI physics*, vol. 1, pp. 1–18, 2014.

[173] I. Alberts, J.-N. Hünermund, G. Prenosil, C. Mingels, K. P. Bohn, M. Viscione, H. Sari, B. Vollnberg, K. Shi, A. Afshar-Oromieh, *et al.*, "Clinical performance of long axial field of view PET/CT: a head-to-head intra-individual comparison of the Biograph Vision Quadra with the Biograph Vision PET/CT," *European journal of nuclear medicine and molecular imaging*, vol. 48, pp. 2395–2404, 2021.

[174] D. R. Osborne and S. Acuff, "Whole-body dynamic imaging with continuous bed motion PET/CT," *Nuclear medicine communications*, vol. 37, no. 4, pp. 428–431, 2016.

[175] E. Dijkers, T. Oude Munnink, J. Kosterink, A. Brouwers, P. Jager, J. De Jong, G. Van Dongen, C. Schröder, M. Lub-de Hooge, and E. De Vries, "Biodistribution of ^{89}Zr-trastuzumab and PET imaging of HER2-positive lesions in patients with metastatic breast cancer," *Clinical Pharmacology & Therapeutics*, vol. 87, no. 5, pp. 586–592, 2010.

[176] S. B. Gaykema, A. H. Brouwers, M. N. Lub-de Hooge, R. G. Pleijhuis, H. Timmer-Bosscha, L. Pot, G. M. van Dam, S. B. van der Meulen, J. R. de Jong, J. Bart, *et al.*, "^{89}Zr-bevacizumab PET imaging in primary breast cancer," *Journal of nuclear medicine*, vol. 54, no. 7, pp. 1014–1018, 2013.

[177] P. K. Börjesson, Y. W. Jauw, R. Boellaard, R. De Bree, E. F. Comans, J. C. Roos, J. A. Castelijns, M. J. Vosjan, J. A. Kummer, C. R. Leemans, *et al.*, "Performance of immuno–positron emission tomography with zirconium-89-labeled chimeric monoclonal antibody U36 in the detection of lymph node metastases in head and neck cancer patients," *Clinical Cancer Research*, vol. 12, no. 7, pp. 2133–2140, 2006.

[178] S. N. Rizvi, O. J. Visser, M. J. Vosjan, A. van Lingen, O. S. Hoekstra, J. M. Zijlstra, P. C. Huijgens, G. A. van Dongen, and M. Lubberink, "Biodistribution, radiation dosimetry and scouting of ^{90}Y-ibritumomab tiuxetan therapy in patients with relapsed B-cell non-Hodgkin's lymphoma using ^{89}Zr-ibritumomab tiuxetan and PET," *European journal of nuclear medicine and molecular imaging*, vol. 39, pp. 512–520, 2012.

[179] A. H. Brouwers, J. van Sluis, J. H. van Snick, C. P. Schröder, I. O. Baas, R. Boellaard, A. W. Glaudemans, R. J. Borra, A. A. Lammertsma, R. A. Dierckx, *et al.*, "First-time imaging of [^{89}Zr]trastuzumab in breast cancer using a long axial field-of-view PET/CT scanner," *European Journal of Nuclear Medicine and Molecular Imaging*, vol. 49, no. 10, pp. 3593–3595, 2022.

[180] K. Alzimami and A. Ma, "Effective dose to staff members in a positron emission tomography/CT facility using zirconium-89," *The British Journal of Radiology*, vol. 86, no. 1030, p. 20130318, 2013.